

**DEVELOPMENT OF CELLULOSE-CHITOSAN SILVER
NANOCOMPOSITES FILMS FOR WOUND DRESSING
APPLICATIONS**

EDWIN SHIGWENYA MADIVOLI

DOCTOR OF PHILOSOPHY

(Chemistry)

**JOMO KENYATTA UNIVERSITY OF
AGRICULTURE AND TECHNOLOGY**

2021

**Development of Cellulose-Chitosan Silver Nanocomposites Films for
Wound Dressing Applications**

Edwin Shigwenya Madivoli

**A Thesis Submitted in Partial Fulfillment of the Requirements for
the Degree of Doctor of Philosophy in Chemistry in the Jomo
Kenyatta University of Agriculture and Technology**

2021

DECLARATION

This thesis is my original work and has not been presented for a degree in any other university.

Signature..... Date

Edwin Shigwenya Madivoli

This thesis has been submitted for examination with our approval as supervisors.

Signature..... Date

Prof. Patrick G. Kareru, PhD

JKUAT, Kenya

Signature Date

Prof. Anthony N. Gachanja, PhD

JKUAT, Kenya

Signature Date

Prof. Samuel M. Mugo, PhD

MacEwan University, Canada

Signature Date

Dr. David M. Sujee, PhD

Karatina University, Kenya

DEDICATION

I dedicate this work to my entire family comprising of my wife Lorine Nyambura Nyakairu, my son Liam Madivoli Shigwenya, my parents Mr. and Mrs. Madivoli and my siblings Eliud, Caroline, Gerishom, Josephine, and Lilian.

ACKNOWLEDGEMENT

I thank God for granting me the grace and opportunity to study.

My sincere appreciation goes to my supervisors, Prof. Patrick Kareru, Prof. Anthony Gachanja, Prof Samuel Mugo and Dr. David Sujee for their effort in guiding me throughout this research project.

I wish to thank and appreciate the Research, Production and Extension (RPE) Division of Jomo Kenyatta University of Agriculture and Technology (JKUAT), African-ai-Japan project 2017/2018, National Research Fund (NRF) and Kenya National Innovation Agency (KENIA) 2019/2020 for financing part of this research work, without which it would not have been possible to undertake. I also take this opportunity to thank the Federal commission of Scholarship (FCS), Switzerland, for a one-year research stay under Prof. Katharina Fromm, University of Fribourg where part of this work was carried out and the assistance accorded to me by Dr. Jihane Hankache, University of Fribourg.

More so, I also appreciate the Department of Chemistry for giving us a chance to study and carry out the research in their laboratory. To the Department of Chemistry laboratory technical staff, Mr. Mawili, Mr. Kung'u, Mr. Nderitu, Mrs. Beatrice, Mrs. Isabela and Mr. Njeru, I acknowledge their support and guidance whenever needed.

Lastly, special thanks go out to my entire family comprising of my wife Lorine Nyambura and son Liam Shigwenya, my parents Mr. and Mrs. Madivoli and my siblings Eliud, Caroline, Gerishom, Josephine, and Lilian. I will forever be grateful for the enduring love and support throughout this academic journey.

TABLE OF CONTENTS

DECLARATION.....	ii
DEDICATION.....	iii
ACKNOWLEDGEMENT.....	iv
TABLE OF CONTENTS.....	v
LIST OF TABLES	xii
LIST OF FIGURES	xiv
LIST OF PLATES	xxii
LIST OF APPENDICES	xxiii
LIST OF ABBREVIATIONS AND ACRONYMS	xxvi
ABSTRACT.....	xxix
CHAPTER ONE	1
INTRODUCTION.....	1
1.1 Background of the Study.....	1
1.2 Post-operative Wound Infections.....	1
1.3 Problem Statement	2
1.4 Justification	3
1.5 Hypothesis.....	4
1.6 Objectives.....	4
1.6.1 General Objective.....	4
1.6.2 Specific Objectives.....	5
CHAPTER TWO	6
LITERATURE REVIEW.....	6
2.1 Nano Reinforcing Polymers.....	6
2.1 Nanocomposites with Combined Antimicrobial Properties.....	6

2.2	Metallic Nanoparticles as Antimicrobial Agents	8
2.3	Biomaterials as Wound Dressings	9
2.3.1	Cellulose Nanofibrils (CNFs) and Cellulose Nanocrystals (CNCs)	9
2.3.2	Chitosan.....	11
2.4	pH Responsive Hydrogels.....	13
2.5	Cellulose Chitosan Composites	13
2.6	Functionalization of Cellulose and Chitosan	14
2.6.1	TEMPO-Mediated Oxidation.....	14
2.6.2	Periodate Oxidation of Cellulose	15
2.6.3	Cellulose Chitosan Schiff-Base Reaction.....	16
2.6.4	Dialdehyde Cellulose Dressings.....	17
2.7	Antimicrobial Activity of Silver Containing Composites.....	19
2.8	Kinetics of Silver Release from Composite Films.....	20
	CHAPTER THREE	22
	MATERIALS AND METHODS	22
3.1	Sample Collection and Preparation.....	22
3.1.1	Isolation of Cellulose from <i>Oryza sativa</i> (Rice) Husks	22
3.1.2	Determination of Elemental Composition.....	23
3.1.3	Morphological Fiber Analysis and Particle Size Distribution.....	24
3.1.4	Periodate Oxidation of Cellulose Pulp.....	24
3.1.5	TEMPO Oxidation of Cellulose Pulp.....	25
3.1.6	Isolation of Chitosan from <i>Oreochromis niloticus</i> (Tilapia) Scales.....	26
3.1.7	Conversion Chitosan to Carboxymethyl Chitosan (CMCS)	27
3.2	Green Synthesis of Iron and Silver Nanoparticles	28
3.3	Preparation of Cellulose Chitosan AgNPs Films.....	29

3.3.1	Determination of Optical Transparency	30
3.3.2	Determination of Film Thickness.....	31
3.3.3	Determination of Film Water Solubility and Swelling	31
3.3.4	Determination of Tensile Strength	31
3.3.5	Biodegradability Studies	32
3.3.6	Silver Release Experiments.....	32
3.4	Determination of Functional Groups Present.....	33
3.5	Determination of Degree of Crystallinity and Crystal size.....	33
3.6	TGA Experimental Protocols.....	34
3.7	DSC Experimental Protocols	34
3.8	TEM and SEM Experimental Protocols.....	35
3.9	DLS Experimental Protocol	35
3.10	<i>In-vitro</i> Studies of TOCNF-DAC-CMCS-Ag/Fe Nanocomposites	36
3.10.1	Inoculation of Microorganisms	36
3.10.2	Disc Diffusion Assay	36
3.10.3	<i>In vivo</i> Studies of Scaffolds.....	37
	CHAPTER FOUR.....	38
	RESULTS AND DISCUSSIONS	38
4.1	Isolation of Cellulose and Chitosan	38
4.1.1	Physical Characteristics.....	38
4.1.2	Determination of Elemental Composition.....	39
4.1.3	Morphological Fibre Analysis.....	40
4.1.4	Particle Size Distribution	42
4.1.5	FTIR Characterization of Cellulose Isolated from Rice husks	43
4.1.6	X-ray Diffractograms of Cellulose.....	46

4.1.7	DSC Thermograms of Cellulose	48
4.1.8	TGA-DTGA Thermogram of Cellulose	49
4.2	Synthesis of Dialdehyde Cellulose (DAC)	51
4.2.1	Variation of Oxidant Concentration	51
4.2.2	Variation of Reaction Time	53
4.2.3	Variation of Reaction Temperature	54
4.2.4	FTIR Characterization of Dialdehyde Cellulose (DAC)	55
4.2.5	X-ray Diffractograms of Dialdehyde Cellulose (DAC)	56
4.2.6	DSC Thermograms of Dialdehyde Cellulose Nanofibrils (DAC)	59
4.2.7	TGA-DTGA Thermogram of Dialdehyde Cellulose	62
4.3	Synthesis of TEMPO Oxidized Cellulose Nanofibrils	66
4.3.1	Variation of NaOCl	66
4.3.2	Variation of Cellulose Source	67
4.3.3	FTIR Characterization of TEMPO Oxidized Cellulose (TOCNF)	68
4.3.4	X-ray Diffractograms of TEMPO Oxidized Cellulose Nanofibrils (TOCNF)	71
4.3.5	DSC Thermograms of TEMPO Oxidized Cellulose Nanofibrils (TOCNF)	73
4.3.6	TGA-DTGA Thermogram of TEMPO Oxidized Cellulose (TOCNF)	74
4.3.7	Hydrodynamic Diameter of TOCNF	76
4.3.8	SEM Micrographs of Cellulose, Dialdehyde Cellulose and TOCNF Fibers .	76
4.3.9	TEM Micrographs of Cellulose, Dialdehyde Cellulose and TOCNF	79
4.4	Synthesis of TOCNF-DAC-AgNPs	82
4.4.1	UV-vis Spectra of AgNPs Synthesized using TOCNF-DAC	82
4.4.2	FTIR Characterization of TOCNF-DAC-AgNPs	83

4.4.3	X-ray Diffractogram of TOCNF-DAC-AgNPs.....	84
4.4.4	DSC Thermograms of TOCNF-DAC-AgNPs.....	86
4.4.5	TGA-DTGA Thermograms of TOCNF-DAC-AgNPs.....	87
4.4.6	SEM Micrographs of TOCNF-DAC-AgNPs	89
4.4.7	TEM Micrographs of TOCNF-DAC-AgNPs.....	89
4.4.8	Hydrodynamic Diameter, Zeta potential and Poly-dispersibility Index.....	90
4.4.9	<i>In-vitro</i> Antimicrobial Activity	91
4.5	Synthesis of Carboxymethyl Chitosan.....	93
4.5.1	Variation of Concentration of Monochloroacetic Acid.....	93
4.5.2	FTIR Characterization of Chitosan and Carboxymethyl Chitosan	94
4.5.3	X-ray Diffractograms Chitosan (CS) and Carboxymethylated Chitosan (CMCS).....	96
4.5.4	DSC Thermograms of Chitosan (CS) and Carboxymethyl chitosan (CMCS).....	98
4.5.5	TGA-DTGA Thermograms of Chitosan and Carboxymethyl chitosan.....	101
4.5.6	SEM Micrographs of Chitosan and Carboxymethyl chitosan.....	103
4.5.7	Proton NMR (¹ H-NMR) of Carboxymethyl chitosan	104
4.6	Green Synthesis of Iron Oxide Nanoparticles.....	105
4.6.1	Variation of Ratio of FeCl ₃ to the Extracts Volume	105
4.6.2	Variation of FeCl ₃ Concentration.....	106
4.6.3	FT-IR Characterization of Iron Oxide Nanoparticles.....	108
4.6.4	Powder X-ray Diffractograms of Iron Nanoparticles.....	108
4.6.5	Single Crystal X-Ray Diffractogram of Iron Nanoparticles	110
4.6.6	TGA and DTGA of Iron Nanoparticles.....	111

4.6.7	SEM Micrographs of Iron Nanoparticles	112
4.6.8	Hydrodynamic Diameter, Zeta potential and Poly-dispersibility Index.....	112
4.6.9	TEM Micrographs of Iron Nanoparticles.....	113
4.6.10	Redox Potential of the Extracts and FeNPs	114
4.6.11	<i>In-vitro</i> Antimicrobial Activity of FeNPs	117
4.7	Green Synthesis of AgNPs.....	119
4.7.1	Variation of the Reaction Time.....	119
4.7.2	Variation of the Concentration of AgNO ₃ to Extract.....	120
4.7.3	Variation of Reaction Temperature.....	121
4.7.4	Determination of Band Gap energy from Tauc plot.....	123
4.7.5	FTIR Spectra of AgNPs	124
4.7.6	X-ray Diffractogram of Silver Nanoparticles.....	125
4.7.7	TGA and DTGA Thermograms of AgNPs	126
4.7.8	SEM Micrographs of AgNPs	126
4.7.9	Hydrodynamic Diameter, Zeta potential and Polydispersibility index of AgNps	127
4.7.10	TEM Micrographs of AgNPs	129
4.7.11	Redox Potential of AgNPs	130
4.7.12	<i>In-vitro</i> Antimicrobial Activity of AgNPs	131
4.8	Development of Cellulose Chitosan Composite Films	133
4.8.1	Effect of Glycerine Content on TOCNF-DAC-CS Film Properties.....	133
4.8.2	Effect of Silver Concentration on TOCNF-DAC-CS Film Properties.....	135
4.8.3	Effect of TOCNF-DAC Content on TOCNF-DAC-CS Film Properties.....	138

4.8.4	Biodegradability Studies of TOCNF-DAC-CS Films.....	141
4.8.5	FTIR Characterization of Cellulose Chitosan Composite Films.....	142
4.8.6	X-ray Diffractogram of Cellulose Chitosan Composite Films.....	145
4.8.7	DSC Thermogram of Cellulose Chitosan Composite Films	147
4.8.8	TGA Thermograms of Cellulose Chitosan Composite Films	150
4.8.9	SEM Micrographs of Cellulose Chitosan Composite Films	157
4.8.10	Silver Release Kinetics.....	160
4.8.11	<i>In-vitro</i> Antimicrobial Activity of Cellulose Chitosan Composite.....	162
4.8.12	<i>In-vivo</i> Wound Healing Studies	165
	CHAPTER FIVE.....	168
	CONCLUSIONS AND RECOMENDATIONS	168
5.1	Conclusions.....	168
5.2	Recommendations	169
	REFERENCES.....	170
	APPENDICES	201

LIST OF TABLES

Table 3.1: ICP-OES instrument operating parameters.....	24
Table 4.1: Physical parameters of Rice Husk cellulose (RHCE) and Chitosan Isolated from <i>O. niloticus</i>	38
Table 4.2: Elemental composition of untreated and chemically treated rice husks .	39
Table 4.3: Average Fiber characteristics of Rice husks cellulose fibers as analyzed by MorFi analyzer.	40
Table 4.4: Circular equivalent diameters of cellulose and chitosan fiber	42
Table 4.5: HS circularity of cellulose and chitosan fibers	42
Table 4.6: Aspect ratio of cellulose and chitosan fibers	42
Table 4.7: Total crystallinity index (TCI), lateral order index (LOI) and hydrogen bond intensity (HBI) of studied fibers	45
Table 4.8: Energy of the hydrogen bond (EH) and Hydrogen bond distances (R) ...	46
Table 4.9: d spacing, percent crystallinity and Z value of cellulose fibers	47
Table 4.10: Influence of amount of KOI ₄ on the degree of crystallinity.....	57
Table 4.11: Influence of reaction time on the degree of crystallinity	58
Table 4.12: Determination of carboxyl content of cellulose pulp from various sources	67
Table 4.13: Influence of amount of NaOCl on the crystallinity and carboxyl content of cellulose	72
Table 4.14: Effect of variation of monochloroacetic acid on the degree of substitution (DS) and swelling capacity of CMCS	94
Table 4.15: 2 theta values and hkl indices for phases identified.....	110
Table 4.16: Hydrodynamic diameter, Zeta potential and Poly-dispersibility index (PDI) of AgNps	128

Table 4.17: Effect of glycerin (Gly) content weight, thickness, solubility and swelling of TOCNF-DAC-CS films	134
Table 4.18: Influence of Ag ⁺ ion concentration on the properties of TOCNF-DAC-CS-AgNPs films	138
Table 4.19: Effect of TONCF-DAC content in TOCNF-DAC-CS films on swelling ratio, wettability and tensile strength (ts) of TOCNF-DAC-CS films ..	140
Table 4.20: Peak temperature and residual ash of composite films with different plasticizer content.....	152
Table 4.21: Peak temperature and residual ash of composite films with different AgNPs content.....	154
Table 4.22: Peak temperature and residual ash of composite films with different TOCNF content	155
Table 4.23: Peak temperature and residual ash of TOCNF-CMCS and TOCNF-CMCS-AgNPs	157

LIST OF FIGURES

Figure 2.1: Chemical structure of cellulose	10
Figure 2.2: Chemical structure of chitosan.....	12
Figure 2.3: General mechanism for TEMPO mediated oxidation of cellulose.....	14
Figure 2.4: General mechanism for periodate oxidation of vicinal alcohols	15
Figure 2.5: Synthesis of dialdehyde cellulose through periodate oxidation	15
Figure 2.6: Schematic representation of Schiff base reaction between carbonyl and amine functional group	16
Figure 2.7: Attack of the carbonyl group by an amine during imine bond formation.....	17
Figure 2.8: Deprotonation of N during C=N formation.....	17
Figure 2.9: Preferential surface modification of dialdehyde CNFs	18
Figure 2.10: Pathways in which AgNPs initiate cell damage leading to death of microorganisms.....	19
Figure 3.1: Rice husk treatment steps to obtain cellulose fibers.....	22
Figure 4.1: Conversion of rice husks (a) to cellulose (b).....	38
Figure 4.2: The average length distribution of rice husks fibers measured by MorFi analyzer	41
Figure 4.3: FT-IR spectra of RHCE, MTCE, USCE and TOCNF.....	43
Figure 4.4: X-ray diffractograms of rice husk cellulose after being subjected to different treatments.	47
Figure 4.5: DSC thermograms of ATRH, RHCE, MTCE, USCE, and TOCNF	48
Figure 4.6: TGA curves of ATRH, RHCE, MTCE, USCE, and TOCNF	50
Figure 4.7: DTGA curves of ATRH, RHCE, MTCE, USCE, and TOCNF	50
Figure 4.8: General mechanism for periodate oxidation of cellulose.....	51

Figure 4.9: Influence of amount of KIO_4 on degree oxidation and percent recovery	52
Figure 4.10: Effect of oxidation time on degree of oxidation and percent recovery (%).....	53
Figure 4.11: Schematic representation of influence of reaction temperature on oxidation of cellulose.....	54
Figure 4.12: FT-IR spectra of cellulose and dialdehyde cellulose.....	55
Figure 4.13: X-ray diffractograms of dialdehyde cellulose obtained with different amounts of oxidant per gram of cellulose.....	56
Figure 4.14: X-ray diffractograms of dialdehyde cellulose at different reaction times.....	58
Figure 4.15: Effect of Reaction temperature on crystallinity of dialdehyde cellulose	59
Figure 4.16: DSC thermogram of Dialdehyde cellulose with different aldehyde content.....	60
Figure 4.17: DSC thermogram of Dialdehyde cellulose after different oxidation times.....	60
Figure 4.18: DSC thermogram of Dialdehyde cellulose after different oxidation temperatures.....	61
Figure 4.19: TGA curves of dialdehyde cellulose with different degree of oxidation	62
Figure 4.20: DTGA curves of dialdehyde cellulose with different degree of oxidation	63
Figure 4.21: TGA curves of dialdehyde cellulose with different oxidation time	64
Figure 4.22: DTGA curves of dialdehyde cellulose with different oxidation time ..	64
Figure 4.23: TGA curves of dialdehyde cellulose with different oxidation temperatures.....	65

Figure 4.24: DTGA curves of dialdehyde cellulose with different oxidation temperatures.....	65
Figure 4.25: Effect of NaOCl concentration on Carboxylic content of TOCNF.....	66
Figure 4.26: Reaction scheme representing conversion of cellulose to TOCNF, DAC and TOCNF-DAC-AgNPs.....	69
Figure 4.27: FT-IR spectra of TEMPO oxidized cellulose pulp with different carboxyl content.....	69
Figure 4.28: FT-IR spectra of TEMPO oxidized cellulose before (COONa) and after (COOH) ion exchange	70
Figure 4.29: X-ray diffractograms of TOCNF with different carboxyl content.....	71
Figure 4.30: X-ray diffractograms of TOCNF with NaCl impurity peaks	72
Figure 4.31: DSC thermograms of TEMPO oxidized cellulose with different carboxyl content.....	73
Figure 4.32: TGA thermograms of TOCNF with different carboxyl content.....	74
Figure 4.33: DTGA thermograms of TOCNF with different carboxyl content.....	75
Figure 4.34: Distribution of hydrodynamic diameter of TOCNF.....	76
Figure 4.35: Fiber length distribution of cellulose. Inset TEM micrograph of cellulose	79
Figure 4.36: Fiber width distribution of cellulose before oxidation. Inset TEM micrograph of cellulose.	80
Figure 4.37: Fiber length distribution of dialdehyde cellulose. Inset TEM micrograph of dialdehyde cellulose.	80
Figure 4.38: Fiber length distribution of TEMPO oxidized cellulose. Inset TEM micrograph of TEMPO oxidized cellulose.	81
Figure 4.39: UV-Vis spectra of AgNPs synthesized from 0.01M AgNO ₃ using TOCNF	82

Figure 4.40: FT-IR spectra of TOCNF-DAC and TOCNF-DAC-AgNPs composite	83
Figure 4.41: X-ray powder diffraction patterns of CNFs and AgNPs@CNF.....	85
Figure 4.42: DSC thermograms of TOCNF-DAC and TOCNF-DAC-AgNPs	86
Figure 4.43: TGA/DTGA thermograms of TOCNF-DAC	87
Figure 4.44: TGA-DTGA thermograms of TOCNF-DAC-AgNPs	88
Figure 4.45: Length Distribution of TOCNF-AgNPs and TEM micrographs of TOCNF-DAC-AgNPs fibers.....	90
Figure 4.46: Hydrodynamic diameters of TOCNF-DAC-AgNPs fibers from rice husks	91
Figure 4.47: <i>In-vitro</i> antimicrobial assay of TOCNF-DAC-AgNPs.....	92
Figure 4.48: FT-IR spectra of chitosan standard and <i>O. niloticus</i> chitosan.....	95
Figure 4.49: FT-IR spectra of carboxymethyl chitosan (Sodium Form COONa)	95
Figure 4.50: WXR D diffractogram of Chitosan synthesized from <i>O. niloticus</i>	97
Figure 4.51: WXR D diffractogram of carboxylmethylchitosan (CMCS) and commercial chitosan (COCS)	97
Figure 4.52: DSC thermogram of commercial chitosan (COCS)	99
Figure 4.53: DSC thermogram of <i>O. niloticus</i> chitosan (ONCS)	99
Figure 4.54: DSC thermogram of carboxymethyl chitosan (CMCS)	100
Figure 4.55: TGA/DTGA curves of <i>O. niloticus</i> Chitosan (ONCS).....	101
Figure 4.56: TGA/DTGA curves of Commercial Chitosan (COCS).....	102
Figure 4.57: TGA/DTGA curves of carboxymethyl chitosan (CMCS).....	102
Figure 4.58: Proton NMR spectra of carboxymethyl chitosan	104
Figure 4.59: UV-vis spectrums showing variations of volume ratio of metal ion to volume of extracts used. Inset showing change in color of FeCl ₃ (A), Extracts (B) and Nanoparticles (C).....	105

Figure 4.60: Phyto-mediated synthesis of iron nanoparticles using plant extracts.	105
Figure 4.61: UV-vis spectrums showing variations of metal ion concentration in solution. Inset showing nanoparticles formed when 0.1M solutions are used.....	107
Figure 4.62: FT-IR spectra of Iron nanoparticles synthesized using <i>L. trifolia</i> extracts.	108
Figure 4.63: Powder X-ray diffractogram of FeNPs synthesized using aqueous extracts of <i>Lantana trifolia</i>	109
Figure 4.64: X-ray diffractogram of iron nanoparticles synthesized using aqueous extracts of <i>Lantana trifolia</i>	110
Figure 4.65: TGA and DTGA thermograms of iron nanoparticles synthesized using <i>L. trifolia</i> extracts.....	111
Figure 4.66: Size distribution of iron oxide nanoparticles synthesized using <i>L. trifolia</i> extracts	113
Figure 4.67: TEM micrographs of Iron nanoparticles synthesized using <i>L. trifolia</i> extracts.....	114
Figure 4.68: Cyclic voltammogram of <i>L. trifolia</i> extracts showing the reduction potential... ..	115
Figure 4.69: Cyclic voltammogram of FeNPs showing the reduction potential.....	115
Figure 4.70: Cyclic voltammogram of 0.1M Ascorbic acid standard showing the reduction potential.	116
Figure 4.71: Proposed chemical structure of Fe-P NPs (A); and (b) proposed condensation mechanism of Fe-polyphenol.	117
Figure 4.72: Antimicrobial activity of FeNPs against <i>S. aureus</i> , <i>B. subtilis</i> , <i>P. aeruginosa</i> , <i>E. coli</i> , and <i>C. albicans</i>	118
Figure 4.73: Variation of synthesis time against measurement of plasmon resonance of AgNPs.....	120

Figure 4.74: Variation of Ratio of Extracts Volume to concentration of AgNO ₃ used.	121
Figure 4.75: Variation of reaction temperature during synthesis of AgNPs.....	122
Figure 4.76: Uv-vis spectrum of AgNPs synthesized at 30 °C. Insert Tauc plot for AgNPs	123
Figure 4.77: FT-IR spectra of AgNPs synthesized using <i>L. trifolia</i> extracts.....	124
Figure 4.78: X-ray diffractogram of Phyto synthesized AgNPs.....	125
Figure 4.79: TGA and DTGA of AgNPs synthesized using <i>L. trifolia</i> extracts.....	126
Figure 4.80: Particle diameter distribution of AgNPs synthesized at 35 °C.	128
Figure 4.81: Size distribution of AgNPs synthesized using <i>L. trifolia</i> extracts. Inset TEM micrographs of AgNPs.	129
Figure 4.82: Cyclic voltammogram of AgNPs synthesized using <i>L. trifolia</i> extracts.	130
Figure 4.83: Zones of inhibition of AgNPs against <i>E. coli</i> , <i>P. aeruginosa</i> <i>S. aureus</i> , <i>C. albicans</i> , and <i>B. subtilis</i>	132
Figure 4.84: Transparency of TOCNF-DAC-CS films with different glycerin content.....	133
Figure 4.85: Plasmon resonance peak of AgNPs in TOCNF-DAC-CS-AgNPs films prepared with different Ag ⁺ (6.75 -100 mM).....	136
Figure 4.86: Optical transparency of TOCNF-DAC-CS-AgNPs composite films with different AgNPs content	137
Figure 4.87: Degradation of TOCNF-DAC-CS-AgNPs films as a function of number of days.....	142
Figure 4.88: FT-IR Spectra of TOCNF-DAC-CMCS and TOCNF-DAC-CMCS Composites.....	143
Figure 4.89: FT-IR Spectra of TOCNF-DAC-CS and TOCNF-DAC-CS-AgNPs composite films.....	144

Figure 4.90: X-ray diffractogram of TOCNF-CMCS Composites.....	145
Figure 4.91: X-ray diffractogram of TOCNF-DAC-CMCS and TOCNF-DAC-CMCS-AgNPs Composites.....	146
Figure 4.92: X-ray diffractogram of TOCNF-DAC-CS-AgNPs Composites	147
Figure 4.93: DSC thermogram of TOCNF-CMCS and TOCNF-CMCS Composites.....	148
Figure 4.94: DSC thermogram of TOCNF-DAC-CMCS and TOCNF-DAC-CMCS-AgNPs Composite.....	148
Figure 4.95: DSC thermogram of TOCNF-DAC-CS-AgNPs films with different AgNPs content	149
Figure 4.96: DSC thermogram of TOCNF-DAC-CS-AgNPs films with different glycerin (Gly) content.....	149
Figure 4.97: DSC thermogram of TOCNF-DAC-CS-AgNPs films with different TOCNF-DAC content.....	150
Figure 4.98: TGA thermograms of TOCNF-DAC-CS films with different Glycerin content.....	151
Figure 4.99: DTGA thermograms of DACNF-CS films with different Glycerin content.....	152
Figure 4.100: TGA thermograms of TOCNF-DAC-CS films with different AgNPs content.....	153
Figure 4.101: DTGA thermograms of TOCNF-DAC-CS films with different AgNPs content.....	153
Figure 4.102: TGA thermograms of TOCNF-DAC-CS films with different TOCNF content.....	154
Figure 4.103: DTGA thermograms of TOCNF-DAC-CS films with different TOCNF content.....	155
Figure 4.104: TGA and DTGA Thermogram of TOCNF-DAC-DAC-CMCS.....	156

Figure 4.105: TGA and DTGA Thermogram of TOCNF-DAC-CMCS-AgNPs ...	156
Figure 4.106: Size distribution of AgNPs distributed on TOCNF-DAC-CS-AgNPs composite films.....	159
Figure 4.107: Slow release of AgNPs from TOCNF-DAC-CS-AgNPs composite films	160
Figure 4.108: Total silver ion released from AgNPs-composite films as determined by ICP-MS	161
Figure 4.109: Pseudo first order plot for silver ion released from composite films.....	162
Figure 4.110: Inhibition zones of TOCNF-DAC-CS and TOCNF-DAC-CS-AgNPs.....	163

LIST OF PLATES

Plate 4.1: SEM image of micrographs of RHCE	77
Plate 4.2: SEM micrographs of dialdehyde cellulose at different view field.....	77
Plate 4.3: SEM micrographs of TEMPO oxidized cellulose (TOCNF).....	78
Plate 4.4: SEM micrographs of TOCNF-DAC and TOCNF-DAC-AgNPs.....	89
Plate 4.5: Swelling of carboxymethyl chitosan (CMCS) in water.	93
Plate 4.6: SEM Micrographs of Chitosan and Carboxymethyl chitosan.....	103
Plate 4.7: SEM micrographs of iron nanoparticles synthesized using <i>L. trifolia</i> extracts	112
Plate 4.8: SEM Micrographs of AgNPS synthesized using <i>L. trifolia</i> extracts.	127
Plate 4.9: Antimicrobial activity of AgNPs against selected microorganisms	131
Plate 4.10: Nanocomposite films prepared using different concentration of Ag ions.	136
Plate 4.11: Raw CMCS (A), TOCNF-DAC (B), and TOCNF-CMCS-AgNPs (C), TOCNF-DAC-CS films	139
Plate 4.12: SEM Micrographs of TOCNF-DAC-CMCS and TOCNF-DAC-CMCS- AgNPs	158
Plate 4.13: SEM micrographs of TOCNF-DAC-CS and TOCNF-DAC-CS- AgNPs	158
Plate 4.14: Zone of Inhibition of AgNPs composite films prepared using 25 mM AgNO ₃	163
Plate 4.15: Zone of Inhibition of AgNPs composite films prepared using 50 mM AgNO ₃	164
Plate 4.16: Wound healing process of composite films (CNF) and cotton gauze (C) after fourteen days	166

LIST OF APPENDICES

Appendix I: Peak temperatures, enthalpy of cellulose obtained from DSC curves	201
Appendix II: Degradation temperatures and residual ash of rice husk after different treatment.....	202
Appendix III: ANOVA of the effect KIO ₃ concentration variation on the DO of DAC	203
Appendix IV: ANOVA of the effect of reaction time variation on the DO of DAC	204
Appendix V: FT-IR Spectra of KIO ₃ generated after the oxidation of Cellulose with KIO ₄	205
Appendix VI: Peak temperatures, enthalpy of DAC obtained from DSC curves.	206
Appendix VII: Peak temperature and residual ash of DAC with different DO	207
Appendix VIII: Peak temperature and residual ash of DAC with different DO	208
Appendix IX: Peak temperature and residual ash of DAC after different oxidation temperatures	209
Appendix X: Potentiometric Titration of cellulose oxidized with 0.2 mmol NaOCl.	210
Appendix XI: Potentiometric Titration of cellulose oxidized with 0.8 mmol NaOCl.	211
Appendix XII: Potentiometric Titration of cellulose oxidized with 1.82 mmol NaOCl.	212
Appendix XIII: Potentiometric Titration of cellulose oxidized with 3.25 mmol NaOCl	213

Appendix XIV: ANOVA of the effect NaOCl concentration variation on the DO of TOCNF.....	214
Appendix XV: ANOVA of the effect of cellulose source variation on the DO of TOCNF.....	215
Appendix XVI: Peak temperatures of TOCNF with different carboxyl content obtained from DSC curves.	216
Appendix XVII: Peak temperature and residual ash of TOCNF with different oxidation time obtained from TGA-DTGA curves.....	217
Appendix XVIII: ANOVA of the effect of monochloroacetic acid concentration variation on the DS of chitosan.....	218
Appendix XIX: ANOVA of the effect of monochloroacetic acid concentration variation on the swelling capacity of chitosan.....	219
Appendix XX: Peak temperatures, enthalpy of chitosan and carboxymethyl chitosan obtained from DSC curves.	220
Appendix XXI: Peak temperature and residual ash of Chitosan (CS) and carboxymethyl chitosan (CMCS).....	221
Appendix XXII: Biosynthesis of AgNPs using <i>L. trifolia</i> at 20 °C.....	222
Appendix XXIII: Biosynthesis of AgNPs using <i>L. trifolia</i> at 25 °C.....	223
Appendix XXIV: Biosynthesis of AgNPs using <i>L. trifolia</i> at 30 °C.....	224
Appendix XXV: Biosynthesis of AgNPs using <i>L. trifolia</i> at 35 °C.....	225
Appendix XXVI: Inhibition zones for standard antibiotics.....	226
Appendix XXVII: ANOVA of the effect of glycerin content on the solubility of TOCNF-DAC-CS films.....	227
Appendix XXVIII: ANOVA of the effect of glycerin content on the swelling of TOCNF-DAC-CS films.....	228
Appendix XXIX: ANOVA of the effect of AgNPs content on the solubility of TOCNF-DAC-CS-AgNPs films.....	229

Appendix XXX: ANOVA of the effect AgNPs content on the swelling of TOCNF-DAC-CS-AgNPs films	230
Appendix XXXI: ANOVA of the effect of TOCNF content on the solubility of TOCNF-DAC-CS-AgNPs films.....	231
Appendix XXXII: ANOVA of the effect TOCNF content on the swelling of TOCNF-DAC-CS-AgNPs films	232
Appendix XXXIII: Second order plot of silver ion release from composite films..	233
Appendix XXXIV: Rate of silver ion released from composite films.	234

LIST OF ABBREVIATIONS AND ACRONYMS

AgNPs	Silver Nanoparticles
AGU	Anhydroglucose units
ANOVA	Analysis of Variance
ATRH	Alkali treated rice husks
CE	Circular equivalent diameter
Cel	Cellulose
CF	Coconut fibers
CH	Coffee husks
CI	Crystallinity index
CMCS	Carboxymethyl chitosan
CNF	Cellulose Nanofibrils
CO	Commercial cellulose
CS	Chitosan
DAC	Dialdehyde cellulose
DAC-CMCS	Dialdehyde cellulose carboxymethyl chitosan
DO	Degree of oxidation
DSC	Differential Scanning Calorimeter
DTGA	Derivative Thermal Gravimetric Analysis

FeNPs	Iron Nanoparticles
FT-IR	Fourier Transform Infrared Spectrophotometer
GO	Graphene Oxide
HS	High sensitivity circularity
ICP-OES	Inductively Coupled Plasma Optical Emission Spectrophotometer
MTRH	Mechanically treated cellulose
RGO	Reduced graphene oxide
RH	Rice husk
RHCE	Rice husk cellulose
SB	Sugar cane bagasse
SEM	Scanning Electron Microscope
TEM	Transmission Electron Microscope
TEMPO	2,2,6,6-tetramethylpiperidine-1-oxyl
T_g	Glass transition temperature
TGA	Thermal gravimetric analyser
TOCNF	Tempo oxidized cellulose
TOCNF-CMCS	Tempo oxidized cellulose nanofibrils carboxymethyl chitosan
TOCNF-DAC	Tempo oxidized dialdehyde cellulose

USCE	Ultra sonicated cellulose
W	load
W_f	Final weight
W_i	Initial weight
WXR	Wide angle X-ray Diffractometer

ABSTRACT

Modern wound dressings keep the wound hydrated but they lack antimicrobial properties hence they cannot prevent infections. In this study, wound dressings were made from tempo oxidized cellulose chitosan nanocomposite embedded with silver nanoparticles (AgNPs). Cellulose was isolated from rice husks (*Oryza sativa*) followed by oxidation of its hydroxyl groups to carboxylic and carbonyl groups resulting in oxidized cellulose nanofibrils. Dispersion of the nanofibrils in silver nitrate-chitosan solution resulted in synthesis of AgNPs in the composite films obtained after solvent casting. The cellulose fibers had mean fiber lengths and diameters of between 23-45 μm and $8.55\pm 7.35 \mu\text{m}$ as determined by MorFi analyzer. The IR spectra of cellulose had peaks at 3329, 2900, 1684 and 1070 cm^{-1} associated with OH, CH₂, bound water and C-O-C functional groups respectively. Introduction of C=O at C₂-C₃ was confirmed by presence of a carbonyl peak at 1720 cm^{-1} and a single amorphous peak in the X-ray diffractogram. For the case of tempo oxidized cellulose, an IR peak at 1720 cm^{-1} was attributed to C=O groups of COOH group at C₆. Morphology of the samples changed upon oxidation to highly porous surface as observed in the SEM micrographs. These treatments also resulted in changes in thermal stability, the degree of crystallinity and fiber lengths. Crosslinking of oxidized cellulose with chitosan was confirmed by the disappearance of the C=O Infra-red vibrational frequency at 1720 cm^{-1} and the absence of cellulose peaks normally observed at 2θ of 16, 22 and 33° in the X-ray diffractograms. Presence of AgNPs in the films was confirmed by the sharp, distinct peaks in the X-ray diffractograms at $2\theta = 28, 32, 38, 45, 55, \text{ and } 59^\circ$ and spherical particles with diameters between 100 - 800 nm in the SEM micrographs. The release of AgNPs from the composite films was confirmed from the gradual increase of its plasmon resonance peak at 412 nm in a first order kinetics with the rate of release being 25 ppm/h. The tensile strength, swelling capacity, transmittance and biodegradability of the films were found to be dependent on the TOCNF, glycerin and AgNPs content of the films. The microbial inhibition of the composite film against *E. coli*, *B. subtilis*, *C. albicans*, *S. aureus*, *P. mirabilis*, *P. aeruginosa* was found to be $12\pm 1, 10.7\pm 0.6, 11\pm 1, 12.7\pm 0.6, 12.7\pm 0.6, 10.3\pm 0.6$ mm attributed to release of AgNPs. As for the control, the inhibitions were found to be $13\pm 1, 7.3\pm 1, 23.3\pm 0.6, 0, 24.7\pm 0.5, 10\pm 0.6$ and 0 mm for *E. coli*, *B. subtilis*, *C. albicans*, *S. aureus*, *P. mirabilis*, *P. aeruginosa*, respectively. *In-vivo* studies revealed that the dressing could accelerate wound healing through release of AgNPs that inhibited the growth of microorganism. In conclusion, the developed nanocomposite films could be used as wound dressings to prevent the growth of microorganisms.

CHAPTER ONE

INTRODUCTION

1.1 Background of the Study

1.2 Post-operative Wound Infections

The emergence of bacterial antimicrobial resistance associated with post-surgical infections make the choice of empirical therapy more difficult and expensive (Andhoga *et al.*, 2002). Wounds have remained a conducive environment for growth of different bacteria, most of which are acquired during post-operative period. Antibacterial agents disrupt one or more of the cellular functions of bacteria leading to their death (Andhoga *et al.*, 2002). For example, depending on the type of antibacterial agent, the mechanism of activity may result in inhibition of DNA replication; inhibition of the production of proteins or cell wall materials; or disruption of cell membrane activities that maintain chemical balance (WHO, 2014). Moreover, due to mutation during gene replication or gene encoding, bacteria can also acquire resistance to one or more of the antibacterial agents to which they would normally be susceptible (Courvallin, 2008). The ease with which resistance can be acquired varies between bacterial types. Unfortunately, some strains of bacteria such as *Staphylococcus aureus*, which are normally not susceptible to antibacterial agents are also easily able to acquire resistance from others which leads to multidrug resistance (Laxminarayan *et al.*, 2013). In extreme cases, bacteria can show resistance to most or all chemical therapeutics (Courvallin 2008; WHO, 2014).

In a study to investigate the organisms present in post wound infections, the most predominant organisms isolated were *Staphylococcus aureus* (54.7 %), *Proteus mirabilis* (15.5 %), *Pseudomonas aeruginosa* (11.9 %) and *Escherichia coli* (2.3 %) (Andhoga *et al.*, 2002). Indiscriminate use of antibiotics has led to both Gram-positive and Gram-negative bacteria showing resistance to commonly used antibiotics. A study conducted by Andhoga *et al.*, (2002) found that *S. aureus* had 80.4 % resistant to methicillin implying that the strain will be resistant to penicillin and cephalosporin. *Pseudomonas* was found to be susceptible to most drugs except ampicillin and

cotrimoxazole. *Proteus* displayed a mixed pattern of sensitivity, being least sensitive to ampicillin (15.3 %) while all *E. coli* were sensitive to gentamicin and nalidixic acid but resistant to ampicillin and cotrimoxazole. In a similar study, Dinda *et al.*, (2013) found that the pathogens in post-operative wounds included Coagulase negative *Staphylococcus* (15.4 %), *S. aureus* (30.8 %), *Pseudomonas aeruginosa* (10.4 %), *Kluyvera spp* (12.7 %), *E coli* (12.8 %), *Klebsiella* species (12.8%), *Serratia marcescens* (2.6 %) and *Escherichia cloacae* (2.6 %). The most prevalent pathogen isolated from the pus swabs taken from patients with post-operative history was *S. aureus* (Dinda *et al.*, 2013).

Development of wound dressings has seen significant improvement since ancient times. These improvements range from use of natural materials to simply protect the wounds to new materials that can be tailored to exhibit various extraordinary functions. For instance, modern bandages are made of electro spun biopolymers which can contain bioactive components that can aid the healing process. Most are fibrous in nature, with the size of fibres segments ranging from tens of nanometres to micrometres. The bandages could be made to contain bioactive components, such as antimicrobial, and anti-inflammatory agents, which could be released to the wounds during healing thereby enhancing recovery (Zahedi *et al.*, 2010). In treatment of burns, hydrocolloids (silicon coated nylons), polyurethane films, biosynthetic skins, fibres, antimicrobial (silver and iodine) dressings (Loke *et al.*, 2000), secondary adhesive dressings, wound dressing pads, and hydrogels (Hoffman 2012) are the most preferred types of dressings. However, removal of these dressings leads to traumatization of newly epithelialized tissues, delayed healing, and pain, as they adhere to the wound surface requiring mechanical debridement for a dressing change. Repeated painful dressing changes and microbial infections further increase tissue damage which lead to the development of periwound maceration (Wasiak *et al.*, 2013).

1.3 Problem Statement

One of the greatest challenges of wound management is the lack of effective therapeutic agents that can prevent the growth and proliferation of microorganisms in the wound area. While this growth can be controlled through subsequent cleaning and

application of antibiotics during dressing changes, this process often leads to additional trauma to the patient resulting in more damage. Moreover, with the rising cases of bacterial resistance to conventional medication being observed the world over, this poses additional challenges in the management of chronic wounds. This is as a result of conventional medication not being able to adequately prevent the rapid microbial colonization which subsequently leads to development of infections that are difficult to treat and often require a cocktail of antibiotics. With such antibiotic regimens, there are increasing cases of resistance against conventional antimicrobial medication being reported, which leads to a subsequent rise in chronic wound infections being observed (osteomyelitis, post-operative wounds infections, endocarditis, septic arthritis among others). In Kenya, most wound infections are caused by *Staphylococcus aureus*, *Proteus*, *Pseudomonas*, and *Escherichia coli* bacterial species although other types of species have also been isolated from wounds. Infections induced by these strains not only puts an additional strain to an already fragile health system but they often lead to deaths of many patients in developing countries such as Kenya. Moreover, a spike in such infections also lead to the need to use more expensive medications hence the need to develop new cost effective, therapeutic agents capable of working against bacteria causing infections in wounds. This study therefore sought to develop wound dressings that can be able to prevent the growth of infections through incorporation of antimicrobial silver nanoparticles within the composite materials.

1.4 Justification

There is great interest to develop materials that can combat microbial colonization in chronic wounds. Development of such biomaterials using nanotechnology is a promising endeavor because it provides new solutions mainly because of small dimensions of the created systems. One of the most effective and promising materials are nanocomposites based on biodegradable biomaterials such as cellulose, chitosan, starch and alginate embedded with antimicrobial agents such as AgNPs. These hybrid materials, based on biodegradable nanocomposites, have gathered much of scientists' attention as they have been reported to have the capability to inhibit microbial

colonization in wounds. Application of nanotechnology in creating new, effective medicines enables application of innovative solutions in fighting pathogenic microorganism. Small dimensions of nanomaterials provide unique physicochemical and biological properties that can be used in wound dressings. As such, cellulose nanocrystals and cellulose nanofibrils have found applications in various fields such as enzyme immobilization, synthesis of antimicrobial and medical devices, green catalysis, biosensing and synthetic drug carriers in therapeutic and diagnostic medicines, among others. As drug carriers, the nanomaterials have several advantages such as hydrophilicity, small size, biodegradable, biocompatibility, and the ease in which they can be functionalized or chemically crosslinked with other polymers such as chitosan. Moreover, cellulose based materials have an open core structure and a high surface area which makes them find applications in biomedical and pharmaceutical industries as they can provide enhanced drug bioavailability and better drug loading capacity. Due to their unique properties, these as synthesized nanomaterials have the potential of being used in various applications such as pH sensors, barrier films, and wound dressings but nanocomposite containing the nanofibrils have many more applications. Hence this study sought to develop cellulose-chitosan nanocomposite films embedded with AgNPs for wound dressing applications.

1.5 Hypothesis

Cellulose-chitosan silver nanocomposite films cannot be used as wound dressings capable of preventing antimicrobial infections in wounds.

1.6 Objectives

1.6.1 General Objective

To develop cellulose-chitosan silver nanocomposites films capable of preventing growth of infection in wounds and aid the healing process.

1.6.2 Specific Objectives

- i. To isolate cellulose and chitosan from *Oryza sativa* husks and *Oreochromis niloticus* scales through chemical treatment and to evaluate their elemental composition, morphology, and particle size using ICP-OES, TEM, SEM, XRD.
- ii. To determine the effect of temperature, time and concentration of potassium periodate, sodium hypochlorite, silver nitrate and ferric chloride on the degree of oxidation, carboxymethyl content and size of DAC, TOCNF, CMCS, FeNPs and AgNPs.
- iii. To determine the effect of chemical crosslinking of cellulose chitosan AgNPs nanocomposites on the functional groups present, the degree of crystallinity, thermal profile, and morphology of the films.
- iv. To determine the influence of AgNPs, cellulose nanofibrils content and glycerine content on the swelling capacity, wettability, and tensile strength of the fabricated nanocomposite films.
- v. To determine the wound healing properties of the composite film using *in-vitro* and *in-vivo* antimicrobial studies.

CHAPTER TWO

LITERATURE REVIEW

2.1 Nano Reinforcing Polymers

Plants and animals are a good source of several nanomaterials such as starch, chitin, and cellulose which are abundant, natural, renewable and biodegradable polymers. These nanomaterials find application in various industries where they could be used as reinforcing fillers in composite materials after several processing techniques (Cerqueira *et al.*, 2017). These biomaterials are often called whiskers and are defect free hence their properties are comparable to perfect crystals. The excellent reinforcing properties of these natural whiskers stem from their hierarchical structure and chemical nature. Over the last decade, many studies have been devoted to imitating biocomposites by mixing natural whiskers from waste biomass sources with various polymer matrices. The presence of crystalline fibrils in the chitinous integuments is already widely reported (Cerqueira *et al.*, 2017; Mohammad *et al.*, 2013). Cellulose and chitin occur as whisker-like micro fibrils that are biosynthesized and deposited in a continuous fashion are a classic example of these reinforcing polymers. These nanocrystals occur as whiskers or rod-like particles, that are typically a few hundred nm long and between 5 and 20 nm in diameter. Nanocomposites materials with drastically enhanced mechanical properties can be prepared by casting combinations of different polysaccharides (Dufrene, 2008).

2.1 Nanocomposites with Combined Antimicrobial Properties

Nanocomposites with antimicrobial function have long been recognized and exploited in various fields for their antimicrobial activity as growth inhibitors, antimicrobial films, antimicrobial agents, and antimicrobial carriers. These composite films are particularly effective against microorganisms due to the enhanced surface reactivity of the nano-sized antimicrobial agents and the high surface – to – volume ratio. These properties make them able to inactivate microorganism more effectively than their micro or macroscale counterparts (Rhim *et al.*, 2013). Nanocomposites materials with antimicrobial properties can be prepared from organically modified nano clay such

quaternary ammonium modified montmorillonite (MMT) (Hong and Rhim, 2008), nitric oxide-loaded zeolite (Neidrauer *et al.*, 2014), metal ions such as silver (Jain *et al.*, 2009), copper (Cady *et al.*, 2011), metal oxide such as ZnO (Katepetch *et al.*, 2013), titanium dioxide (Hérault *et al.*, 2020) and natural biopolymers such as chitosan (Loke *et al.*, 2000). Enzymes such peroxidase, lysozyme, natural antimicrobial agents containing thyme essential oil (Mehdizadeh *et al.*, 2012) and synthetic antimicrobial agents such as quaternary ammonium salts (Xue *et al.*, 2015), collagen EDTA (Brett, 2008), can also be incorporated in nanocomposite to impart antimicrobial properties. Combinations of more than one antimicrobials incorporated into nanocomposites materials have also been investigated (Rhim *et al.*, 2013). For instance, Konwar *et al.*, (2016) fabricated a chitosan-iron oxide coated graphene oxide nanocomposites hydrogel through co-precipitation of iron oxide followed by gel-casting of composite solution. Measurement of the mechanical properties and thermodynamic stability of the films indicated a significant improvement in thermal and mechanical properties. The developed nanocomposites films displayed an enhanced antimicrobial activity against Gram-positive and Gram-negative bacteria (Konwar *et al.*, 2016).

Tian *et al.*, (2014) developed a recyclable and synergistic nanocomposite by growing both iron oxide nanoparticles (IONPs) and silver nanoparticles (AgNPs) on the surface of graphene oxide (GO). In comparison to AgNP, the nano composite obtained had much higher antibacterial efficacy toward both Gram-negative bacteria *E. coli* and Gram-positive bacteria *S. aureus* (Tian, et al., 2014). The unique reinforcing behaviour of graphene sheets have also been investigated in detail in chitosan biopolymers. For instance, incorporation of 1 wt.% graphene oxide improved the tensile strength and young's modulus of graphene oxide/chitosan nanocomposites by 122% and 64%, respectively (Kang *et al.*, 2009; Yang *et al.*, 2010).

In a similar study, Dang and Seppala (2015) demonstrated that incorporation of 1 – 10% reduced graphene oxide (RGO) on nano-fibrillated cellulose (NFC) improved the mechanical properties of cellulose nanofibril (CNF) sheets in high-humidity conditions. When the temperature reached 50 °C, the neat NFC paper was broken but the young's modulus of the NFC/RGO composite paper was significantly higher than

that of neat NFC paper (Dang and Seppala, 2015). Compared to carbon nanotube (CNTs) based composites, the graphene-based composites have one major advantage in that the metallic impurities in CNTs limits their applications as drug carriers and biomedical sensors (Fan *et al.*, 2010).

2.2 Metallic Nanoparticles as Antimicrobial Agents

Due to their unique physical, chemical, and biological properties, metallic nanoparticles have attracted great attention in fields such as photocatalysts in environmental remediation and in the medical field as antimicrobial agents and drug carriers (Azam *et al.*, 2012; Khan *et al.*, 2020). Many biological systems such as plants (Mittal, Chisti, and Banerjee, 2013), algae (Govindaraju *et al.*, 2008), diatoms (Scarano & Morelli, 2002), bacteria (Lengke, Fleet, & Southam, 2007; Khan *et al.*, 2020), yeast (Kowshik *et al.*, 2002), fungi (Rautaray *et al.*, 2003), and human cells (Anshup Venkataraman, *et al.*, 2005) have been employed to reduce inorganic metal ions into metal nanoparticles via the reductive capacities of the metabolites found in these organisms. However, several physical and chemical production methods such as mechanical milling (Karimi *et al.*, 2014), sodium borohydride (Cai *et al.*, 2013; Woo *et al.*, 2014), ethylene glycol (Raveendran *et al.*, 2003), solvothermal method (Basavaraja *et al.*, 2011), and carbothermal synthesis (Shen, 2015) have been also been employed for their preparation (Makarov *et al.*, 2014). Metallic nanoparticles synthesized via these routes rapidly agglomerate to form clusters due to interparticle Van der Waals and magnetic forces and may further undergo rapid oxidation (Stanckic *et al.*, 2016; Huang *et al.*, 2017). However, secondary metabolites found in plant extracts such as terpenoids, alkaloids, phenolic acids, polyphenols, sugars and proteins can play a significant role in the bio-reduction of the metal ions to nanoparticles (Makarov *et al.*, 2014; Sebastian *et al.*, 2018). This synthesis approach does not require heating and the metabolites act as reducing and capping agents thereby protecting the nanoparticles formed from autooxidation (Makarov *et al.*, 2014; Herlekar *et al.*, 2014; Phan & Nguyen, 2017; Sebastian *et al.*, 2018). These metallic nanoparticles have been shown to have antimicrobial activity against several microorganism with the activity being dependent on the NP concentration, physiology, and metabolism of the given

species, as well as the selective permeability of intracellular membranes which is governed by the kind of bacterial cell (Khan *et al.*, 2020). Moreover, they can inhibit biofilm formation which makes them excellent candidates to combat rising cases of antimicrobial resistance associated with medical devices (Priebe *et al.*, 2017; Hérault *et al.*, 2020).

2.3 Biomaterials as Wound Dressings

A range of biomaterials have been researched for their applications in wound dressings. These biomaterials can be broadly divided into three categories based on the source; *i*) natural biopolymers of plant or animal origin such as starch, cellulose, chitosan, alginate, soy protein *ii*) synthetic biodegradable polymers such as polyvinyl alcohol, polylactic acid, poly(glycolic acid) *iii*) biopolymers produced by microbial fermentation like microbial polyesters, such as poly(hydroxy alkanates) (PHAs) (Rhim *et al.*, 2013). These materials have the potential to be functionalized at the surface thus they offer a wide range of applications to wound sites as they can be formulated as solids (powder or granular), semi solids (such as pastes and gels) as well as sheet and sponge configuration (Martin *et al.*, 2013). A variety of biomaterials have been used to form both artificial skin products and support layer for cultivated epidermal cells in skin substitutes. In this regard, cellulose-rich biomass and chitin have acquired enormous significance as biomaterial feed stocks, since they contain functional groups which are suitable to chemical functionalization (Varshney & Sanjay, 2011).

2.3.1 Cellulose Nanofibrils (CNFs) and Cellulose Nanocrystals (CNCs)

Owing to their excellent biological and physical properties, in particular, their biocompatibility, biodegradability and low toxicity, nano-cellulose materials have undergone rapid development in recent years as promising biomedical materials (Jorfi & Foster, 2015). Cellulose nanofibrils (CNF) and cellulose nanocrystals (CNCs) are usually prepared using either chemical, physical, biological or oxidation methods or a combination of these (Szcześna-Antczak *et al.*, 2012; Kazimierczak & Antczak, 2012; Kar *et al.*, 2015). Chemical methods are used to prepare CNCs, and they involve the use of

strong acids where the amorphous domains present in the fibers are cleaved yielding nano fibrillated fibers in which surface hydroxyl groups are esterified to yield corresponding acid esters (Torres *et al.*, 2013; Karimi & Taherzadeh 2016). When cellulose is subjected to mechanical treatment such as high-speed grinding, high intensity ultrasonic treatment, and steam explosion one can be able to obtain or prepare CNFs of nanometer dimensions (Boufi & Chaker , 2016). In the case of biological treatment, cellulose is treated with enzymes such as cellulase that are produced by fungi, bacteria, protozoans, plants, and animals to cleave the $\beta - 1, 4$ linkages of the fiber structures into simpler ones (Zhang & Zhang, 2013). Since such treatment takes more time, they are often coupled with mechanical/chemical methods to reduce the process time and yield better CNF. Biological treatment as compared to acid hydrolysis, which leads to esterified CNF, produces nanofibrils that are biocompatible and can be used to produce biomedical and pharmaceutical products. Enzymatic processes are also widely considered environmentally friendly as compared to the use of acid hydrolysis and they result in longer fibrils that are characterized by a greater number of connections between nanofibrils (Corgie *et al.*, 2011). These are desirable characteristic of CNF used in biomedical application such as wound dressings and reinforcement in nanocomposites. (Szczęsna-Antczak *et al.*, 2012). CNF can also be obtained through oxidation of pulp mediated through 2,2,6,6-tetramethylpiperidine-1-oxyl (TEMPO) as a catalyst which allows the formation of a carboxyl group in the C₆ position from the hydroxyl groups present on the surface of the fibers (Figure 2.1). The exposure of TEMPO oxidized fibers to mechanical treatment results in easier fibril defibrillation due to the presence of negative charges that repels the microfibrils against each other inside the cell wall resulting in cellulose nanofibrils with a diameter of 3 – 4 nm (Isogai, 2018).

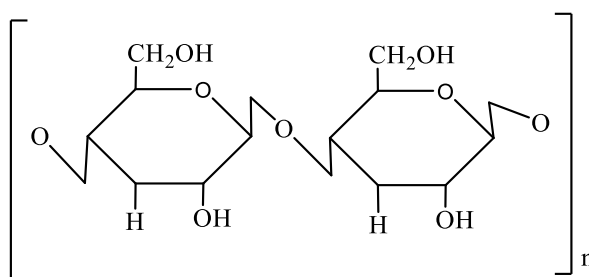


Figure 2.1: Chemical structure of cellulose

Modified cellulose filaments have been employed as sutures with the most recent and evolving clinical applications of cellulose films being temporary skin substitute, hemostatic agent, culture material and post-operative adhesion barriers (Hoenich, 2006). Cellulose and its derivatives do not intrinsically have antimicrobial properties. To impart antimicrobial properties onto the nanofibrils, antimicrobial agents, such as benzalkonium chloride (Liu *et al.*, 2013), copper nanoparticles (Ma *et al.*, 2016), sorbic acid (Kampalanonwat *et al.*, 2013) and silver chloride nanoparticles (Son *et al.*, 2006) have been incorporated onto the nanofibrils. In addition, chemical grafting of functional groups onto the surface of CNFs network can also be used to impart antimicrobial properties to the membranes. For instance, to impart antimicrobial properties on CNFs, quaternary ammonium groups have also been immobilized onto the nanofibrils network through reversible addition-fragmentation chain transfer (RAFT) (Roy *et al.*, 2008). CNFs functionalized with amino silane groups (Saini *et al.*, 2016) and amino groups (Roemhild *et al.*, 2013) have also been reported to have effectively inhibited growth of *S. aureus* and *E. coli*.

2.3.2 Chitosan

Chitosan is a non-toxic, biodegradable, and biocompatible polysaccharide of β -(1,4)-linked D-glucosamine and N-acetyl-D-glucosamine (Figure 2.2). A derivative of natural chitin, chitosan presents remarkable properties that have paved the way for the utilization of chitosan in the biomedical and pharmaceutical fields. However, its properties, such as poor solubility in water or common organic solvents limits its utilization in various application. One way to improve or to impart desirable properties to chitosan is the chemical modification of the chain, generally by grafting of functional groups, without modification of the initial skeleton in order to conserve the original properties. This functionalization is carried out on the primary amine group (Figure 2.2), generally by quaternization, or on the hydroxyl group (Riva *et al.*, 2011). Covalently binding or grafting chitosan onto man-made polymers or clays strengthens its structure. Such modifications are not desirable because they inadvertently alter chitosan unique properties, making it not biocompatible or toxic (Duri *et al.*, 2013). (Sinha *et al.*, 2004; Thai, *et al.*, 2020).

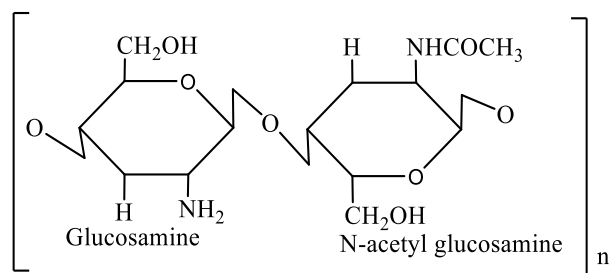


Figure 2.2: Chemical structure of chitosan

Loke *et al.*, (2000) developed a non-adherent wound dressing with sustained anti-microbial capability. The wound dressing consisted of an upper layer of carboxymethyl chitin hydrogel material and a lower layer of anti-microbial impregnated biomaterial. The hydrogel layer acted as a mechanical and microbial barrier capable of absorbing wound exudate (Loke *et al.*, 2000). The carboxymethylated chitin hydrogel swelled considerably in physiological fluid, taking up to four times its own weight in water, and was also highly porous to water vapor. The moisture permeability of the dressing prevented the accumulation of fluid in heavily exuding wounds seen in second-degree burns. The lower layer fabricated from chitosan acetate foam was impregnated with chlorhexidine gluconate. From the *in vitro* release studies, the loading concentration was optimized to deliver the required dosage needed to sustain anti-microbial activity in the wound area for 24 h (Loke *et al.*, 2000). Tanigawa *et al.*, (2008) developed a scaffold of chitosan (CS) with a porous sponge structure for an artificial skin. The scaffolds were prepared from both CS/citric and CS/acetic solutions. It was found that CS/acetate had low crystallinity, but CS/citrate was in an amorphous state, resulting in a large ductility with rubbery softness. Despite the different morphologies of CS/citrate and CS/acetate scaffolds, both scaffolds exhibited the wound healing effect available for tissue engineering (Tanigawa *et al.*, 2008). Apart from the hemostatic, antimicrobial, and permeable (for both water vapor (WV) and O₂) properties, chitosan dressings are non-irritating and do not cause allergic reactions, especially when prepared using lactic acid (LA) as the solvent instead of acetic acid (Shen *et al.*, 2016).

2.4 pH Responsive Hydrogels

One of the most preferable routes for drug delivery is oral delivery because it is easy to administer the drug, patient compliance and the flexibility in formulations. Pharmaceutical preparations in the form of capsules, tablets, liquids, creams, and injections as drug carriers have mostly accomplished treatment of acute disease (Joshi *et al.*, 2011). Hydrogels are three dimensional, cross-linked polymeric networks that can absorb large quantities of water hence can be used to as drug delivery carriers. The networks consist of hydrophilic homo polymers or co polymers cross-linked either chemically or physically. Entanglements, crystallites or weak association like Van der Waal forces or hydrogen bonds form part of the physical crosslinks which provide the physical integrity and the network structure for the hydrogels (Hoffman, 2012). In the case of pH dependent hydrogels, the swelling behavior in different pH media is as a result of presence of ionizable pendant groups such as carboxylic acid (acidic) and amine (basic). These pendant groups ionize and develop fixed charges on the gel thereby increasing the swelling force in the gel when placed in a medium of optimum pH and ionic strength. This increase in the swelling force increases is due to localization of fixed charges on the pendant group and as a result, the mesh size of the network changes with small change in pH (Joshi *et al.*, 2011; Hoffman, 2012; Zhang *et al.*, 2020).

2.5 Cellulose Chitosan Composites

Despite the potential use of cellulose and chitosan as individual polymers, there are drawbacks, which severely limit their applications. For example, both cellulose and chitosan (CS) have a network of intra- and intermolecular hydrogen bonds that enable them to adopt ordered structures, which make them insoluble in most solvents (Duri *et al.*, 2013). Dissolution of the two polymers involves the use of corrosive and volatile solvents, requires high temperatures and suffers from side reactions and impurities, which lead to changes in the structure and properties of the polysaccharides. As such chemical functionalization such TEMPO mediated oxidation, periodate oxidation, carboxymethylation and methylation are often employed to make the two polymers soluble. Moreover, introduction of functional groups such as carbonyl (C=O), and

carboxyl (COOH) on the network also implies that they will be prone to further functionalization when nanocomposites are the desirable product (Isogai *et al.*, 2011; Hoglund, 2015).

2.6 Functionalization of Cellulose and Chitosan

2.6.1 TEMPO-Mediated Oxidation

TEMPO mediated oxidation cellulose transforms the C₆ hydroxyl groups of cellulose into carboxylic acid according to the schematic representation in figure 2.4.

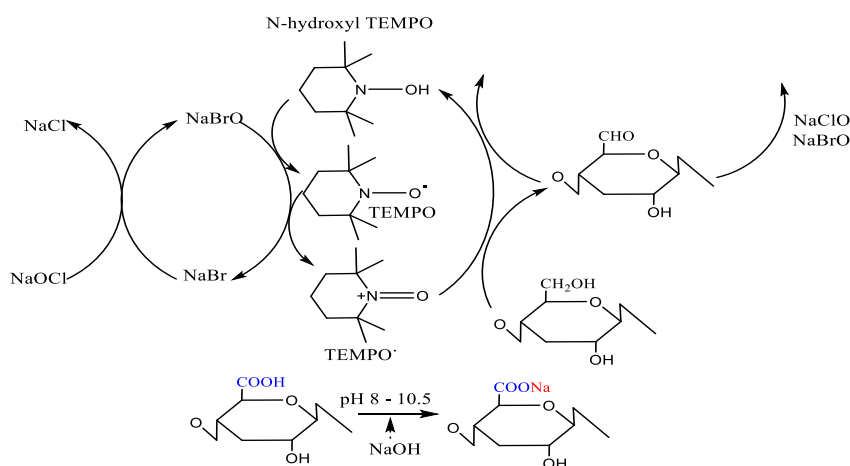


Figure 2.3: General mechanism for TEMPO mediated oxidation of cellulose

CNF can also be obtained through oxidation of pulp mediated through 2,2,6,6-tetramethylpiperidine-1-oxyl (TEMPO) as a catalyst which allows the formation of a carboxyl group in the C₆ position from the hydroxyl groups present on the surface of the fibers. The exposure of TEMPO oxidized fibers to mechanical treatment results in easier defibrillation due to the generation of negative charges that repels the microfibrils against each other inside the cell wall resulting in cellulose nanofibrils with a diameter of 3 – 4 nm (Isogai *et al.*, 2011; Menon *et al.*, 2017; Isogai, 2018).

2.6.2 Periodate Oxidation of Cellulose

Periodate oxidation cleaves bonds between vicinal diols and transforms primary alcohols into formaldehyde and secondary ones into aldehyde groups according to figure 2.5.

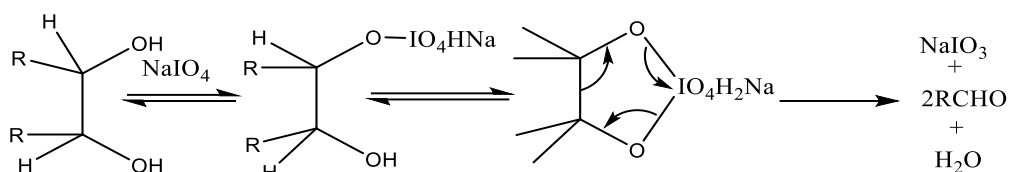


Figure 2.4: General mechanism for periodate oxidation of vicinal alcohols

The vicinal diols are also present on cellulose glucose monomer between the C₂ and C₃ positions (Figure 2.6). In this heterogeneous reaction, when cellulose is reacted with potassium periodate, the hydroxyl groups at position C₂ and C₃ undergo oxidation to yield the corresponding aldehydes thereby introducing C=O groups at these two positions (Leguy *et al.*, 2018).

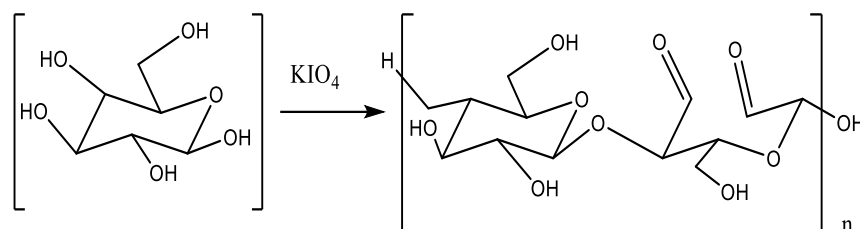


Figure 2.5: Synthesis of dialdehyde cellulose through periodate oxidation

This reaction is characterized by the degree of oxidation that represents the average number of aldehyde groups introduced per anhydroglucose unit (AGU) and it is influenced by factors such as temperature, cellulose source, oxidant concentration and overall reaction time. Most of the periodate oxidation reactions of cellulose have been performed on a single cellulose source, at room temperature and longer reaction times hence the influence of these parameters on the oxidation have largely not been explored (Leguy *et al.*, 2018; Leguy *et al.*, 2018). Moreover, with sufficient oxidation of cellulose, 2,3-dialdehyde cellulose becomes soluble in hot water unlike its cellulose

making it more susceptible to further functionalization into primary ($R^1\text{-CH=NH}$) or secondary aldimines ($R^1\text{-CH=N-R}^2$) and Schiff bases ($R^1\text{-CR}^3\text{=N-R}^2$). This makes dialdehyde cellulose an interesting candidate for covalent immobilization of high molecular weight nitrogenous compounds which include polypeptides and proteins such as antibodies, enzymes, gelatin, collagen and chitosan (Kimura *et al.*, 2011; Liu *et al.*, 2001; Plappert *et al.*, 2018). Immobilization of these nitrogenous compounds can be employed in waste water treatment (Ruan *et al.*, 2018), wound dressings (Dong & Li, 2018), biochemical sensors (Nypelo *et al.*, 2018), drug delivery (Chen *et al.*, 2018), surgical materials (United States of America Patent No. 15/450,706, 2017), and tissue scaffolds (Hou *et al.*, 2018)

2.6.3 Cellulose Chitosan Schiff-Base Reaction

Cellulose and Chitosan can be linked together through a Schiff base reaction between carbonyl and amine groups present on their network according to figure 2.6.

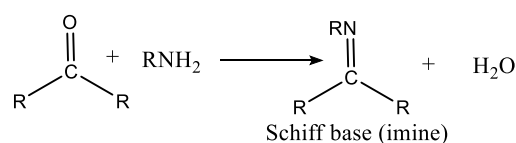


Figure 2.6: Schematic representation of Schiff base reaction between carbonyl and amine functional group

The electrophilic carbon atoms of aldehydes and ketones are prone to nucleophilic attack by amines. The resulting compound known as an imine or Schiff's base has C=O double bond that has been replaced by a C=N double bond (Yang *et al.*, 2015; Yang *et al.*, 2016). The formation of an imine involves two steps in which the amine nitrogen acts as a nucleophile and attacks the carbonyl carbon as represented in figure 2.8.

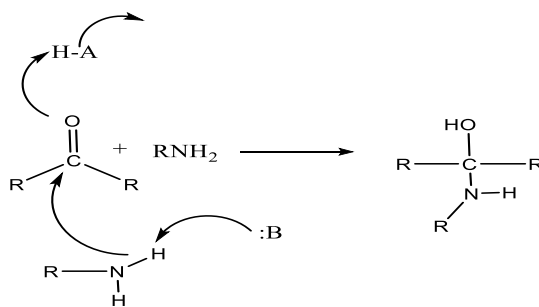


Figure 2.7: Attack of the carbonyl group by an amine during imine bond formation

Then the nitrogen is deprotonated and the electrons from the N-H bond push the oxygen off the carbon leaving a C=N double bond and a displaced water molecule (Figure 2.9).

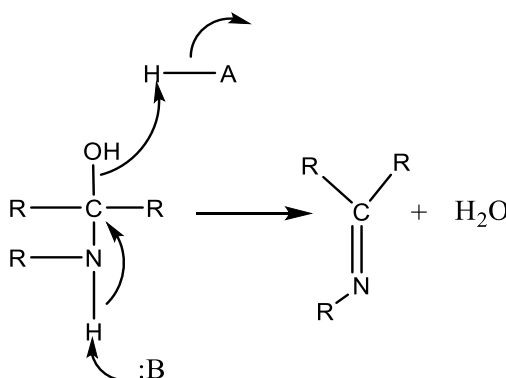


Figure 2.8: Deprotonation of N during C=N formation

Similar reactions do occur when dialdehyde cellulose is reacted with chitosan due to the presence of C=O in dialdehyde cellulose and -NH₂ in chitosan respectively (Yang *et al.*, 2015; Yang *et al.*, 2016).

2.6.4 Dialdehyde Cellulose Dressings

Despite being biodegradable, readily abundant, biocompatible, and easily functionalized, cellulose lacks antimicrobial activity which hinders its application in the biomedical field. To impart antimicrobial properties to the fibers, they are normally modified through introduction of new functionalities that opens the door for

immobilization of different moieties (Katepetch *et al.*, 2013; Plappert *et al.*, 2018). One such method is the introduction of aldehyde groups through periodate oxidation which leads to cleavage of C₂ and C₃ of the glucopyranose rings (Figure 2.10) (Hoglund, 2015; Leguy *et al.*, 2018; Leguy *et al.*, 2018). The presence of the aldehyde groups at this position has been further utilized to impart antimicrobial activity to the fibers by *In-situ* reduction of metal ions thereby enhancing their ability to prevent the growth of microorganism (Dong & Li, 2018; Errokh *et al.*, 2018).

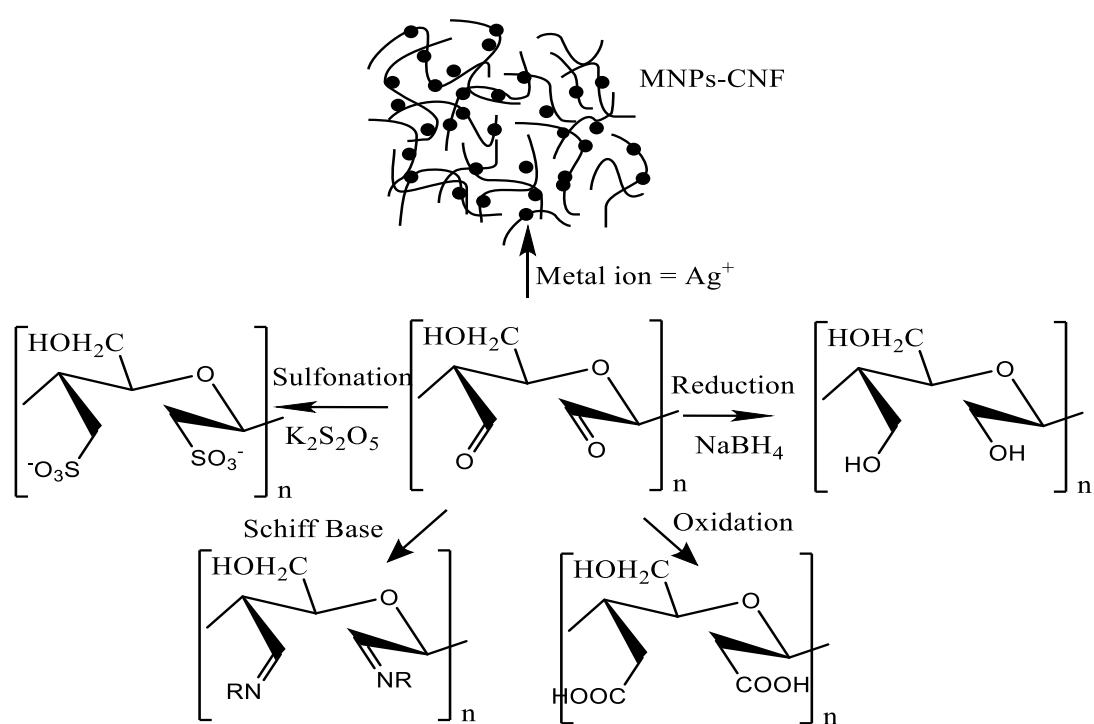


Figure 2.9: Preferential surface modification of dialdehyde CNFs

For instance, Li *et al.*, (2018) prepared dialdehyde nano fibrillated cellulose silver nanocomposite (DATCNF) films containing silver nanoparticles with an average size of 31.08 nm. The composite material displayed a control release mechanism of silver ions with a rate of 0.63% per two days and a long-term antibacterial activity against selected microorganisms (Li *et al.*, 2018). In a dissimilar approach, Dong and Li (2018) fabricated an antimicrobial film based on chitosan dialdehyde cellulose and AgNPs for wound dressing applications. Cellulose and chitosan were chemically crosslinked through a Schiff base reaction between the aldehyde groups of cellulose

and the amine groups present in chitosan. AgNPs were then generated through reduction of silver ions in solution using the aldehyde groups leading to nanocomposite films that inhibited the growth of various microorganisms (Dong & Li, 2018).

2.7 Antimicrobial Activity of Silver Containing Composites

By having bactericidal and fungicidal properties, the utilization of the silver-containing nanocomposite extends from biomedical applications to optical materials. The nanoparticles are normally incorporated in materials such wound dressings (Ito *et al.*, 2018; Dong & Li, 2018), diabetic socks, sanitization materials in healing centers, therapeutic materials (Jain *et al.*, 2009), and dental implants (Priebe *et al.*, 2017) among others. Incorporation of AgNPs into these materials normally results in slow release of the nanoparticles to prevent the growth and proliferation of microbial organisms in the target area. Presence of AgNPs results in cell death has been reported to occur via various mechanisms which prevent the normal functioning of the cell (Figure 2.11) (Khan *et al.*, 2020).

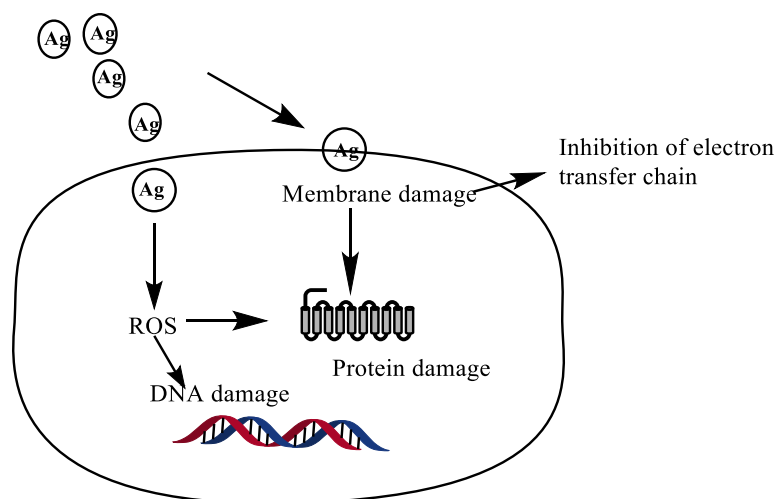


Figure 2.10: Pathways in which AgNPs initiate cell damage leading to death of microorganisms.

The antimicrobial action is linked to cell damage as a result of adhesion of AgNPs onto the surface of the cell wall followed by cell penetration which leads to cellular

toxicity. This damages intracellular structures such as mitochondria. This toxicity has also been linked to oxidative stress caused by generation of reactive oxygen species (ROS) and free radicals, and modulation of signal transduction pathways (Dakal *et al.*, 2016). These nanoparticles have the advantage that they display a broad spectrum of antibacterial and antifungal activities, are comparatively less reactive than silver ions, and are therefore well suited for use in clinical and therapeutic applications (Khan *et al.*, 2020).

2.8 Kinetics of Silver Release from Composite Films

The toxicity and or effectiveness of drug loaded wound dressings is dependent on the amount of the encapsulated drug released over time (Kim *et al.*, 2019). As such, there is need to predict the migration pattern and the amount of AgNPs released from a polymeric network and to account for their safety when they are embedded in wound dressings. This in turn helps to understand the dissolution behaviour of the nanoparticles in biological systems within a stipulated time interval thus controlling the rate and amount released during this time frame (Kim *et al.*, 2019; Héroult *et al.*, 2020). By measuring the changes in concentration of the released AgNPs during diffusion, the rate of release can be determined using rate order equations (Ebbing & Gammon, 2016). For the case of slow-release devices such as titanium nanorattles and wound dressings embedded with AgNPs, this can be accomplished by placing the composite in an appropriate solvent such as water for an extended period (Priebe *et al.*, 2017). Aliquots are then withdrawn at specific time intervals and the SPR of AgNPs is then measured using a Uv-Vis spectrophotometer while the amount released is determined from inductively coupled plasma-Mass spectrometry (ICP-MS) measurements (Héroult *et al.*, 2020). The data obtained in such experiments are then fitted to first and second order equations given by:

$$\ln[A]_t = -kT + \ln[A]_0 \dots \dots \dots 1.1$$

$$\frac{1}{[A]_t} = -kT + \frac{1}{[A]_0} \dots \dots \dots 1.2$$

Where $[A]_t$ and $[A]_0$ are the concentration of the given species at time t and initial concentration respectively while k is the rate constant for the given reaction (Ebbing & Gammon, 2016).

CHAPTER THREE

MATERIALS AND METHODS

3.1 Sample Collection and Preparation

Oryza sativa husks (Rice Husks) and *Lantana trifolia* were collected between January – May 2017 from Juja, Kiambu County. The plant samples were identified with the help of a taxonomist in the field and voucher specimens collected and confirmed with those deposited previously in the Botany Department, Jomo Kenyatta University of Agriculture and Technology (JKUAT). After drying the collected samples were washed with distilled water several times, dried in an oven set at 105 °C and ground into fine powders using a milling machine (locally made mechanical grinder that has no model number) at the Mechanical Engineering workshop of JKUAT.

3.1.1 Isolation of Cellulose from *Oryza sativa* (Rice) Husks

Cellulose fibers were isolated from *O. sativa* husks according to the following reaction scheme before modification (Figure 3.1).

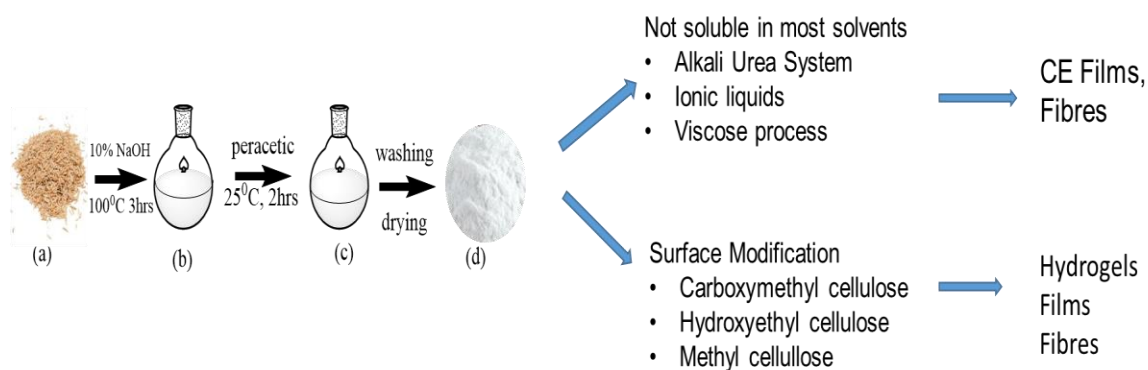


Figure 3.1: Rice husk treatment steps to obtain cellulose fibers

Dried and ground biomass was mixed with 10% aqueous NaOH solution in a ratio of 1:10. The mixture was stirred for 3 h at 100 °C followed by filtration of the pretreated biomass which was then washed with 10% ethanol and distilled water repeatedly to remove the base. The hemicelluloses-free biomass cake was then dried in an oven set at 105 °C to constant mass (Murigi *et al.*, 2014). Peracetic acid was prepared by mixing

acetic acid and hydrogen peroxide in a ratio of 1.5:1 and 1.5% (v/v) sulphuric acid added to the solution to catalyze the reaction. The solution was left to stand at room temperature in the laboratory for 48 h after which the hemicellulose free biomass was mixed with the peracetic acid in a ratio of 1:5 (m/v) of the initial mass. The mixture was then heated under constant stirring for 2 h at 80 °C, the residue filtered and washed with distilled water repeatedly. After the peracetic acid treatment, the recovered residue was then bleached with 15 % H₂O₂, washed with distilled water repeatedly and oven dried at 105 °C to constant weight (Murigi *et al.*, 2014)

3.1.2 Determination of Elemental Composition

Typically, presence of metallic ions in the pulp fibers after isolation affects the performance of the isolated fibers. As such, the effectiveness of the isolation procedure can be determined through evaluation of the elemental composition before and after fiber isolation. In this study, the elemental composition of rice husk (*Oryza sativa*) biomass before and after chemical treatment was analyzed with an Agilent 720 ICP-OES (Agilent Technologies, Mulgrave Victoria, Australia). One gram of the sample was weighed into 50 mL porcelain crucibles and placed in a muffle furnace. The temperature of the furnace was gradually increased until a temperature of 550 °C was attained. The samples were ashed for 5 h, left to cool at room temperature and then dissolved in 5 mL portions of 2 N HCl while mixing with a glass rod. After 20 min, the ashed samples were filtered using Whatman filter paper no. 42 into 50 mL volumetric flask and topped to the mark with deionized water to await analysis by ICP-OES (Estefan *et al.*, 2013). An Agilent 720 ICP-OES was employed for the analysis of trace and other elements. To determine the concentration of metal ions in the samples, the light intensities of the samples measured at various wavelengths were compared to those of standard solutions. Instrumental parameters used in the analysis are shown in table 3.1.

Table 3.1: ICP-OES instrument operating parameters

Condition	Setting
Power (Kw)	1.20
Plasma gas flow (L/min)	18.0
Auxiliary gas flow (L/min)	1.5
Spray chamber type	Glass single-pass cyclone
Torch	Standard one-piece quartz axial
Nebulizer type	Sea spray
Nebulizer flow (L/min)	0.7
Pump speed (rpm)	0 – 50
Total sample usage (mL)	1
Replicate read time (s)	5
Number of replicates	3
Sample uptake delay time (s)	75
Sample Intake	1.5 ml/min
Stabilization time (s)	60
Rinse time (s)	20
Fast pump	Off
Background correction	Fitted

3.1.3 Morphological Fiber Analysis and Particle Size Distribution

To determine the morphology and particle size distribution of the pulp fibers, A Techpap Morfi Optical fibre analyser (Techpap, France) was used to determine their diameters and lengths. The pulp fibers were first disintegrated with a laboratory disintegrator and diluted to make 0.1 g/L solution (Chen *et al.*, 2014; Osterling, 2015). Particle size distribution was determined using a Malvern G3S system (Malvern Instruments, Worcestershire UK) microscope-based image analyzer. 5 mm³ samples were loaded into a special holder with both sides sealed by 25 mm aluminium foil, placed in a dispersion unit and fibers were dispersed on a glass plate with a pneumatic pressure of 0.5 MPa, injection time of 10 ms and settling time of 60 s. The fibers were measured using a 503 objective lens and the 2D projection of the particles converted to a circle with the same area (Wang *et al.*, 2017).

3.1.4 Periodate Oxidation of Cellulose Pulp

Introduction of C=O groups at C₂ and C₃ of bleached *O. sativa* husks cellulose was accomplished through periodate oxidation of the fibers (Yang *et al.*, 2016; Lindh *et al.*, 2016; Alam and Christopher, 2018). 1.0 g of cellulose pulp was dispersed in

MilliQ water for 1 h followed by disintegration in an ultrasonic bath. Next 8.86 mmol KCl and KIO₄ (0.43 - 6.1 mmol/g cellulose) were dissolved in water, and the wet pulp added to make the total volume of water to be 50 mL. The reaction beaker was wrapped with several layers of aluminum foil to prevent penetration of light and the oxidation performed at 50 °C for 0.5-24 h. At the end of the reaction, ethanol was added into this mixture to quench the residual periodate followed by washing the oxidized fibers with water to remove impurities followed by drying in an oven at 105 °C to constant weight (Yang *et al.*, 2015; Yang *et al.*, 2016; Errokh *et al.*, 2018). The carbonyl content described as the degree of oxidation was then determined using hydroxyl amine hydrochloride in which the oxidized fibers were first reacted with the reagent followed by titrating with NaOH (Hoglund, 2015). After drying, 0.1 g of the oxidized fibers were dispersed in 25 mL of 0.2 M solution of hydroxylamine hydrochloride at pH 3.2 and stirred for 3 h. The mixture was then back titrated to pH 3 using a 0.01 M NaOH solution. A blank measurement was performed similarly with non-oxidized as-prepared cellulose and the aldehyde content was determined from equation 2.1:

$$Aldehyde\ content = \frac{(V_s - V_b) \times C_{NaOH}}{M_C} \dots \dots \dots 3.1$$

where V_S and V_B= Volume of sample and the blank while C_{NaOH} and m_c are the concentration of NaOH solution and the weight of the dry cellulose sample (Errokh *et al.*, 2018; Alam & Christopher , 2018; Hoglund, 2015).

3.1.5 TEMPO Oxidation of Cellulose Pulp

Introduction of COOH group on CNF from *Oryza sativa* husks was accomplished using an already established method by Isogai (2018). To oxidize the fibers, 2 g of microcrystalline cellulose was dispersed in 50 mL deionized water containing 0.32 mmol TEMPO and 5 mmol sodium bromide followed by addition of NaClO solution (0.05 – 3.25 mM). The reaction was maintained at pH 10 by periodic addition of NaOH (0.5 M) and it was deemed complete when the pH of the solution remained constant at pH 10 without further addition of NaOH solution. The reaction was quenched by

addition of ethanol followed by washing to neutral pH and centrifugation several times to remove inorganics salts and TEMPO (Boufi & Chaker, 2016; Lichtenstein & Lavoine, 2017; Zhou *et al.*, 2018). To prepare tempo oxidized dialdehyde cellulose (TOCNF-DAC), TOCNF was oven dried to constant weight at 105 °C and reacted with potassium periodate. To prepare TOCNF-DAC-AgNPs composite, 0.2 g of the TOCNF-DAC was dispersed in 50 mL solution of 0.01 M silver nitrate solution and stirred in the dark for 2 h to form TOCNF-DAC-Ag through ion exchange. The solution was then heated at 80 °C to allow the reduction of silver ions to form TOCNF-DAC-AgNPs composite that was washed to remove excess silver ions and dried to constant weight. The degree of oxidation which is a measure of the number of oxidized hydroxyl groups oxidized was evaluated using potentiometric titration of the fibers after TEMPO oxidation. 0.1 g of TOCNF was redispersed in 20 mL distilled water and stirred for 1 h. The carboxyl content was determined through potentiometric titration with NaOH (0.1M) solution and calculated using equation 3.2:

$$C_0 = \left(\frac{N \times V \times 100}{M} \right) \dots \dots \dots 3.2$$

Where C_0 is the carboxyl content, N is the titrant concentration, V is the volume (mL) at the equivalence point and M is the mass of dried TOCNF (Barbosa, *et al.*, 2013; Gilbert & Martin, 2016).

3.1.6 Isolation of Chitosan from *Oreochromis niloticus* (Tilapia) Scales

Chitosan was isolated from *O. niloticus*, and its characteristics compared to those of commercial chitosan isolated from shrimp shells. The dried *O. niloticus* scales were then demineralised using 1.0 M HCl at room temperature with constant stirring for 2 h, using a solid: acidic solution ratio of 1:13 (w/v). The demineralized fish scales were then rinsed with distilled water to remove acid and salt then washed with methanol and dried at 60 °C in an oven (Sinha *et al.*, 2004; Kumari & Rath, 2014). After drying, the samples were deproteinized using 1 M sodium hydroxide solution (1:13 w/v) at 60 °C for 5 h, the residue collected, washed with distilled water to neutral pH and dried in an oven (Sinha *et al.*, 2004; Kumari & Rath, 2014). To obtain chitosan from the isolated chitin, the dried sample was slowly added into a flask containing 10 % sodium

hydroxide to obtain a solid to alkaline solution ratio of 1:10 (w/v). The reaction vessel was refluxed at 100 °C for 8 h to remove the acetyl groups from amino groups on the polymer, washed with distilled water and the residue obtained dried in an oven. The prepared chitosan was then dissolved in 5 % acetic acid in a solid to acid solution ratio of 1:10 (w/v) at 80 °C for 3 h. The clear supernatant liquid was then taken in a beaker and sodium hydroxide solution (5%, w/v) was added drop wise into the acidic chitosan solution to obtain the precipitate of purified chitosan. The precipitate was thoroughly washed with distilled until neutral pH and oven dried at 100 °C (Mohammad *et al.*, 2013; Kumari *et al.*, 2015).

3.1.7 Conversion Chitosan to Carboxymethyl Chitosan (CMCS)

Carboxymethylation of chitosan was carried out according to a previously described method (Kimani *et al.*, 2016; Deng *et al.*, 2017). 1.0 g of high molecular weight chitosan was added to NaOH (10%): isopropanol solution (8:2), stirred, and allowed to swell at room temperature for 1 h. Subsequently, monochloroacetic acid (11, 21, 32, 42 mmol) was then added and the mixture was let to react for 2 h at 50 °C. The reaction was stopped by addition of 50 mL of 70% ethanol and filtered through a Whatman filter paper. The white solid retained on the filter paper was washed 4 times with 80 % ethanol and then dried in an oven at 50 °C (Kimani *et al.*, 2016; Deng *et al.*, 2017). The degree of substitution was determined by weighing 1 g from the dried sample into a 250 mL beaker followed by addition of 50 mL ethanol and stirring to obtain a slurry. To this mixture, 5 mL of concentrated nitric acid was then added while agitating the solution followed by heating for 5 minutes at 30 °C. After 15 minutes of agitation, the solution was filtered while washing with ethanol that had been heated for 60 minutes until all the acid was removed, and it was then dried in an oven set at 105 °C to constant weight. 0.1 g of the dried sample was then dispersed in 50 mL water followed by addition of 25 mL of 0.1 M NaOH. The solution was then heated and titrated with 0.1 M HCl to a phenolphthalein end point. The degree of substitution (DS) was then determined using the following equation (Kimani *et al.*, 2016):

$$A = \frac{BC - DE}{F} \dots \dots \dots 3.3$$

$$DS = \frac{0.162A}{1 - 0.0584A} \dots\dots\dots 3.4$$

where:

A = milliequivalents of acid consumed per gram of sample, B = NaOH solution added, mL, C = normality of the NaOH solution, D = HCl required for titration of the excess NaOH, mL, E = normality of the HCl, F = acid carboxymethyl chitosan used, g, 162 = gram molecular mass of the anhydroglucose unit of chitosan, and 58 = net increase in molecular mass of anhydroglucose unit for each carboxymethyl group substituted.

3.2 Green Synthesis of Iron and Silver Nanoparticles

To synthesize silver and iron nanoparticles using secondary metabolites, Dry *Lantana trifolia* plant materials were first collected from Juja, Kiambu County in Kenya washed with distilled water and dried in the oven for 48 h at 70 °C. After cooling, the biomaterial was finely ground (in-house fabricated mechanical grinder) and 100 g of the ground material was then mixed with 1000 mL distilled water, boiled for 5 min and allowed to cool. The solution was filtered thrice through Whatman filter paper no.1 to get a clear extract that was refrigerated at 4 °C before further studies (Kumar *et al.*, 2014). To evaluate the ability of the extract to act as a reducing agent, their redox potential was measured using a Metro ohm Autolab (MetroOhm Autolab B.V. The Netherlands) made up of a potentiostat-galvanostat equipped with NOVA 2.0 software (Born *et al.*, 1996; Kilmartin, 2001; Simić *et al.*, 2007; Keffous *et al.*, 2016). The cyclic voltammetry experiments were performed in a single-compartment Pyrex cell using a conventional three-electrode configuration. 2.0 mL glassy carbon disk working electrode (GCE) polished before each measurement, a platinum wire counter electrode, and an Ag/AgCl saturated KCl reference electrode were used. 20 mL of the supporting solution were dispensed into an electrochemical cell followed by addition of an appropriate volume of plant extracts. Cyclic voltammograms measurements were performed at positive potentials, at a scan rate of 100 mVs⁻¹ at room temperature in the presence of KCl (0.1 M) as a supporting electrolyte (Keffous *et al.*, 2016).

After measurement of their redox potential, the aqueous plant extract was mixed with 0.1 M FeCl₃.6H₂O and 0.1 M AgNO₃ prepared in double distilled water in different ratios (1:1 – 1:5 v/v) and concentrations (0.5 – 1000 mM). For the reduction of Ag⁺ and Fe³⁺ ions, different volumes of aqueous plant extracts were added slowly to aqueous metallic ions in solution and vortexed (Vortex Genie 2, scientific industries, USA) for three minutes at room temperature. During synthesis, the effects of temperature, concentration of oxidants, reaction time and amount of extracts were monitored in a quartz cuvette using a Shimadzu UV-Vis 1800 spectrophotometer (Shimadzu corporation, Japan) in the range of 300–800 nm (Eslami *et al.*, 2018). The formation of FeNPs and AgNPs was indicated by a change in color of the solution from light yellow to black for the case of iron nanoparticles and from colorless to brick red for the case of AgNPs (Kulkarni *et al.*, 2017). The precipitates were obtained by centrifugation at 1000 rpm (Hettich zentrifugen, Andreas Hettich group Tuttlingen, Germany), washed several times with MilliQ water, dried at 60 °C in an oven to constant weight and then stored in a desiccator until further analysis (Sebastian *et al.*, 2018). In the synthesis of AgNPs, the effects of temperature, concentration of AgNO₃ solution and reaction time extracts were investigated to ascertain their role during the reaction process. In 3 mL aqueous solution of AgNO₃ solution (0.5, 1, 1.5 mM), 1 mL of the plant extracts was added into the solution and the formation of AgNPs monitored using a Shimadzu UV-Vis 1800 spectrophotometer in the range of 300–800 nm.

3.3 Preparation of Cellulose Chitosan AgNPs Films

To prepare TOCNF-DAC-CS-AgNPs composite films, TOCNF-DAC (0 - 0.5 g/g CS), 1.0 g commercial CS and 100 mL silver nitrate solutions (5, 10, 25, 50, and 100 mM) were mixed in different ratios in acidified DI water for 0.5 h at 25°C to obtain mixtures with different ratios. The influence of the plasticizer content on the properties of the films was evaluated by preparing TOCNF-DAC-CS films with different amounts of glycerol (0.5 – 2.5 % v/v). The different polymer solutions were degassed by ultrasonication to remove bubbles, poured into plastic moulds, and then dried in an oven set at 60 °C to constant weight. To investigate the influence of TOCNF content

on TOCNF-DAC-CS films, CS was dissolved in 2% acetic acid solution, followed by addition of 2% glycerol, and TOCNF (0 - 0.5 g/g CS) (Stevens & Poliks, 2003). The solutions were degassed in an ultrasonicated bath for 3 h, poured in plastic moulds and dried in an oven set at 60 °C to constant weight. Finally, the TOCNF-DAC-CS-AgNPs composites with different TOCNF, Ag and glycerin content were gently peeled out of the mould and stored in a desiccator before their thickness, swelling, solubility and tensile strength were evaluated (Yang *et al.*, 2010; Gilbert & Martin, 2016; Zimet *et al.*, 2019; Afonso *et al.*, 2019).

TOCNF-DAC-CMCS nanocomposites were prepared according to Yasmeen, *et al.*, (2016). 1 g carboxymethyl chitosan (CMCS) was dissolved in 100 ml of 100 mM AgNO₃ containing 1 % acetic acid and the solution stirred for 3 h. This was followed by addition of 0.3 g of TOCNF-DAC and 2 % glycerol into the gel like solution and the mixture was stirred for 3 h to obtain a homogenous solution (Stevens & Poliks, 2003). To prepare composite films using AgNPs synthesized using *lantana trifolia* extracts, the above procedure was adopted but without incorporating silver nitrate. After continuous stirring, 50 mL of the solution containing AgNPs synthesized using *lantana trifolia* extracts was then added and the solution mixed to obtain a homogenous solution. Both solutions were then poured into separate plastic moulds and dried in an oven set at 60 °C to constant weight. The dried composite films were then peeled out of the mould and stored in a desiccator before their thickness, swelling capacity, solubility and tensile strength properties were evaluated (Yasmeen *et al.*, 2016).

3.3.1 Determination of Optical Transparency

To determine the presence of AgNPs and transparency of AgNPs-TOCNF-DAC-CS composite films, the films were cut into 2 x 2 cm pieces and mounted on the sample holder of the spectrophotometer with TOCNF-DAC-CS films as the blank (Rhim & Wang, 2014; Afonso *et al.*, 2019).

3.3.2 Determination of Film Thickness

The thickness of the films was measured using a micrometre screw gauge to the nearest 0.001 mm. Measurements were made in at least seven random locations of each preconditioned film and the values were reported as mean \pm standard deviation (SD). The mean values were used to determine the mechanical properties of the dried films (Zimet *et al.*, 2019; Afonso *et al.*, 2019).

3.3.3 Determination of Film Water Solubility and Swelling

To determine the films solubility and swelling capacity, film pieces (20 \times 20 mm) were dried at 105 °C to constant weight followed by immersion in 50 mL of distilled water and shaken gently for 24 h at 25 °C. The solutions were poured onto a filter paper (Whatman #1) to recover the undissolved films which were then weighed, and the wettability calculated using equation 3.5 (Zhang *et al.*, 2020):

$$\text{Swelling (\%)} = \frac{\text{Final wet weight} - \text{initial dry mass}}{\text{Initial dry mass}} \times 100 \dots \dots \dots 3.5$$

The films solubility was determined as the percentage dry matter of the remaining film after immersion in water. The samples were then rinsed with distilled water and dried at 105 °C to constant weight and the solubility calculated according to equation (3.6) (Zimet *et al.*, 2019; Zhang *et al.*, 2020):

$$\text{Solubility (\%)} = \frac{\text{Initial dry mass} - \text{final dry mass}}{\text{Initial dry mass}} \times 100 \dots \dots \dots 3.6$$

3.3.4 Determination of Tensile Strength

The tensile strength was measured using an in house fabricated tensile strength device constructed from a laboratory ring stand to which a top horizontal support was attached. A weighing pan was used to hold the weights. The film specimens were clamped in place and the total weight on the pan was increased by adding weights in a regular manner. The tensile strength was calculated by dividing the total load at the break point (in newtons) by the original cross-sectional area of the segment of the

specimen that broke (in square meters) according to the following equation (Stevens & Poliks, 2003; ASTM D882-10, 2010; Zhang *et al.*, 2020):

$$tS = \frac{W (kg) \cdot \left(9.80 \frac{N}{kg}\right)}{A \left(10^{-4} \frac{m^2}{cm^2}\right)} \dots\dots\dots 3.7$$

Where W = total load, A = cross sectional area of the film

3.3.5 Biodegradability Studies

The biodegradability of TOCNF-CS-Ag nanocomposite was studied by covering the films in a mound of soil in a petri dish and measuring the weight loss after each day for maximum of one week (Stevens & Poliks, 2003). The percent degradation was then calculated using formulae 3.8 where W_i is the initial weight and W_f is the final weight:

$$\text{Percent degradation} = \frac{W_i - W_f}{W_i} \times 100 \dots\dots\dots 3.8$$

3.3.6 Silver Release Experiments

To determine the amount of AgNPs released from the composite films, 0.1 g of the composite film was immersed in 200 mL distilled water to allow swelling of the films (Priebe *et al.*, 2017). Aliquots of 20 mL were subsequently drawn from the solution at 30 min intervals and the absorbance of the solution measured using a Shimadzu 1800 Uv-vis spectrophotometer (Shimadzu Corporation, Japan). To determine the amount of silver ions released from the composite films, the solution was then acidified with 3 mL concentrated HNO₃ and stored before ICP-MS analysis (Ghasemzadeh *et al.*, 2016; Hérault *et al.*, 2020).

To determine the order of the reaction, the experimental data were plotted first assuming a first-order reaction (Equation 3.9), then a second-order reaction (Equation 3.10), and the reaction order determined from the graph that gave the best line of fit to the experimental data (Ebbing & Gammon, 2016).

$$\ln[A]_t = -kT + \ln[A]_0 \dots \dots \dots 3.9$$

$$\frac{1}{[A]_t} = -kT + \frac{1}{[A]_0} \dots \dots \dots 3.10$$

3.4 Determination of Functional Groups Present

The functional groups present in all the samples were determined using a Bruker Tensor II Fourier Transform Infrared spectrophotometer (Bruker Optik GmbH, Ettlingen, Germany). The KBr pellets of the samples were prepared by mixing 10 mg of samples with 250 mg KBr (FT-IR grade) and finely ground with a mortar and pestle. The 13 mm KBr pellets were prepared in a standard device under a pressure of 7.5×10^8 Pa for 3 min. The spectral resolution was set at 4 cm^{-1} and the scanning range from 400 to 4000 cm^{-1} (Ponce *et al.*, 2013; Murigi *et al.*, 2014).

3.5 Determination of Degree of Crystallinity and Crystal size

X-ray powder diffraction was used for phase identification of the resulting materials used to develop the composite wound dressings. Changes in crystallinity of cellulose and chitosan that were occasioned by the chemical treatment the polymers were subjected to and the peaks associated with these two materials were used to identify them. In comparison with crystallographic library, metallic nanoparticles were also identified from their X-ray diffractograms through the presence of peaks associated with the nanoparticle's crystal planes. The degree of crystallinity and crystal size were determined using a STOE STADIP P X-ray Powder Diffraction System (STOE and Cie GmbH, Darmstadt, Germany). The X-ray generator was equipped with a copper tube operating at 40 kV and 40 mA irradiating the sample with a monochromatic $\text{CuK}\alpha$ radiation with a wavelength of 0.1545 nm. The XRD spectra were acquired at room temperature over the 2θ range of $10 - 60^\circ$ at 0.05° intervals with a measurement time of 1 second per 2θ intervals (Madivoli *et al.*, 2016).

The XRD Crystallinity Index (CI_{XRD}) for native cellulose was calculated using the peak height method using equation 3.11:

$$CI(\%) = \left[\frac{I_{002} - I_{am}}{I_{002}} \right] \times 100 \dots\dots\dots 3.11$$

where I_{002} is the intensity of the 002 crystalline peak at 22° and I_{am} the height of the minimum (I_{am}) between the 002 and the 001 peaks (Madivoli *et al.*, 2016).

The average size of crystallite was calculated from the Scherrer equation with the method based on the width of the diffraction patterns obtained in the X-ray reflected crystalline region. The crystalline size D_{002} was determined using the diffraction pattern obtained from the 002 lattice planes of cellulose using equation 3.12:

$$D_{002} = \frac{K\lambda}{B_{002}\cos\theta} \dots\dots\dots 3.12$$

where k is the Scherrer constant (0.94), λ is the X-ray wavelength (0.1545nm), B in radians is the full-width at half of the peak of 002 reflection and θ the corresponding Bragg's angle (Terinte *et al.*, 2011).

3.6 TGA Experimental Protocols

A Mettler Toledo TGA/DSC 3+ (Mettler-Toledo GmbH, Switzerland) was used to measure changes in the mass of the sample with increase in temperature over the course of the pyrolysis reaction. Thermogravimetric curves were obtained at a heating rate of $10^\circ\text{C}/\text{min}$ between $25 - 600^\circ\text{C}$. Nitrogen gas was used as an inert gas to displace air in the pyrolysis zone, thus avoiding unwanted oxidation of the sample. The sample mass used were approximately 10 mg (Ponce *et al.*, 2013; Murigi *et al.*, 2014; Lichtenstein & Lavoine, 2017).

3.7 DSC Experimental Protocols

The DSC analysis was carried out using a Mettler Toledo TGA/DSC 3+ (Mettler-Toledo GmbH, Switzerland). All the samples (10 mg) were heated from $25 - 600^\circ\text{C}$, cooled to 20°C and reheated to 600°C at $10^\circ\text{C}/\text{min}$ (Ciolacu *et al.*, 2011; Ponce *et al.*, 2013).

3.8 TEM and SEM Experimental Protocols

The morphology and size of the oxidized cellulose nanofibrils, chitosan, metallic nanoparticles, and the cellulose-chitosan composites films were analyzed at the Department of Chemistry, University of Fribourg, Switzerland. The dried CNF, chitosan and metallic nanoparticles were resuspended in ultrapure water (18 M Ω .cm Barnstead Genpure UV-TOC, Thermo scientific, Germany) and ultrasonicated to obtain a solution of suspended nanoparticles. The individual solutions were then drop casted in carbon films 300 mesh (Electron microscopy science, CF300-CU) and dried to evaporate the solvent before TEM analysis. TEM analysis was performed on a Tecnai G2 Spirit (Thermo fischer scientific, Oregon USA) operated at 120 kV equipped with a veleta 2048 x 2048 wide angle detector and an eagle 4096 x 4096 bottom mount detectors. Morphological analysis of cellulose-chitosan-silver nanocomposites were performed using Tescan Mira3 LM FE Scanning electron microscope (TESCAN, Brno, Czechia) operated at an accelerating voltage of 20 kV at an aperture size of 30 μ m (Ponce *et al.*, 2013).

3.9 DLS Experimental Protocol

To determine the particle size distribution, zeta potential and poly-dispersibility index of the suspended nanoparticles, the dried CNF and metallic nanoparticles were resuspended in ultrapure water (18M Ω .cm Barnstead Genpure UV-TOC, Thermoscientific, Germany) and ultrasonicated to obtain a solution of suspended nanoparticles (Barbash *et al.*, 2017; Boufi and Chaker, 2016). The solutions were then filtered through 0.25 μ M PTFE syringes into glass vials and 45 μ L of each solution was then transferred onto quartz cuvettes before analysis. The particle size distribution, zeta potential and poly-dispersibility index were then measured using a Bechman Coulter DelsaMax pro dynamic light scattering analyzer (Beckman Coulter, Indianapolis, United States) (Barbash *et al.*, 2017; Boufi & Chaker, 2016).

3.10 *In-vitro* Studies of TOCNF-DAC-CMCS-Ag/Fe Nanocomposites

3.10.1 Inoculation of Microorganisms

The interaction between TOCNF-DAC-CMCS-Metal nanocomposites with various kinds of pathogenic microorganisms mostly found in wounds were studied. The experimental studies focused on the measurements of the mortality rate for various bacterial strains namely *E. coli* (ATCC-25922), *P. aeruginosa* (ATCC-27853), *C. albicans* (ATCC 90028), *S. aureus* (ATCC-25923), *B. subtilis*, and *P. mirabilis*. The nutrient agar medium was prepared by dissolving 28 g of nutrient agar in 1000 mL of hot distilled water and allowed to cool. The mixture was then sterilized by autoclaving at 120 °C for about 15 min at 15 psi pressure and cooled to 50 °C (Ooko *et al.*, 2009). The medium was dispensed into petri dishes to yield a depth of 4 mm and isolated colonies were aseptically transferred to nutrient broth in the petri-dishes and incubated at 37 °C for 24 h to mimic human body temperature since the bacteria that were used are human pathogens (Ooko *et al.*, 2009).

3.10.2 Disc Diffusion Assay

The TOCNF-DAC-CS-AgNPs composite films were screened for their antimicrobial activity against *E. coli* (ATCC-25922), *P. aeruginosa* (ATCC-27853), *C. albicans* (ATCC 90028), *S. aureus* (ATCC-25923), *B. subtilis* (AT 23857), and *P. mirabilis* activity by using disc diffusion method in Botany Department, J.K.U.A.T (Zaidan *et al.*, 2005). Inoculum suspension (108 CFU/ML) were spread over the nutrient agar surface by sterile collection swab and 6 mm TOCNF-DAC-CS-AgNPs discs sterilized at 120 °C for 15 min were placed onto the petri dishes using flamed forceps and incubated at 37 °C for 24 h. Standard antibiotic discs containing sulphamethoxazole (25 µg), gentamicin (10 µg), amoxyclav (20/10 µg), norfloxacin (10 µg), ceftriaxone (30 µg), nitrofurantoin (200 µg), floxacin (10 µg), and nalidixic acid (30 µg) were then loaded separately to act as positive controls. The inhibition zones (ZOI) were measured using a ruler in millimeters around the disc as low activity (1-6 mm), moderate activity (7-10 mm), high activity (11-15 mm), very high activity (>16 mm) and no activity (-) (Zaidan *et al.*, 2005).

3.10.3 *In vivo* Studies of Scaffolds

To determine the wound healing properties of the scaffolds, a nude rabbit was prepared by shaving of the hair from a section of the rabbits back (Tanigawa *et al.*, 2008). Using a cotton swab, part of the back was scrubbed off by rubbing a depilatory on the epidermis of the skin and a wound with the length of 2 cm was made. Further, three line cuts a little less than 1 mm deep were made using a surgical blade in the wounded part so as to reach the dermis layer. This procedure was carefully carried out to avoid damaging the subcutaneous tissue under the dermis. The prepared scaffold was stuck on the wound part and the healing condition observed for 10 days (Tanigawa *et al.*, 2008).

CHAPTER FOUR

RESULTS AND DISCUSSIONS

4.1 Isolation of Cellulose and Chitosan

4.1.1 Physical Characteristics

Table 4.1 depicts the percent recovery, tapped density, bulk density, compressibility factor of cellulose and chitosan isolated from rice husks and *O. niloticus* respectively. The percent yield of cellulose from rice husks was calculated to be 27.2 ± 1.1 %. The bulk and tapped density of cellulose and chitosan were evaluated according to method described by (Bhimte & Tayade, 2007).

Table 4.1: Physical parameters of Rice Husk cellulose (RHCE) and Chitosan Isolated from *O. niloticus*

Physical Parameter	RHCE	<i>O. niloticus</i>
Percent yield	27 ± 1	27 ± 2
Tapped Density (g/cm^3)	0.2 ± 0.0	1.0 ± 0.1
Bulk Density (g/cm^3)	0.1 ± 0.0	0.8 ± 0.0
Compressibility (%)	34.5	N/A
Moisture Content (%)	1.0 ± 0.0	N/A
Degree of Deacetylation (DDA)	N/A	51.1



Figure 4.1: Conversion of rice husks (a) to cellulose (b)

From the results obtained (Table 4.1), the bulk and tapped density of cellulose obtained from rice husks was estimated to be 0.1 ± 0.0 and 0.2 ± 0.0 g/cm^3 respectively while the bulk and tapped density of chitosan was evaluated to be 0.8 ± 0.0 and 1.0 ± 0.1 g/cm^3 respectively. Compressibility was calculated from bulk density and tapped bulk density and is a measure of powder flow properties. Compressibility value of 20 % and above indicates a powder that is not free flowing while materials with compressibility of 40 % to 50% are particularly difficult to discharge from a hopper.

Cellulose obtained from rice husks had a compressibility of 34.54 % indicating that it had poor flow properties (Bhimte & Tayade, 2007; Murigi *et al.*, 2014).

4.1.2 Determination of Elemental Composition

Table 4.2 represents the concentration of different elements present in both raw rice husks and cellulose obtained from rice husks that were measured using an Agilent 720s ICP-OES. The concentrations of metals in untreated rice husks were significantly higher than those in the treated rice husk (Table 4.2).

Table 4.2: Elemental composition of untreated and chemically treated rice husks

Element	Rice Husks (mg/Kg)	Cellulose from Rice husks (mg/Kg)
Fe	5919±40	290.9±2
Al	2742 ± 6	387.5±10
Ca	1730±6	834±6
K	839±10	162.4±0.1
Na	669±200	407±200
Mg	496±20	163.3±0.6
P	391±3	54.0±7
Mn	271±3	4.40±0.7
B	264±0.1	277±0.2
S	231±8	118±1
Ba	20.8±0.1	3.70±0
Zn	15.2±0.5	5.60±1
Ni	8.50±0	0.0500±2
Cr	6.60±0.3	0.600±0.2
V	5.20±0.1	0.400±0
Cu	4.11±0.2	1.20±0
Cd	0.400±0.1	0.300±0

Generally, the concentrations of Al, Ca, Cd, Cr, Cu, Fe, K, Mg, Mn, Na, P, S, and Zn in the untreated rice husks were higher than those in the chemically treated rice husk. Quantitative analysis by ICP-OES showed the predominance of K, Ca, and Na (Table 4.2). The high concentration of metals in the untreated biomass can be attributed to the high metal uptake in plants germinated in soils enriched with metals from anthropogenic sources (Bilo *et al.*, 2015). In addition, high concentrations of Al, Ca, and Fe in untreated rice husks can be attributed to the favourable availability of these metals in plants, mainly those cultivated in flooded soils, as in the specific case of rice (Tarley & Arruda, 2004). In a similar study (Zhang *et al.*, 2014), showed that treatment

of rice husks with phosphoric acid increases the relative quantities of sodium (Na), silicon (Si), and phosphorus (P) and a decrease in potassium (K) and calcium (Ca) compared to raw rice husk.

4.1.3 Morphological Fibre Analysis

Figure 4.2 and Table 4.3 represent the average fiber characteristics as measured using a MorFi optical length fiber analyser v7.11.05 (Hon & Shiraishi, 2000; Chen *et al.*, 2014). The Techpap MorFi fibre analyser measures fibre fibrillation which is defined as the length of all the micro fibrils attached to the fibres in relation to the total fibre length.

Table 4.3: Average Fiber characteristics of Rice husks cellulose fibers as analyzed by MorFi analyzer.

Average characteristics	
Fibres (million/g)	2.76
Length arithmetic and weighted in length	0.300, 0.327
Width (μm)	41.5
Coarseness (mg/m)	0.898
Kink angle ($^{\circ}$)	126
Kinked fibers (%)	10.1
Curl (%)	9.8
Rate in Length of Microfibrils (%)	1.34
Broken Ends (%)	68.1
Fine Elements (% in length)	94.2
Percentage of fine elts (% in area)	35.5

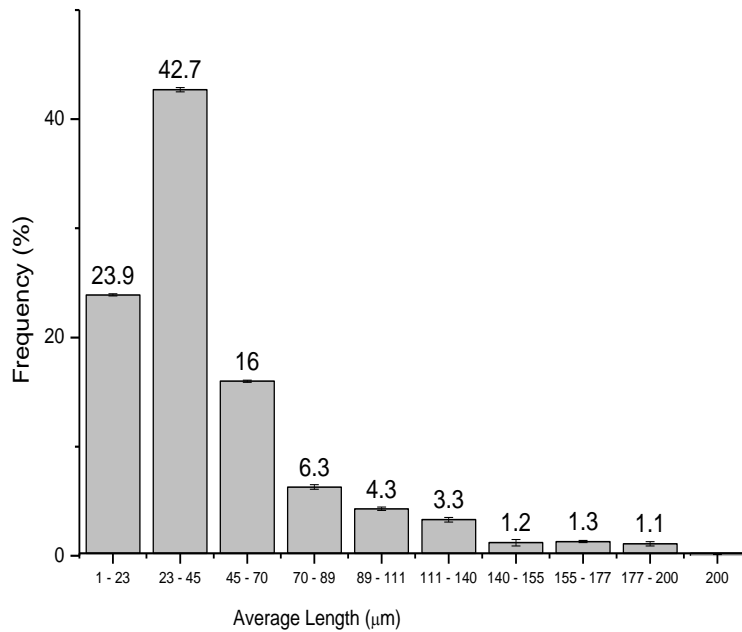


Figure 4.2: The average length distribution of rice husks fibers measured by MorFi analyzer

The data in figure 4.2, table 4.3 show the average fibre characteristics of rice husks cellulose in which a total of 42.7% of rice husks fibres had fibre weighted mean lengths ranging between 23 – 45 µm (Figure 4.2). Fibre length distribution affects the tensile strength, tear, opacity, porosity and many other paper properties (Ring & Bacon, 1997). The average weighted length of hard wood pulp and soft wood pulp have been reported to be 0.65 and 2.22 mm respectively (Chen *et al.*, 2014). Relatively narrow distribution is usually obtained when the fibre length of un-pulped wood is measured, and the average value are characteristic of a species. For instance, hardwood species have average fibre lengths of about 1 mm while softwood species have fibre lengths of more than 3 mm. Specific examples of hardwoods include: sugar maple, 1.0 mm; silver birch, 1.2 mm and aspen, 0.9 mm while specific examples of softwoods include: jack pine, 3.5 mm; ponderosa pine, 3.6 mm and redwood, 7.0 mm (Ring & Bacon, 1997).

4.1.4 Particle Size Distribution

Tables 4.4 - 4.6 represent the circle equivalent diameter, high sensitivity (HS) circularity and the aspect ratio of cellulose and chitosan.

Table 4.4: Circular equivalent diameters of cellulose and chitosan fiber

	CE diameters mean (μm)			
	Mean	D[n,0.1]	D[n,0.5]	D [n, 0.9]
Cellulose	9 \pm 7	2.13	6.28	16.15
Chitosan	7 \pm 6	1.71	5.87	12.66

Table 4.5: HS circularity of cellulose and chitosan fibers

	HS circularity			
	Mean	D[n,0.1]	D[n,0.5]	D [n, 0.9]
Cellulose	0.79 \pm 0.2	0.51	0.86	0.94
Chitosan	0.73 \pm 0.2	0.43	0.78	0.919

Table 4.6: Aspect ratio of cellulose and chitosan fibers

	Aspect ratio			
	Mean	D[n,0.1]	D[n,0.5]	D [n, 0.9]
Cellulose	0.74 \pm 0.2	0.49	0.78	0.92
Chitosan	0.80 \pm 0.1	0.63	0.82	0.94

The mean diameters of cellulose and chitosan were in the micron scale dimensions with a vast majority being smaller than 10 μm . Most CNF lose nano scale dimensions because of agglomeration from capillary forces, van der Waals forces and hydrogen bonding during drying. HS circularity of cellulose and chitosan were closer to 1 because of the aspect ratio and the shape were more spherical than fibril. Since particle size influences many properties of composite material it is a valuable indicator of quality and performance of these materials. Hence knowing the morphology of CNF is critical to modifying the rheological properties of the resulting polymer composites (Wang *et al.*, 2017). Particle shape often has a significant influence on final product performance parameters such as flow ability, abrasive efficiency, bioavailability, so some way of characterizing shape is required (Peng *et al.*, 2012; Wang *et al.*, 2017).

4.1.5 FTIR Characterization of Cellulose Isolated from Rice husks

Figure 4.3 represent the IR spectra used to determine the functional groups present in alkali treated rice husks (ATRH), rice husks cellulose (RHCE), mechanical treated cellulose (MTCE), Ultrasonicated Cellulose (USCE) and TEMPO oxidized cellulose (TOCNF). From figure 4.3, the vibrational frequencies observed at 3329 and 2900 cm^{-1} are due to the surface hydroxyl groups and to CH_2 stretching vibrations while the peak at 1329 cm^{-1} in the spectra is representative of a change of symmetry of the C – H group.

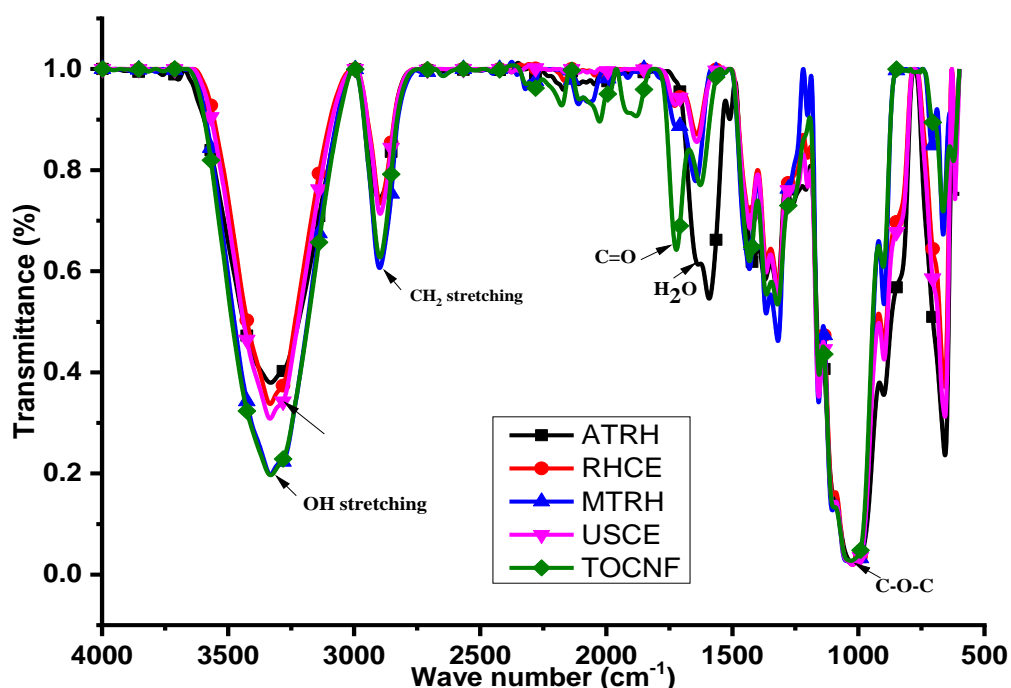


Figure 4.3: FT-IR spectra of RHCE, MTCE, USCE and TOCNF

The absorption at around 1213 cm^{-1} in the spectra refers to the bending vibrational frequency of C – H, O-H, or CH_2 while the absorption peak at 1070 and 851 cm^{-1} refers to the C-H stretching vibration of C- O – C (Johar *et al.*, 2012). The bands from 465 cm^{-1} to 485 cm^{-1} belongs to bending vibration of O-Si-O while a peak at 1640 cm^{-1} corresponds to –OH bending vibrations (Socrates, 2004; Begun *et al.*, 2013; Murigi *et al.*, 2014). Another intramolecular hydrogen bond in cellulose normally occurs at 3342 cm^{-1} . The vibrational frequencies in the region between 3221 – 3280 cm^{-1} are

assigned to the two crystalline cellulose allomorphs, cellulose I α and cellulose I β while a very small peak normally shifted to lower wavenumbers at 3147 cm⁻¹, is attributed to hydrogen bonds only in cellulose I α (Poletto *et al.*, 2014; Socrates, 2004). The positions and intensities of the OH stretching vibration bands vary for the different polymorphic forms of cellulose. For example, one form has two strong bands near 3480cm⁻¹ and 3345 cm⁻¹, whereas another form has its dominant OH band near 3350 cm⁻¹ (Socrates, 2004).

From figure 4.3, the ratio of intensities of preselected absorption bands were used to calculate the degree of crystallinity of cellulosic materials (Camacho *et al.*,2013). The infrared peak ratios between 1429 cm⁻¹ and 897 cm⁻¹ (H1429/H897) and between 1372 cm⁻¹ and 2900 cm⁻¹ (H1372/H2900) are a measure of crystallinity in cellulosic material. According to Poletto *et al.*, (2014), the band at around 1420–1430 cm⁻¹ is associated with the amount of the crystalline structure of the cellulose, while the band at 898 cm⁻¹ is assigned to the amorphous region in cellulose. The ratio between the two bands is an empirical crystallinity index defined as a lateral order index (LOI) (Karimi & Taherzadeh, 2016). The total crystalline index (TCI) is the ratio between the bands at 1372 and 2900 cm⁻¹, and it is used to evaluate the infrared crystallinity (IR) ratio. The hydrogen bond intensity (HBI) of cellulose is closely related to the crystal system and the degree of intermolecular regularity, that is, crystallinity, as well as the amount of bound water. The ratio between the absorbance bands at 3400 and 1320 cm⁻¹ was used to study the HBI of the fibers (Poletto *et al.*, 2014). The TCI is proportional to the degree of crystallinity of cellulose while the LOI is correlated to the overall degree of order in the cellulose (Corgie *et al.*, 2011).

Table 4.7 represent the crystallinity index, lateral order index and hydrogen bond intensities that were calculated from IR spectra of different samples. From the results obtained (Table 4.7), untreated rice husks (URH) had the lowest TCI (0.563) and LOI (0.526) as compared to alkali treated rice husks (ARH) (TCI = 0.788, LOI = 0.670), rice husk cellulose (RHCE) (TCI = 0.813 LOI = 1.704), mechanically treated cellulose (MTCE) (TCI = 0.856 LOI = 1.12) and ultrasonicated cellulose (TCI = 0.828 LOI = 1.46) respectively.

Table 4.7: Total crystallinity index (TCI), lateral order index (LOI) and hydrogen bond intensity (HBI) of studied fibers

Sample	FT-IR Crystallinity ratio		HBI
	H1372/H2900(TCI)	H1429/H897(LOI)	A3400/A1320
URH	0.563	0.526	0.963
ARH	0.788	1.72	0.670
RHCE	0.813	1.71	0.573
MTCE	0.856	1.12	0.436
USCE	0.828	1.46	0.572

Ultrasonicated cellulose showed the highest TCI while ATRH had the highest LOI values, indicating the highest degree of crystallinity and a more ordered cellulose structure than untreated and bleached rice husks (Poletto *et al.*, 2014). These results indicate that the ultrasonicated cellulose contains chains in a highly organized form as compared to the raw biomass and alkali treated rice husks. This results in higher hydrogen bond intensity between neighboring cellulose chains and a more packed cellulose structure as well as higher crystallinity (Auxenfans *et al.*, 2017).

The energy of the hydrogen bonds E_H for several OH stretching bands has been calculated using the following equation (Poletto *et al.*, 2013; Poletto *et al.*, 2014);

$$E_H = \frac{1}{k} \left[\frac{v_0 - v}{v_0} \right] \dots \dots \dots 3.1$$

Where v_0 is the standard frequency corresponding to free OH groups (3650 cm^{-1}); v is the frequency of the bonded OH groups of the sample; and k is a constant ($1/k = 2.625 \times 10^2 \text{ kJ}$).

The hydrogen bond distances (R) are obtained using Equation 3.2:

$$\Delta v(\text{cm}^{-1}) = 4430 \times (2.84 - R) \dots \dots \dots 3.2$$

where $\Delta\nu = \nu_0 - \nu$; ν_0 is the monomeric OH stretching frequency, which is taken to be 3600 cm^{-1} ; and ν is the stretching frequency observed in the infrared spectrum of the sample.

Table 4.8 depicts the energy of the hydrogen bond and hydrogen bond distances calculated from IR spectra of different samples. Different samples had different hydrogen bond distances which was attributed to the intermolecular association within the samples.

Table 4.8: Energy of the hydrogen bond (E_H) and Hydrogen bond distances (R)

Sample	3342 cm^{-1}	
	E_H (kJ)	R (Å)
ATRH	19.3 ± 0.01	2.78 ± 0.05
RHCE	19.5 ± 0.02	2.77 ± 0.05
MTCE	20.0 ± 0.03	2.76 ± 0.05
USCE	19.5 ± 0.01	2.77 ± 0.05

The hydrogen bond distances (R) for all the samples under study were almost similar as shown in table 4.9. However, the hydrogen bond energy (E_H) values were different for untreated, alkali treated and rice husk cellulose. The energy of the hydrogen bond (E_H) for alkali treated rice husks (ATRH) was highest while the energy of the hydrogen bonds was lowest in mechanically treated rice husk cellulose. The higher hydrogen bond energies can be associated with lower hydrogen bond distance which contribute to higher interactions between intramolecular cellulose chains (Poletto et al., 2014; Ciolacu et al., 2011).

4.1.6 X-ray Diffractograms of Cellulose

Figure 4.4 depicts the diffractograms of rice husk after different treatments during conversion of the husks to cellulose as obtained from an X-ray diffractometer. The diffractogram obtained were typical of semi crystalline material since they were composed of a broad amorphous peak and a crystalline peak.

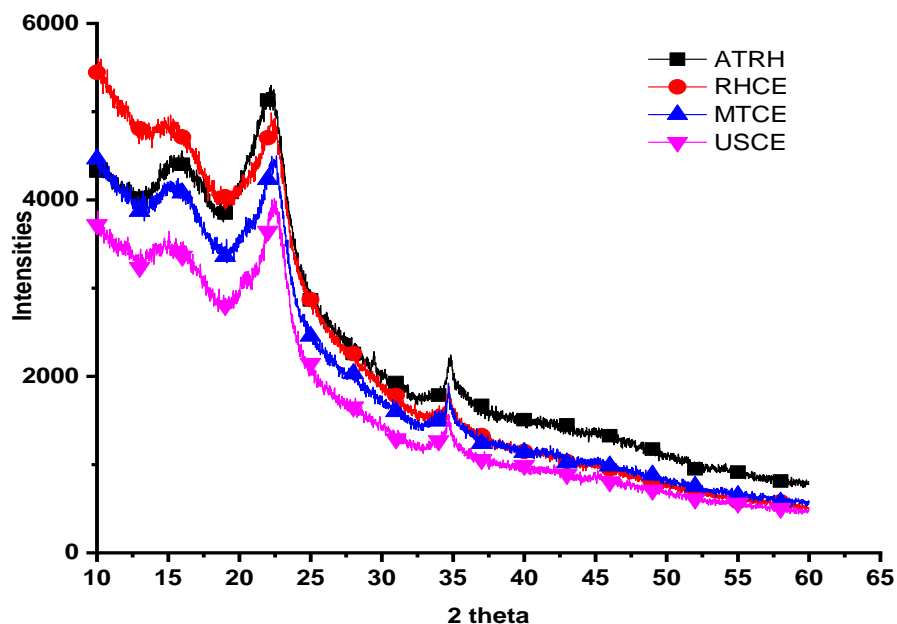


Figure 4.4: X-ray diffractograms of rice husk cellulose after being subjected to different treatments.

The crystalline structure was responsible for the peak observed at 22° whereas the amorphous domains are responsible for the peak observed at 16° (Nascimento *et al.*, 2016). These peaks at 2θ angles = 16° , 22° and 34° are attributed to the diffraction planes of (101) and (002) which are characteristic of type 1 cellulose (Kallel, *et al.*, 2016; Barbash *et al.*, 2017; Hooshmand *et al.*, 2017; Daicho *et al.*, 2018).

Table 4.9 represent the crystallinity index of alkali treated cellulose, rice husk cellulose, mechanical ground cellulose and ultra-sonicated cellulose as calculated using the Scherer equation.

Table 4.9: d spacing, percent crystallinity and Z value of cellulose fibers

Samples	2θ	FWHM	d (200) (nm)	Cr. I (%)	L_{200} (nm)
ATRH	22	1.41	0.40	23.02	4.7
RHCE	22	1.23	0.40	24.15	3.7
MTCE	22	1.23	0.40	22.95	3.7
USCE	22	1.14	0.40	27.65	4.0

Key: Cr. I = Crystallinity index, L_{200} = crystallite size

From the results obtained, the FWHM decreased in the order ATRH> RHCE> MTCE> USCE while the d spacing for the 200 crystal planes were the same for all samples. Half width is related to crystalline dimensions as a large half width corresponds to smaller crystalline sizes while a smaller half width corresponds to bigger crystallite sizes (Hon & Shiraishi, 2000). The average crystal size of the samples after each treatment were determined using the Scherer equation and the results revealed that RHCE had the smallest crystal size as compared to all the other samples (Table 3.10). Alkali treated rice husks had the largest crystal size which can be attributed to the presence of residual lignin and hemicellulose within the sample.

4.1.7 DSC Thermograms of Cellulose

Figure 4.5 represent the DSC thermograms of rice husks samples subjected to different treatment methods. The samples had very distinct endothermic peaks at the selected working range with endothermic peaks associated with cellulose being observed in all the samples.

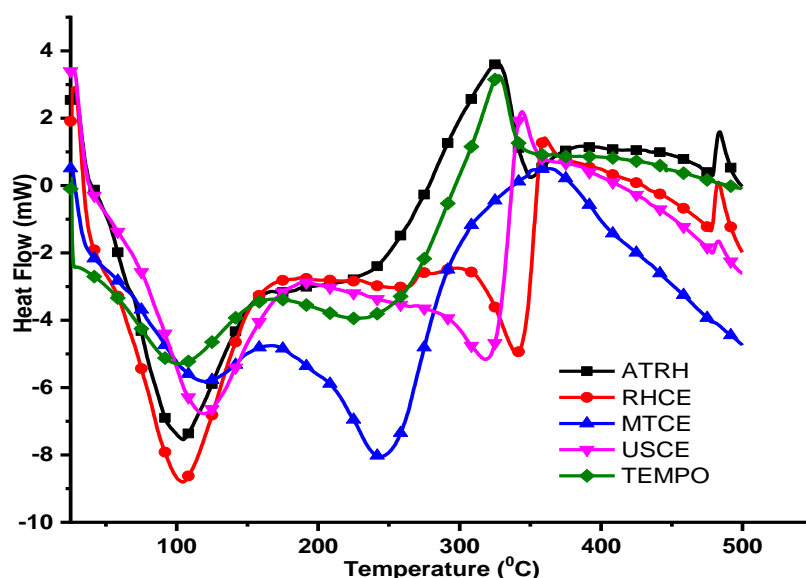


Figure 4.5: DSC thermograms of ATRH, RHCE, MTCE, USCE, and TOCNF

It is known that natural lignocellulosic material includes hemicelluloses, lignin, and cellulose, which have different structures that can be differentiated by their degradation profile during thermal analysis. These differences can be attributed to the

different structural and chemical characteristics of samples that are related to the content of cellulose, hemicellulose and lignin (Cengiz *et al.*, 2017). The first endothermic change occurs between 70 - 100 °C due to evaporation of water. The second endothermic reaction generally shows the degradation of hemicellulose structure and it is usually observed between 180-300 °C (Poletto, 2016). Of all the samples analyzed, only alkali treated rice husks had a small peak at this region, which is an indication of presence of residual hemicellulose after alkali treatment. Absence of this peak in rice husk cellulose, mechanical ground cellulose and ultrasonicated cellulose is an indication that chemical treatment of the alkali treated rice husks with peracetic acid was effective at removing residual hemicellulose from the samples. A large endothermic peak related to cellulose degradation reaction occurred between 300-360 °C (Poletto, 2016; Poletto *et al.*, 2014). The degradation reaction of cellulose starts at 300 °C and continues to 400 °C with maximum mass loss occurring at 242, 340, 246, and 318 °C for alkali treated rice husks (ATRH), rice husks cellulose (RHCE), mechanically treated (MTCE) and ultrasonicated cellulose (USCE) respectively (Appendix A). Generally, CNF derived from natural fibers have high thermal stabilities due to α -cellulose of lignocellulosic structures (Cengiz *et al.*, 2017; Blaine, 2013).

4.1.8 TGA-DTGA Thermogram of Cellulose

Figure 4.6 - 4.7 depicts the TGA/DTGA thermograms of rice husks after different treatment methods which resulted in changes in the thermal profile of the samples. All samples had two degradation stages between 50 -100 °C and 250 – 400 °C except TOCNF which had a third degradation stage with a maximum centered at 302 °C.

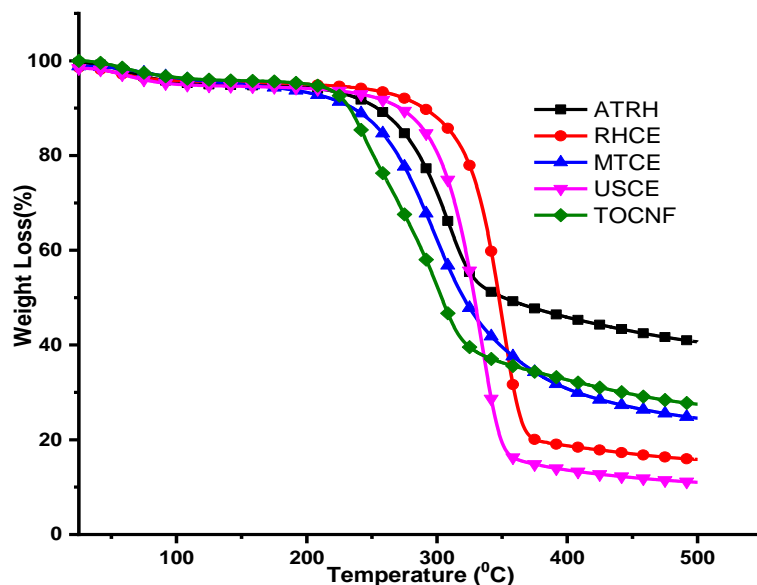


Figure 4.6: TGA curves of ATRH, RHCE, MTCE, USCE, and TOCNF

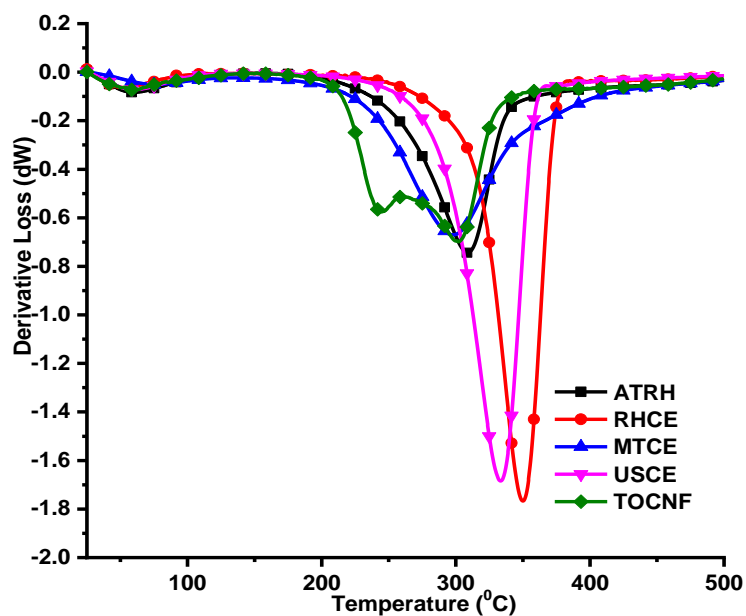


Figure 4.7: DTGA curves of ATRH, RHCE, MTCE, USCE, and TOCNF

The first stage of sample weight loss occurred in the range between 50 – 100 °C and it was mainly attributed to evaporation of water adsorbed on the surface of the samples. Second stage of degradation that accounted to approximately 70% weight loss can be attributed to thermal degradation of cellulose which was observed in all samples, but

residual weight loss and onset temperatures were different for all samples (Appendix B). Chemical treatment of cellulose has been reported decrease the thermal stability of the fibers hence the observed lower onset degradation temperatures (Isogai, 2018). It was also observed that thermal stability of ATRH, RHCE, MTCE, USCE, TOCNF was in the order TOCNF < MTCE < ATRH < USCE < RHCE with RHCE being the most stable. Lower thermal stability has been reported to be linked to increased crystallinity, fibril and particle sizes as highly crystalline and small particle size materials have a higher heat transfer ability due to increased surface area. Moreover, smaller particle sizes increase the number of end chains which in turn decompose at lower temperatures yielding higher amount of char while presence of inorganic salts and acids have been known to act as flame retardants during pyrolysis thereby increasing char yield (Yildirim & Shaler, 2017; Nascimento *et al.*, 2016).

4.2 Synthesis of Dialdehyde Cellulose (DAC)

4.2.1 Variation of Oxidant Concentration

Periodate oxidation of cellulose occurs at C₂ and C₃ is similar to that of vicinal diols following the general mechanism in figure 4.8 in which the primary alcohol transforms into formaldehyde and secondary ones into aldehyde groups (Leguy *et al.*, 2018; Leguy *et al.*, 2018; Gilbert & Martin, 2016).

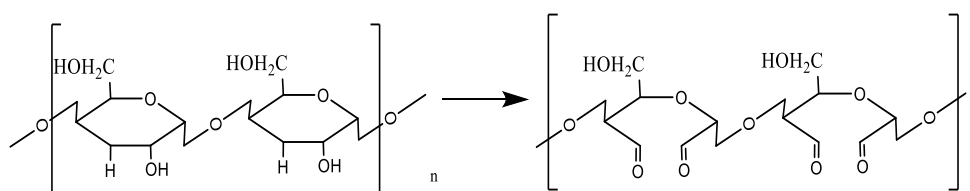


Figure 4.8: General mechanism for periodate oxidation of cellulose

Upon oxidation, potentiometric titration was used to determine the degree of oxidation which was found to increase with increase in oxidant concentration as it can be observed in figure 4.9. From the results obtained (Figure 4.9), the aldehyde content of the fibers increases with a subsequent increase in potassium periodate hence the

amount of KIO_4 plays a critical role in the degree of oxidation of the fibers, but it resulted in a subsequent decline in the percent yield of dialdehyde cellulose (DAC).

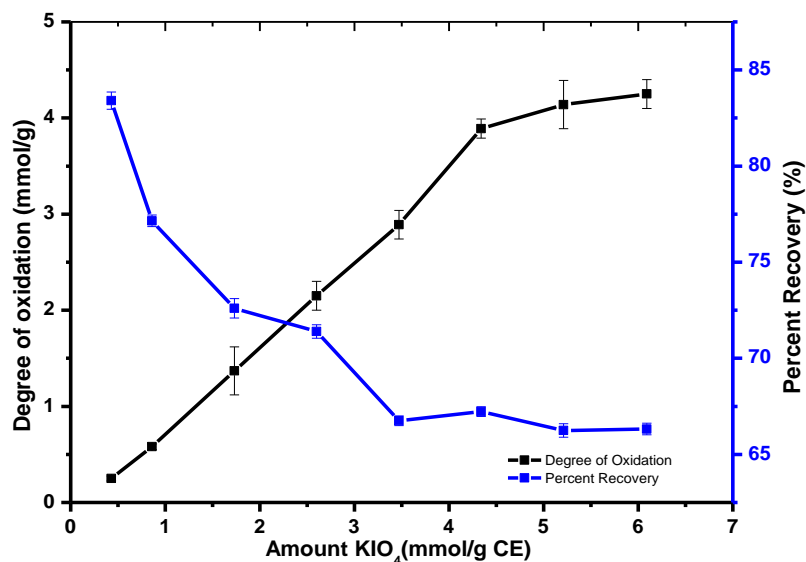


Figure 4.9: Influence of amount of KIO_4 on degree oxidation and percent recovery

Similar results were reported when cellulose fibers from bamboo were subjected to oxidation with sodium periodate (Wei, *et al.*, 2016; Nematdoust *et al.*, 2020). This is a heterogeneous reaction since the salt is soluble in water, but cellulose is not, and it is a highly selective reaction that only cleaves vicinal diols hence limiting the number of reaction products generated. It is also characterized by the degree of oxidation, which represents the average number of aldehyde groups introduced per AGU (Hoglund, 2015). Statistical analysis of the data obtained revealed that there was a significant difference ($p \leq 0.05$) in the degree of oxidation of cellulose oxidized when the concentration of KIO_4 was varied. ANOVA showed that an increase in the amount of the oxidant used significantly increased the degree of oxidation of the pulp fibers, $F(8,9) = 750.75$ $P = 8.63\text{E-}12$ (Appendix C).

4.2.2 Variation of Reaction Time

Figure 4.10 depicts the effect of changes in reaction time on the percent recovery and degree of oxidation of fibers in which the degree of oxidation increased with longer reaction times. On the other hand, the percent recovery decreased with this increase in reaction time

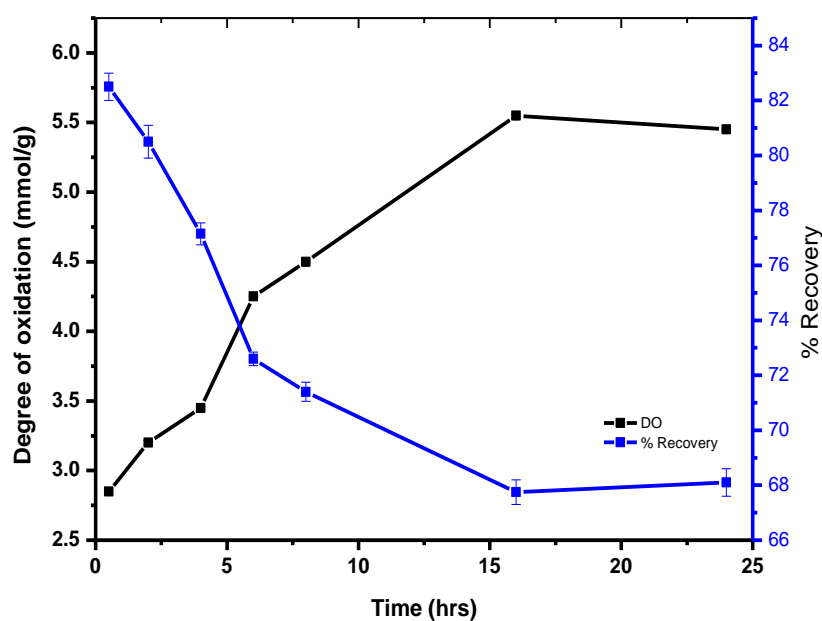


Figure 4.10: Effect of oxidation time on degree of oxidation and percent recovery (%)

The optimum reaction time was found to be 16 h (Figure 4.10) as above this the DO of cellulose decreased because longer reaction time led to formation of undesirable side products. This was also observed when the oxidized cellulose was analysed to determine the effect of reaction time on degree of oxidation and percent recovery. Longer reaction time leads to a decrease in the percent recovery of the oxidized cellulose as an increase in reaction time subjected the fibers to prolonged oxidation which in turn resulted in cleavage of more amorphous domains. Moreover, depending on the substrate used, the reaction time affects the degree of oxidation of cellulose in that with an increase in reaction time, the degree of oxidation of cellulose increases up to a maximum after which the DO starts to decrease. (Hoglund, 2015; Nematdoust *et al.*, 2020). Statistical analysis of the data obtained revealed that there was a significant

difference ($p \leq 0.05$) in the degree of oxidation of cellulose oxidized when the reaction time was varied. ANOVA showed that an increase in the reaction time significantly increased the degree of oxidation of the pulp fibers, $F(7, 8) = 5.46$ $P = 1.45E-2$ (Appendix D).

4.2.3 Variation of Reaction Temperature

Figure 4.11 depicts the reaction that were carried out at different reaction temperatures and the resultant products. From the results obtained in this study, it was observed that the reaction temperature determined the products formed at the end of the reaction as impurities such as iodine and KIO_3 were formed at higher temperatures.

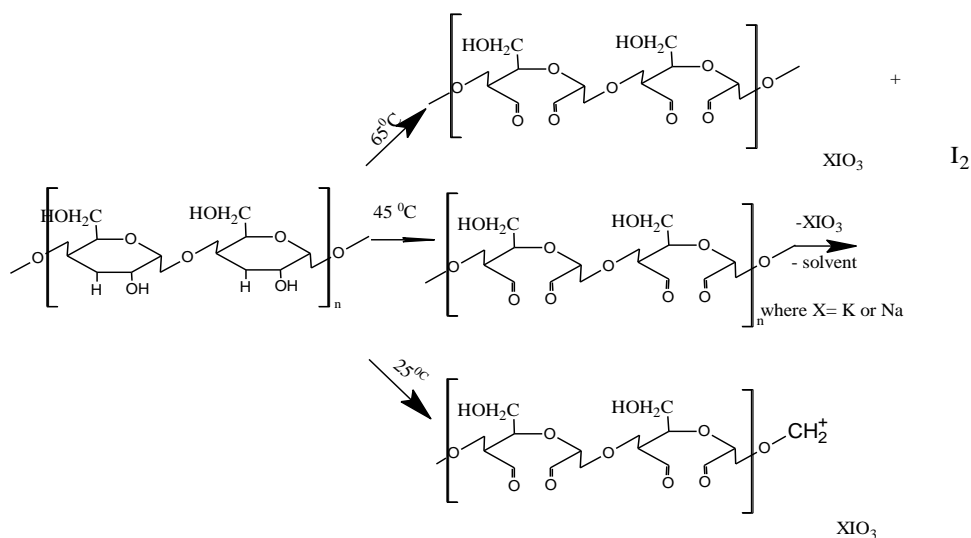


Figure 4.11: Schematic representation of influence of reaction temperature on oxidation of cellulose

At 25 °C, the degree of oxidation was low, and the reaction proceeded for longer periods as compared to 45 °C while above this temperature undesirable side products were observed (Appendix E). Above 45 °C, the decomposition of potassium periodate into iodine and potassium iodate was observed as compared to lower temperatures in which this side products were not generated though the reaction took more time to complete (Hoglund, 2015). Potentiometric titrations further revealed that the degree of oxidation increased with increase in reaction time but led to a decrease in percent recovery at the end of the reaction. Moreover, the result indicates that the periodate

decomposition takes place when the oxidation is performed at elevated temperatures (>85 °C) (Hoglund, 2015; Nematdoust *et al.*, 2020).

4.2.4 FTIR Characterization of Dialdehyde Cellulose (DAC)

Figure 4.12 depicts the IR spectra of cellulose obtained before and after introduction of the carbonyl functional groups at C₂ and C₃. The characteristic cellulose peak, such as a broad peak at around 3400 cm⁻¹ was observed and attributed to the OH stretching vibration while the peak at 2900 cm⁻¹ was attributed to CH₂ stretching vibrations (Figure 4.12).

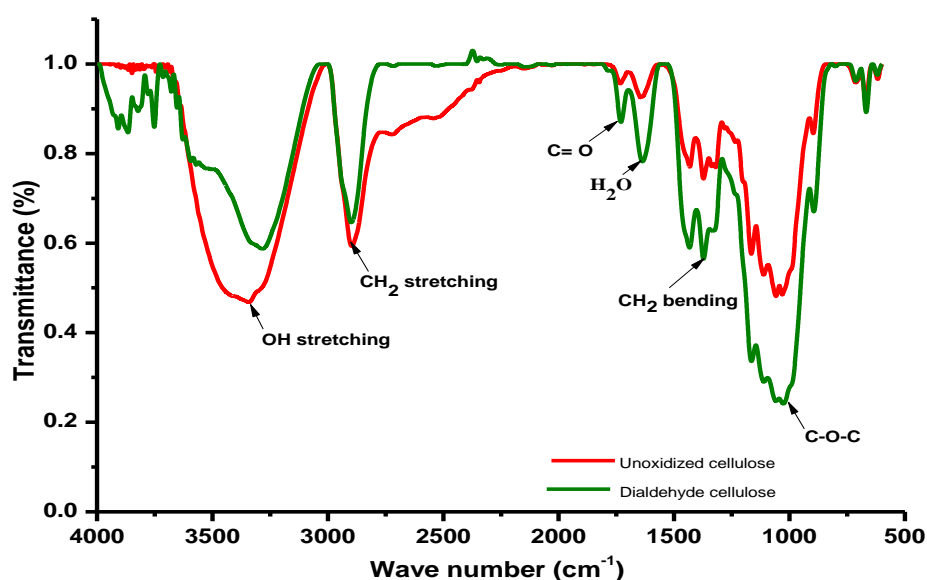


Figure 4.12: FT-IR spectra of cellulose and dialdehyde cellulose

The spectral bands observed in the region of 1632 cm⁻¹ was due to OH bending of adsorbed water (Abou-Zeid *et al.*, 2018; Socrates, 2004). All samples showed absorption bands characteristic of dialdehyde cellulose at around 1740 and 880 cm⁻¹ respectively in which the former was assigned to the C-O stretching of free aldehyde and the latter to hemiacetal structure (Gilbert & Martin, 2016). The intensity of the aldehyde band around 1740 cm⁻¹ increased with increase in cellulose to oxidant ratio with maximum intensity attained when the ratio of cellulose to the oxidant was 1:1.4 (w/w). Variations of reaction temperature led to synthesis of side products in the reaction as when the temperature of the reaction was varied between 25, 45 and 65 °C

it led to formation of either KIO_3 and iodine or both respectively (Appendix E). Higher reaction temperatures favored the formation of iodine while lower reaction temperatures favoring formation of KIO_3 as reported in literature (Hoglund, 2015; Nematdoust *et al.*, 2020).

4.2.5 X-ray Diffractograms of Dialdehyde Cellulose (DAC)

Figure 4.13 depicts the X-ray diffractograms of cellulose having different degree of oxidation resulting in different degree of crystallinity are shown in Table 4.10. With successive cleavage of pyranose rings and hydrogen bonds present in cellulose, a remarkable decrease in the crystallinity of cellulose can be observed from the XRD pattern (Plappert, *et al.*, 2018). At higher oxidant concentrations, the two peaks of cellulose at 2θ values of 16° and 22° that correspond to 001 and 200 crystal planes in cellulose structure were merged into one peak at 18° . This is an indication that periodate oxidation results into a more amorphous structure in which the cellulose peaks observed in unoxidized fibers are merged into one centered at this value (Errokh *et al.*, 2018; Poletto *et al.*, 2014).

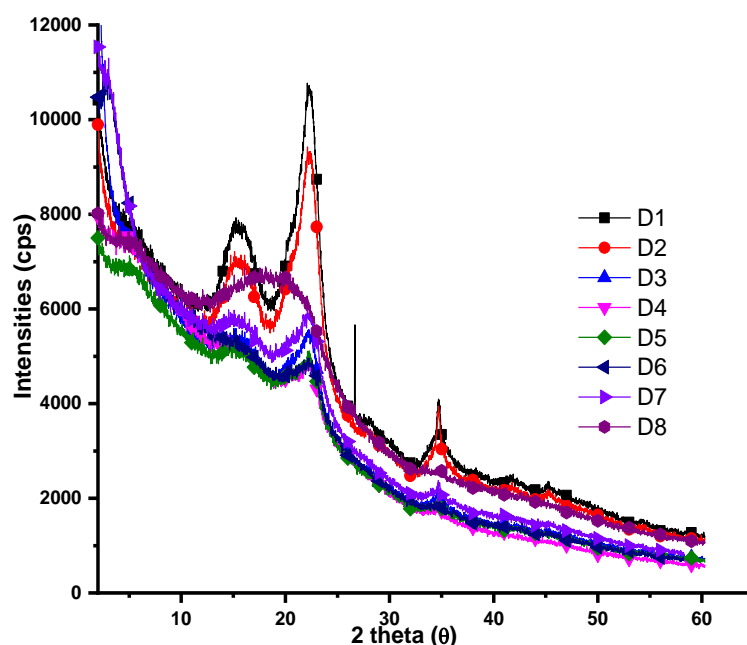


Figure 4.13: X-ray diffractograms of dialdehyde cellulose obtained with different amounts of oxidant per gram of cellulose

Table 4.10: Influence of amount of KOI₄ on the degree of crystallinity

Sample ID	CI (%)	DO (mmol/100g)
D0	42.3	0
D1	38.6	0.25
D2	26.5	0.43
D3	14.8	1.07
D4	10.7	1.55
D5	12.9	1.99
D6	9.60	2.84
D7	9.10	2.34
D8	-	3.80

The amorphous peak at 18° has been used by numerous authors as a basis for the calculation of the empirical crystallinity index of cellulose using Segal's method (Besbes et al., 2011; El Achaby, et al., 2018; Segal *et al.*, 1959; Poletto *et al.*, 2014; Ciolacu *et al.*, 2011). This can also be explained by the fact that periodate oxidation opens up the glucopyranose ring in native cellulose thereby leaving the amorphous domain intact while at the same time destroying the ordered packing of cellulose (Leguy, *et al.*, 2018). Moreover, the crystallinity of the fibers decreased with an increase in oxidant concentration as at higher concentrations the material became completely amorphous hence the disappearance of the crystalline peaks often observed at $2\theta = 22^\circ$ as observed after 16 h of oxidation (Lindh *et al.*, 2016; Nematdoust *et al.*, 2020).

Figure 4.14 depicts the X-ray diffractograms of dialdehyde cellulose synthesized at different reaction temperature resulting in different degree of oxidation resulting and crystallinity index (Table 4.11).

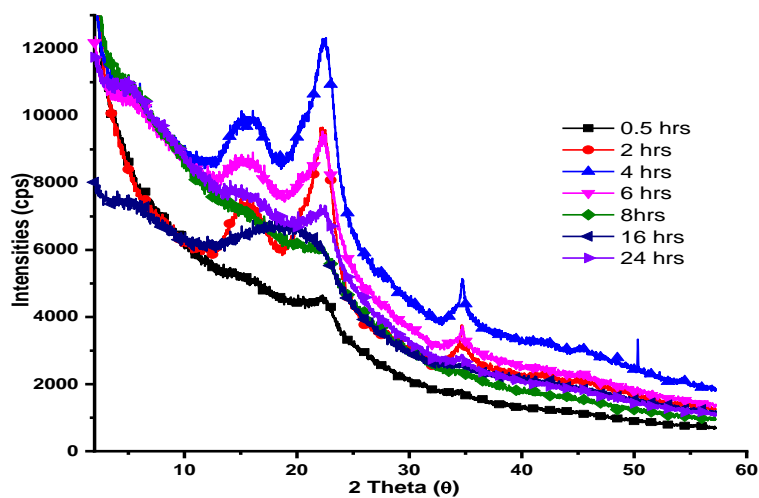


Figure 4.14: X-ray diffractograms of dialdehyde cellulose at different reaction times

Table 4.11: Influence of reaction time on the degree of crystallinity

Oxidation Time	CI (%)	DO (mmol/100g)
0.5	54	2.85
2	39	3.20
4	31	3.45
6	19	4.25
8	1	4.51
16	0	5.55
24	7	5.45

Figure 4.15 depicts the influence of the reaction temperature on cellulose crystallinity during oxidation reaction. As observed in figure 4.15 cellulose crystallinity changed depending on the temperature of the reaction media as at 45 °C, the cellulose peak that is usually observed at $2\theta = 22^\circ$ and $2\theta = 18^\circ$ disappeared.

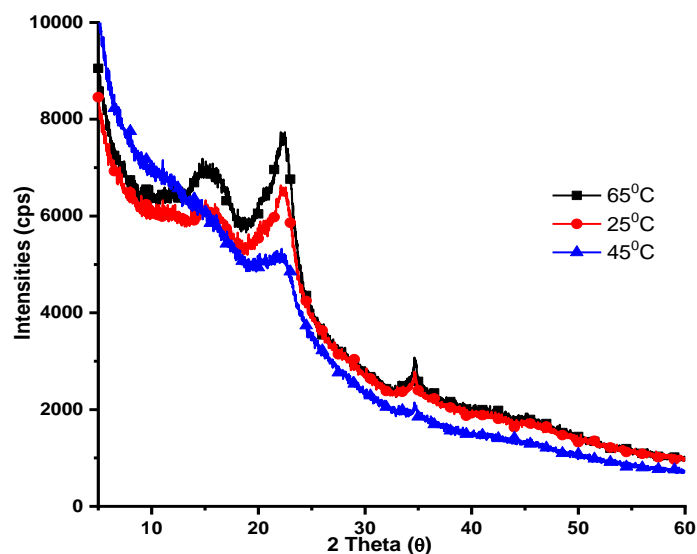


Figure 4.15: Effect of Reaction temperature on crystallinity of dialdehyde cellulose

This was an indication of conversion of cellulose to dialdehyde cellulose which cleaves the C₂ and C₃ carbons in cellulose thereby rendering the material more amorphous (Leguy, 2018). When the temperature of the reaction media was increased to 65 °C, this change from semi-crystalline material to amorphous material was not observed which can be attributed to the fact that higher reaction temperatures led to decomposition of periodate ion. This decomposition decreased the degree of oxidation of cellulose which in turn did not yield an amorphous material as observed in the diffractograms of the subsequent materials formed at the end of the reaction (Hoglund, 2015; Nematdoust *et al.*, 2020).

4.2.6 DSC Thermograms of Dialdehyde Cellulose Nanofibrils (DAC)

Figure 4.16 – 4.18 depict DSC thermograms of dialdehyde cellulose showing changes in thermal stability of the material after oxidation using varying amounts of potassium periodate. From the DSC thermograms, it was observed that cellulose fibers had two endothermic peaks, a broad peak centered at 109 °C corresponding to water loss and a sharp peak centered at 340 °C corresponding to cellulose decomposition ($\Delta H_g = 33.93$ J/g).

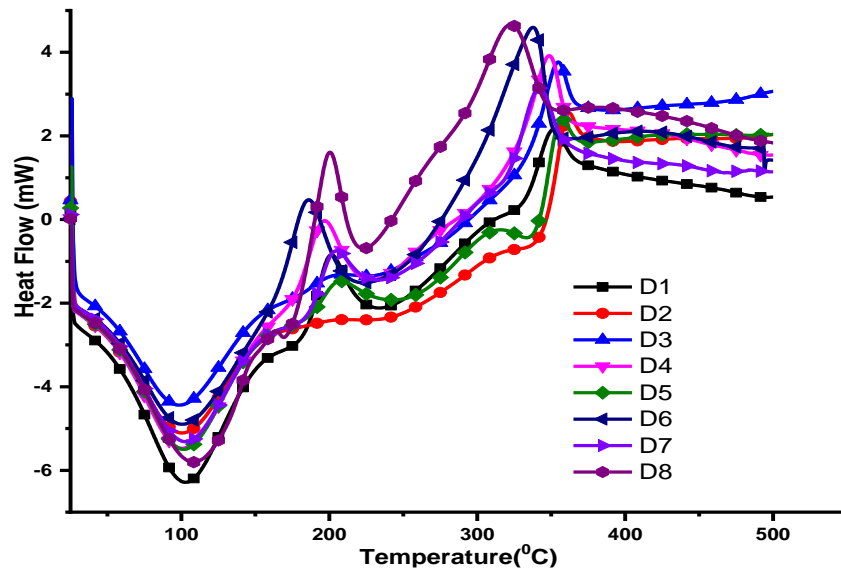


Figure 4.16: DSC thermogram of Dialdehyde cellulose with different aldehyde content

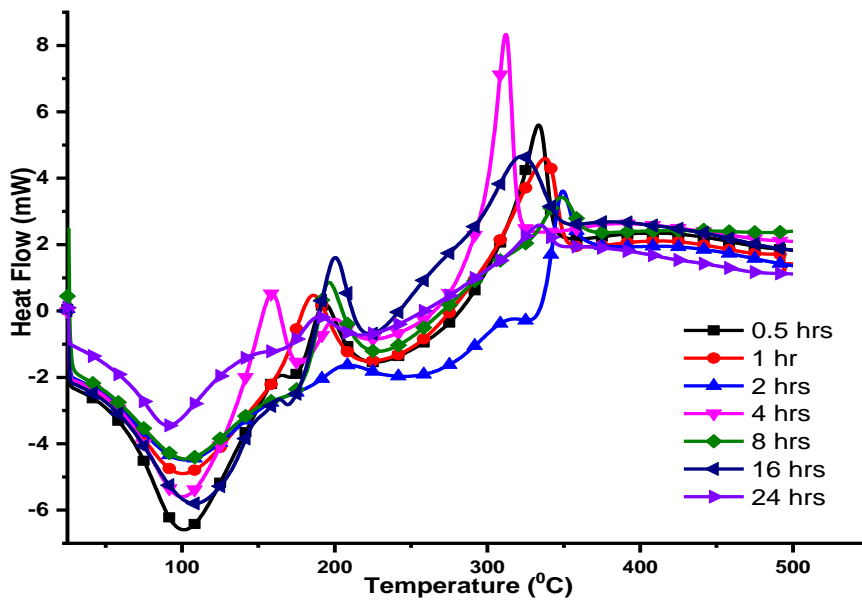


Figure 4.17: DSC thermogram of Dialdehyde cellulose after different oxidation times

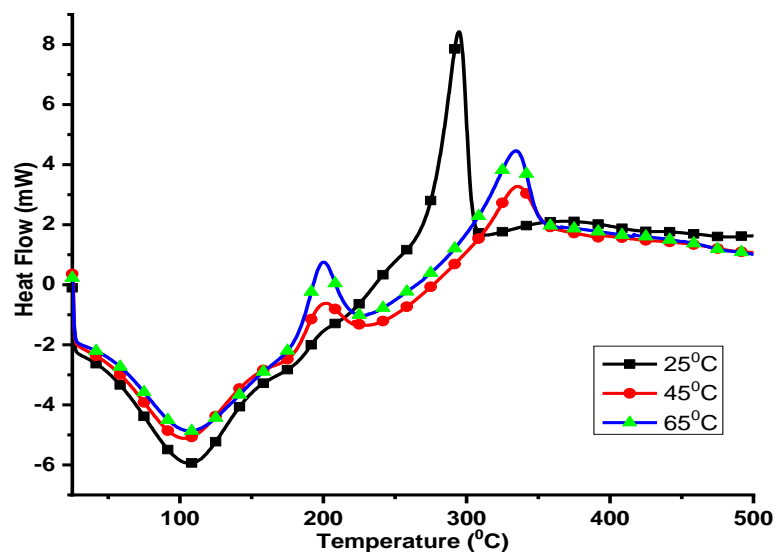


Figure 4.18: DSC thermogram of Dialdehyde cellulose after different oxidation temperatures

The DSC thermogram of dialdehyde cellulose with different aldehyde contents were similar to that of cellulose but the peak at 340 °C became increasingly shorter and smaller (Zhang *et al.*, 2017). These samples possessed one endothermic peak between 100-110 °C and two exothermic peaks between 190-205 °C and 320-365 °C with a subsequent disappearance of the endothermic peak centered at around 340 °C (Appendix F). The disappearance of the endothermic peak at around 340 °C, while the new exothermic peaks produced, was attributed to the destruction of the ordered structure of cellulose during oxidation with potassium periodate that reduced the crystallinity as reported elsewhere (Zhang, Ge, Xu, Cao, & Dai, 2017). The loss of crystallinity due to ring opening of AGU during oxidation of cellulose disrupts cellulose ordered structure leading to formation of two new exothermic peaks in DSC curves of periodate oxidized cellulose when C₂–C₃ bond are cleaved during oxidation of MCC (Li *et al.*, 2011). These leads to a variation in the structure, crystallinity, and degree of polymerization, which in turn affect its physical and chemical properties. Moreover, Mou *et al.*, (2017) reported that oxidation of cellulose imparts antimicrobial activity to the oxidized fibers against *Staphylococcus aureus* and improved the biocompatibility with mammalian cells as the oxidized fibers showed good blood compatibility (Mou, Li, Wang, Cha, & Jiang, 2017).

4.2.7 TGA-DTGA Thermogram of Dialdehyde Cellulose

Figure 4.19 – 4.20 depict TGA thermograms of dialdehyde cellulose showing changes in thermal stability of the material after oxidation using varying amounts of potassium periodate. From figure 4.19 - 4.20, all the sample were characterized by two degradation stages with different weight loss apart from cellulose oxidized for 16 h which had three degradation stages.

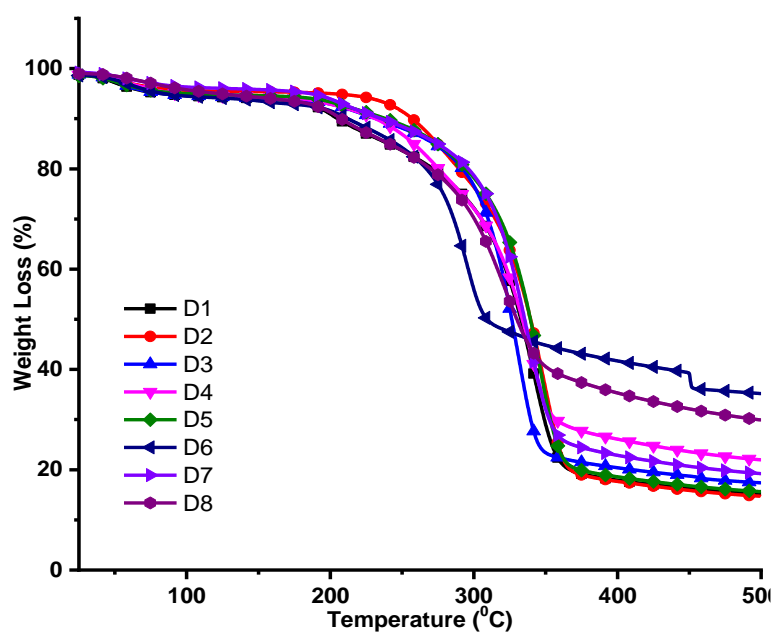


Figure 4.19: TGA curves of dialdehyde cellulose with different degree of oxidation

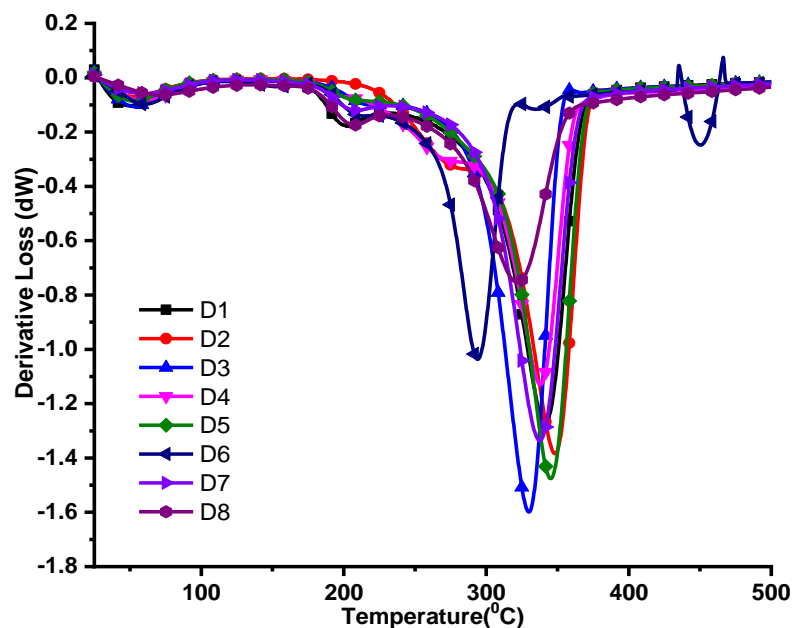


Figure 4.20: DTGA curves of dialdehyde cellulose with different degree of oxidation

The first degradation cycle occurred between 50 - 100 °C and it can be attributed to loss residual water present on the surface of the polymers, while the second degradation cycle which occurred between 180 - 300 °C was attributed to decomposition of cellulose (Appendix G). The thermal stability of the sample was greatly influenced by the oxidation times as it was observed that at lower oxidation time, cellulose was thermally stable as compared to when the samples were subjected to an oxidation time of 16 h.

Figure 4.21 – 4.22 depict TGA thermograms of dialdehyde cellulose showing changes in thermal stability of the material after oxidation of cellulose at different reaction times. It was also observed that an increase in the oxidation time (24 h) resulted in fibers which were more thermally stable which was attributed to changes in the fiber structure as a result of cleavage of the anhydroglucose units (Appendix H).

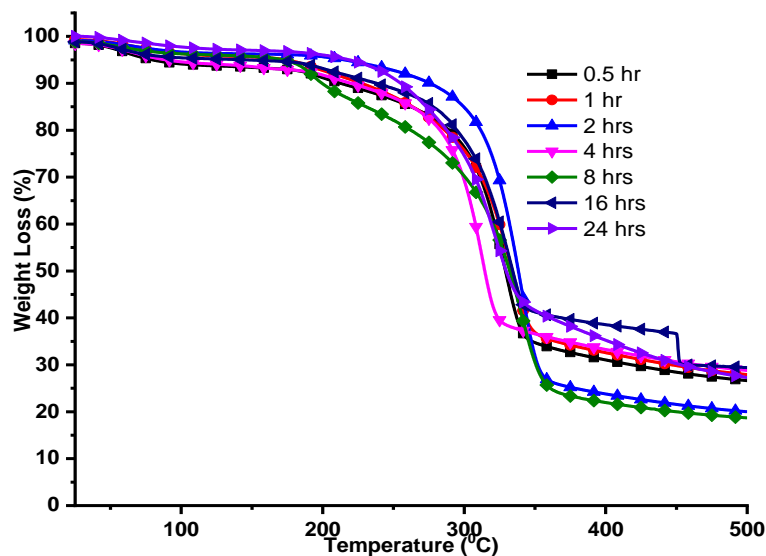


Figure 4.21: TGA curves of dialdehyde cellulose with different oxidation time

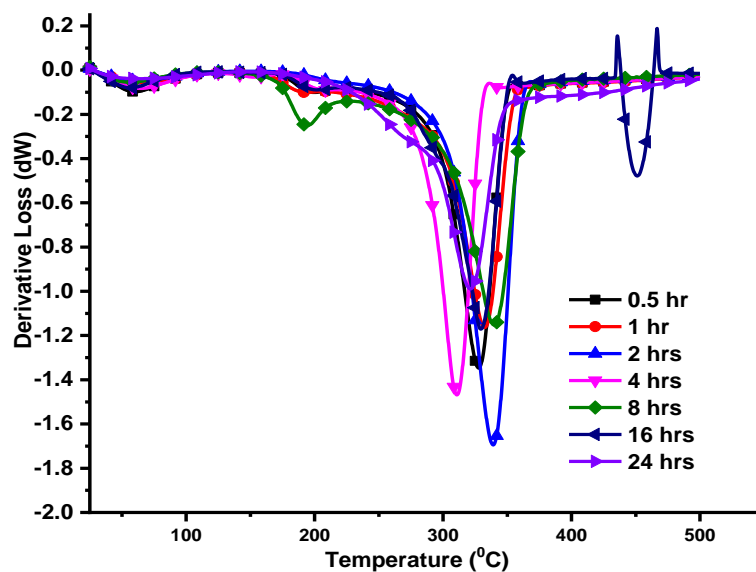


Figure 4.22: DTGA curves of dialdehyde cellulose with different oxidation time

Higher oxidation times led to decomposition of potassium periodate and formation of side products in the reaction system which reduced the degree of oxidation of dialdehyde cellulose (Leguy *et al.*, 2018; Leguy, 2018).

Figure 4.23 and 4.24 depicts the influence of temperature on thermal stability of dialdehyde cellulose. With respect to the reaction temperatures, it was observed that

temperatures exceeding 45 °C resulted in the decomposition of the oxidant which in turn reduced the degree of oxidation of cellulose (Figure 4.23-4.24).

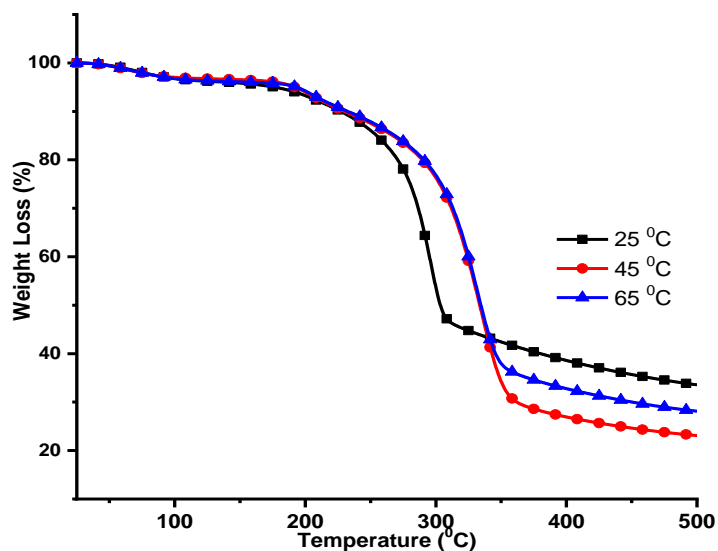


Figure 4.23: TGA curves of dialdehyde cellulose with different oxidation temperatures

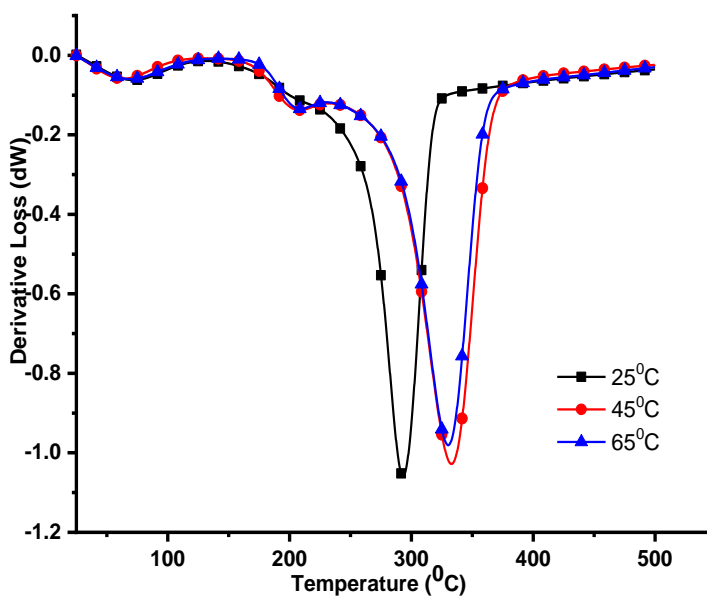


Figure 4.24: DTGA curves of dialdehyde cellulose with different oxidation temperatures

Since thermal stability is influenced by particle size as of a polymer, increasing the oxidation temperatures decreased the thermal stability of dialdehyde cellulose (Appendix I). This is because smaller particle size which resulted from oxidation of cellulose to dialdehyde cellulose tend to dissipate heat faster as compared to larger particles (Nematdoust *et al.*, 2020).

4.3 Synthesis of TEMPO Oxidized Cellulose Nanofibrils

4.3.1 Variation of NaOCl

Figure 4.25 depicts the variation in the carboxyl content of cellulose when the concentration of sodium hypochlorite was varied during synthesis of TOCNF. The DO of the fibers increased with a subsequent increase in the concentration of NaOCl used with optimum DO's observed when the concentration was 2.0 mM.

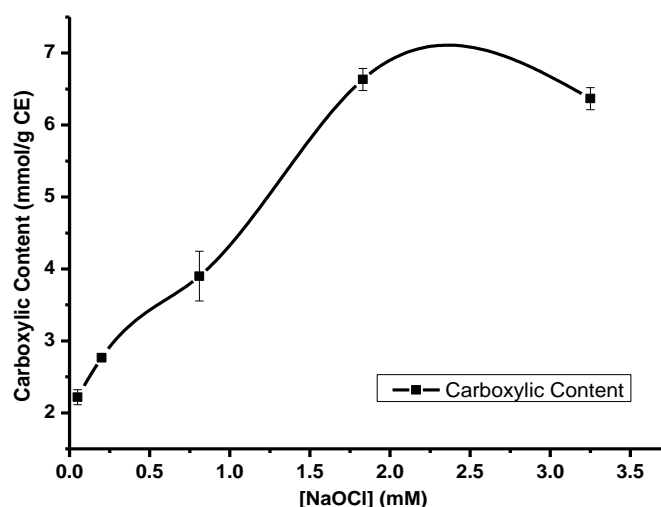


Figure 4.25: Effect of NaOCl concentration on Carboxylic content of TOCNF

TEMPO-mediated oxidation is regioselective surface modification of cellulose which oxidized the primary C₆ hydroxyl groups of rice husk cellulose into carboxylic acid which were then ionized to sodium carboxylates at pH 10. The predominantly charged sodium carboxylate CNF was then protonated at the end of the reaction to convert sodium carboxylates into carboxylic acid using acetic acid. Potentiometric titration of aqueous TOCNF suspensions facilitated the determination of COOH content, and the

results indicate that there was a slight increase in carboxyl content with variation of NaOCl which declined at higher oxidant concentrations (Figure 4.25). The surface COOH content at the plateau region was calculated to be 2.21 ± 0.11 , 2.76 ± 0.21 , 3.90 ± 0.34 , 6.63 ± 0.15 and 6.37 ± 0.16 mmol/g for T1, T2, T3, T4, and T5 respectively. From the potentiometric graphs (Appendix J-M), it was observed that there was an initial increase in the carboxyl content and subsequent decrease in the DO when higher NaOCl concentrations were used (Jiang & Hsieh, 2018). Statistical analysis of the data obtained revealed that there was a significant difference ($p \leq 0.05$) in the degree of oxidation of cellulose when the concentration of NaOCl was varied. ANOVA showed that an increase in the concentration of the oxidant significantly increased the degree of oxidation of the pulp fibers, $F(4,5) = 179.03$ $P = 1.39E-5$ (Appendix N).

4.3.2 Variation of Cellulose Source

Table 4.12 depicts the changes observed in the carboxyl content of TEMPO oxidized cellulose nanofibrils synthesized using cellulose extracted from different biomasses. The influence of the cellulose source on the degree of oxidation (DO) revealed that there was very little change in the carboxyl content of the oxidized fibers when cellulose was obtained from different agricultural residues.

Table 4.12: Determination of carboxyl content of cellulose pulp from various sources

Sample	Mass (g)	DO (mmol/g)	Homogeneous Dispersion
MCC CO	0.1	12.9 ± 1.7	No
CH Cellulose	0.1	10.4 ± 0.8	No
RH Cellulose	0.1	7.8 ± 0.1	No
CO Cellulose	0.1	12.7 ± 0.6	No
SB Cellulose	0.1	12.2 ± 0.6	No

Key: RH-Rice Husk, CH-Coffee husks, CF-Coconut fibers, SB-Sugar cane bagasse, CO-commercial cellulose

As it can be observed in table 4.12, the biomass used to isolate cellulose had little or no effect on the carboxyl content and dispersibility of the fibers in water as the resultant fibers were not homogenous. A solution is described

being homogeneous mixture if one material that is dispersed into another does not settle when the solution is left standing for prolonged periods of time. As has been reported earlier, the properties TOCNF dispersion are not dependent on the source, but type of cellulose used during oxidation with reaction conditions employed during synthesis having little or no effect on the dispersibility of TOCNF. Similar results have been reported in which cotton linters, bleached kraft pulp and bacterial cellulose were all oxidized using TEMPO/NaBr/NaClO system, over extended reaction times and in mild and harsh reaction conditions, without forming homogenous dispersions (Isogai *et al.*, 2011). But when regenerated and ball milled cellulose were subject to this oxidation system, clear water-soluble homogenous dispersions were obtained as the reaction progressed due to the accessibility of OH groups occasioned by changes in the crystalline structure of the starting material. It has been shown that native cellulose is composed of cellulose I crystal structure which contains extensive hydrogen bonding as compared to regenerated or mercerized cellulose which contains cellulose II allomorphs. Due to this difference in crystalline structure, clear dispersions of cellulose are obtained only when regenerated or mercerized cellulose samples are used during oxidation to produce water soluble polyglucuronic acid (da Silva Perez *et al.*, 2003; Isogai, Saito, & Fukuzumi, 2011). Statistical analysis of the data obtained revealed that there was a statistically significant difference ($p \leq 0.05$) in the degree of oxidation when the source of cellulose was varied. ANOVA showed that when the source of cellulose was changed the degree of oxidation of the pulp fibers changed significantly, $F(4, 10) = 15.88$ $P = 2.48E-4$ (Appendix O).

4.3.3 FTIR Characterization of TEMPO Oxidized Cellulose (TOCNF)

Figure 4.26 depicts the reaction scheme used functionalize cellulose by introduction of carboxyl groups at C₆ and subsequent reduction of Ag ions in solution to obtained cellulose nanofibrils containing AgNPs.

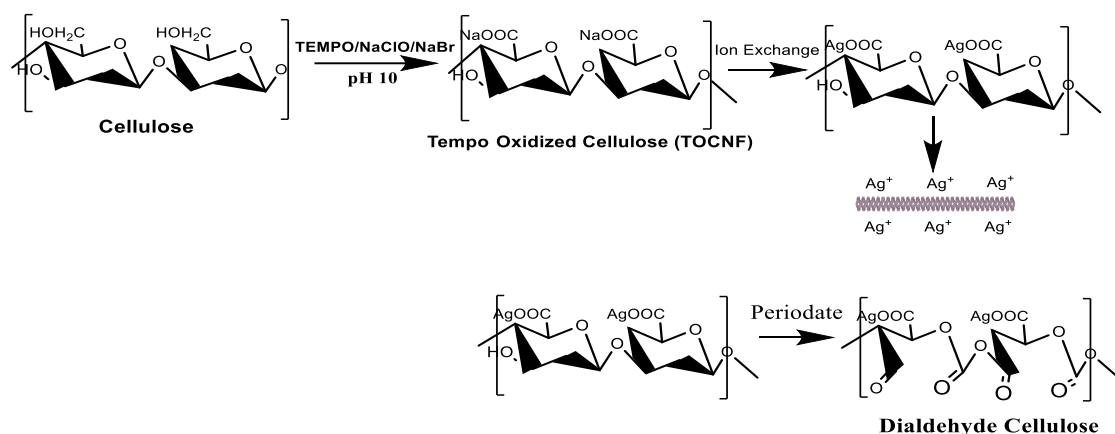


Figure 4.26: Reaction scheme representing conversion of cellulose to TOCNF, DAC and TOCNF-DAC-AgNPs

While periodate oxidation is specific to C₂ and C₃ of cellulose, TEMPO mediated oxidation converts C₆ OH groups into sodium carboxylate groups which can be converted to carboxylic groups through ion exchange. This conversation was observed in IR spectra in Figure 4.26-4.27 in which the carbonyl vibrational frequency was observed to increase with increase in the amount of oxidant used during the synthesis and subsequent ion exchange to obtain fully protonated fibrils.

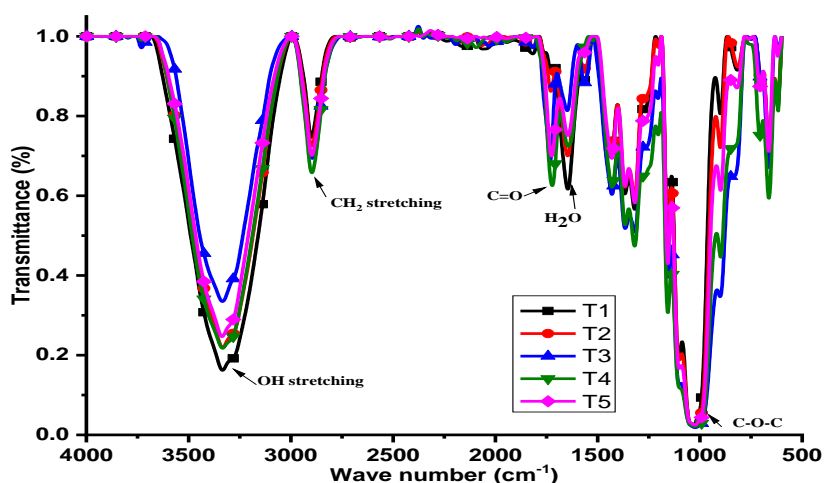


Figure 4.27: FT-IR spectra of TEMPO oxidized cellulose pulp with different carboxyl content

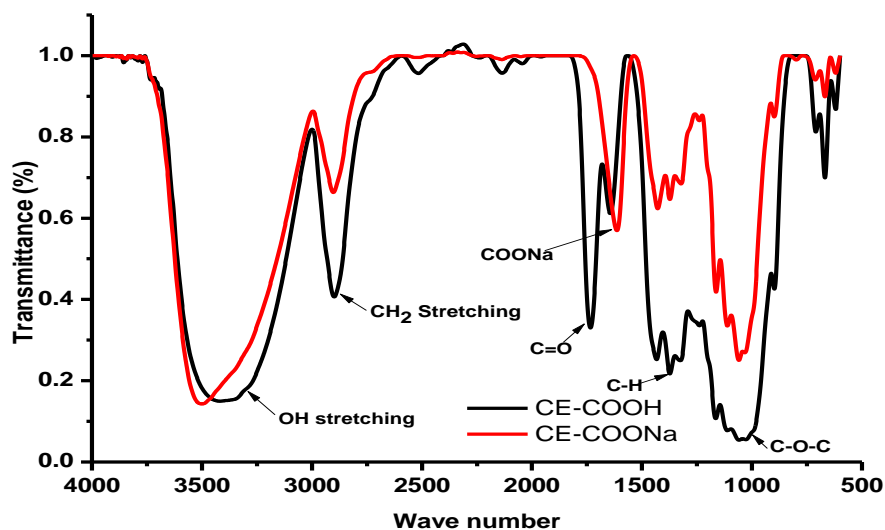


Figure 4.28: FT-IR spectra of TEMPO oxidized cellulose before (COONa) and after (COOH) ion exchange

This conversation was confirmed from the IR spectra TOCNFs which showed cellulose characteristic peaks at 3400 cm^{-1} (OH stretching), 2900 cm^{-1} (CH_2 stretching), 1417 cm^{-1} (H-C-H stretching), 1300 cm^{-1} , (H-C-H wagging vibration) and 1100 cm^{-1} (C-O-C asymmetric stretching) vibration of cellulose (Socrates, 2004; Gilbert & Martin, 2016). The major difference lied in 1619 cm^{-1} and 1728 cm^{-1} corresponding to COONa and COOH stretching vibrations observed in TOCNF before and after ion exchange (Figure 4.28) (Jiang & Hsieh, 2018; Lichtenstein & Lavoine, 2017). A sharp peak at 1619 cm^{-1} confirmed the presence of COONa that upon ion exchange shifted to 1730 cm^{-1} indicating the conversion of surface COONa to COOH in TEMPO oxidized cellulose (TOCNF). For unidentate complexes the coordinated carboxylate groups have a strong band due to the C=O stretching vibration in the range $1650\text{-}1590\text{ cm}^{-1}$. The position of this band is dependent on the metal atom, the frequency increasing as the metal-oxygen bond becomes more covalent. These results also indicated that with increase in the concentration of NaOCl during the oxidation reaction, the intensities of the carbonyl functional group at 1730 cm^{-1} also increased (Jiang & Hsieh, 2018; Lichtenstein & Lavoine, 2017). The main difference between native rice husk cellulose, mechanical treated cellulose, ultrasonicated cellulose and TEMPO oxidized cellulose (TOCNF) is the 1619 cm^{-1} peak present in oxidized

cellulose which corresponds to COO^-Na^+ group. The disappearance of this peak in acid treated cellulose (TOCNF) confirmed the conversion of COONa to COOH with the $\text{C}=\text{O}$ peak appearing at around 1730 cm^{-1} (Isogai, 2018; Lichtenstein & Lavoine, 2017).

4.3.4 X-ray Diffractograms of TEMPO Oxidized Cellulose Nanofibrils (TOCNF)

Figure 4.29 depicts the changes in the crystallinity observed when cellulose was functionalized by variation of NaOCl concentrations. It was observed that the crystallinity of cellulose increased with increase in the amount of oxidant.

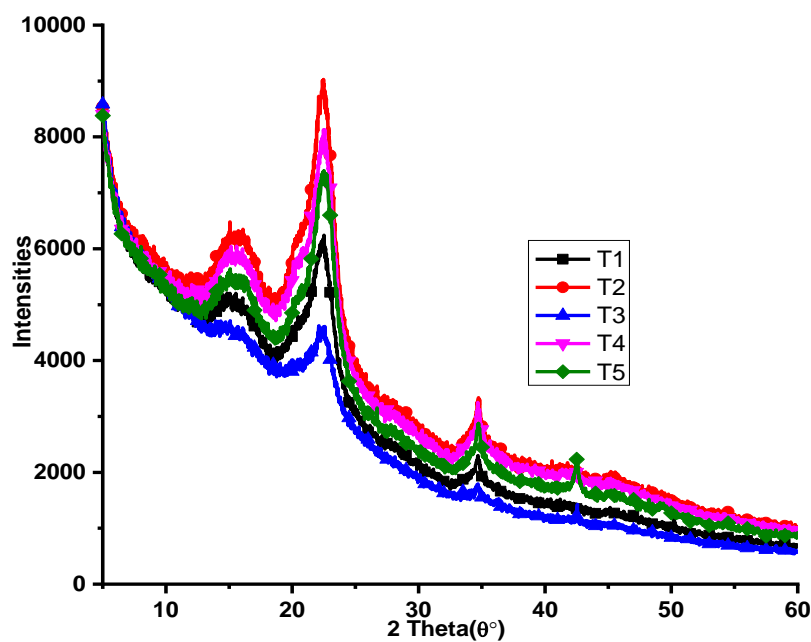


Figure 4.29: X-ray diffractograms of TOCNF with different carboxyl content

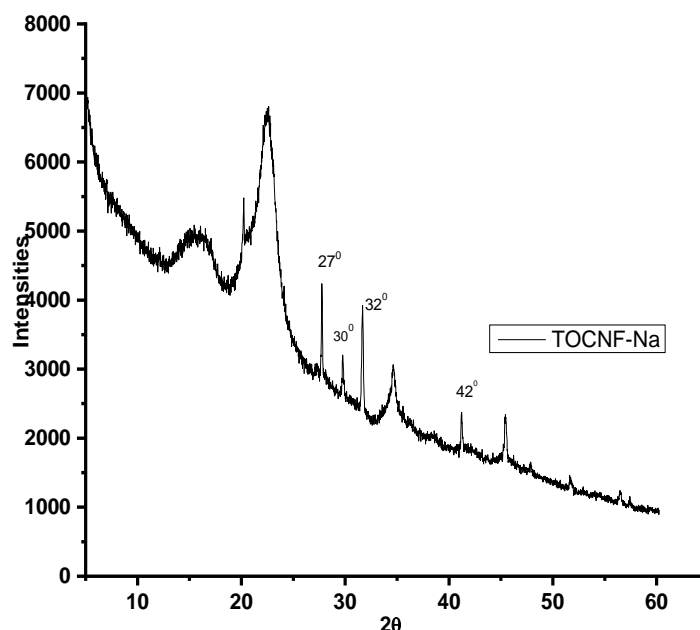


Figure 4.30: X-ray diffractograms of TOCNF with NaCl impurity peaks

Table 4.13: Influence of amount of NaOCl on the crystallinity and carboxyl content of cellulose

Sample ID	2θ	CI (%)	DO (mmol/100g)
T1	22	26	2.21±0.11
T2	22	34	2.76±0.21
T3	22	39	3.90±0.34
T4	23	45	6.63±0.15
T5	23	42	6.37±0.16

When compared to native cellulose and DAC fibers, TOCNF showed an increase in the degree of crystallinity (Figure 4.30). While DAC was more amorphous rather than crystalline, it was observed that TEMPO oxidation of native cellulose led to an increase in crystallinity which was influenced by the amount of NaOCl used during the oxidation. This increase in crystallinity is as a result of presence of species such as NaBr and NaOCl which makes the fibers more susceptible to oxidation at C₆ OH groups. This in turn leads to cleavage of amorphous domains of cellulose thereby increasing the crystallinity of TOCNF hence the observed increase in crystallinity when compared to all other samples under study. Even though there was a change in the crystallinity of cellulose, the two peaks of cellulose at 2θ values of 16° and 22° that

correspond to 001 and 200 crystal planes in cellulose structure were observed in TOCNF (Besbes *et al.*, 2011; Poletto *et al.*, 2014). The oxidation of cellulose could also be confirmed from diffractograms of TOCNF before ion exchange in which presence of sharp peaks linked to sodium ions used during oxidation were observed (Figure 4.30).

4.3.5 DSC Thermograms of TEMPO Oxidized Cellulose Nanofibrils (TOCNF)

Figure 4.31 depicts the differences observed on the thermal profile of TOCNF synthesized using different concentrations of NaOCl. From the DSC thermograms (Figure 4.31), it was observed that TEMPO oxidation of cellulose fibers resulted into the disappearance of the endothermic peaks of cellulose usually observed between 250-320 °C (Appendix P).

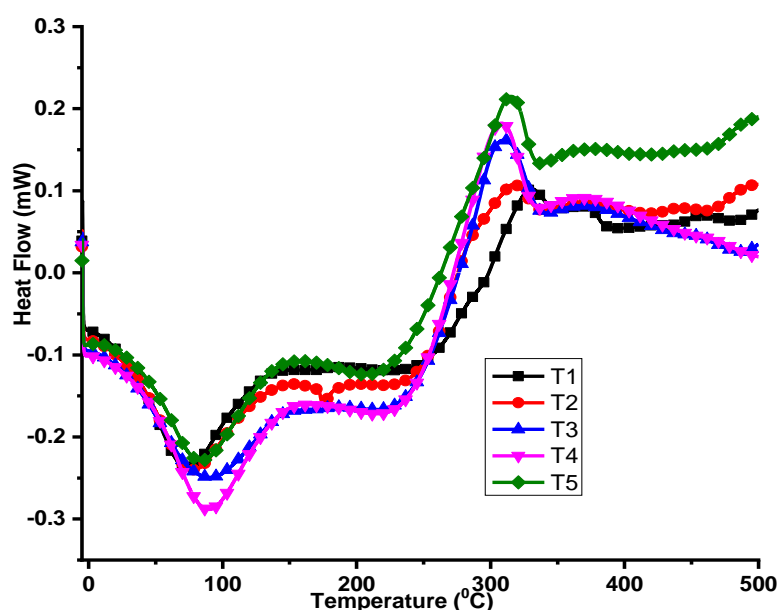


Figure 4.31: DSC thermograms of TEMPO oxidized cellulose with different carboxyl content

This disappearance can be attributed to the fact that oxidation cellulose using TEMPO alters the structure of cellulose by introduction of COOH groups within the polymer (Barbash *et al.*, 2017; Isogai *et al.*, 2011). The glass-liquid transition, or glass transition, is the gradual and reversible transition in amorphous materials from a hard

and relatively brittle "glassy" state into a viscous or rubbery state. From figure 3.39, it was also observed that, after TEMPO oxidation of cellulose, the glass transition temperature was absent in the thermograms which was attributed to changes in the structure of cellulose and the increase in crystallinity. It is important to note that the glass transition temperatures of polymers result from the presence of crystalline and amorphous domains within the polymer network. But during TEMPO oxidation, the amorphous domains of cellulose are normally cleaved off leaving a more crystalline material (Isogai *et al.*, 2011).

4.3.6 TGA-DTGA Thermogram of TEMPO Oxidized Cellulose (TOCNF)

Figure 4.32 depicts the differences in thermal properties observed when TOCNF was synthesized using different NaOCl concentrations. All the TOCNF samples were characterized by two degradation stages with different residual ash content.

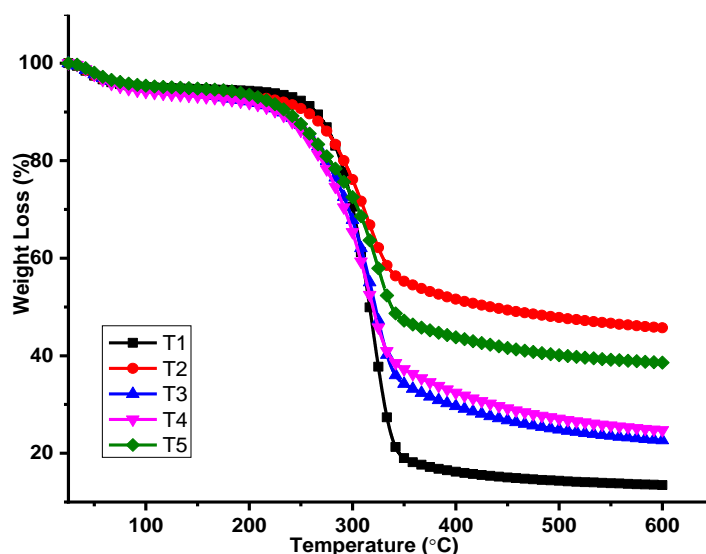


Figure 4.32: TGA thermograms of TOCNF with different carboxyl content

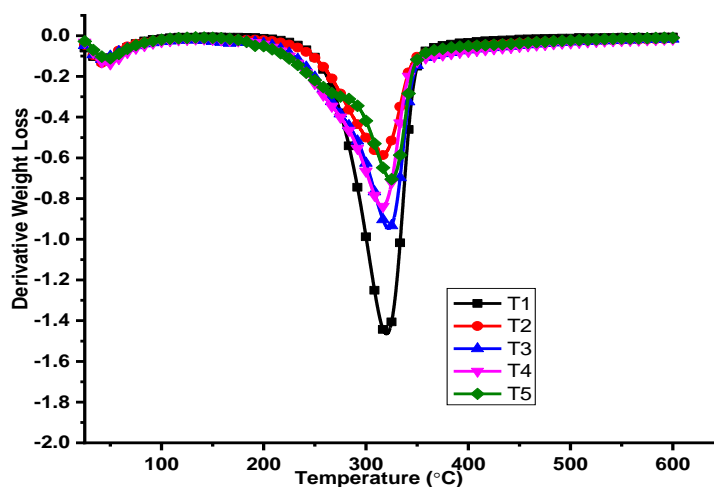


Figure 4.33: DTGA thermograms of TOCNF with different carboxyl content

The first degradation cycle occurred between 50-100 °C which can be attributed to water present on the surface of the polymers and the second degradation cycle occurred between 220 - 380 °C (Figure 4.32 – 4.33, Appendix Q). The thermal stability of TOCNF were greatly influenced by the concentration of NaOCl used as it was observed that at lower oxidant concentrations, TOCNF was thermal stable as compared to when the samples were subjected to higher oxidant concentrations (Leguy, 2018; Leguy, et al., 2018; Lichtenstein & Lavoine, 2017). Thermal degradation of TOCNF began at approximately 215 °C in a nitrogen atmosphere, while for the original cellulose sample, degradation began at 280 °C. Thus, the formation of sodium carboxylate groups on the C₆ hydroxyl of cellulose microfibril surfaces by TEMPO-mediated oxidation resulted in a significant decrease in the thermal stability (Isogai, 2018). Surface modification has been reported to negatively impact the thermal stabilities of cellulose fibers and diminishes the degree of mechanical reinforcing as it reduces their interaction (Nicharat *et al.*, 2015). Moreover, TEMPO oxidation yields shorter fibers in which heat can easily be dissipated during thermal analysis hence the reduction in the thermal stability of TOCNF which comprises of shorter fibers. Therefore, the presence of carboxyl groups on the fibrils surface is responsible for the lower thermal stability of TOCNF (Lichtenstein & Lavoine, 2017).

4.3.7 Hydrodynamic Diameter of TOCNF

Figure 4.34 depicts the hydrodynamic diameter of TOCNF obtained from DLS measurements. It was observed that the diameter of TOCNF was distributed between 2-40 nm (Figure 4.34). Upon oxidation of cellulose, the TOCNF solutions comprises of CNF which have greater uniformity, but they tend to aggregate upon drying.

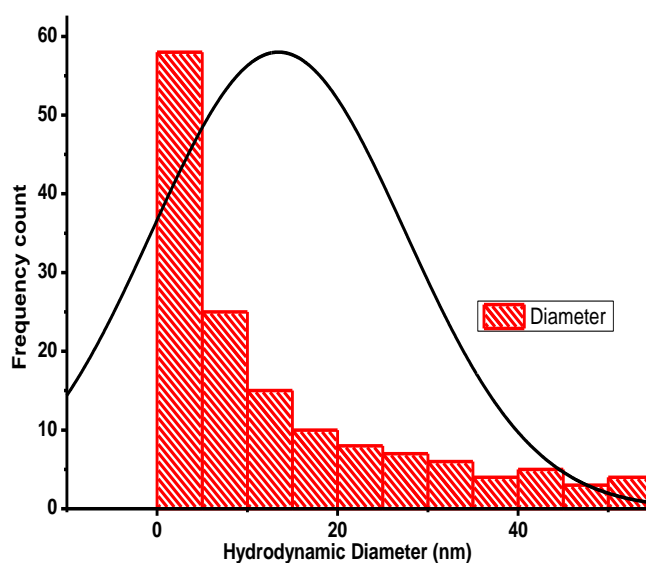


Figure 4.34: Distribution of hydrodynamic diameter of TOCNF

As observed in this study, most of the fibers had hydrodynamic diameters between 2-5 nm while some fibers had diameters above this value which can be attributed to the presence of aggregates. The diameter of TOCNF fibers is influenced by the source of cellulose as TOCNF isolated from Acacia pulp, Alfa, sugarcane bagasse, wheat straw, wood, and coconut fibers have diameters ranging between 5-80 nm. The production of these nanoparticles with diameters below 100 nm is challenging because of the strong tendency to agglomerate which occur upon oven drying of aqueous cellulose suspensions (Rojas *et al.*, 2015).

4.3.8 SEM Micrographs of Cellulose, Dialdehyde Cellulose and TOCNF Fibers

Plate 4.1 – 4.3 depicts changes in morphology of cellulose observed from SEM measurements after being subjected to different chemical treatments. It was observed

that cellulose fibers had micrometer size and low aspect ratios with varying fiber lengths depending on the treatment steps undertaken to isolate them (Vizireanu *et al.*, 2018).

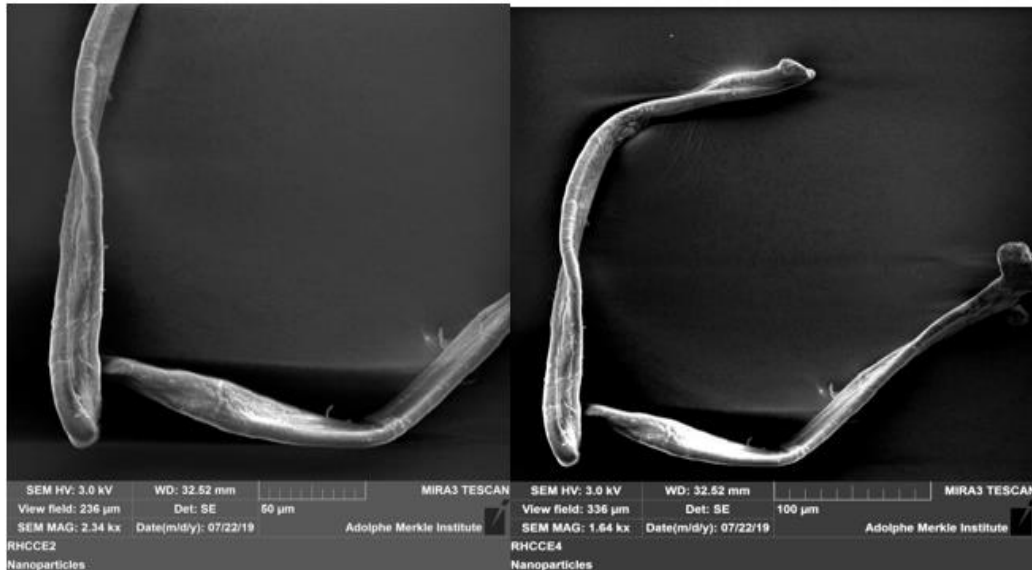


Plate 4.1: SEM image of micrographs of RHCE

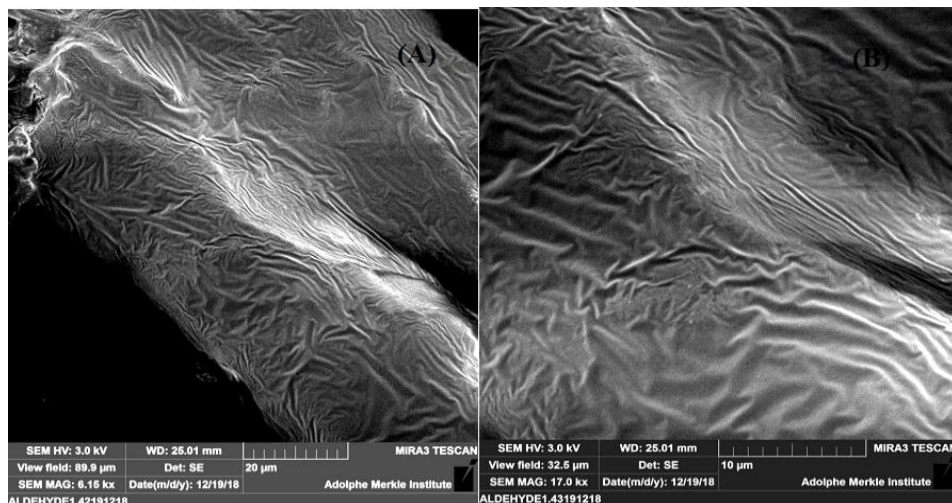


Plate 4.2: SEM micrographs of dialdehyde cellulose at different view field

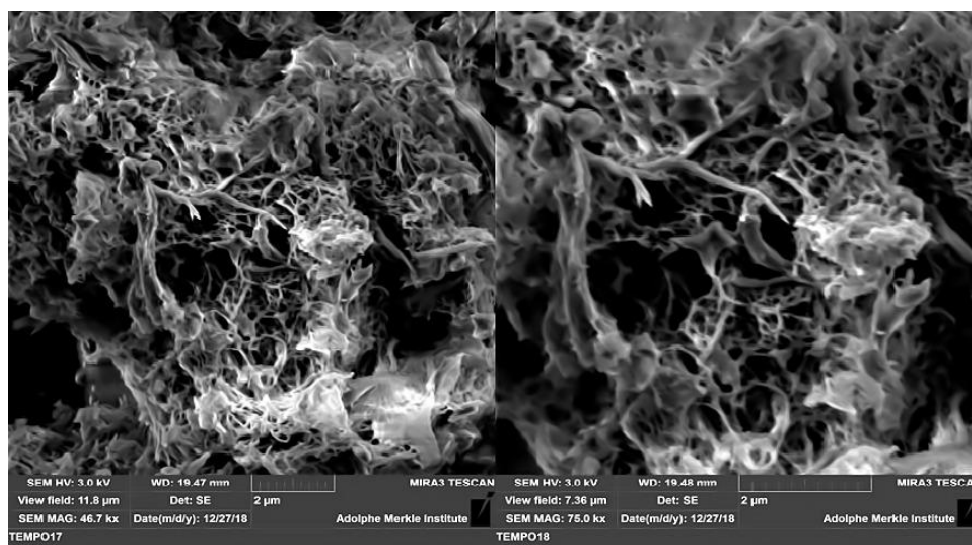


Plate 4.3: SEM micrographs of TEMPO oxidized cellulose (TOCNF)

Ultrasonication has been reported to cause fiber defibrillation and breaking leading to an increase in the aspect ratio of the fibres as compared to raw cellulose fibers (Hu *et al.*, 2017). In our study, ultrasonication did not break down the fibers into single strands as reported in literature possibly due to power of ultrasonication used which was 45 kHz. Despite this fact, use of ultrasonication increased the crystallinity of cellulose as discussed earlier which led to investigation of fiber morphology to determine if there were any changes. As observed in plate 4.1, ultrasonication changed fiber morphology as compared to native cellulose as the surface became smoother when compared to native cellulose. The same observations were made when cellulose was converted to 2,3 dialdehyde cellulose but for the case of TOCNF, TEMPO oxidation led to fiber disintegration as the fibers were highly networked and appeared like a sponge consisting of microporous structures (Plate 4.2) (Tanigawa *et al.*, 2008). This led to the conclusion that of all the chemical and physical treatments the fibers were subjected to, only TEMPO mediated oxidation led to disintegration of the fibers to form a network of microporous structure as compared to periodate oxidation in which the surface was compact (Plate 4.3). Similar results have also been reported for periodate oxidized fibers where instead of formation of single strands the fibers were compact with fiber-like morphology increasingly vanishing upon oxidation (Hoglund, 2015; Lindh *et al.*, 2016; Nematdoust *et al.*, 2020). It was also observed that variation

of reaction parameters for the case of dialdehyde cellulose did not induce significant changes in fiber morphology as all the fibers appeared to have compact and smooth surfaces. Moreover, strong intermolecular hydrogen bonds develop during oven drying to form a continuous fiber network and a solid bulk material with smooth surfaces which is an indication of denser packing. The agglomerates formed during oven-drying caused a difficulty during re-dispersion because breaking down strong intramolecular hydrogen bonds formed during the process is an energy intensive process (Nicharat *et al.*, 2015).

4.3.9 TEM Micrographs of Cellulose, Dialdehyde Cellulose and TOCNF

Figure 4.35 – 4.38 depicts the distribution of fibre lengths and widths for risks husk cellulose (RHCE), dialdehyde cellulose (DAC) and TOCNF measured from TEM micrographs. It was observed that the fiber lengths were affected by the chemical treatment steps the fibers were subjected too with oxidation of cellulose reducing the length of the fibers.

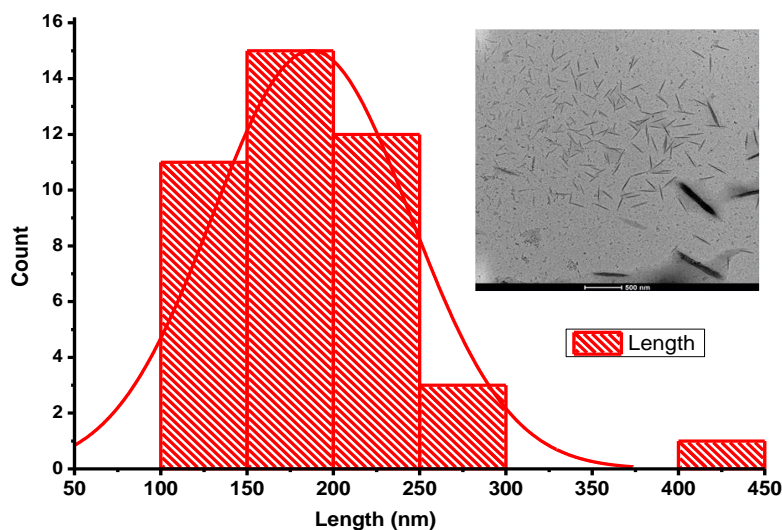


Figure 4.35: Fiber length distribution of cellulose. Inset TEM micrograph of cellulose

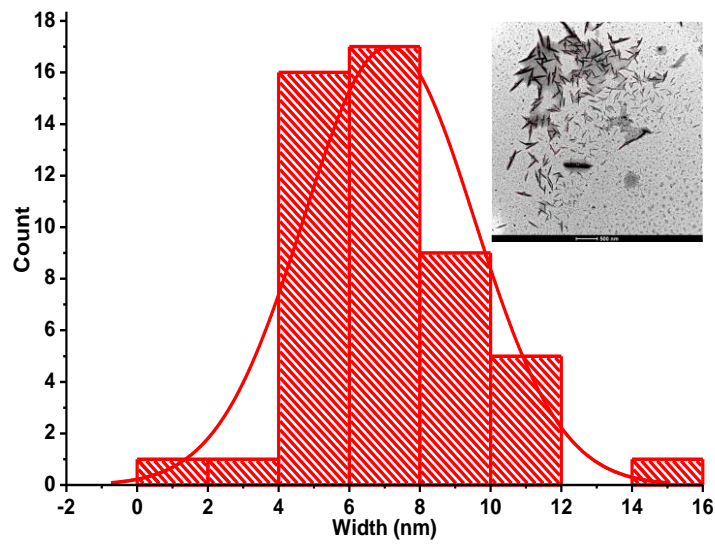


Figure 4.36: Fiber width distribution of cellulose before oxidation. Inset TEM micrograph of cellulose.

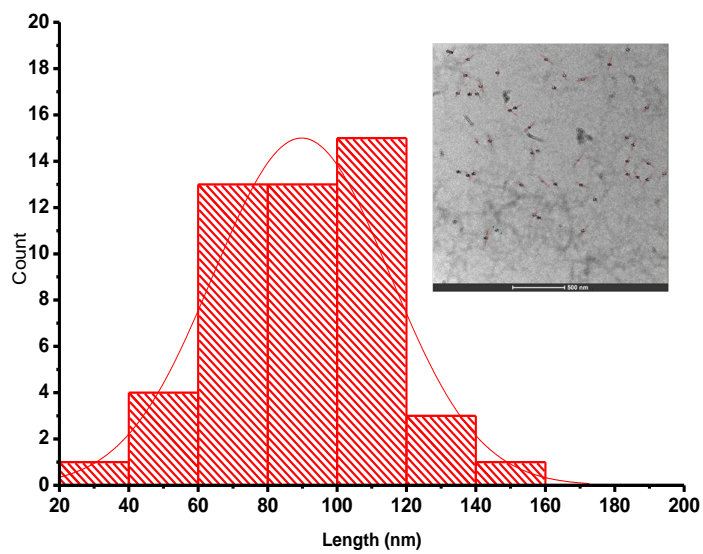


Figure 4.37: Fiber length distribution of dialdehyde cellulose. Inset TEM micrograph of dialdehyde cellulose.

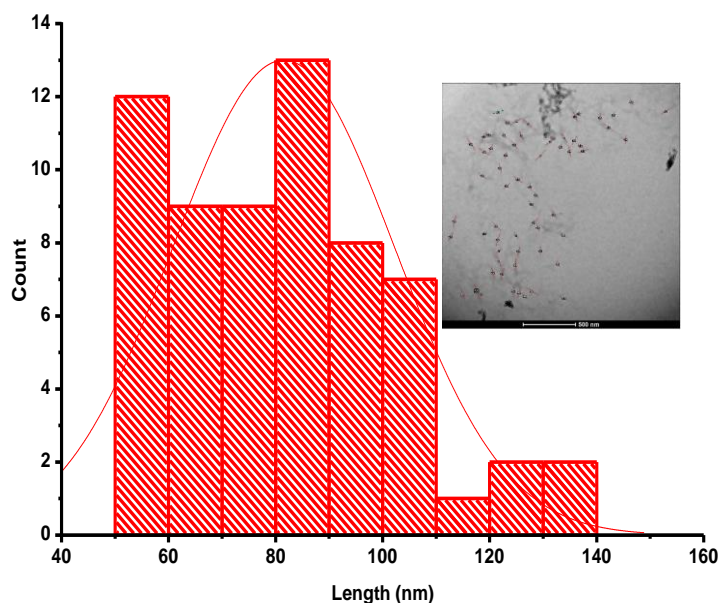


Figure 4.38: Fiber length distribution of TEMPO oxidized cellulose. Inset TEM micrograph of TEMPO oxidized cellulose.

From figure 4.34 - 4.38, it can be observed that the fiber lengths were distributed within the nanometer range though in the case of native cellulose formation of aggregates were clearly visible. In the case of DAC, TOCNF aggregation of the fibers was absent because TOCNF introduces negative charges on the surface which leads to repulsion hence absence of aggregates (Isogai, 2018). It was also observed that native cellulose had larger dimensions in terms of fiber length as compared to TOCNF and DAC as length distribution lied between 100 - 450 nm for native cellulose while TOCNF and DAC had length distributions between 50 – 100 nm and 20 – 160 nm respectively. On the other hand, the width of cellulose fibers lied between 5 – 16 nm, which was also higher (Figure 4.35) as compared to DAC and TOCNF which were difficult to measure with the help of the imaging software ImageJ. This led to the conclusion that different treatment steps had a huge impact on the width as compared to length of the fibers as the width of fibers was higher in native cellulose as compared to TOCNF and DAC. However, it should be worth noting that the width of the fibers was not uniform as it appeared that towards the end of each strand the width was smaller as compared to the middle of each fiber measured. Due to their hydrophilic surface, as a result of high density of hydroxyl moieties, CNF and nanocrystals have

been reported to form inter-particle hydrogen bonds and aggregates (Isogai *et al.*, 2011).

4.4 Synthesis of TOCNF-DAC-AgNPs

4.4.1 UV-vis Spectra of AgNPs Synthesized using TOCNF-DAC

Synthesis of AgNPs using TOCNF-DAC was monitored using Uv-vis spectroscopy and the results are shown in figure 4.39. Synthesis of AgNPs was confirmed by the presence of AgNPs plasmon resonance peak which has previously been reported as a qualitative indicator of the presence of the AgNPs in a solution.

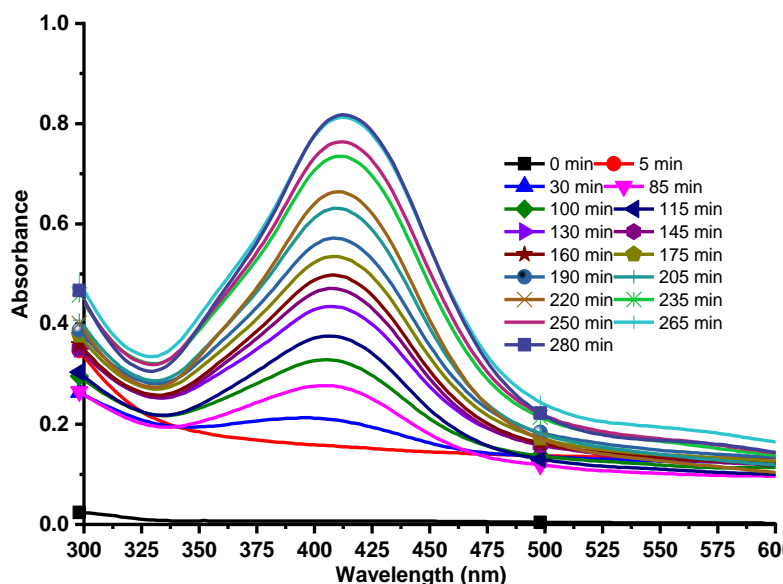


Figure 4.39: UV-Vis spectra of AgNPs synthesized from 0.01M AgNO₃ using TOCNF

From figure 4.39, it can be observed in the Uv spectra, the peak centered at 412 nm and the change of color of the solution from colorless to brick red have been reported to be the initial indicators of the presence of AgNPs. The interaction between TOCNF-DAC and Ag⁺ resulted in the formation of AgNPs due to presence of carbonyl functional group in the oxidized fibers which initiated the reduction through transfer of electrons needed to reduce Ag⁺ ions (Errokh *et al.*, 2018; Errokh *et al.*, 2019). This peak centered at 412 nm has also been observed when AgNPs have been synthesized

using different reducing agents such as secondary metabolites and is often used as a qualitative indicator of the reduction (Akmaz *et al.*, 2013; Chung *et al.*, 2016; Jiang *et al.*, 2011; Vasylevskiy *et al.*, 2017). This reduction of Ag^+ in solution can be attributed to the presence of COOH and C=O in TOCNF-DAC which have been reported to be able to produce electrons needed to reduce silver ion in solution at elevated temperatures (Xu *et al.*, 2019; Ito *et al.*, 2018).

4.4.2 FTIR Characterization of TOCNF-DAC-AgNPs

Figure 4.40 depicts the IR spectra of TOCNF-DAC and TOCNF-DAC-AgNPs. The IR spectra of TEMPO-dialdehyde oxidized cellulose (TOCNF-DAC) had similar cellulose peak that had been observed in native cellulose but with an introduction of C=O functional group while shift in vibrational frequencies were observed in that for TOCNF-DAC-AgNPs.

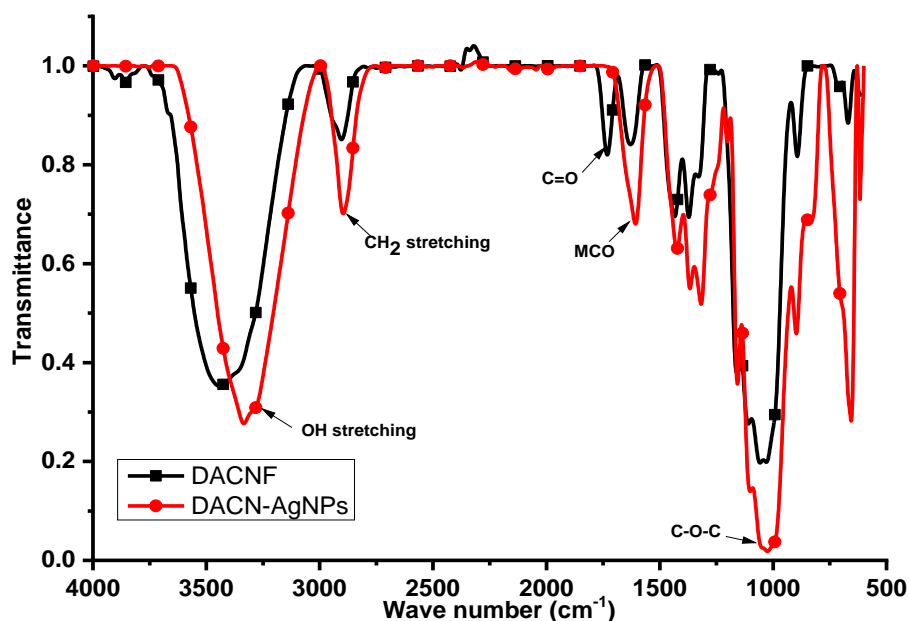


Figure 4.40: FT-IR spectra of TOCNF-DAC and TOCNF-DAC-AgNPs composite

The peaks at 3480, 2905, 1050 cm^{-1} were attributed to OH, CH₂ and C-O-C stretching vibrations respectively while the peak at 1722 and 1622 cm^{-1} were attributed to presence of C=O stretching vibration of the carbonyl groups that resulted from

oxidation of cellulose and water adsorbed on the surface of oxidized cellulose (Leguy, 2018; Hoglund, 2015). From the FT-IR spectrum of TOCNF-DAC-AgNPs (Figure 4.40), it was observed that upon reduction of Ag^+ to AgNPs using TOCNF-DAC, the carbonyl vibrational peak that was initially observed at 1722 cm^{-1} had shifted to 1610 cm^{-1} (Xu *et al.*, 2019). This shift in the carbonyl vibrational band could be attributed to the fact that the carbonyl group participated in the reduction of AgNPs and resulted in the interaction of the C=O and AgNPs hence the absence of the C=O vibrational in the spectrum of TOCNF-DAC-AgNPs (Errokh *et al.*, 2019). Interaction of the surface OH groups with AgNPs was also observed from the shift in the OH vibrational peak which initially was centered at 3445 cm^{-1} but shifted to 3333 cm^{-1} upon introduction of AgNPs with the matrix of TOCNF-DAC. This shift has been linked to the formation of a chemical bond or an electrostatic interaction between the AgNPs and oxygen containing functional groups present in TOCNF-DAC. Presence of the vibration peak of the C-O-C at 1050 cm^{-1} was also an indication that the polysaccharide structure of cellulose was sustained even after oxidation and the reduction of silver ions (Ito *et al.*, 2018; Xu *et al.*, 2019).

4.4.3 X-ray Diffractogram of TOCNF-DAC-AgNPs

The X-ray diffractograms of TOCNF-DAC and TOCNF-DAC-AgNPs are shown in figure 4.41. From TOCNF-DAC diffractograms, it was observed that the two peaks of cellulose that are usually present at 2θ values of 16° and 22° that correspond to 001 and 200 crystal planes in cellulose structure were present (Besbes *et al.*, 2011; Poletto *et al.*, 2014).

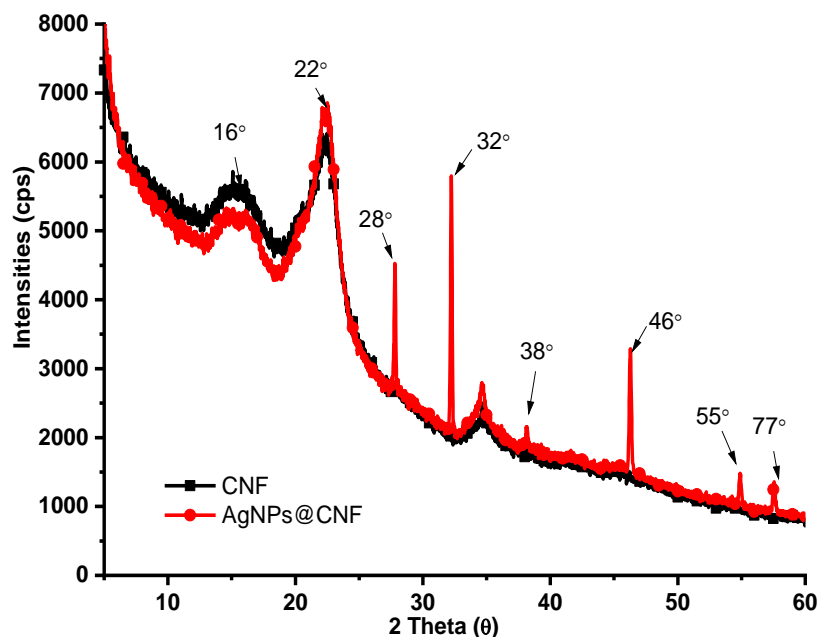


Figure 4.41: X-ray powder diffraction patterns of CNFs and AgNPs@CNF

One interesting observation was that, while periodate oxidation of native cellulose resulted in a completely amorphous DAC, periodate oxidation of TOCNF did not yield an amorphous material but rather a more crystalline cellulose. One possible explanation to this is that TEMPO oxidation produces a crystalline cellulose which upon periodate oxidation would not yield amorphous derivative as previously observed but rather crystalline cellulose since amorphous domains are subsequently removed during TEMPO oxidation. Upon TEMPO and periodate oxidation of cellulose to yield TOCNF-DAC the oxidized fibers were used to synthesize TOCNF-DAC-AgNPs to impart antimicrobial properties to the fibers. From the TOCNF-DAC-AgNPs diffractograms obtained (figure 3.52), it was observed that TOCNF-DAC was able to reduce Ag^+ ion in solution to AgNPs as peaks belonging to AgNPs were observed. The peaks observed at $2\theta = 38, 55, 58, 68,$ and 77 have been previously indexed with (111), (200), (220) and (311) crystalline planes of face-centered cubic crystalline structure of metallic silver in the fibers (Xu *et al.*, 2019; Ito *et al.*, 2018). The diffraction patterns of the doped AgNPs are consistent with the standard reported values and they indicate that the synthesized nanoparticles deposited on the surface of the nanofibrils were in the zero valent state. The peaks centered at $2\theta = 28, 32,$ and 46

have been associated with presence of AgCl nanoparticles that are synthesized in situ in the presence of chloride ions in the system associated with use of HCl during protonation of TOCNF-DAC. This drawback can be overcome by careful choice of the deprotonation solvent or by use of UV radiation which have been reported to have the ability to reduce AgCl nanoparticles further to AgNPs (Vasylevskyi, et al., 2017; Khan, et al., 2020).

4.4.4 DSC Thermograms of TOCNF-DAC-AgNPs

Figure 4.42 shows the DSC thermograms of TOCNF-DAC and TOCNF-DAC-AgNPs. It was observed that TOCNF-DAC comprised of an initial endothermic peak centred at 68 °C an exothermic peak centred at 331 °C and a final endothermic peak centred at 416 °C.

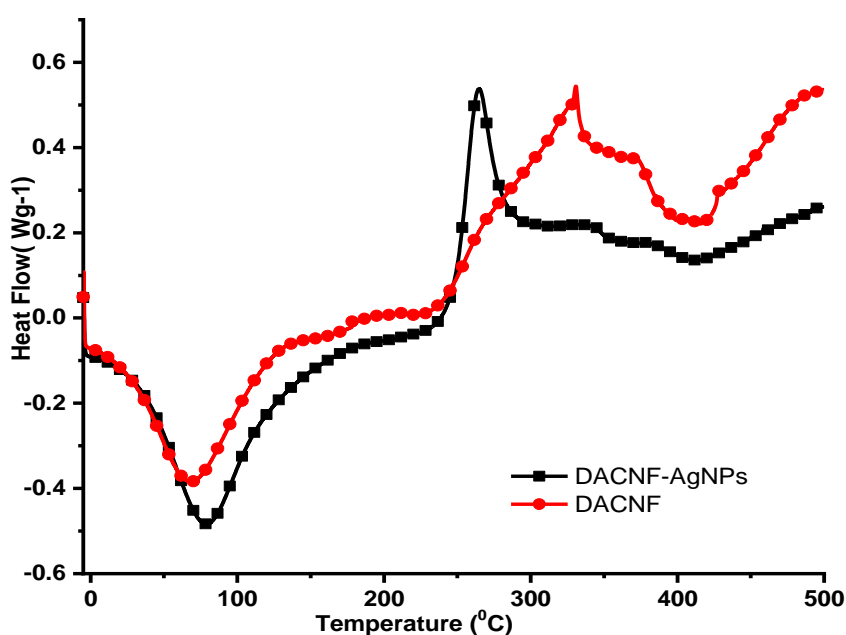


Figure 4.42: DSC thermograms of TOCNF-DAC and TOCNF-DAC-AgNPs

From figure 4.42, the initial endothermic peak was as a result of water adsorbed on the surface of cellulose that evaporated during the analysis while the final endothermic peak may be attributed to decomposition of residual lignin which has been reported to occur at this temperature. One thing to note is that the endothermic peak of cellulose which is normally observed between 250 - 330 °C degrees was absent and this can be

associated with the changes that occurred during synthesis of TOCNF-DAC and TOCNF-DAC-AgNPs. It can be noted that, during this synthesis, the structure of cellulose changes as both oxidation processes result in the introduction of a carboxyl group (COOH) at C₆ and a carbonyl (C=O) functional group at C₂ and C₃ of cellulose thereby cleaving the C₂-C₃ bond in cellulose (Isogai *et al.*, 2011; Hoglund, 2015; Ito *et al.*, 2018).

4.4.5 TGA-DTGA Thermograms of TOCNF-DAC-AgNPs

Figures 4.43 show TGA and DTGA thermograms of TOCNF-DAC and TOCNF-DAC-AgNPs. The thermal parameters selected were onset temperature, which is the initial weight loss temperature, and maximum degradation temperature, which is the highest thermal degradation rate temperature obtained from the peak of DTGA thermograms.

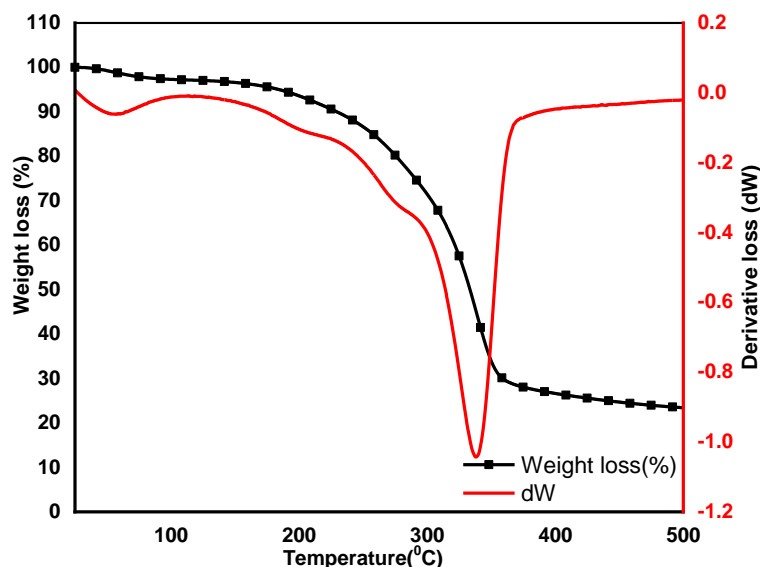


Figure 4.43: TGA/DTGA thermograms of TOCNF-DAC

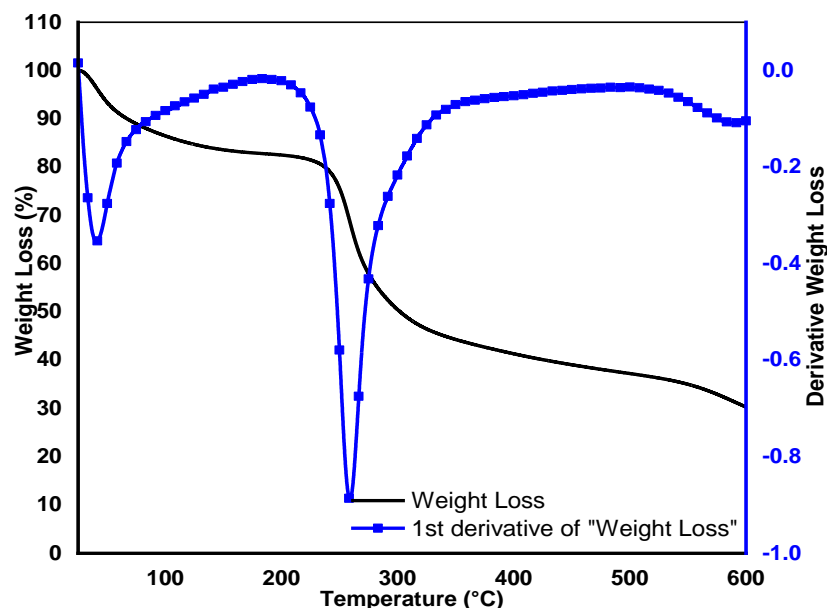


Figure 4.44: TGA-DTGA thermograms of TOCNF-DAC-AgNPs

From figure 4.43 – 4.44, the first degradation stage which accounted for 4% weight loss was associated with evaporation of water molecules adsorbed on TOCNF-DAC samples. The second degradation stage which accounted for 80% weight loss with maximum degradation peak centered at 338 °C was attributed to the degradation of cellulose. Comparison of TGA and DTGA profiles of RHCE, DAC, TOCNF and TOCNF-DAC revealed that the thermal stability was dependent on the chemical treatment the samples were subjected to with TOCNF-DAC being less thermally stable as it had a lower onset degradation temperature. Presence of AgNPs within the oxidized fibers affected the thermal stability of the fibers as it was observed that the maximum degradation temperature of TOCNF-DAC-AgNPs was lower as compared to that of TOCNF-DAC. From the TGA-DTGA thermograms it was observed that TOCNF-DAC-AgNPs had the highest degradation at 260 °C with a percent ash content of 30% as compared to TOCNF-DAC which had the maximum degradation occurring at 338 °C with a percent ash content of 23 %. But when comparing the onset degradation temperature, TOCNF-DAC-AgNPs had a higher onset degradation temperature of 200 °C as compared to TOCNF-DAC whose onset degradation temperature was 140 °C. Presence of metallic species within the cellulose matrix has

been reported to increase the thermal stability and the residual ash content of the fibers after thermal analysis (Ito *et al.*, 2018).

4.4.6 SEM Micrographs of TOCNF-DAC-AgNPs

Plate 4.4 depicts the morphology of the fibers after TEMPO and periodate oxidation. From Plate 4.4, changes in morphology of TOCNF-DAC and TOCNF-DAC-AgNPs can be visualized.

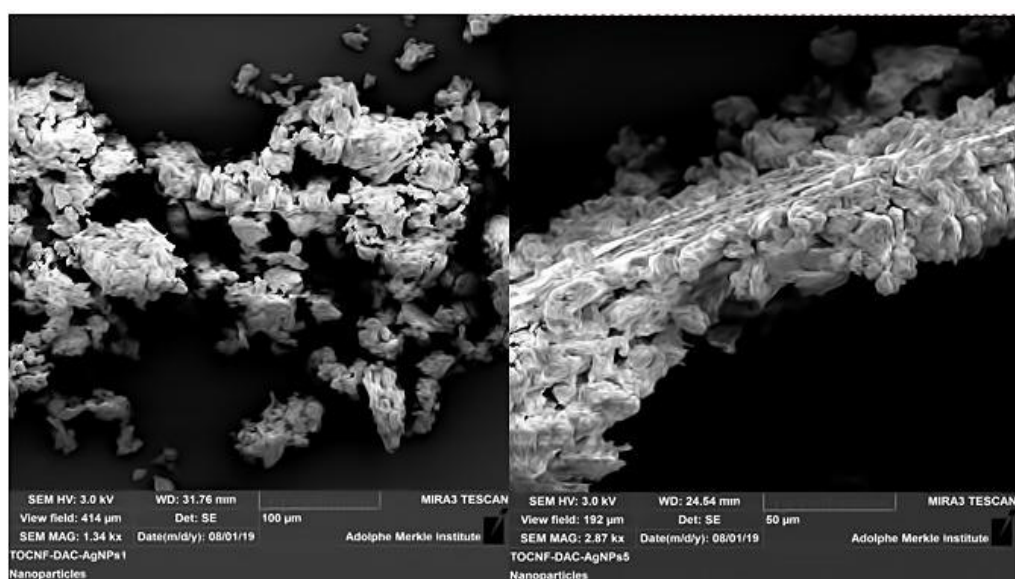


Plate 4.4: SEM micrographs of TOCNF-DAC and TOCNF-DAC-AgNPs

As it can be observed, both TOCNF-DAC and TOCNF-DAC-AgNPs fiber morphology were significantly different when compared to TOCNF, DAC and native cellulose fibers. While TOCNF was composed of porous surface that appeared like a mesh, TOCNF-DAC and TOCNF-DAC-AgNPs had sponge like surface that was porous (Leguy, 2018).

4.4.7 TEM Micrographs of TOCNF-DAC-AgNPs

The length of fibers obtained through TEMPO and Periodate oxidation are shown in figure 4.45. The fiber length distribution of TOCNF-DAC was found to be between 50 - 400 nm in length.

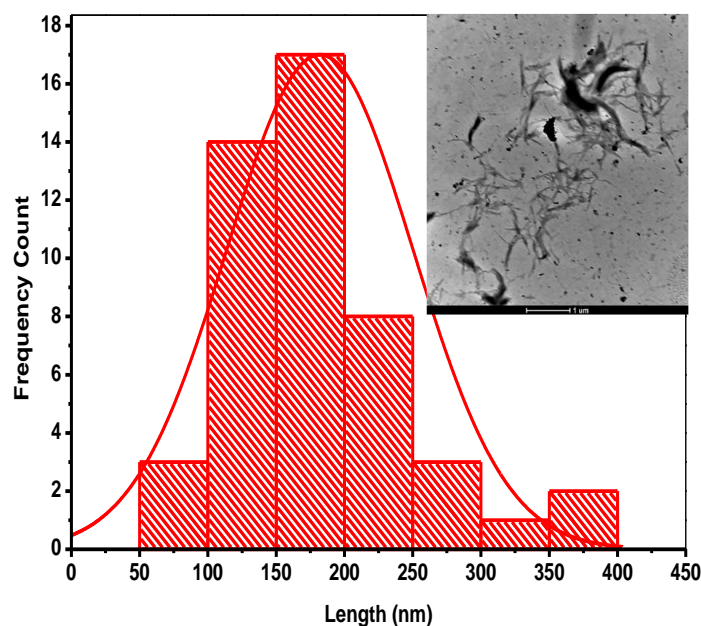


Figure 4.45: Length Distribution of TOCNF-AgNPs and TEM micrographs of TOCNF-DAC-AgNPs fibers

When compared to TOCNF, DAC and native cellulose, the length distribution was within the range of fibers isolated in this study. TEMPO oxidation of cellulose fibers has been reported to reduce fiber length while periodate on the other hand has little effect on the length of the fibers though it removes crystalline domains present in cellulose. Presence of carbonyl functional groups in TOCNF-DAC implies that, when they were re-dispersed in AgNO_3 solution, the Ag^+ ions were reduced to AgNPs hence the observation of spherical dark particle in the TEM micrographs. These spherical dark particles were attributed to be those of AgNPs which were generated when TOCNF-DAC was redispersed in AgNO_3 solution as reported in literature (Xu *et al.*, 2019).

4.4.8 Hydrodynamic Diameter, Zeta potential and Poly-dispersibility Index

Figure 4.46 depicts the size distribution of TOCNF-DAC obtained from DLS measurements after synthesis of the nanoparticles. From the DLS measurements obtained, the average size, polydispersibility index and zeta potential of TOCNF-DAC-AgNPs composite was found to be 97.8 ± 17.9 nm, 0.5393 ± 0.09 and -23.78 ± 3.71 (mV) respectively.

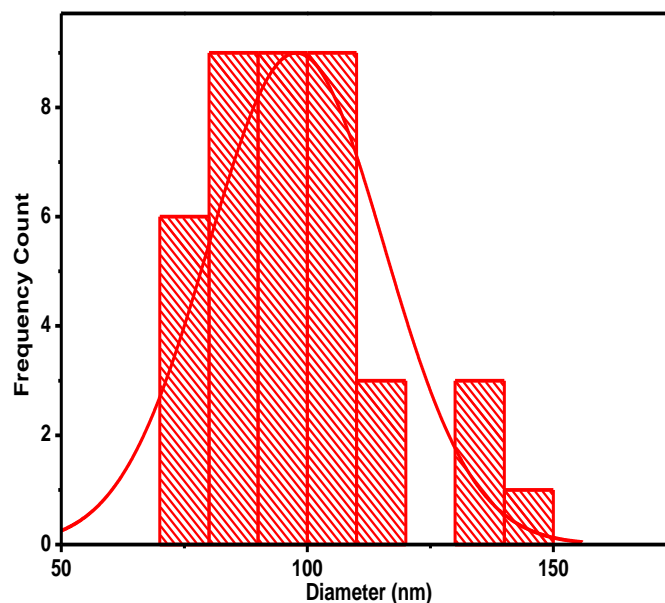


Figure 4.46: Hydrodynamic diameters of TOCNF-DAC-AgNPs fibers from rice husks

With the high zeta potential of TOCNF-DAC-AgNPs, the tendency of this composite to aggregate was low which implied that TOCNF-DAC could work as a capping agent during synthesis of AgNPs within the cellulose matrix. In similar studies, the zeta potential of DAC-AgNPs was found to be -28.8 mV while that for TOCNF-AgNPs composite was found to be -40.8 mV respectively (Ito *et al.*, 2018; Xu *et al.*, 2019). The higher zeta potential implies that the tendency of the particles to agglomerate is reduced as it has been reported that particles whose zeta potential is further away from zero tend to have long term stability and remain in solution without the possibility to agglomerating (Ito *et al.*, 2018; Xu *et al.*, 2019).

4.4.9 *In-vitro* Antimicrobial Activity

Figure 4.47 depicts the antimicrobial activity of TODAC-AgNPs that was evaluated against selected microorganism using disc diffusion assay. The antibacterial activity was calculated based on the formation of an inhibition zone around the test film after incubation for 24 h. The TODAC-AgNPs composites film had lower antibacterial activity against Gram- negative pathogens *E. coli*, *P. mirabilis* and *P. aeruginosa* as

compared to Gram- positive bacteria *B. subtilis* and *S. aureus* and the fungi *C. albicans*.

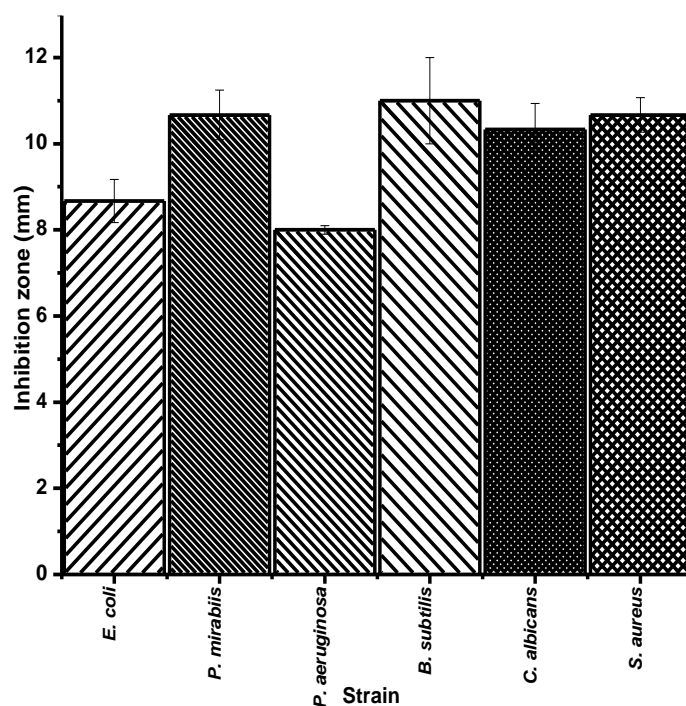


Figure 4.47: *In-vitro* antimicrobial assay of TOCNF-DAC-AgNPs

The difference in the antibacterial potency of the composite between Gram-negative and Gram-positive bacteria lies in the structure of their cell wall (Khan *et al.*, 2020). For Gram-negative bacteria, the cell walls are composed of a multilayer structure comprising a thin peptidoglycan layer, a lipoprotein layer, a lipopolysaccharide, or phospholipids layer. However, Gram-positive bacteria's cell walls only contain a single layer of peptidoglycan that is many times thicker than that found in Gram-negative bacteria, and they also lack an outer membrane (Khan *et al.*, 2020). Due to these differences in cell wall structure, Gram-positive bacteria have been found to be less susceptible to AgNPs as compared to Gram-negative bacteria. But in our case, AgNPs@CNF was found to be more potent to Gram-positive bacteria than Gram-negative bacteria hence the observed higher activity in *B. subtilis* and *S. aureus* and the fungi *C. albicans* (Khan *et al.*, 2020). When compared to standard antibiotics, the composite films had higher antimicrobial activity as compared to standard films

loaded with 10 µg of gentamycin which exhibited an inhibition zone of 13.0±0, 9.0±0.0, 8.0±0.0 and 8.0±0.0 mm for *E. coli*, *P. aeruginosa*, *S. aureus* and *B. subtilis* respectively. The disc diffusion results indicate that the nanocomposite can inhibit the growth and multiplication of *E. coli*, *P. mirabilis*, *P. aeruginosa*, *B. subtilis*, *S. aureus* and the fungi *C. albicans*. Previous studies have reported that the ability to inhibit his growth is because of cellular deformation after interaction with AgNPs present in the nanocomposite which may results to cell death due to generation of reactive oxygen species upon interaction of the microorganism with AgNPs (Khan *et al.*, 2020).

4.5 Synthesis of Carboxymethyl Chitosan

4.5.1 Variation of Concentration of Monochloroacetic Acid

Table 4.14 depicts the effect of variation of monochloroacetic aid on the swelling capacity of carboxymethyl chitosan and its ability to swell is depicted in plate 4.5 after absorbing water. As it can be observed, variation in monochloroacetic acid concentration influenced the degree of substitution and the swelling capacity of CMCS. At higher monochloroacetic acid content, the degree of substitution and the swelling capacity of CMCS increased as compared to lower monochloroacetic acid content which can be attributed to an increase in the hydrogen bond introduced into the network of the polymer.

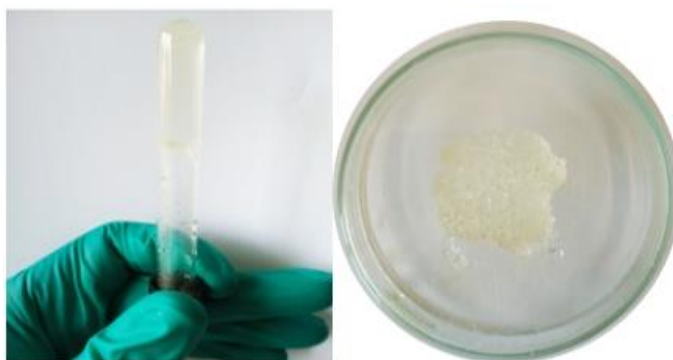


Plate 4.5: Swelling of carboxymethyl chitosan (CMCS) in water.

Table 4.14: Effect of variation of monochloroacetic acid on the degree of substitution (DS) and swelling capacity of CMCS

[Acid] mmol	DS	Swelling capacity
11	0.31±0.05	930 ± 17
21	0.46±0.11	1016± 21
32	0.68±0.04	1093±15
42	0.89±0.09	1166±12
64	0.99±0.61	1170±26
85	0.96±0.31	1460±34
106	0.65±0.58	1006±49

A higher DS value is an indication of the number of carboxymethyl groups introduced into the polymer network which in turn is directly related to the increase in swelling and solubility of the resultant polymer. This can be explained by the fact that reaction of monochloroacetic acid with chitosan introduces the carboxymethyl groups on N-terminal and O-terminal of chitosan (Deng *et al.*, 2017). Statistical analysis of the data obtained revealed that there was a significant difference ($p \leq 0.05$) in the DS and swelling capacity of chitosan when the concentration of monochloroacetic acid was varied. ANOVA showed that an increase in the concentration of the monochloroacetic acid significantly increased the degree of substitution and swelling capacity of the polymer (Appendix R and S).

4.5.2 FTIR Characterization of Chitosan and Carboxymethyl Chitosan

Figure 4.48 depicts the IR spectra of chitosan and carboxymethyl chitosan after introduction of the carboxymethyl group within the structure of chitosan. A broad absorption band observed at around 3421 and 3191 cm^{-1} indicated the intermolecular hydrogen linking formation due to the axial deformation of O–H which appeared overlapping the bond of axial deformation of N–H.

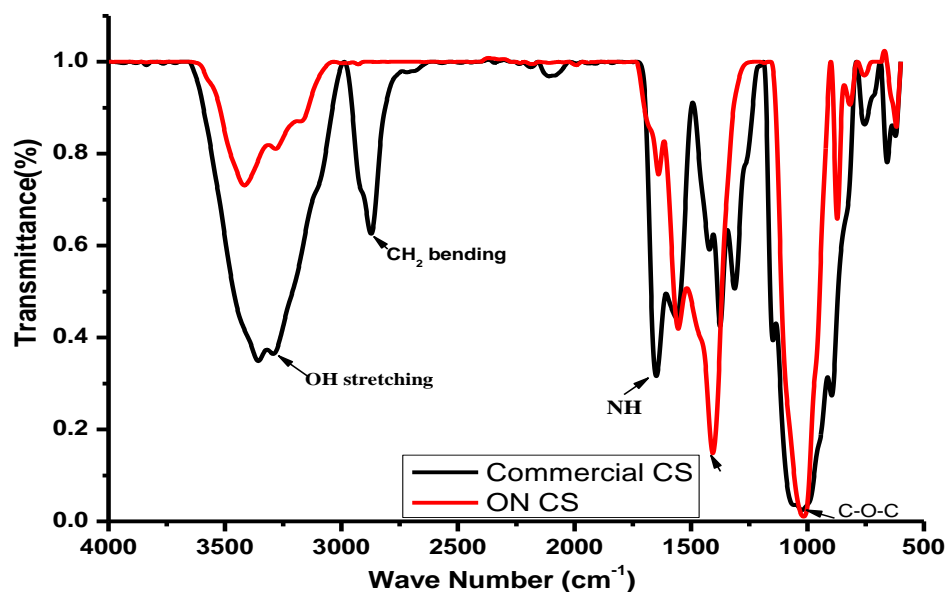


Figure 4.48: FT-IR spectra of chitosan standard and *O. niloticus* chitosan

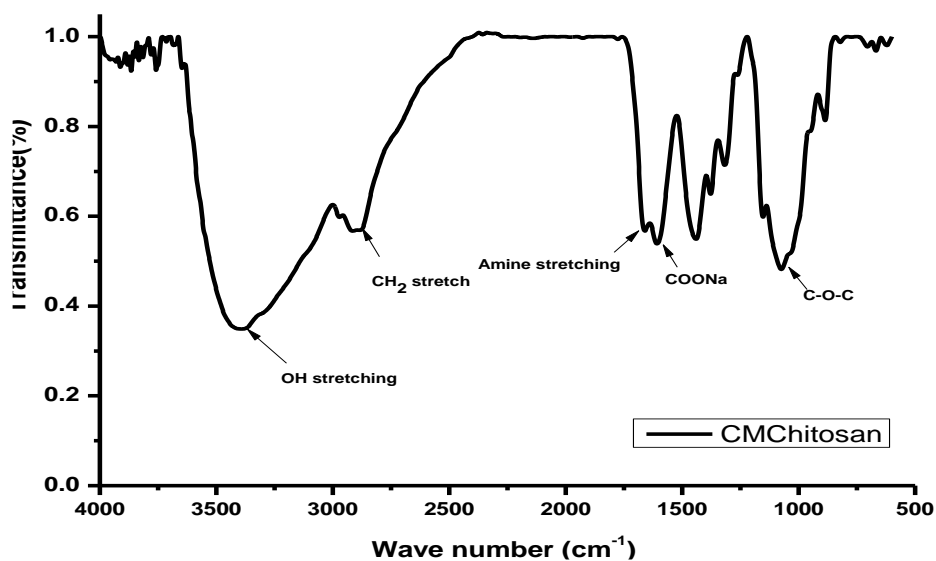


Figure 4.49: FT-IR spectra of carboxymethyl chitosan (Sodium Form COONa)

During the *N*-deacetylation of chitin, the band at 1651 cm^{-1} gradually decreased, while that at 1575 cm^{-1} increased, indicating the prevalence of NH_2 groups (Deng *et al.*, 2017). The band at 1576 cm^{-1} displayed a greater intensity than the one at 1651 cm^{-1} and demonstrated the effective deacetylation of chitin (Kumirska *et al.*, 2010). The most significant parts of chitosan spectra are those showing the amine bands at

approximately 1651, 1576 and 1412 cm^{-1} and are associated with the presence of the C=O stretching of the amide band, bending vibration of the N – H, and the C – H bending respectively (Anicuta *et al.*, 2010; Ouellette and Rawn, 2019). The peak at 3371 cm^{-1} was attributed to the amine NH symmetric vibration. Absence of amide N-H stretch between 3700 – 3500 cm^{-1} in the FTIR spectra of chitosan is indicative of absence of this functional group since amides produce zero to two N-H absorptions. The N–H bending vibration of primary amines is observed in the region 1651 cm^{-1} while the bending of NH_2 is observed at 872 cm^{-1} . A strong broad peak at 1042 cm^{-1} is indicative of C – O stretching vibrations (Anicuta *et al.*, 2010). Moreover, presence of two N-H stretching vibrations in the chitosan spectra is because of asymmetric and symmetric stretching of primary amines as compared to a single stretching vibrations of secondary amine groups present in the chitin spectrum. This is because asymmetric stretching vibrations require more energy as compared to symmetric stretching vibrations (Anicuta *et al.*, 2010; Rwegasila *et al.*, 2016).

4.5.3 X-ray Diffractograms Chitosan (CS) and Carboxymethylated Chitosan (CMCS)

Figure 4.50 depicts the changes in crystallinity of chitosan and carboxymethyl chitosan after being functionalized. The XRD diffractogram of commercial chitosan (Figure 4.50) showed a broad diffraction peak at $2\theta = 8^\circ$ and $2\theta = 22^\circ$ while that of chitosan isolated from from *O. niloticus* exhibited sharp characteristic peaks at about $2\theta = 10, 26, 32, 47, 50, 53$ (Akmaz *et al.*, 2013).

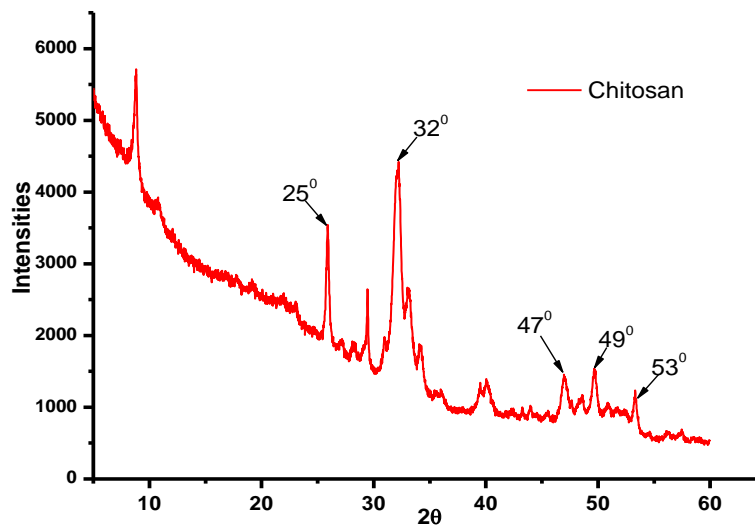


Figure 4.50: WXR D diffractogram of Chitosan synthesized from *O. niloticus*.

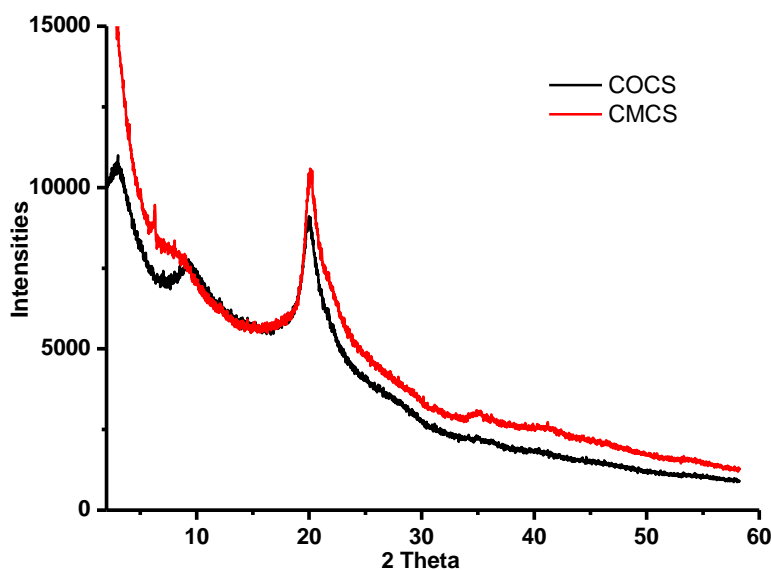


Figure 4.51: WXR D diffractogram of carboxymethylchitosan (CMCS) and commercial chitosan (COCS)

Similar diffraction peaks have been reported by several authors who isolated chitosan from various sources with these peaks associated with impurities isolated together with chitosan (Kumari *et al.*, 2015; de Queiroz Antonio *et al.*, 2017). Presence of OH and NH₂ groups in the structure of chitosan that form stronger inter and intramolecular hydrogen bonds ensure that the molecules of chitosan form crystalline regions easily.

The band at 10° is due to incorporation of bound water molecules into the crystal lattice as reported elsewhere (Guirguis *et al.*, 2016; Mullah *et al.*, 2017). In a similar study done by Kumar *et al.*, (2014), chitosan extracted from *Labeo rohita* fish scales exhibited crystalline reflections between 2θ values in the range $10 - 80^\circ$ respectively. The broad peaks centred at about $2\theta = 18^\circ$ and $2\theta = 32^\circ$ in commercial chitosan isolated from shrimp shells can be attributed to the amorphous nature of chitosan (Figure 4.51). Several parameters such as source or origin of chitin (α -chitin, β -chitin or γ -chitin), treatment of the polymer during extraction from biomass, post-treatments of the polymer (dissolving, re-precipitation, freeze-drying, chemical grafting etc.), and polymer conditioning affect the degree of crystallinity of chitosan (Desbrieres and Guibal, 2010). It was observed that chitosan extracted from *O. niloticus* had few different reflections compared to commercial grade chitosan, due to the presence of some minerals in the prepared chitosan; some other peaks are also seen at 35° in the spectra as shown (El-hefian *et al.*, 2010). Moreover, chitosan extracted from different sources differs significantly in terms of their molecular weight and molecular weight distribution, degree of deacetylation, and purity level (Mullah *et al.*, 2017).

4.5.4 DSC Thermograms of Chitosan (CS) and Carboxymethyl chitosan (CMCS)

The DSC thermograms of chitosan isolated from *O. niloticus* (ONCS), commercial chitosan (COCS) and carboxymethyl chitosan (CMCS) are shown in figure 4.52 – 4.54. From the DSC thermograms (Figure 4.52-4.54), a large endothermic peak associated with solvent evaporation mainly water was observed above 100°C in all the three samples under study (Al Sagheer *et al.*, 2009).

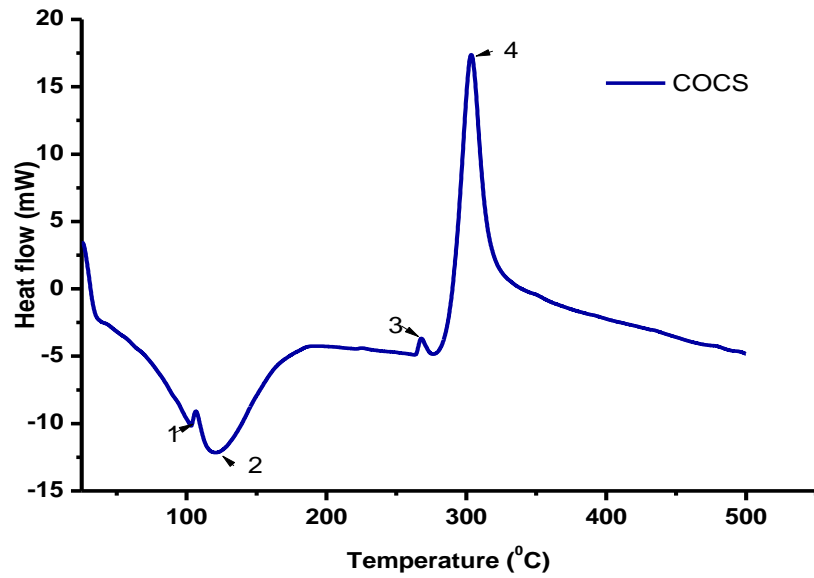


Figure 4.52: DSC thermogram of commercial chitosan (COCS)

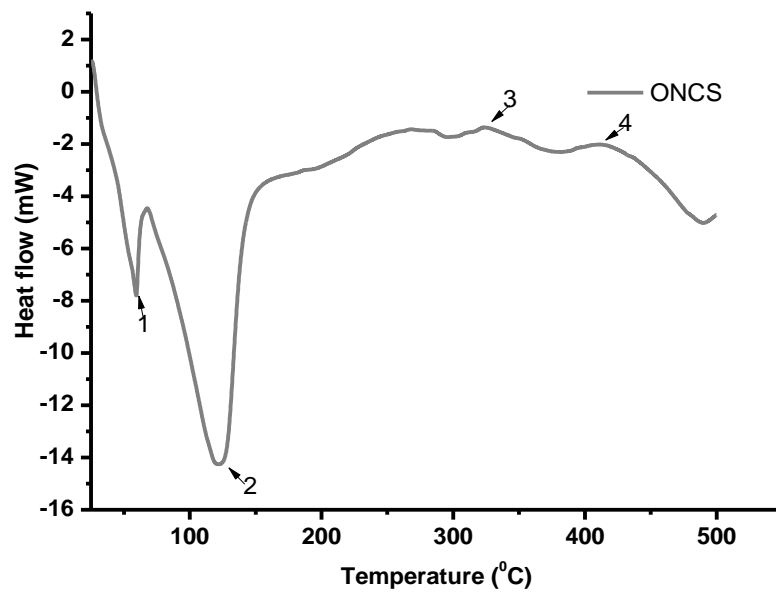


Figure 4.53: DSC thermogram of *O. niloticus* chitosan (ONCS)

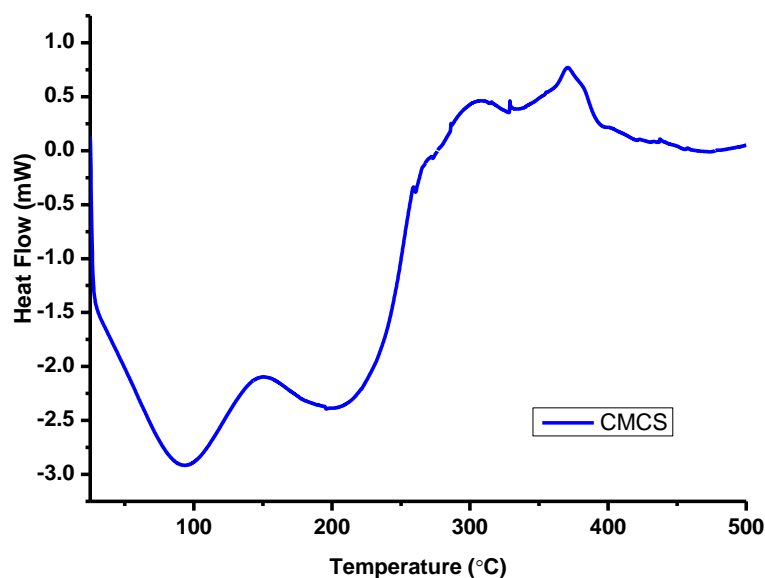


Figure 4.54: DSC thermogram of carboxymethyl chitosan (CMCS)

All the chitosan samples had a wide endothermic peak centered between 119 – 130 °C with an onset at around 68 °C and 107 °C for *O. niloticus* chitosan and commercial chitosan respectively (Appendix T) (Yuan *et al.*, 2011). As it can be observed from the thermograms, the broad endothermic peak with T_2 occurring between 119 - 130 °C is related to the evaporation of water during the DSC scan. It has been reported that polysaccharides usually have a strong affinity and in the solid state, these macromolecules have disordered structures that are easily hydrated (Kittur *et al.*, 2002). The primary and supramolecular structures of these polysaccharides affect their hydration properties hence the endotherm related to the evaporation of water reflects the physical and molecular changes occurring during the N-deacetylation of chitin. With an increase in N-Deacetylation, there is a subsequent increase in ΔH values, which is an indication that there is a direct correlation between the water holding capacity and chemical and supramolecular structures of these polymers. The two exothermic peaks T_3 and T_4 in the thermograms can be associated with the thermal decomposition of amine (GlcN) and acetyl (GlcNAc) residues characteristic of chitosan samples (Guinesi & Cavalheiro, 2006).

4.5.5 TGA-DTGA Thermograms of Chitosan and Carboxymethyl chitosan

Figures 4.55 – 4.57 shows TGA curves and derivative thermograms (DTGA) of chitosan and carboxymethyl chitosan. From figure 4.55- 4.57 and Appendix U, COCS and CMCS had two degradation stages that occurred between 50 - 100°C and between 200 - 320°C. The first degradation stage was associated with evaporation of water molecules adsorbed on the surface of chitosan while the second degradation stage was associated with decomposition of chitosan main chain and cleavage of substituent groups in CMCS (Mullah *et al.*, 2017).

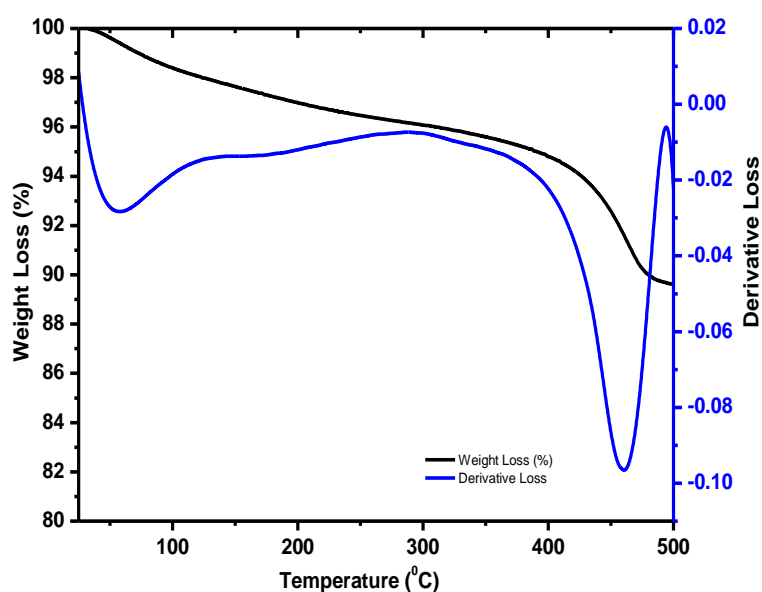


Figure 4.55: TGA/DTGA curves of *O. niloticus* Chitosan (ONCS)

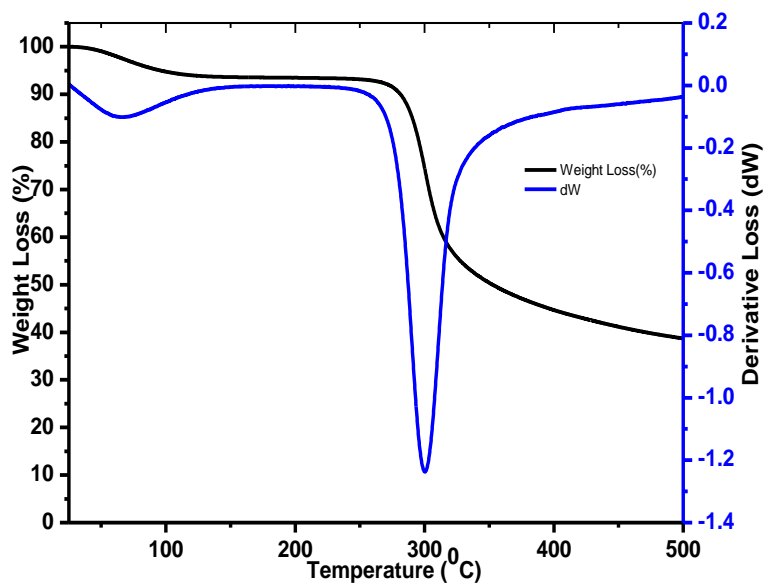


Figure 4.56: TGA/DTGA curves of Commercial Chitosan (COCS)

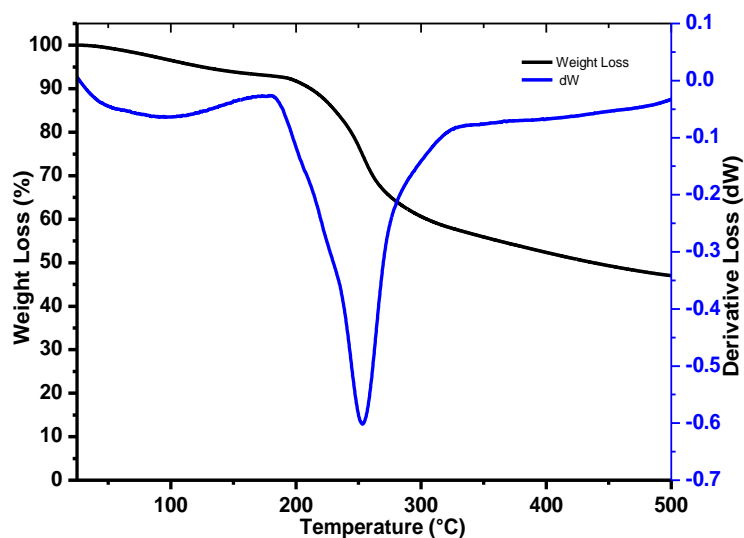


Figure 4.57: TGA/DTGA curves of carboxymethyl chitosan (CMCS)

Thermal properties of chitosan before and after carboxymethylation revealed that there were significant changes in thermal properties after carboxymethylation. The ash content and onset degradation temperature of carboxymethyl chitosan were higher as compared to chitosan possibly due to the introduction of sodium carboxylate groups on chitosan. It should be noted however that the thermal stability of CMCS was lower than that of COCS which was as a result of carboxymethylation while the residual ash

of CMCS was higher as compared to COCS which can be linked to the carboxymethylation of COCS and the presence of sodium ion in CMCS ash (Mullah *et al.*, 2017). On the other hand, due to the presence of a high concentration of impurities in ONCS (Figure 4.55), the residual ash content and thermal stability of ONCS was higher as compared to COCS and carboxymethyl chitosan. The high ash content and increased degradation temperatures have been associated with presence of metallic species which have high degradation temperatures and thermal stability (de Queiroz Antonio *et al.*, 2017; Kumari *et al.*, 2015).

4.5.6 SEM Micrographs of Chitosan and Carboxymethyl chitosan

The morphology of chitosan before and after surface modification were examined using SEM and the micrographs are shown in Plate 4.6. From plate 4.6, it can be observed that introduction of the carboxymethyl group on COCS did not alter the morphology of COCS. This would be expected because carboxymethylation only introduces the carboxymethyl group on the structure of COCS, but it does not convert the particle of COCS to nanoparticles as in the case of treatment with tripolyphosphate ions (Yuan *et al.*, 2011).

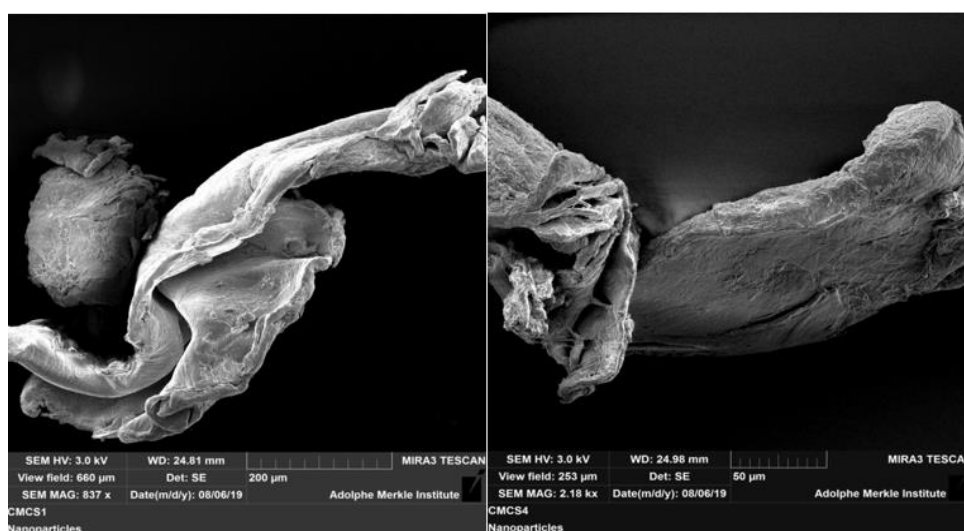


Plate 4.6: SEM Micrographs of Chitosan and Carboxymethyl chitosan

Treatment of chitosan with tripolyphosphate ions convert it into nanoparticles but for the case of carboxymethylation such treatment only serves to introduce a functional

group within the network. As it can be observed, commercial chitosan samples under study appeared as a solid rigid mass with little change in morphology or size even after treatment with monochloroacetic acid while ONCS were not subjected to carboxymethylation due to presence of impurities (Yuan *et al.*, 2011).

4.5.7 Proton NMR ($^1\text{H-NMR}$) of Carboxymethyl chitosan

Proton NMR was used to evaluate changes in chitosan after carboxymethylation and the results are shown in figure 4.58. From figure 4.58, the signal centered at 1.08 ppm were attributed to the presence of impurities while the signal centered at 1.96 ppm corresponds to the hydrogens of the methyl moieties belonging to the acetamido groups.

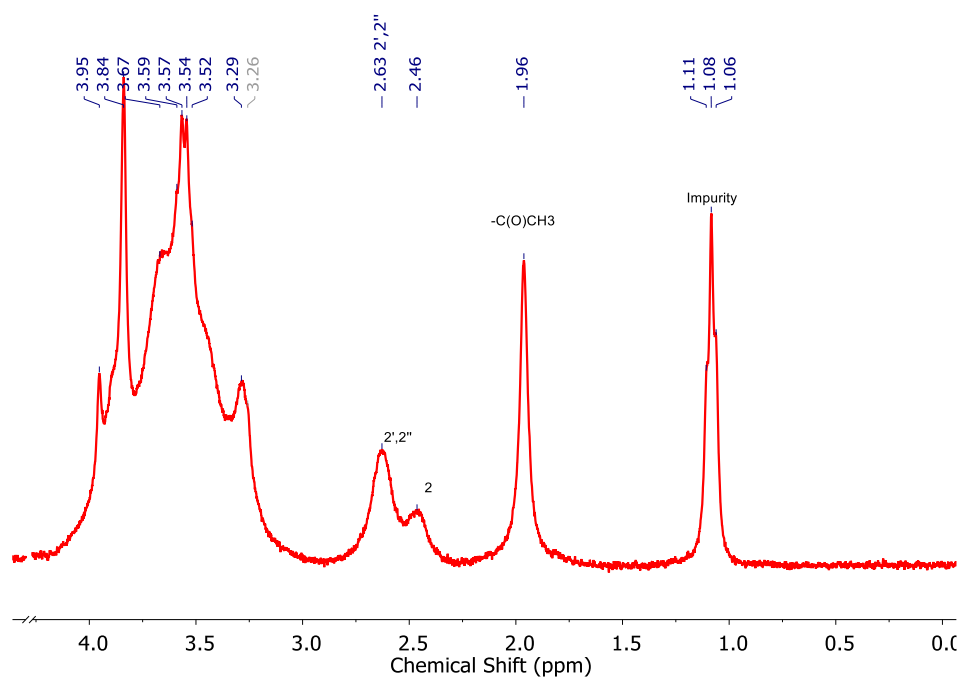


Figure 4.58: Proton NMR spectra of carboxymethyl chitosan

The signal observed between 2.25 - 2.75 ppm corresponds to the hydrogen bonded to the C₂ glucosamine ring, while the signals between 3.0 - 4.00 ppm correspond to hydrogens bonded to the carbon atoms C₃, C₄, C₅ and C₆ of the glucopyranose that are overlapped (Abreu & Campana-Filho, 2005).

4.6 Green Synthesis of Iron Oxide Nanoparticles

4.6.1 Variation of Ratio of FeCl₃ to the Extracts Volume

Synthesis of iron nanoparticles involved variation of metal ion concentration to extract concentration and the results are shown in figure 4.59 – 4.60. In the case of chemical and biological synthesis of nanoparticles, the aqueous metal ion precursors from metal salts are reduced and as a result a color change occurs in the reaction mixture (Figure 4.59 – 4.60). This was the first qualitative indication that the nanoparticles had been (Eslami *et al.*, 2018) but they did not settle out of solution under atmospheric conditions, and they were not magnetic (Truskewycz *et al.*, 2018).

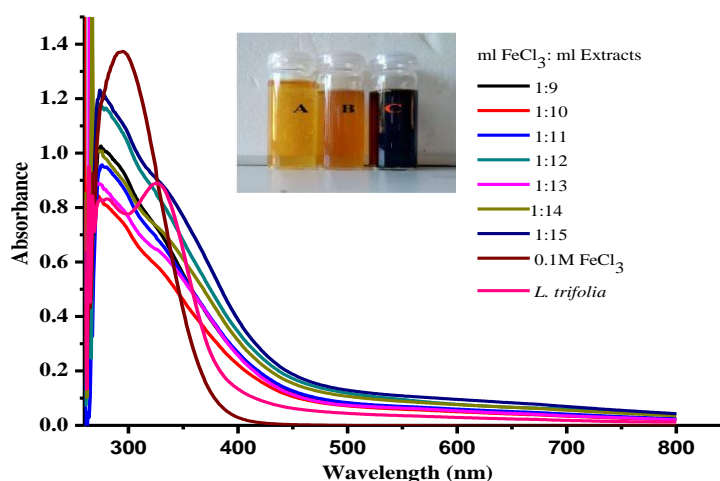


Figure 4.59: UV-vis spectrums showing variations of volume ratio of metal ion to volume of extracts used. Inset showing change in color of FeCl₃ (A), Extracts (B) and Nanoparticles (C)

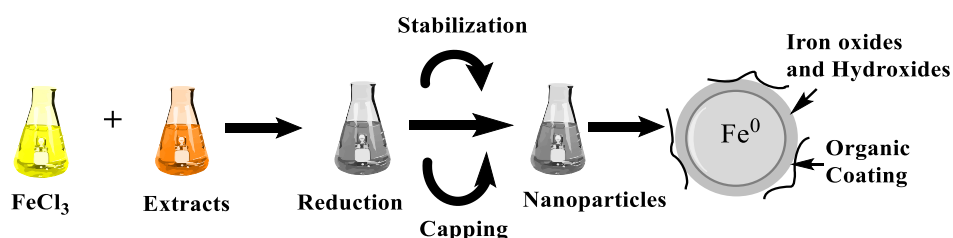
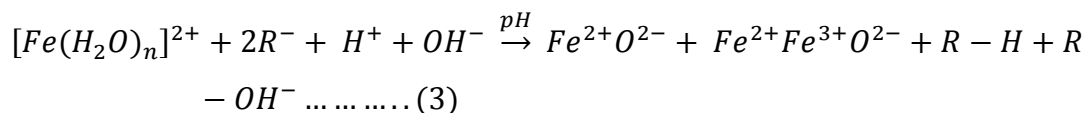
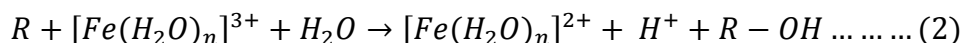
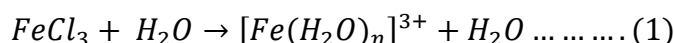


Figure 4.60: Phyto-mediated synthesis of iron nanoparticles using plant extracts.

The presence of biomolecules or combinations of chemically complex biomolecules, such as, enzymes, amino acids, proteins, vitamins, and polysaccharides, and organic acids may act as reducing and capping agents in nanoparticle synthesis (Eslami *et al.*, 2018). The mechanism behind plant extract mediated metallic nanoparticle formation has not been clearly defined as not a single plant extract biomolecule has been linked in the fabrication of nanoparticles (Saif *et al.*, 2016). Various plant components are rich in secondary metabolites which are responsible for metallic nanoparticles synthesis. Secondary metabolites such as polyphenols, tannic acid, flavonoids, terpenoids, ascorbic acids, aldehydes, carboxylic acids, and amides that are present in the extracts possess ideal redox potentials that allow efficient reduction of metal precursors for conversion into their corresponding metallic nanoparticles (Saif *et al.*, 2016; Marslin *et al.*, 2018). The bio reduction process can be induced in the following way (Saini *et al.*, 2016):



The presence of phenolic-OH groups and ortho-dihydroxyphenyl groups in chemical structure of tannins are involved in the formation of complexes with iron and also take part in redox reactions (Saini *et al.*, 2016). In the formation of iron oxide NPs by tannins, the reactions undergo changes in electron structure as tannins are oxidized to quinines and, by this reaction, iron salt is reduced to iron oxide nanoparticles (Eslami *et al.*, 2018).

4.6.2 Variation of FeCl₃ Concentration

Figure 4.61 depicts synthesis of iron nanoparticles carried out with varying concentrations of iron chloride solutions. After the reaction, the nanoparticles were separated from the colloid solution by high-speed centrifugation and then examined using various characterization techniques (Shah *et al.*, 2015).

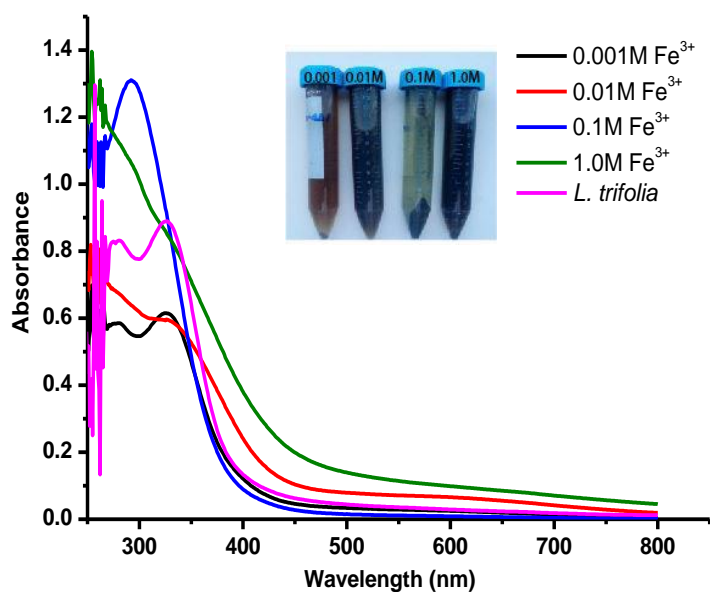


Figure 4.61: UV-vis spectrums showing variations of metal ion concentration in solution. Inset showing nanoparticles formed when 0.1M solutions are used.

From the results obtained (Figure 4.61), variation of metal ion concentration revealed the synthesis of iron nanoparticles occurred at 0.1M FeCl_3 concentration as at lower and higher metal ion concentration, the solutions did not become turbid indicating that the synthesis is concentration dependent (Saif *et al.*, 2016). Moreover, upon evaluating the effect of different concentrations of FeCl_3 in the reaction mixture, 0.1M FeCl_3 had the highest maximum optical density. The metal ion concentration is an important factor that needs to be considered and this may be adjusted by dilution. In fact, the diffusive behavior of charged particles is affected by the electrostatic forces arising between particles and this effect is concentration dependent, with a maximum occurring at a point called “gel-formation”. Aggregation rate increases with a subsequent increase in particle concentration, but this can be overcome by diluting the sample though the aggregation state of the sample will be affected (Chekli *et al.*, 2016). As aggregation of charged particles is also pH-dependent with maximum aggregation occurring at the point of zero charge (PZC) reducing or increasing the pH far away from the PZC could be one way to form stable dispersions (Saini *et al.*, 2016).

4.6.3 FT-IR Characterization of Iron Oxide Nanoparticles

Figure 4.62 depicts the IR spectra for iron nanoparticles obtained after synthesis using *L. trifolia*. The peak at 3400 was attributed to OH stretching vibrations, while the peaks at 2925, 1624, 1415 and 1025 cm^{-1} were attributed to CH_2 , C=C, CH, C-O-C stretching vibrations of secondary metabolites present in *Lantana trifolia* extracts and acted as capping and stabilizing agents during synthesis of the particles.

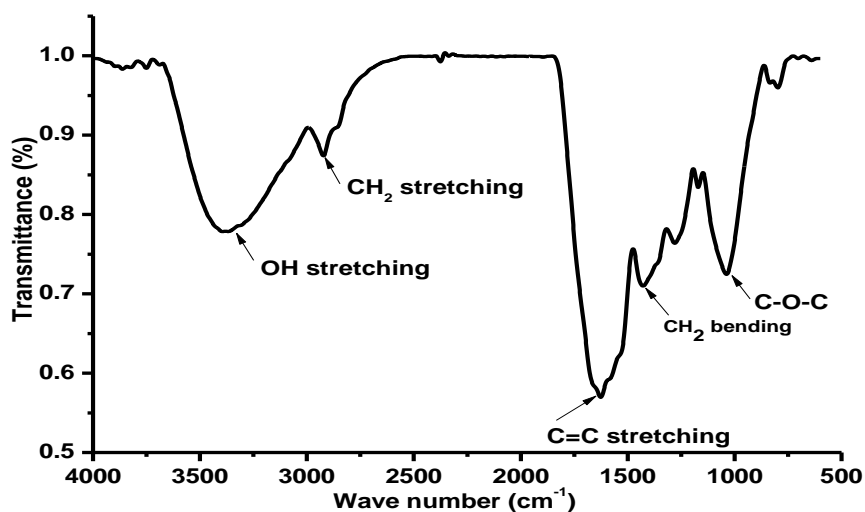


Figure 4.62: FT-IR spectra of Iron nanoparticles synthesized using *L. trifolia* extracts.

The results indicate that the plant polyphenols are part of the components in the iron nanoparticles and besides clinging on the surface of the particles they act as capping agents during synthesis (Saif *et al.*, 2016). Similar results were reported when iron nanoparticles have been synthesized with extracts from different plants such as being *Eucalyptus tereticornis*, *Melaleuca nesophila*, *Rosemarinus officinalis* (Wang *et al.*, 2014), and green tree extracts (Weng *et al.*, 2013)

4.6.4 Powder X-ray Diffractograms of Iron Nanoparticles

The X-ray diffractogram of iron nanoparticles synthesized using aqueous extracts of *L. trifolia* are shown in the figure 4.63. From the results obtained, the diffractogram

revealed that green synthesized iron nanoparticles are amorphous in nature as only a broad shoulder at 2θ angles at around 17° was observed (Figure 4.63).

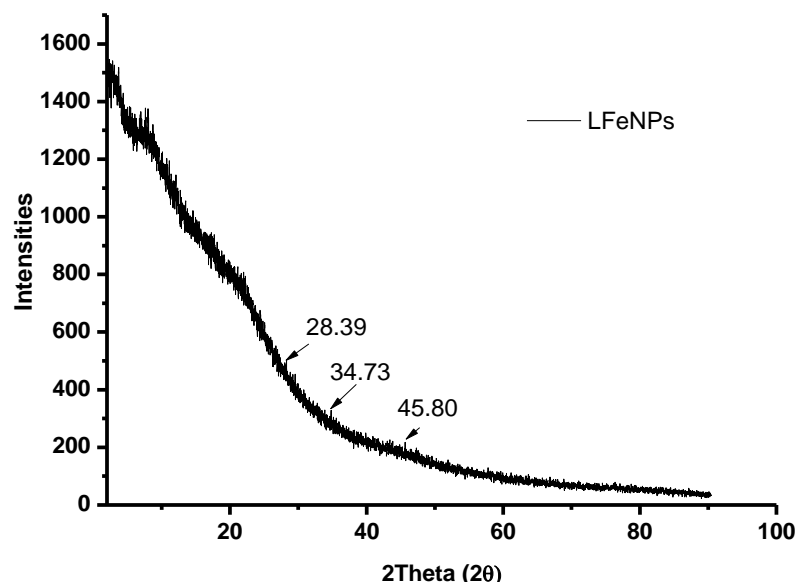


Figure 4.63: Powder X-ray diffractogram of FeNPs synthesized using aqueous extracts of *Lantana trifolia*.

At low FeNPs concentrations, their presence can be confirmed by UV-Vis spectroscopy because they are invisible in XPD due to presence of a large background resulting from the secondary metabolite coating, which impart an amorphous and non-crystalline phase to the nanoparticles (Chekli *et al.*, 2016). Hence secondary metabolites may efficiently mask presence of FeNPs and hence act as capping and stabilizing agents. Similar observation was made in a study in which AgNPs were encapsulated onto a silica shell which made their identification with powder XRD difficult due to the amorphous nature of silica (Priebe *et al.*, 2017; Priebe & Fromm, 2015). Moreover, use of a copper radiation in the analysis of iron containing materials leads to a high background because of fluorescence which hinders measurements. The diffractograms thereof show that some peaks that are used for identification are of equal heights as the background noise (Mos *et al.*, 2018). Hence the dried powder of Fe-P NPs, which was prepared using *lantana trifolia* extracts were organic and amorphous in nature (Wang *et al.*, 2014).

4.6.5 Single Crystal X-Ray Diffractogram of Iron Nanoparticles

Single crystal x-ray diffractogram of iron nanoparticles synthesized using aqueous extracts of *Lantana trifolia* are shown in the figure 4.64. From the data obtained from single crystal X-ray diffractogram (Figure 4.64, Table 4.15), the synthesized nanoparticle comprised of iron nanoparticles with a cubic crystal system.

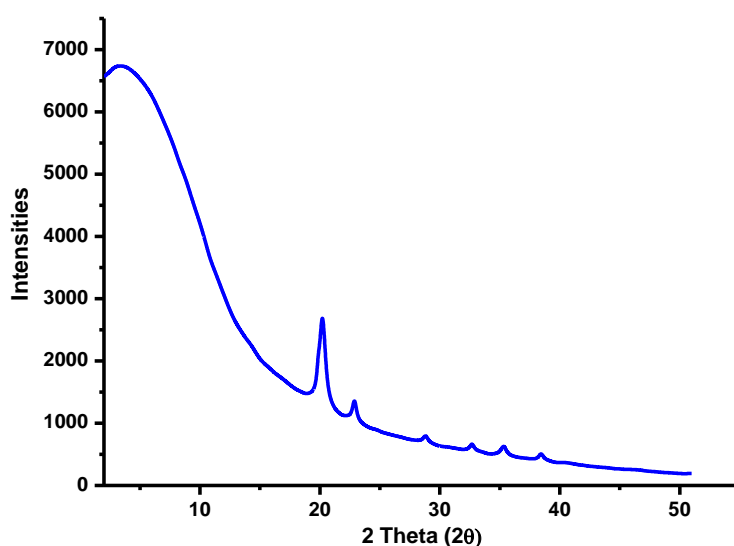


Figure 4.64: X-ray diffractogram of iron nanoparticles synthesized using aqueous extracts of *Lantana trifolia*.

Table 4.15: 2 theta values and hkl indices for phases identified.

No.	2theta [°]	d [Å]	FWHM	Hkl (a)	Hkl (b)
1	20	2.0602	0.2640		1,1,1
2	20	2.0246	0.5756	1,0,1	
3	23	1.7914	0.4014		2,0,0
4	29	1.4283	0.4653	2,0,0	
5	33	1.2630	0.4064		2,0,2
6	35	1.1714	0.5204	2,1,1	
7	39	1.0793	0.4694		3,1,1
8	40	1.0333	0.4198		2,2,2
9	41	1.0128	0.4166	2,0,2	
10	46	0.9058	0.3870		4,0,0

A search in the crystal data base revealed that the 2θ values at 20, 23, 33, 39 and 40° correspond to iron nanoparticles as reported by (Nishihara *et al.*, 2012) while 2θ at 20,

29, 35 and 41° correspond to cubic crystal system that have been reported by (Zhang & Guyot, 1999). The broad amorphous background is due to the secondary metabolites surrounding the iron nanoparticles and this explains their role as capping agents (Markova *et al.*, 2014).

4.6.6 TGA and DTGA of Iron Nanoparticles

Thermal analysis was employed to study the thermal properties of iron nanoparticles synthesized using *L. trifolia* and the results are shown in figure 4.65. From figure 4.65, an initial weight loss observed at 100 °C was attributed to loss of residual water adsorbed on the surface of the particles. The second degradation step centered at 250 °C in DTGA was linked to the decomposition of the organic layer surrounding the particles.

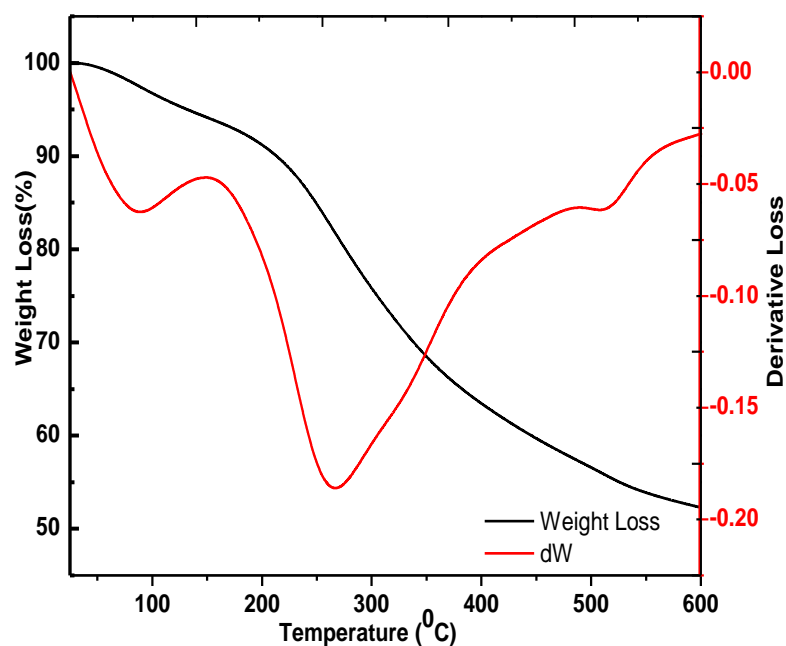


Figure 4.65: TGA and DTGA thermograms of iron nanoparticles synthesized using *L. trifolia* extracts.

This decomposition makes the main peak in the DTGA curve as it has been reported that phyto mediated synthesis of nanoparticles affords them an organic capping layer (Ebrahimezhad *et al.*, 2017; Eslami *et al.*, 2018).

4.6.7 SEM Micrographs of Iron Nanoparticles

SEM micrographs of iron nanoparticles are shown in Plate 4.7. Fe–P NPs C shows different structures, in which they were aggregated like grapes which was attributed to different components and concentrations of polyphenols in *L. trifolia* plant extracts. These secondary metabolites played a key role in dictating the final structures and size of the iron nanoparticles and the extent of aggregation.

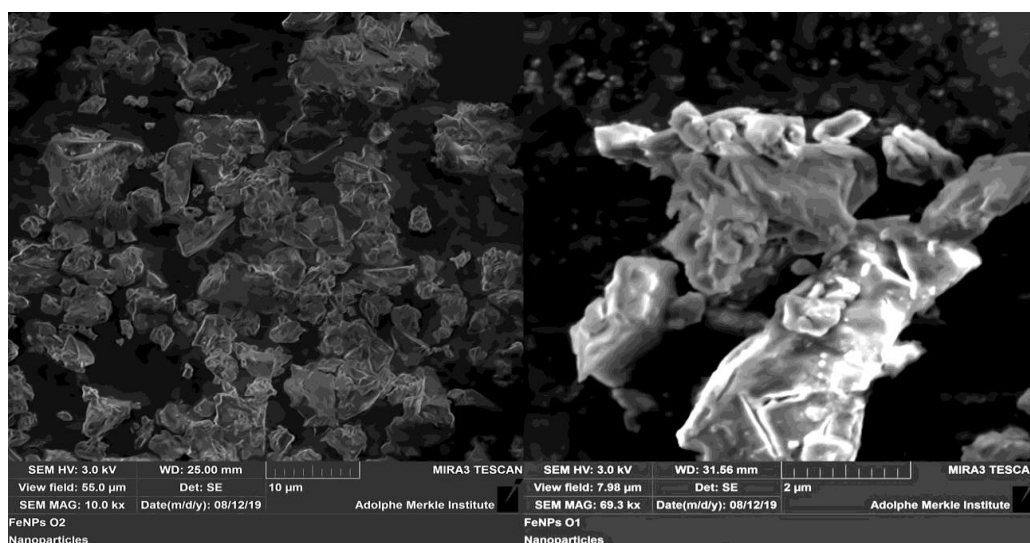


Plate 4.7: SEM micrographs of iron nanoparticles synthesized using *L. trifolia* extracts

As it can be observed from plate 4.7, the absence of clear and distinct particles in the micrographs implied that while it has been reported that use of secondary metabolites can limit the extent of aggregation, this was not the case in this study. As a result, the nanoparticles synthesized using *L. trifolia* aggregated during drying due to the inability of the secondary metabolites to limit the particle association hence the appearance of microstructures (Wang *et al.*, 2014).

4.6.8 Hydrodynamic Diameter, Zeta potential and Poly-dispersibility Index

The size distribution, zeta potential and poly-dispersibility index were determined by DLS and the results are shown in figure 4.66. From the DLS results obtained, the synthesized iron nanoparticles had an average hydrodynamic diameter,

polydispersibility index and zeta potential of 150 - 700 nm, 0.56 ± 0.1 and -0.10 ± 0.1 (mV) respectively.

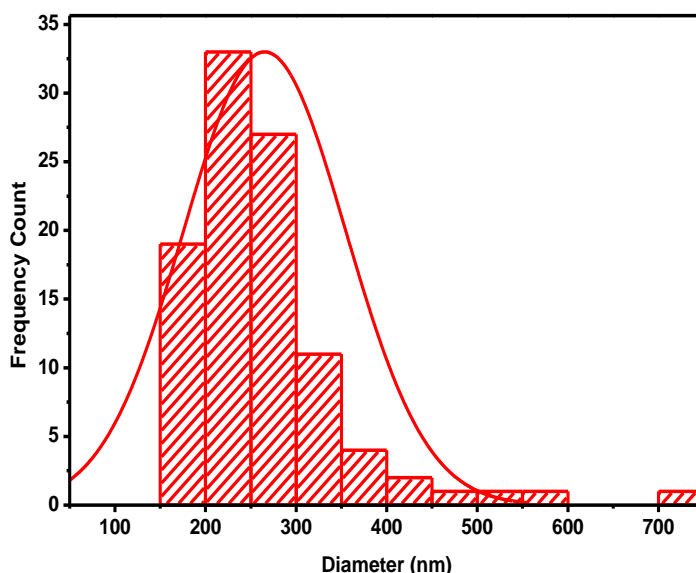


Figure 4.66: Size distribution of iron oxide nanoparticles synthesized using *L. trifolia* extracts

DLS measures the hydrodynamic diameter, which is the diameter of the particle plus ions or molecules that are attached to the surface and moves with the FeNPs in solution. With the low zeta potential value, the particles were more likely to aggregate in solution and as a result their size increased though this can be avoided if they are redispersed in a suitable matrix such as cellulose chitosan composite. It has been reported that particle which exhibit zeta potential further away from a value of zero, either on the negative or positive side, tend to aggregate less (Markova *et al.*, 2014; Wang *et al.*, 2014).

4.6.9 TEM Micrographs of Iron Nanoparticles

Figure 4.67 depicts the TEM micrographs of iron nanoparticles synthesized using *L. trifolia*. From TEM micrographs (Figure 4.67), it was observed that the particles were aggregated possibly due to drying after synthesis, but an organic coating could be observed around them.

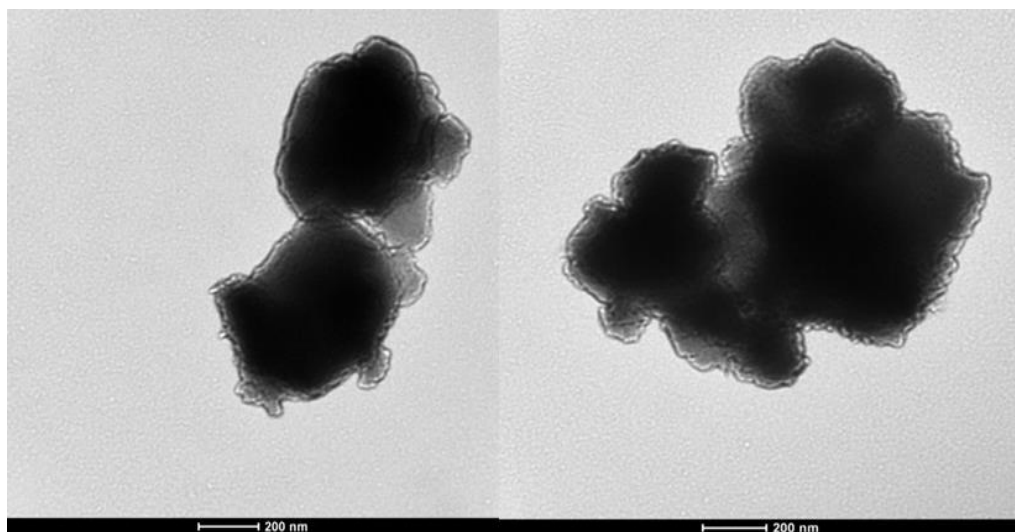


Figure 4.67: TEM micrographs of Iron nanoparticles synthesized using *L. trifolia* extracts

Presence of this organic coating affords the amorphous nature of the nanoparticles which resulted to a large amorphous background in the diffractograms. Presence of aggregates posed a challenge in determination of the size of nanoparticles as absence of single particles meant that use of image processing software was not possible though those that were measured lied between 200 - 500 nm. Biosynthesized FeNPs were aggregated like grapes which was attributed to different components and concentrations of polyphenols in *L. trifolia* plant extracts, that played a key role in dictating the final structures and size of the nanoparticles (Wang *et al.*, 2014).

4.6.10 Redox Potential of the Extracts and FeNPs

The redox potentials of the extracts, iron nanoparticles and ascorbic acid standard were measured the results are shown in figure 4.68 – 4.70. The voltammograms of Ascorbic acid in an aqueous solution containing KCl (0.1 M) as supporting electrolyte at pH 3.2 showed one irreversible anodic peak at 0.9 V versus Ag/AgCl reference electrode that corresponds to the oxidation of ascorbic acid to dehydro-ascorbic acid which is unstable and degrades, as no corresponding reduction peak appears. The extracts showed the peak anodic currents around +0.3V and +0.7V which means that they have

strong free radical scavenging capabilities, and they are oxidized at relatively low potential (Amidi *et al.*, 2012).

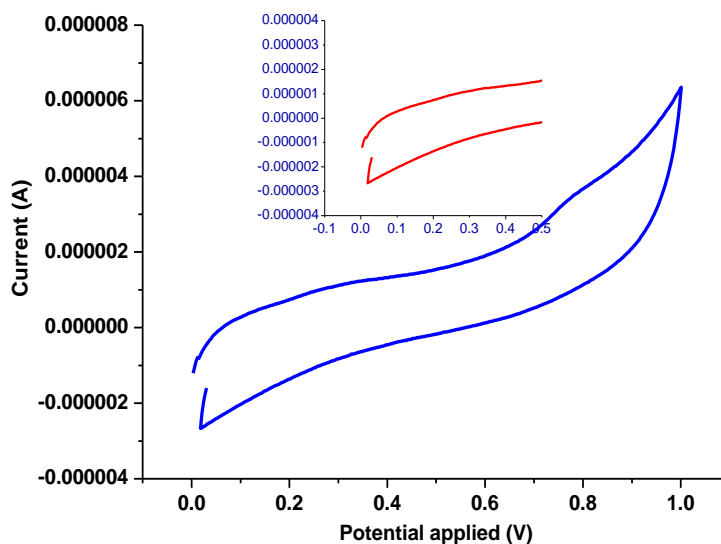


Figure 4.68: Cyclic voltammogram of *L. trifolia* extracts showing the reduction potential

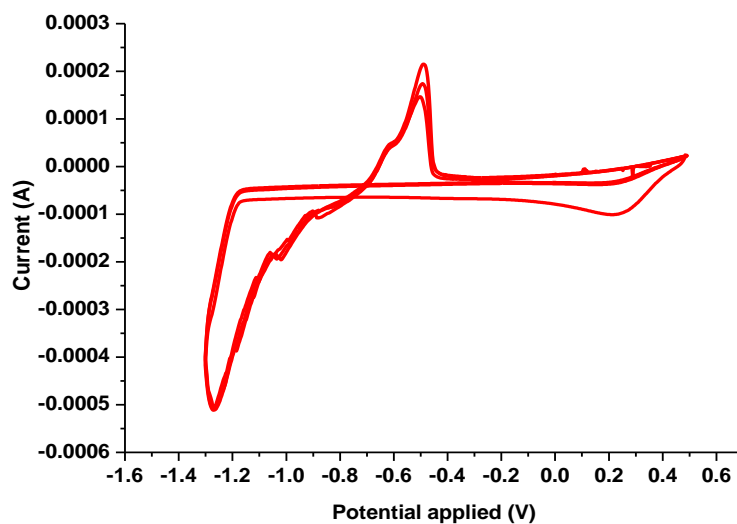


Figure 4.69: Cyclic voltammogram of FeNPs showing the reduction potential

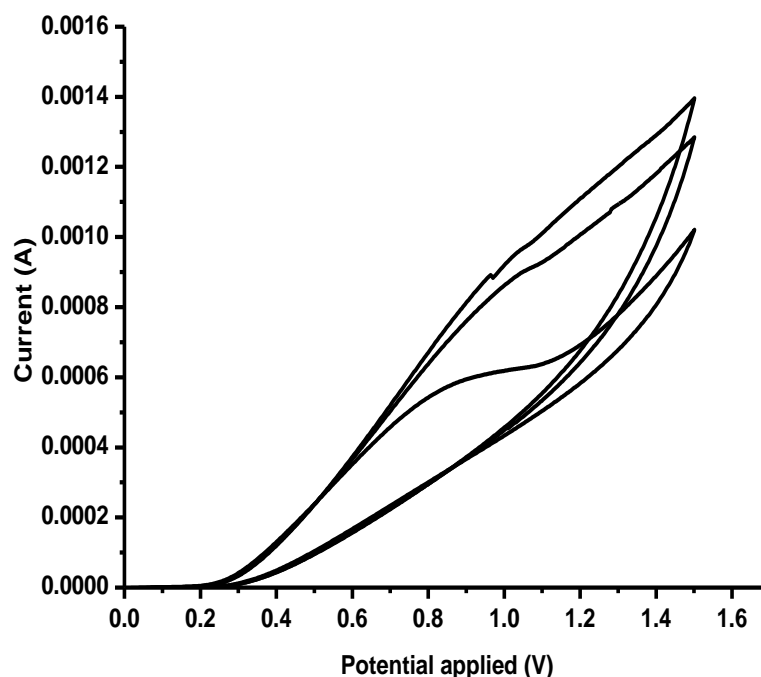


Figure 4.70: Cyclic voltammogram of 0.1M Ascorbic acid standard showing the reduction potential.

The other aspect of voltammogram is that it showed the reversibility of the redox reaction which takes place near the electrode. The peak anodic and peak cathodic currents usually have equal magnitudes in a reversible process while for an irreversible reaction, the cathodic and anodic peaks are not equal and where the oxidation is very slow, no cathodic peak is observed (Elgrishi *et al.*, 2018). Therefore, cyclic voltammetry was used to characterize the redox behavior of plant extracts. The peak potential correlates with the type of reductant; low oxidation potentials are associated with a greater facility or strength of a given molecule for the electron donation and, thus, to act as antioxidant (Hoyos-Arbeláez *et al.*, 2017). The reduction potential of the plant extract is due to presence of polyphenols which make them able to reduce Fe^{3+} into Fe^{2+} and in the process form iron polyphenol complex (Figure 4.71) (Somchaidee & Tedsree, 2018; Saini *et al.*, 2016).

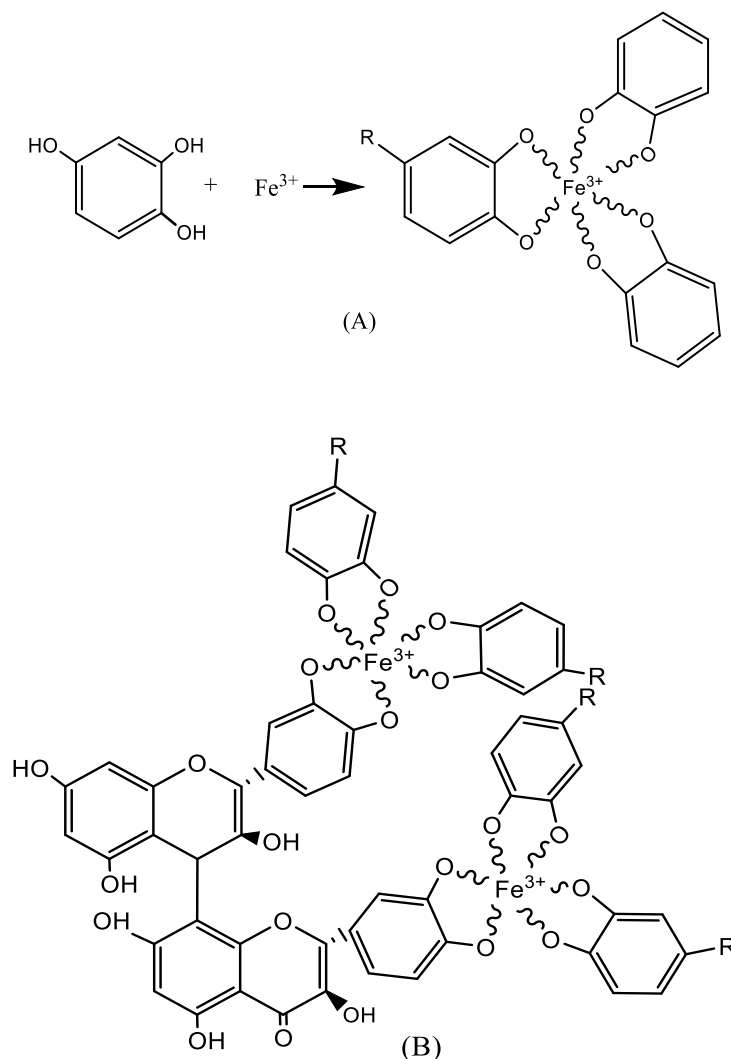


Figure 4.71: Proposed chemical structure of Fe-P NPs (A); and (b) proposed condensation mechanism of Fe-polyphenol.

However, the extract does not completely reduce the Fe^{2+} to zero-valent iron as they are strongly stabilized due to the presence of polyphenols ligands (Figure 4.71). It also rapidly oxidizes in the presence of oxygen to give Fe^{3+} polyphenol complexes in a phenomenon known as autoxidation (Saini *et al.*, 2016).

4.6.11 *In-vitro* Antimicrobial Activity of FeNPs

The antimicrobial activity of the synthesized nanoparticles against selected microorganisms was evaluated and the results are shown in figure 4.72. From figure 4.72, the iron nanoparticles had moderate activity against the selected organisms.

However, the highest activity was observed against *E. coli*, as compared to *P. aeruginosa*, *B. subtilis*, *S. aureus* and *C. albicans*, respectively.

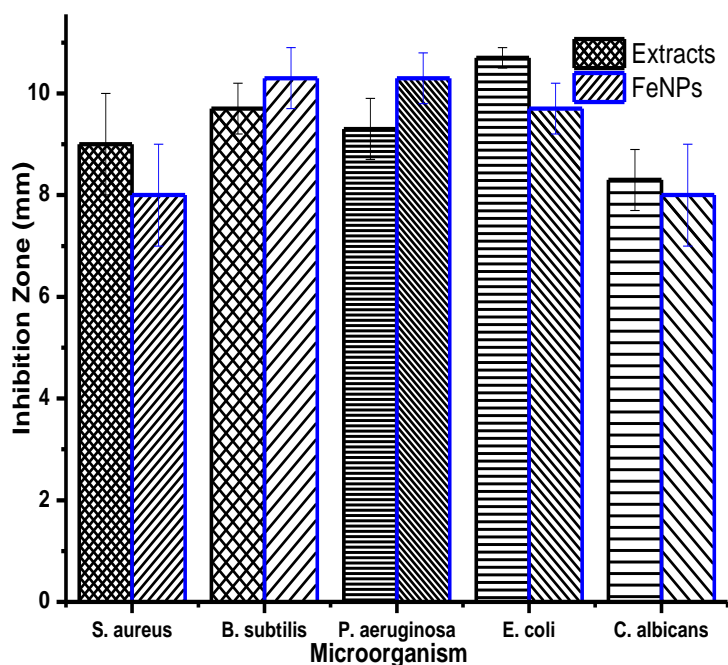


Figure 4.72: Antimicrobial activity of FeNPs against *S. aureus*, *B. subtilis*, *P. aeruginosa*, *E. coli*, and *C. albicans*

The antimicrobial activity against the selected microorganisms was due to the small size of the iron oxide nanoparticles which penetrate the bacterial cell (Mirza *et al.*, 2018). In Gram-negative bacteria such as *P. aeruginosa* and *E. coli*, the bacterial cells are covered by a thin layer of peptidoglycan cell wall surrounded by a lipopolysaccharide outer membrane while Gram-positive bacteria such as *B. subtilis* and *S. aureus* only have a thick layer peptidoglycan layer many times thicker than is found in Gram-negative bacteria (Silhavy *et al.*, 2010). It has been shown that the antibacterial activity of NPs is based on the ability to release ions, although other mechanisms can be involved as well (Khan *et al.*, 2020). The cell wall destruction occurs due to the physical interaction between the bacteria cell wall and the nanoparticles and is more detrimental for Gram-negative bacteria due to absence of the thick peptidoglycan layer found in Gram-positive bacteria which acts as a protective layer (Slavin *et al.*, 2017). The plant extracts were active against bacteria

and the enhancement of antibacterial activity is due to the treatment of plant species leaf extract on the surface of nanoparticle. It is to be noted that the microorganisms have negative charge while iron nanoparticles are positively charged thereby creating an electromagnetic interaction (Mirza *et al.*, 2018). Due to this interaction, bacteria are denatured as interaction of metallic nanoparticles with protein thiol groups releases ions which lead to breakdown of bacterial cell surface leading to death (Rezaei-Zarchi *et al.*, 2010; Slavin *et al.*, 2017; Baptista *et al.*, 2018). From our study, comparison of antibacterial activity of the precursor metal ion in solution revealed that FeCl₃ was not active against some microorganisms when compared to the synthesized nanoparticles. This is because when metal ions are exposed to bacterial cell wall, they are uniformly distributed around the bacteria cell with no specific localization (Slavin *et al.*, 2017). In contrast, interaction between metallic nanoparticles with bacterial cell wall produces a large number of radicals that are concentrated at a given focal point leading to cytotoxicity of the nanoparticles as they can be able to perforate the cell wall leading to cell death (Khan *et al.*, 2020). Hence iron nanoparticles had a higher antibacterial activity as compared to its bulk counterpart which is an indication that generation of radicals contribute to their toxicity (Slavin *et al.*, 2017; Baptista *et al.*, 2018). However, the toxicity of metallic particles is greatly influenced by the size of the particles as larger particles that result from particle aggregation reduces their toxicity. Aggregated and clustered nanoparticles have a different motion from that of the primary nanoparticles and this results in the difference in the number of particles interacting with the cell's surface in vitro thereby affecting uptake and cytotoxicity (Moore *et al.*, 2015; Wang *et al.*, 2017).

4.7 Green Synthesis of AgNPs

4.7.1 Variation of the Reaction Time

Figure 4.73 illustrates the time dependence of the AgNP formation using *L. trifolia* extracts as determined by UV-vis spectroscopy (plasmon resonance) (Vasylevskiy *et al.*, 2017). The absorption spectrum of AgNPs spanned a wide range from 330 to 600 nm with a prominent SPR peak centered at 440 nm which is a qualitative indicator of the formation of AgNPs.

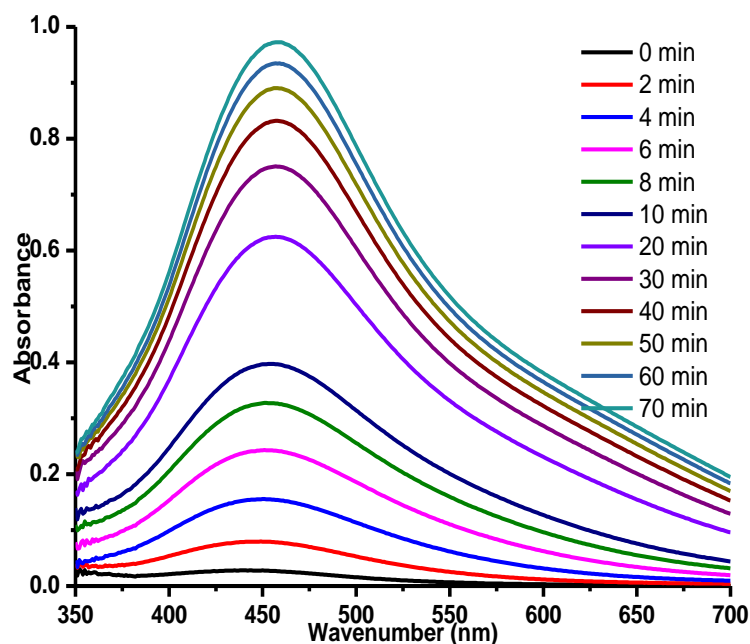


Figure 4.73: Variation of synthesis time against measurement of plasmon resonance of AgNPs

Moreover, the broad plasmon band that extends from 360 to 550 nm with an absorption tail in the higher wavelength could be due to the multi-size distribution of biosynthesized AgNPs. Synthesis of AgNPs was time dependent as with an increase in the reaction time there was a subsequent increase in the intensity of the color of the solution and the height of the SPR band observed. This can be explained by the fact that there was more interaction between the secondary metabolites and Ag^+ ions present in solution which resulted in the production of AgNPs hence the increase in the SPR band (Ndikau *et al.*, 2017).

4.7.2 Variation of the Concentration of AgNO_3 to Extract

The influence of silver nitrate concentration on synthesis of AgNPs were evaluated and the results are shown in figure 4.74. From figure 4.74, it was observed that the oxidant concentration had a profound effect on the size of the nanoparticles synthesized. When the concentration of the oxidant (AgNO_3) used was 0.0005 M, a broad absorption band and a bathochromic shift was observed while at 0.001 M and 0.0015 M a narrow absorption band and a hypsochromic shift was observed.

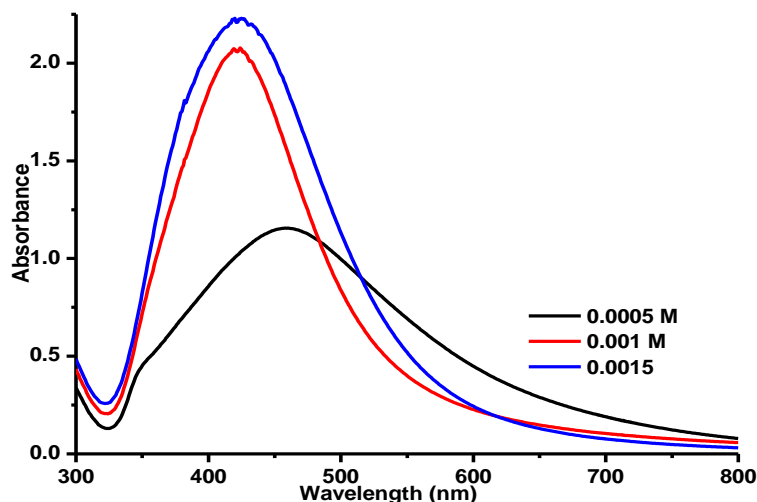


Figure 4.74: Variation of Ratio of Extracts Volume to concentration of AgNO_3 used.

The size of the nanoparticles has been reported to influence the intensity of the SPR band being observed as larger particles cause scattering of radiation and a shift to longer wavelength and a broad SPR band. As such the size of the SPR band can be used as an indirect indicator of the size of nanoparticles as larger particles have been reported to produce a broad SPR band when compared to smaller particles which produce sharp and narrow SPR. Surface plasmon resonances are typically studied as physical properties of metal nanostructures rather than chemical tools since they can control overgrowth and ultimate particle dimensions (Ndikau *et al.*, 2017; Vasylevskyi *et al.*, 2017).

4.7.3 Variation of Reaction Temperature

To investigate the influence of temperature in the synthesis of AgNPs, the synthesis was carried out between 20 – 35 °C and the results are shown in figure 4.75. From figure 4.75, variation of the reaction temperature revealed that at 20 °C, the rate of AgNPs formation was lower as compared to reactions carried out at 25 °C but above this temperature, the rate of formation decreased.

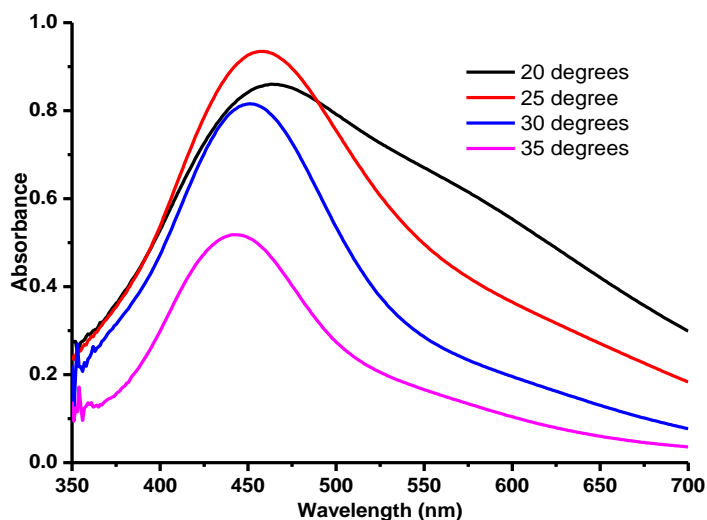


Figure 4.75: Variation of reaction temperature during synthesis of AgNPs

Indeed, the SPR spectra of AgNPs derived from the lower concentration of plant extract showed a sharper and strong absorption band at 443 nm as compared to higher concentration of plant extracts. Moreover, the broad plasmon band that extends from 360 to 550 nm with an absorption tail in the higher wavelength could be due to the multi-size distribution of biosynthesized AgNPs (Masum *et al.*, 2019). The change in the reaction temperature influences the morphology and structure of nanomaterials as particle morphology is strongly dependent upon the supersaturation which in turn is dependent on the solution temperature (Pawar *et al.*, 2012). The reduction in the overall surface energy is the true driving force for the grain boundary enlargement and consequently the particle size increases as a function of the temperature. A change in temperature facilitates the movement of atoms or molecules through the mechanism of mass transport and results in grain growth. It has been reported that smaller particles absorb Uv-vis radiation at shorter wavelengths while large particles absorb radiation at longer wavelengths. The findings in this study are in agreement with observations made in literature since a bathochromic shift in the Uv-vis spectra was observed when the temperature of the reaction media was decreased from 35 °C to 20 °C (Jiang *et al.*, 2011; Ndikau *et al.*, 2017). However, it is also interesting to note that a decrease in temperature also resulted to a broad band being observed which is associated with the presence of larger particles. As it can be observed from Appendix V-Y, the

nanoparticles aggregated at lower temperatures hence the broad UV spectra observed at 20 °C as compared to 35 °C in which a decrease in the optical density and the SPR was as a result of an increase in the number of synthesized nanoparticles. The red shift observed was due to delocalization and sharing of conduction electrons near each particle surface among neighboring particles (Ahmad *et al.*, 2018). Broadening and a bathochromic shift are associated with agglomeration or increase in size of the particles which increase scattering of the solution (Ndikau *et al.*, 2017).

4.7.4 Determination of Band Gap energy from Tauc plot

The band gap energy of AgNPs synthesized using *L. trifolia* extracts was evaluated and the results are shown in figure 4.76.

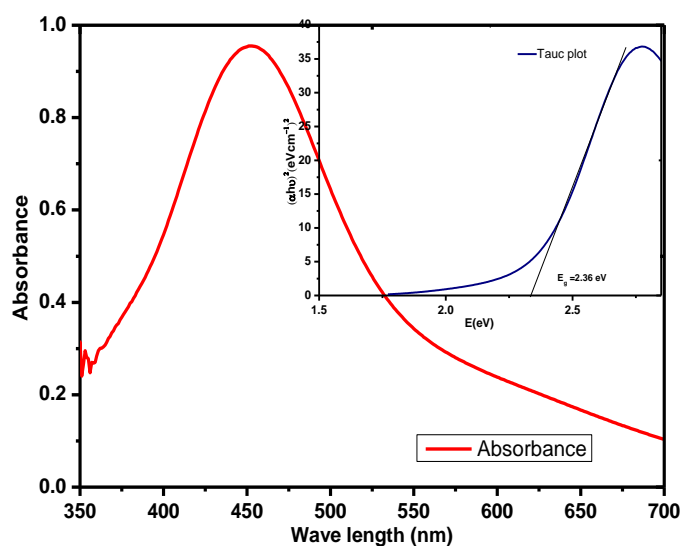


Figure 4.76: UV-vis spectrum of AgNPs synthesized at 30 °C. Inset Tauc plot for AgNPs

The energy band gap was estimated from Tauc plot between $(\alpha h\nu)^2$ versus energy of photon ($h\nu$). The intercept of the tangent on the Tauc plot gives a direct band gap for $n = 1$. The band gap energy for AgNPs synthesized at 30 °C was determined from Tauc plot (Figure 4.76) and it was found to be 2.36 eV (Ndikau *et al.*, 2017).

4.7.5 FTIR Spectra of AgNPs

The functional group present in the synthesized AgNPs were determined using an FT-IR spectrophotometer and the results are shown in figures 4.77. From the IR spectra of AgNPs (Figure 4.77), the vibrational frequencies at 3362 (OH stretching), 2918 (C-H stretching), 1379 (OH bending for phenolic compounds), and 1258 cm^{-1} (C-N stretching of amines or C-O aromatic stretching) are typically reported to be present in secondary metabolites such as flavonoids, phenolic acids, terpenes and terpenoids, and in nitrogen containing compounds such as alkaloids, amino acids and indoles (Vanaja *et al.*, 2014).

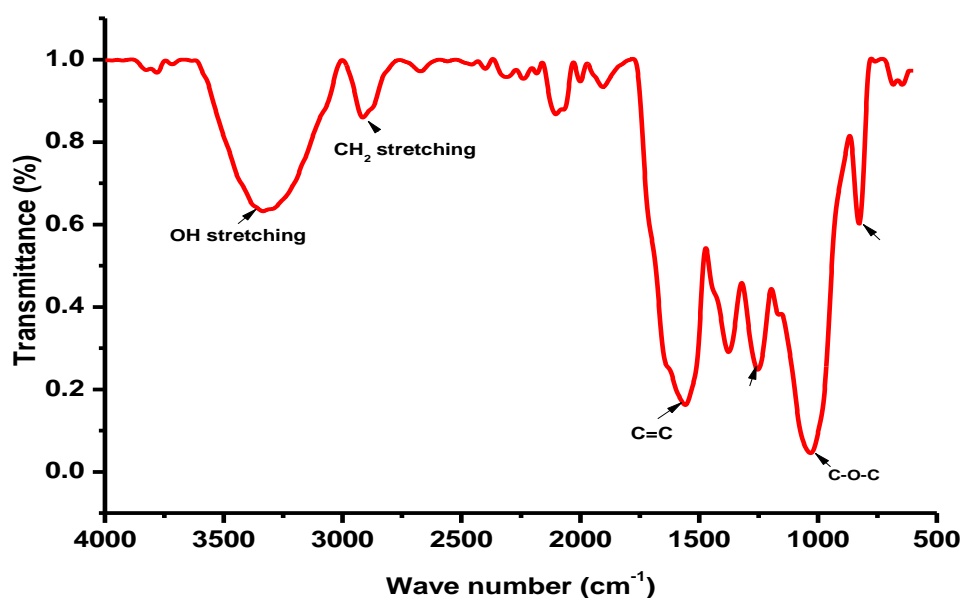


Figure 4.77: FT-IR spectra of AgNPs synthesized using *L. trifolia* extracts.

The absorption frequencies at 1040, 814, 753 and 684 cm^{-1} are typical of C-O stretching, C=C bending, C-H bending and C=C bending respectively (Socrates, 2004). It is worth noting that the position of the bands due to the C=C stretching vibration and the CH_2 in-plane deformation vibration are influenced by presence of a metal- π bond coordination system (Socrates, 2004). Coordination of an organic molecule to a metal atom through π -bonding reduces the C=C stretching frequency and brings it closer to the CH_2 deformation frequency which allows increased coupling to occur. As a result, coordination of Ag to an organic molecule decreases the C=C

stretching frequency which means that the band due to C=C vibration occurs at 1596.21 cm^{-1} rather than at around 1620 cm^{-1} (Socrates, 2004).

4.7.6 X-ray Diffractogram of Silver Nanoparticles

The X-ray diffractograms of green synthesized AgNPs are shown in figure 4.78. From the results obtained (Figure 4.78), it can be observed that the diffractograms comprised of distinct sharp peaks at $2\theta = 38, 44, 55,$ and 59 which correspond to the silver crystal planes (111), (200), (220), and (311), respectively.

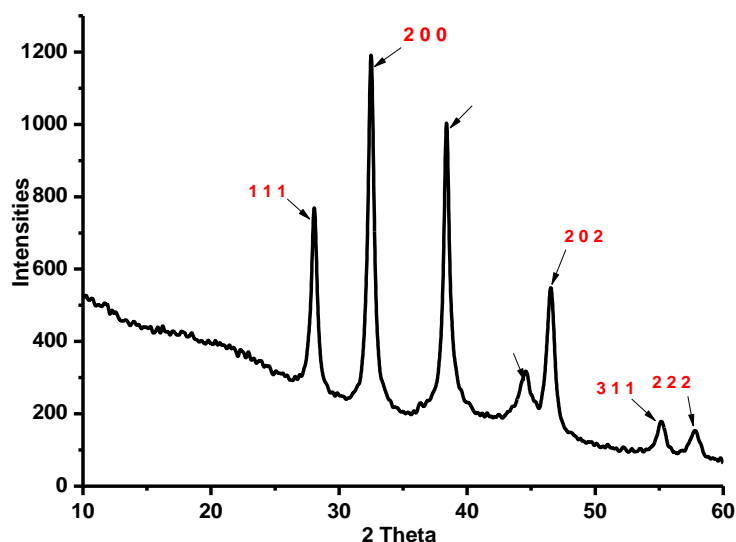


Figure 4.78: X-ray diffractogram of Phyto synthesized AgNPs

However, the peaks at $2\theta = 28, 33, 47$ correspond to AgCl planes (111), (200) and (202) which can be attributed to presence of chloride ion in the aqueous extracts which results in the formation of AgCl together with Ag^0 (Masum *et al.*, 2019). It is worth noting that pristine AgNPs are not chemically stable in the environment hence they react with inorganic ligands such as sulphide and chloride once the silver is oxidized. Being one of the most prevalent monovalent anions in the natural aqueous systems, Cl^- is present in plant extracts used during biosynthesis of AgNPs (Levard *et al.*, 2013). As such during synthesis of AgNPs, the interaction between Cl^- and Ag^+ leads to formation of a layer of AgCl on the AgNPs hence their presence in the XRD profile (Ndikau *et al.*, 2017).

4.7.7 TGA and DTGA Thermograms of AgNPs

The thermal properties of AgNPs synthesized using *L. trifolia* are shown in figure 4.79. From figure 4.79, the TGA thermograms of AgNPs synthesized using *L. trifolia* had three distinct degradation phases at 48, 173, and 251 °C with maximum degradation occurring at 313 °C.

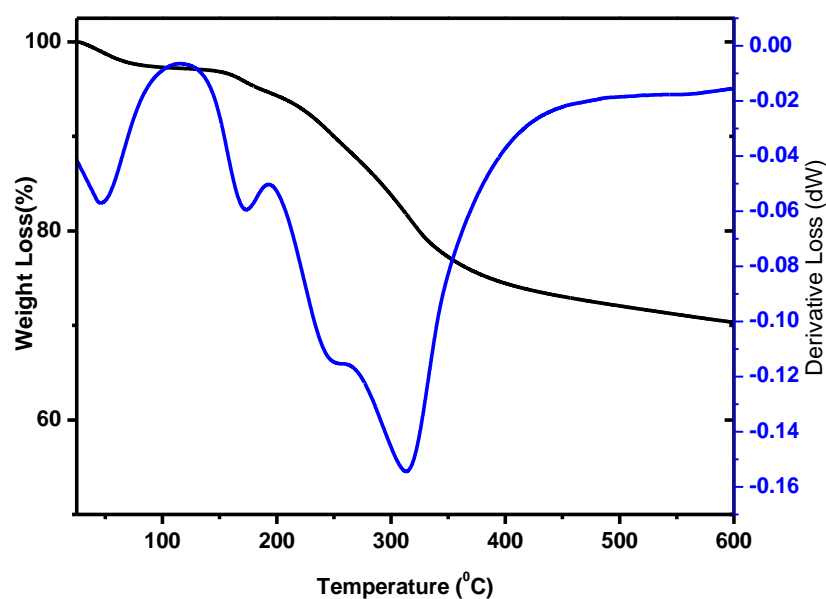


Figure 4.79: TGA and DTGA of AgNPs synthesized using *L. trifolia* extracts

These degradation stages were followed by subsequent changes in mass of the sample with a final mass loss of 28.9 % being observed. The decomposition occurring at 173 °C can be associated with the removal of the organic layer surrounding the nanoparticles which can also be linked to the decrease in the residual ash. The low percentage weight loss was as a result of present of silver nanoparticles in the residual ash as metallic species require extreme high temperature to be decomposed (Tao *et al.*, 2017).

4.7.8 SEM Micrographs of AgNPs

The morphology of AgNPs synthesized using *L. trifolia* are shown in plate 4.8. From SEM micrograph of AgNPs (Figure 4.80), it was observed that the particle appeared to be amorphous in nature. While green synthesis of metallic nanoparticle has in the

recent past obtained much attention due to their environmental friendliness, one major drawback of this approach is that the nanoparticles are usually amorphous in nature (Ahmed *et al.*, 2016).

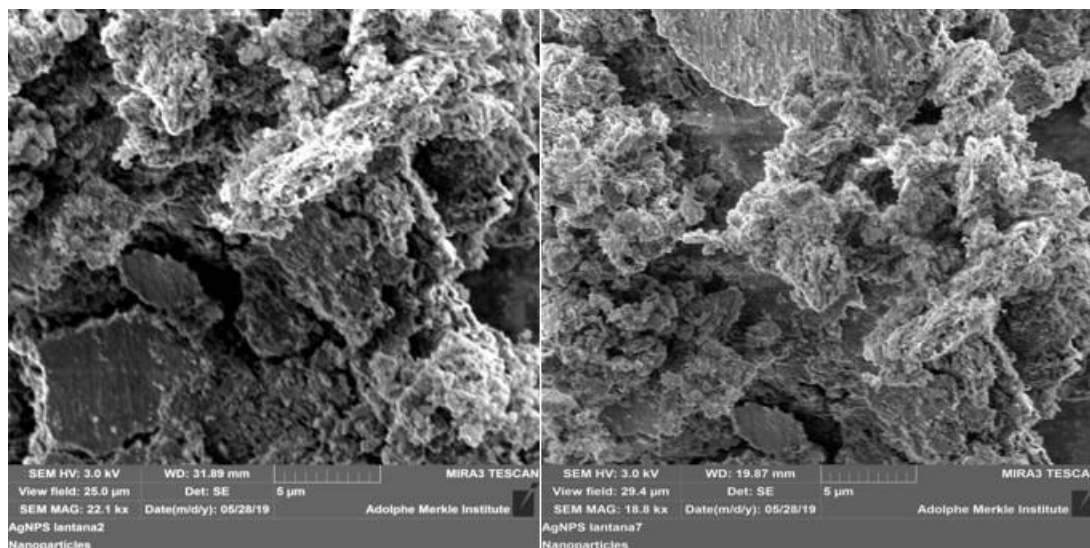


Plate 4.8: SEM Micrographs of AgNPS synthesized using *L. trifolia* extracts.

The amorphous nature of the nanoparticles is due to the presence of a secondary metabolite coating that surrounds the nanoparticles which prevents their reaction with species such OH^- present in the reaction media thereby preventing formation of metallic oxides. The organic coating surrounding AgNPs can also be accounted for in the IR spectra, in which, the presence of functional groups associated with secondary metabolites were also observed (Chung *et al.*, 2016; Ahmed *et al.*, 2016).

4.7.9 Hydrodynamic Diameter, Zeta potential and Polydispersibility index of AgNps

The hydrodynamic diameters, zeta potential and polydispersibility index of AgNPs synthesized using *L. trifolia* are shown in figure 4.80. The results show that the average particle diameter in optimal conditions was in the range of 35-70 nm.

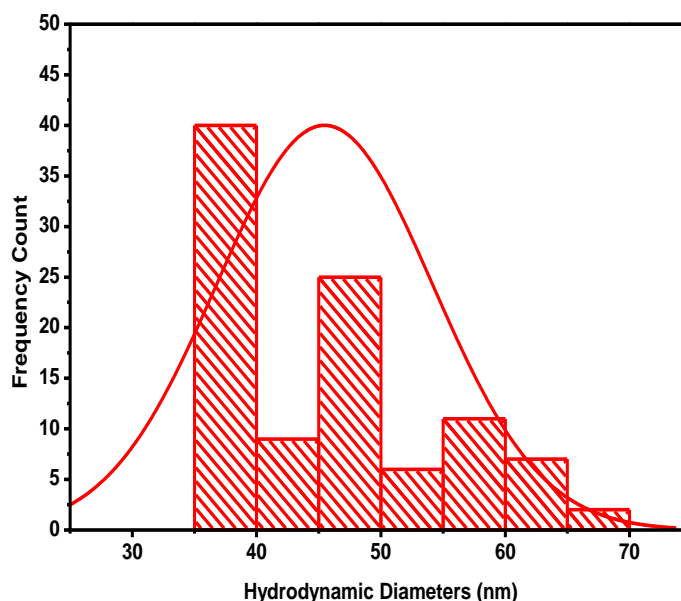


Figure 4.80: Particle diameter distribution of AgNPs synthesized at 35 °C

Table 4.16 shows the influence of temperature on the diameters of the nanoparticles synthesized using *L. trifolia*. From the results obtained (Table 4.16), different temperature resulted in different size of the nanoparticles, zeta potential and polydispersibility index of the resultant nanoparticles.

Table 4.16: Hydrodynamic diameter, Zeta potential and Poly-dispersibility index (PDI) of AgNps

Sample	Hydrodynamic Diameters (nm)	Zeta potential (mV)	PDI
T20	94.5±4.4	-21.1 ± 1.9	0.5708±0.00
T25	64.8±4.9	-20.5 ± 2.7	0.5708±0.00
T30	75.0±3.5	-19.1 ± 2.8	0.5551±0.00
T35	71.2±1.4	-22.4 ± 1.2	0.5658±0.00

From table 4.16, the size of AgNPs synthesized at 35, 30, 25, 20 °C were found to be 71.2±1.4, 75.0±3.5, 64.8±4.9 and 94.5±4.4 nm which implied that increase in temperature resulted in a subsequent decrease in the size of AgNPs. It has been reported that the size and shape of AgNPs could be influenced by the reaction temperature which is one of the major factors that is considered when studying chemical reactions (Jiang *et al.*, 2011). The hydrodynamic diameter is the diameter of

the particle, plus ions or molecules that are attached to the surface and moves with the AgNPs in solution. It was concluded that the size of the synthesized nanoparticles was influenced by the temperature of the reaction media during synthesis and the high polydispersibility index indicated that the particles were stable in solution (Jiang *et al.*, 2011).

4.7.10 TEM Micrographs of AgNPs

TEM micrographs and size distribution of green synthesized AgNPs are shown in figure 3.98. From figure 4.81, it was observed that, under optimal reaction conditions, AgNPs were spherical in nature with variable sizes ranging between 5 - 70 nm in diameter (Keshari *et al.*, 2018).

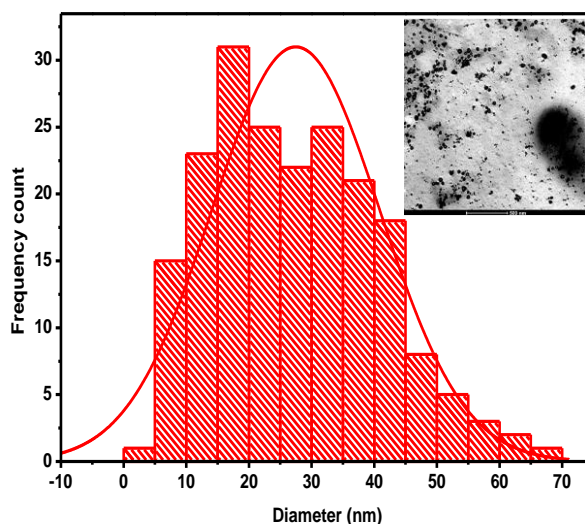


Figure 4.81: Size distribution of AgNPs synthesized using *L. trifolia* extracts. Inset TEM micrographs of AgNPs.

The size and shapes of nanoparticle is usually determined by the reaction conditions involved during synthesis, the choice of the reducing agent and the presence or absence of capping agents. While most nanoparticle are stable in the reaction media, they tend to agglomerate during drying hence the need of capping and stabilizing agents (Cai *et al.*, 2013; Kulkarni *et al.*, 2017). Various authors have used different capping and stabilizing agents, but secondary metabolites present in plant extracts

have been reported to be efficient and less toxic especially when the nanoparticles are to be used for medical applications (Ahmed *et al.*, 2016; Chung *et al.*, 2016). In our case, secondary metabolites present in *L. trifolia* extracts were used as the stabilizing agents though the exact secondary metabolite used as the capping agent could not be reported due to the wide array of metabolites present in plant extracts. While this might seem as a drawback, presence of secondary metabolites coating on nanoparticles not only serves as a capping and stabilizing agent, but they have been reported to enhance the antimicrobial activity of the synthesized nanoparticles (Mittal *et al.*, 2013). This coating not only reduced the chances of agglomeration of the nanoparticles as observed from zeta potential results, but they also afforded the spherical shape of the nanoparticles as observed from TEM micrographs.

4.7.11 Redox Potential of AgNPs

Figure 4.82 represent the cyclic voltammograms of AgNPs synthesized using *L. trifolia* extracts and it shows their redox potential. From figure 4.82, it follows that the most important parameters are the peak potential and the peak current. The cyclic voltammograms gave an anodic (positive) peak at 159 mV, which correspond to the total oxidation potential of AgNPs (Jara-Palacios *et al.*, 2017).

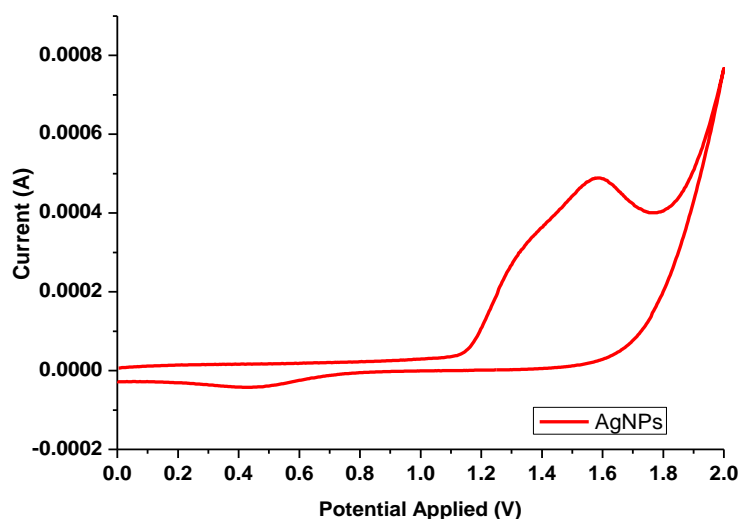


Figure 4.82: Cyclic voltammogram of AgNPs synthesized using *L. trifolia* extracts.

The peak potential correlates with the type of reductant; low oxidation potentials are associated with a greater facility or strength of a given molecule for the electron donation and, thus, act as an antioxidant; peak current is directly proportional to the antioxidant concentration. The total reducing power is defined as the ability of certain molecules to act as electron donors or protons receptors in oxidation-reduction reactions (Hoyos-Arbeláez *et al.*, 2017; Fitzmaurice *et al.*, 2011).

4.7.12 *In-vitro* Antimicrobial Activity of AgNPs

The antimicrobial activity of the synthesized nanoparticles against selected microorganisms was evaluated and the results are shown in figure 4.83 and plate 4.9. From figure 4.83, the synthesized AgNPs were more potent on Gram-positive bacteria *S. aureus* as compared to Gram-negative bacteria *E. coli* and *P. aeruginosa*, Gram-negative bacteria *B. subtilis* and the fungal strain *C. albicans*.

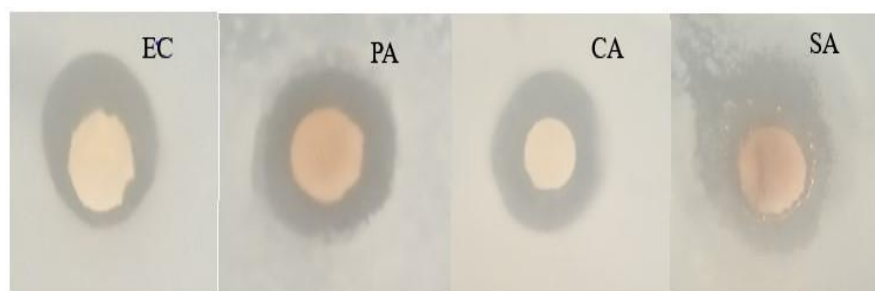


Plate 4.9: Antimicrobial activity of AgNPs against selected microorganisms

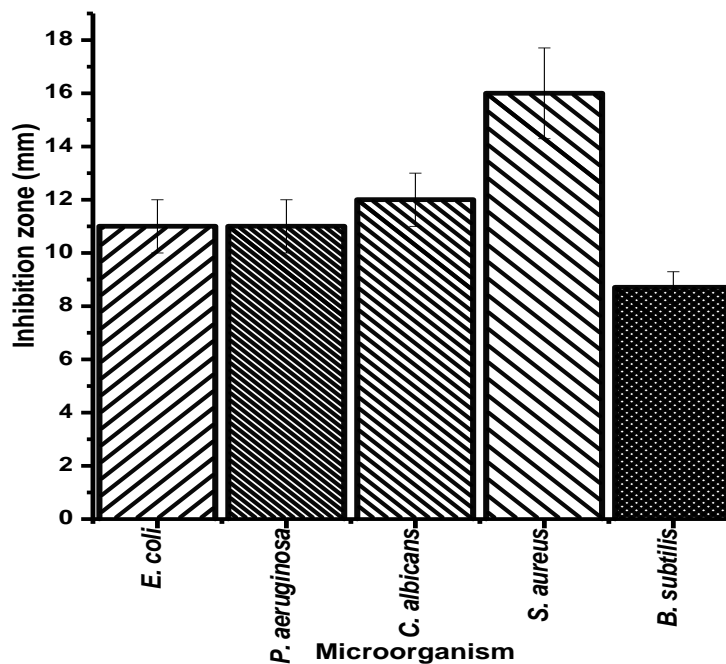


Figure 4.83: Zones of inhibition of AgNPs against *E. coli*, *P. aeruginosa*, *S. aureus*, *C. albicans*, and *B. subtilis*

The zones of inhibition were highest in *S. aureus* followed by *C. albicans*, *E. coli* and *P. aeruginosa* and lowest in *B. subtilis* (Figure 4.83). When compared with standard antibiotics, AgNPs had activity against all the microorganisms under study while the standard antibiotics had selective antimicrobial activity against test microorganisms (Appendix Z). It has been demonstrated that the antibacterial effect of AgNPs on Gram-negative bacteria is higher than on Gram-positive bacteria as a result of the thickness of cell wall. In Gram-positive bacteria, the cell wall thickness is 30 nm while in Gram-negative bacteria the cell wall thickness is between 3-4 nm and is mainly composed of peptidoglycan (Dakal *et al.*, 2016; Yun'an Qing, *et al.*, 2018). Due to this difference, Gram-negative bacteria are more susceptible to AgNPs which are able to anchor themselves on bacteria cell wall, infiltrate it and thereby damaging the cell membrane leading to cellular content leakage and bacterial death (Yun'an Qing *et al.*, 2018; Khan *et al.*, 2020). The AgNPs were more potent on Gram-negative bacteria *E. coli* and *P. aeruginosa* as compared to the Gram-positive bacteria *B. subtilis*. However, when compared to the Gram-positive bacteria *S. aureus*, AgNPs had higher

potency to this strain of bacteria as compared to the Gram-negative bacteria that were studied. The antimicrobial and antifungal activity of biosynthetic NPs such as AgNPs can be explained in terms of reactive oxygen species and it can be enhanced by capping agents attached to the NP during the biosynthesis process (Khan *et al.*, 2020).

4.8 Development of Cellulose Chitosan Composite Films

4.8.1 Effect of Glycerine Content on TOCNF-DAC-CS Film Properties

The effect of glycerine content on the thickness, transparency, swelling and water solubility of TOCNF-DAC-CS films were investigated, and the results are shown in figure 4.84 and table 3.19. Glycerol was used as the plasticizer of choice and its effect on optical transparency, tensile strength, solubility, swelling, and thickness of the films were studied. From figure 4.84, the optical properties of TOCNF-DAC-CS films were greatly influenced by the glycerine content used in the composite films as at low and high glycerine content (0.5 and 2.5%), the films were able to absorb 90% of UV-vis radiation above 400 nm. At a glycerine content of 1 %, 80% of the incident radiation above 400 nm was absorbed by the composite films while the amount of radiation below 400 nm that was absorbed was even higher.

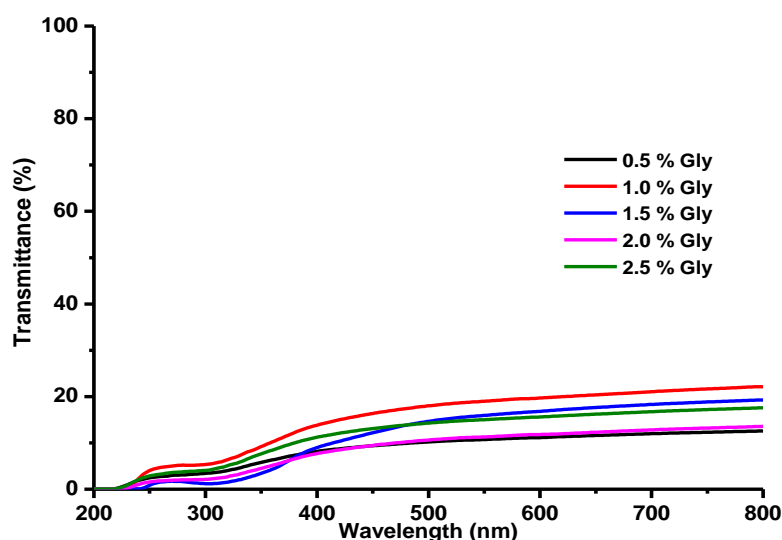


Figure 4.84: Transparency of TOCNF-DAC-CS films with different glycerin content

Moreover, the amount of radiation in the UV region that was absorbed by the films was even higher as compared to the amount of radiation absorbed in the visible range of the spectrum.

Table 4.17 shows the influence of glycerine content on the thickness, solubility and swelling of the composite films. It was observed that an increase in the glycerol content resulted in an increase in the solubility but a decrease in the transparency of the films with the film thickness and swelling having little or no change (Farahnaky *et al.*, 2013). This observation is as a result of little interaction between polymer chains which decreases the stiffness but increases the flexibility of the composite.

Table 4.17: Effect of glycerin (Gly) content weight, thickness, solubility and swelling of TOCNF-DAC-CS films

Gly (%)	Wt (g)	Thickness(μM)	A_{600 nm}	Solubility (%)	Swelling (%)
0.5	3.27	11 \pm 1.7	1.4494	52.1 \pm 1.0	37.0 \pm 2.7
1	3.49	13 \pm 1.3	0.7059	46.3 \pm 5.3	38.8 \pm 1.8
1.5	3.60	11 \pm 1.7	0.7747	53.3 \pm 0.7	40.0 \pm 0.5
2	4.42	15 \pm 0.8	0.9278	62.5 \pm 2.0	36.8 \pm 4.9
2.5	4.82	16 \pm 1.7	0.8070	68.4 \pm 1.0	37.1 \pm 1.0

Water solubility of the films is an important parameter which can be used to evaluate the release of encapsulated additives embedded within a composite matrix to enable it function as a slow-release device (Wang & Copeland, 2012; Thai *et al.*, 2020). A high glycerol content reduced hydrogen bond interaction between the polymer matrix which in turn reduced the cohesiveness of the cellulose chitosan matrix but increased their interaction with water molecules thereby increasing film solubility in water (Farahnaky *et al.*, 2013). It is worth noting that chitosan can be able to form films through dissolution in citric acid and solvent casting of the polymer solution. By joining the polymer through chemical cross-linking with citric acid, a measure of rigidity is imparted to the films that are subsequently formed upon casting. In addition to the cross-links, the molecules have extensive intra- and intermolecular hydrogen-bonding, which also effects a form of cross-linking, albeit a weak one. Hence addition of glycerol as a plasticizer reduces the intra and intermolecular interactions thereby reducing the rigidity of the polymer especially when TOCNF-DAC is added to the

matrix to form composite films (Gilbert & Martin, 2016). Glycerine is a hydrophilic plasticizer that is used to either limit covalent crosslinking or to change the pH of the solution and directly act on the hydrophilic and hydrophobic interactions between polymers (Vicente *et al.*, 2011). The efficiency of a plasticizers is the result of a complex interplay between these interactions, and as such it is highly dependent on the type of polymer. A wide range of plasticizers ranging from hydrophilic (water, glycerol, sorbitol) to hydrophobic (phthalates) have been successfully tested with glycerol reported to be the most preferred because of its sweet-taste, low toxicity, strong moisture-holding ability and its ability to improve the mechanical properties of biocomposite films (Audic & Chaufer, 2005; Farahnaky *et al.*, 2013; Stevens and Poliks, 2003). Statistical analysis of the data obtained revealed that there was a statistically significant difference ($p \leq 0.05$) in the solubility of TOCNF-DAC-CS films when the plasticizer content was varied. ANOVA showed that when the glycerine content was varied the solubility of the films changed significantly, $F(4,5) = 12.73$ $P = 7.83E-3$ (Appendix AA). But this variation in the plasticizer content did not have any significant difference on the swelling capacity of the films $F(4,5) = 0.5110$ $P = 7.35E1$ when the glycerine content was varied (Appendix BB).

4.8.2 Effect of Silver Concentration on TOCNF-DAC-CS Film Properties

Figure 4.85 show the formation of the plasmon resonance pink of silver when TOCNF-DAC was added to a solution of silver ion in chitosan. Upon addition of TOCNF-DAC on chitosan silver nitrate solution, the solution was left standing to allow the reduction of Ag^+ to AgNPs which occurred due to presence of COOH and C=O within the cellulose matrix. This reduction was observed from the change in colour of the solution from a clear solution to slightly brick red solution and from the UV spectrum resultant films (Figure 4.85).

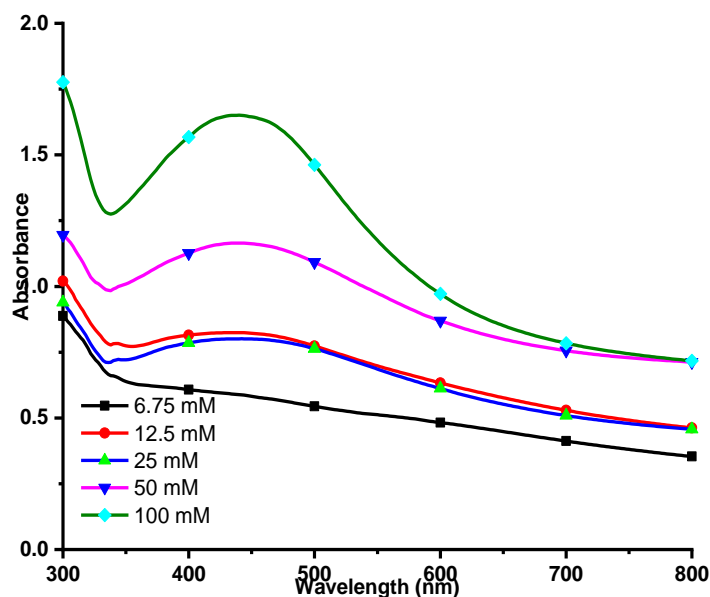


Figure 4.85: Plasmon resonance peak of AgNPs in TOCNF-DAC-CS-AgNPs films prepared with different Ag⁺ (6.75 -100 mM).

The plasmon resonance peak of AgNPs was also observed when the concentration of the oxidant in the films was increased from 6.75 mM to 100 mM (Rhim & Wang, 2014). This was attributed to the fact that an increase in silver ions in solution resulted in formation of more of AgNPs during the interaction of silver ion with TOCNF-DAC.

Plate 4.10 depicts the composite films made using different amounts of silver ions in solution that were reduced to silver nanoparticles. It was observed that the increase in the concentration of silver ions in solution resulted to films which were more translucent as compared to films that didn't contain AgNPs.

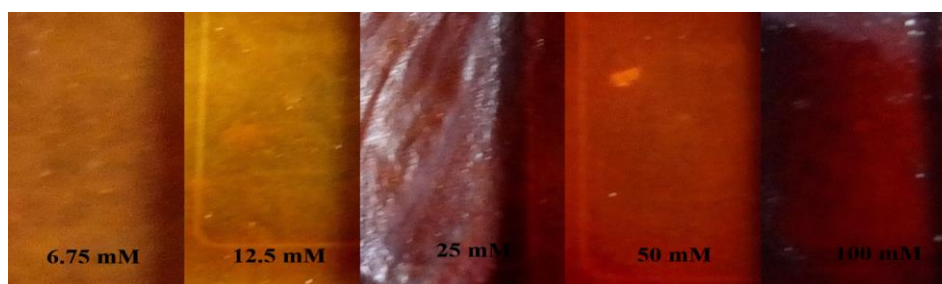


Plate 4.10: Nanocomposite films prepared using different concentration of Ag ions.

Figure 4.86 depicts the effect of AgNPs on the optical transparency of the composite films. This reduction of Ag^+ to AgNPs within the TOCNF-DAC-CS solution also altered the optical properties of the developed films as it was observed that the amount of Uv radiation that could pass through the films decreased (Figure 4.86).

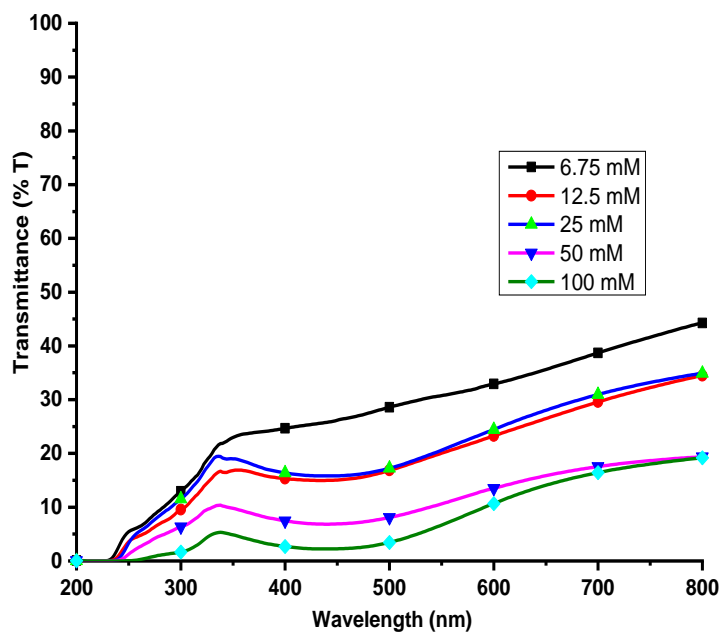


Figure 4.86: Optical transparency of TOCNF-DAC-CS-AgNPs composite films with different AgNPs content

The observed decrease was attributed to the presence of AgNPs within the polymer matrix which were effective in shielding the passage of the Uv radiation through the films hence working as Uv blockers (Jamroz *et al.*, 2019). Normally, inorganic fillers and additives are bound together with a polymer matrix to form the composite biopolymer. A wide variety of fillers in different forms such as spheroidal, fibrous, or porous have been reported to enhance the performance of nanocomposites when they are incorporated within the polymer matrix (Sudhakar *et al.*, 2018; Rhim & Wang, 2014).

Table 4.18 shows the effect of variation of the concentration of Ag^+ ion used during in-situ synthesis AgNPs on the transparency, swelling, water solubility and tensile strength (ts) of TOCNF-DAC-CS-AgNPs films. The addition of AgNPs had a

pronounced effect on the solubility of the biocomposite films as it was observed that an increase in the AgNPs decreased the solubility of films (Table 4.18). The decrease in solubility was due to creation of stronger structures and bonds within the polymer matrix as a result of their interaction with AgNPs which results in the reduction in the hydrophilicity of the composite films (Akmaz *et al.*, 2013; Jamroz *et al.*, 2019).

Table 4.18: Influence of Ag⁺ ion concentration on the properties of TOCNF-DAC-CS-AgNPs films

[Ag ⁺] (mM)	Wt	Thickness	A _{600 nm}	Solubility (%)	Swelling (%)	Ts (kPa)
6.25	4.58	14.3±1.0	0.4825	78.8 ±0.6	110.6±4.4	8.3±1.13
12.5	4.23	13.3±1.2	0.6334	76.5±1.4	131.6±1.4	17.1±4.3
25	5.07	13.8±0.5	0.6121	74.5±1.3	50.9±2.7	19.7±3.5
50	3.52	14.3±0.5	0.8694	68.1±2.0	22.2±3.9	15.6±1.2
100	4.63	14±0.8	0.9717	65.6±1.6	21.1±4.7	8.7±2.5

This decrease can also be attributed to the fact that AgNPs have very low solubility compared to the polymer chains which reduces the hydrophilicity of the polymer matrix. On the other hand, incorporation of AgNPs within the polymer matrix improved the degree of swelling of the films, though this was dependent on the amount of AgNPs, as at higher concentrations the degree of swelling decreased. In general, the interaction of inorganic fillers with a polymer matrix can either increase or decrease the degree of swelling of the resultant films due to an increase or decrease of hydrogen bonding within the matrix (Jamroz *et al.*, 2019; Thai *et al.*, 2020). Statistical analysis of the data obtained revealed that there was a statistically significant difference ($p \leq 0.05$) in the swelling and solubility of TOCNF-DAC-CS-AgNPs films when the concentration of AgNPs was varied (Appendix CC). ANOVA showed that when the Ag ion concentration was varied the swelling capacity and the solubility of the resultant composite films changed significantly, $F(4,5) = 396.17$ and 30.49 $P = 1.94E-6$ and $1.05E-3$, respectively (Appendix DD).

4.8.3 Effect of TOCNF-DAC Content on TOCNF-DAC-CS Film Properties

Plate 4.11 shows differences in flexibility of films prepared using chitosan, TOCNF and TOCNF-CMCS-AgNPs. From plate 4.11, raw CMCS and TOCNF films were brittle and rigid while TOCNF-DAC-CMCS and TOCNF-DAC-CS films were

flexible and could easily be folded without breaking the films. The addition of glycerol as a plasticizer increased the mobility because it decreased the intermolecular forces in the polymer chain thereby increasing the flexibility of the composite films. Moreover, the mechanical properties of chitosan films are influenced by the chemical composition of chitosan where the elasticity and stiffness of the resulting network are dependent on the content of glucosamine and N-acetyl-glucosamine units (Afonso *et al.*, 2019).



Plate 4.11: Raw CMCS (A), TOCNF-DAC (B), and TOCNF-CMCS-AgNPs (C), TOCNF-DAC-CS films

The preparation of biodegradable films must include at least one biopolymer that could form a suitable cohesive and continuous matrix. Generally, these films are prepared either by solubilizing the polymer in a suitable solvent followed by solvent casting or through utilization of the thermo plastic properties of the biopolymer at low moisture conditions (Sudhakar *et al.*, 2018; Yang *et al.*, 2018; Wang & Copeland, 2012).

Table 4.19 depicts the effect of TOCNF-DAC content on the wettability, thickness, transparency, and mechanical properties of TOCNF-DAC-CS-AgNPs composite films. Increasing the TOCNF-DAC content improved the mechanical properties of the films, but it decreased the swelling capacity of the films. This was attributed to the increased hydrogen bond interaction between the surface hydroxyl groups of the two polymers that led to formation of a 3D network (Miller-Chou & Koenig, 2003). This interaction reduces the likelihood of hydrogen bond interactions between surface hydroxyl groups and water molecules hence a reduction in the amount of water absorbed by the composite films. It was also observed that increasing the TOCNF-

DAC content in the matrix increased the solubility of composite films as films with higher TOCNF-DAC content were more soluble in water (Table 4.19).

Table 4.19: Effect of TONCF-DAC content in TOCNF-DAC-CS films on swelling ratio, wettability and tensile strength (ts) of TOCNF-DAC-CS films

TOCNF (%)	Wt	Thickness	A _{600 nm}	Solubility (%)	Swelling (%)	ts (kPa)
10	4.25	14.3±1.0	1.8	54.8±2.6	29.9±1.1	4.9±0.2
20	4.2	16.25±1.0	2.18	58.8±2.3	26.8±4.1	4.5±1.4
30	4.94	15.5±0.6	2.78	71.6±0.2	22.8±3.8	9.1±0.8
40	4.96	17.5±0.7	2.49	75.5±3.5	19.9±5.9	5.8±0.5
50	5.16	17.5±0.6	2.41	66.6±2.9	16.8±2.6	4.1±0.5

Moreover, increase in solubility may lead to a subsequent increase in the amount of AgNPs that diffuse from the composite films which implies that more AgNPs could diffuse from the composite films into the surrounding environment. This in turn would increase the amount of AgNPs that would be released on the wound environment thereby limiting the growth and proliferation of microorganism during wound healing. Solubility of polymers are influenced by any specific interactions, especially H-bonds, polymer morphology (crystallinity), cross-linking, and changes in temperature (Miller-Chou & Koenig, 2003; Wang & Copeland, 2012; Jamroz *et al.*, 2019). The decrease in swelling capacity and increase in solubility were attributed to the disruption of side chains of the two polymers as at higher TOCNF-DAC content the degree of crosslinking between TOCNF-DAC and CS also increased (Wang & Copeland, 2012). This increase in hydrogen bond interaction between surface hydroxyl groups present in TOCNF-DAC and those present in CS between the two polymers has been reported to be responsible for the reduction in the swelling capacity of the nanocomposite films (Jamroz, *et al.*, 2019). Moreover, because the deprotonation or protonation of hydroxyl groups in cellulose requires either an extremely high or an extremely low pH, the swelling in TOCNF-DAC is usually attributed to the ionization of a small number of carboxylic acid groups as well as to capillary water uptake by the pores in the film (Afonso *et al.*, 2019).

It was also observed that the tensile strength of the films was dependent on the nature and composition of the solutions used during solvent casting (Table 4.19). As such an

increase in the TOCNF content in the composite matrix was expected to increase the tensile strength of the resultant polymer but an increase in the TOCNF content above 30% of the polymer solution reduced the tensile strength of the resultant composite. At a TOCNF content between 10-30 %, the tensile strength gradually increased but above 30% the tensile strength gradually dropped. Since cellulose required extreme or even harsh reaction conditions for it to dissolve, chitosan was used as the matrix and cellulose as a reinforcing element within the polymer matrix. Presence of carbonyl functional groups in cellulose ensured that the two polymers underwent chemical crosslinking during curing to form the composite films embedded with CNF. By joining strands of the polymer through such cross-links, a measure of rigidity is imparted to the molecular array that has been formed. In addition to the cross-links, the molecules have extensive intra- and intermolecular hydrogen-bonding, which also effects a form of cross-linking, albeit a weak one. Statistical analysis of the data obtained revealed that there was a statistically significant difference ($p \leq 0.05$) in the swelling of TOCNF-DAC-CS-AgNPs composite films when the TOCNF-DAC content was varied. ANOVA showed that when the TOCNF content of the composite films was varied the swelling capacity of resultant films varied significantly, $F(4,10) = 16.28$ $P = 2.23E-4$ (Appendix EE). These variations also had a pronounced effect on the solubility of the films as ANOVA showed that the solubility of the resultant films was significantly different, $F(4, 5) = 22.03$ $P = 2.25E-4$ (Appendix FF).

4.8.4 Biodegradability Studies of TOCNF-DAC-CS Films

The percent degradation of the composite films as a function of number of days was evaluated and the results are shown in figure 4.87. It was observed that the percent degradation of the composite films increased with an increase in the number of days in which the samples were covered in soil.

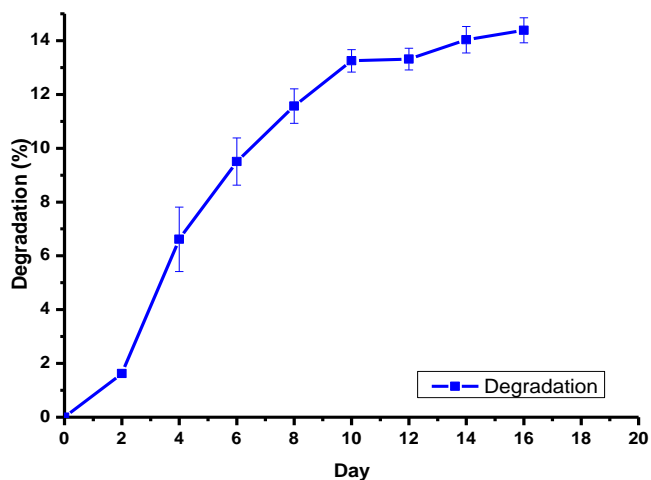


Figure 4.87: Degradation of TOCNF-DAC-CS-AgNPs films as a function of number of days

The degradation of composite films is influenced by various factors such as light, moisture content and presence of soil microorganism which are responsible in breaking down the macromolecular structure into simple compounds (Stevens & Poliks, 2003). As a result of this, it is worth mentioning that due to these factors, the rate of degradation was hampered due to the challenges involved with maintaining the necessary conditions that are required to aid in the degradation. The term biodegradation is often used to describe the process that leads to a general damage of a material, and it is related to terms such as ecology, waste management, environment and of course plastic, due to their long-life duration. This process is often triggered by microorganisms such as bacteria and fungi that are present in the soil and can break down the macromolecular chains (Stevens & Poliks, 2003). This process is largely influenced by environmental conditions such as light, heat, moisture, temperature and polymer characteristics such crystallinity, molecular weight, plasticizers or additives, chain mobility, type of functional groups and substituents present in the polymer matrix (Siracusa, 2019).

4.8.5 FTIR Characterization of Cellulose Chitosan Composite Films

The functional groups present in TOCNF-DAC-CMCS, TOCNF-DAC-CMCS-AgNPs, TOCNF-DAC-CS and TOCNF-DAC-CS-AgNPs were evaluated using FT-

IR and the results are shown in figure 4.88. When compared to DAC and TOCNF which had distinct C=O vibrational frequency at around 1700 cm^{-1} , TOCNF-DAC-CMCS films composed of OH vibrational frequency at 3400 cm^{-1} , CH₂ bending at 2900 cm^{-1} and C-O-C vibration at 1052 cm^{-1} (Figure 4.88). Absence of C=O vibrational peak at 1700 cm^{-1} was an indication that Schiff's base reaction between carbonyl groups present cellulose nanofibrils and the amine groups present in chitosan had occurred.

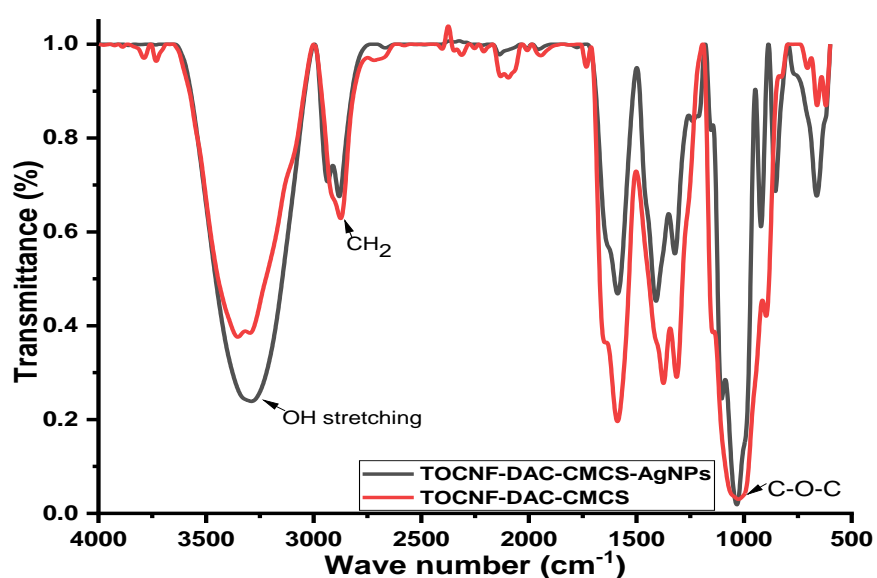


Figure 4.88: FT-IR Spectra of TOCNF-DAC-CMCS and TOCNF-DAC-CMCS Composites

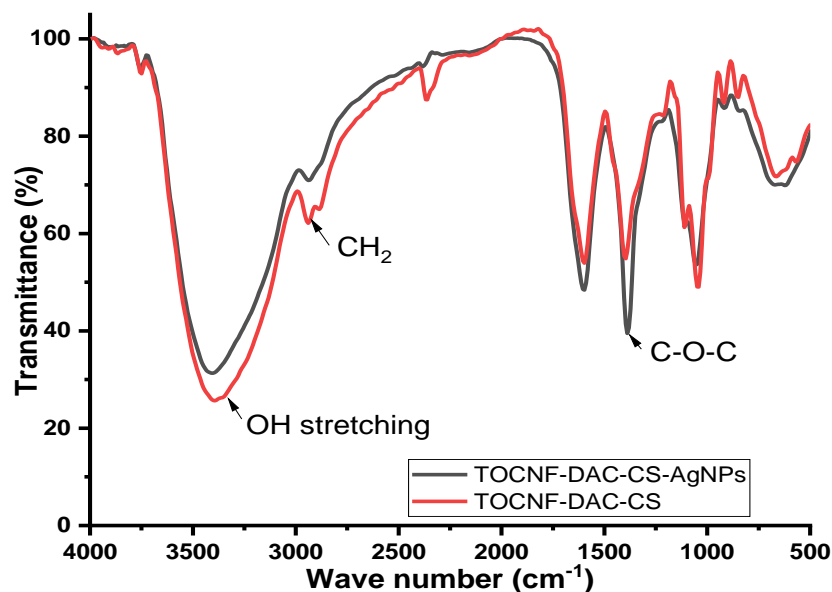


Figure 4.89: FT-IR Spectra of TOCNF-DAC-CS and TOCNF-DAC-CS-AgNPs composite films

TOCNF-DAC and CMCS undergoes Schiff's base reaction forming imines with a weak C=N stretching vibration occurring in the region $1690\text{-}1620\text{ cm}^{-1}$ (Socrates, 2004; Ouellette & Rawn, 2019). This band for $\text{RHC}=\text{N-R}_2$ was observed in TOCNF-DAC-CMCS to be at 1600 cm^{-1} and was thus an indication that reaction between TOCNF-DAC and CMCS could have occurred through a Schiff's base reaction between the amine and the carbonyl groups present in the two polymers. Previous studies, however, have suggested that the imine band at $1,610\text{ cm}^{-1}$ may represent the stretching vibrations of the C=N bond formed in Schiff's base reaction between aldehyde and chitosan. Although the crosslinked films had a new strong peak at approximately $1,600\text{ cm}^{-1}$, crosslinking could not be verified from the IR spectra due to possible overlap with amide I and unreacted -NH_2 stretching (Alam and Christopher, 2018). Moreover, because less energy is required to stretch a single bond than a double bond, any structural feature that stabilizes the contributing polar resonance form with a carbon-oxygen single bond will cause the infrared absorption to occur at lower wavenumber position. Thus, the nitrogen atom donates electrons to the carbonyl atom thereby decreasing the double bond character of the C=O group resulting in absorption at lower wavenumbers (Ouellette & Rawn, 2019). Presence of the C=O

band in the spectra was also an indication that not all aldehyde groups present in TOCNF-DAC participated in the Schiff's base reaction hence their presence in TOCNF-DAC-CMCS films¹ (Socrates, 2004). Bridging carbonyl compounds, in which a carbonyl group is associated with two metal atoms, absorb at 1900-1700 cm⁻¹, that is, at lower frequencies than those for terminal CO groups. As mentioned, most other carbonyl groups absorb above 1900 cm⁻¹ except in the case of complexes with strong electron-donor ligands or with a large negative charge. The in-plane bending vibration of the M-CO group of metal carbonyl compounds gives rise to strong intensity band at 790 - 275cm⁻¹ and the stretching vibration of the M-C group of these compounds gives a band of very-strong-to-medium intensity at 640 - 340cm⁻¹ (Socrates, 2004; Ouellette & Rawn, 2019).

4.8.6 X-ray Diffractogram of Cellulose Chitosan Composite Films

Figure 4.90 depicts the XRD diffractograms of TOCNF-CMCS composite films. It was observed that while TEMPO mediated oxidation increased the crystallinity of cellulose use of TOCNF as a reinforcing matrix in carboxymethyl chitosan decreased the crystallinity of the composites. From the results obtained, the crystalline peaks of cellulose which are normally centered at $2\theta = 16$ and 22° were nearly absent in TOCNF-CMCS composite.

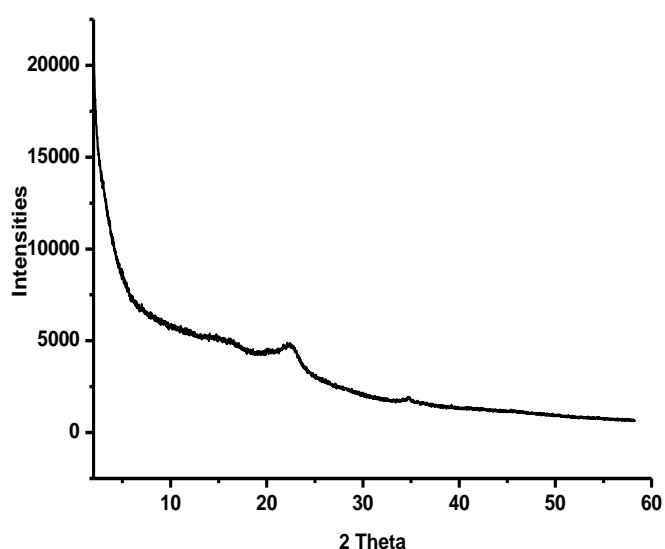


Figure 4.90: X-ray diffractogram of TOCNF-CMCS Composites

TOCNF-DAC-CS and TOCNF-DAC-CMCS composite a chitosan peak centered at $2\theta = 20^\circ$ was observed together with cellulose peak at $2\theta = 22^\circ$. The interaction between TOCNF and CS lead to changes in the crystal structure of the resulting films hence the disappearance of cellulose peak. On the other hand, the composite films were prepared using AgNO_3 solution, characteristic peaks associated with AgNPs/AgCl nanoparticles were observed as depicted in Figure 4.91-4.92. In the XRD diffractogram of TOCNF-CMCS-AgNPs,

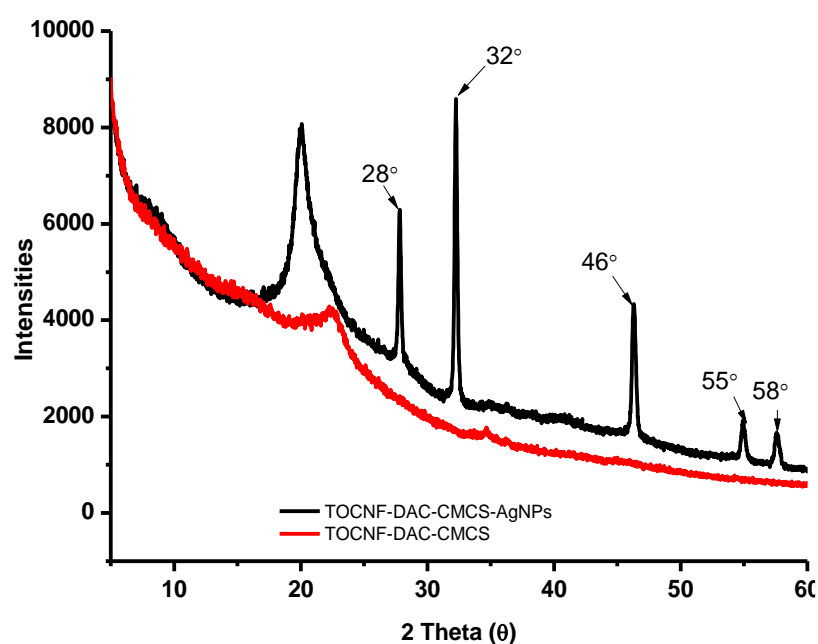


Figure 4.91: X-ray diffractogram of TOCNF-DAC-CMCS and TOCNF-DAC-CMCS-AgNPs Composites

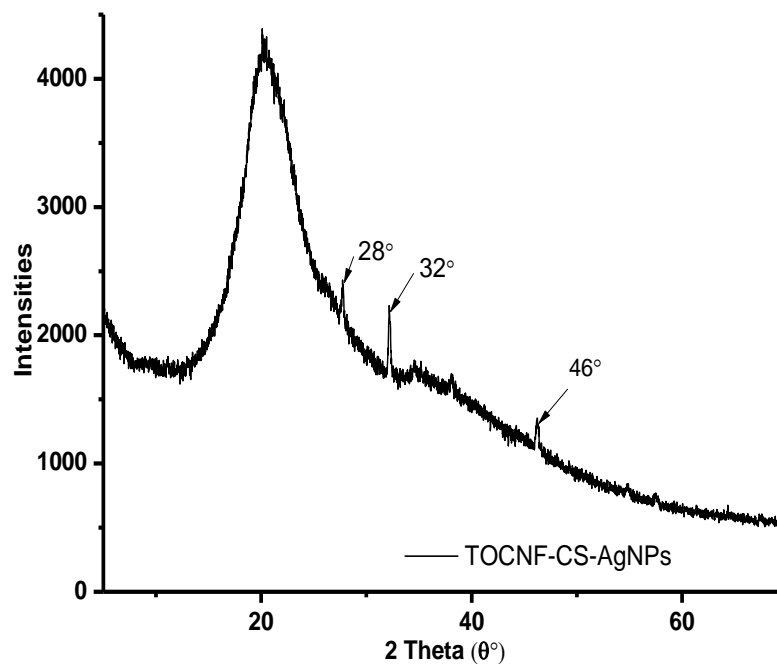


Figure 4.92: X-ray diffractogram of TOCNF-DAC-CS-AgNPs Composites

The presence of carbonyl and carboxylic groups on the polymer matrix led to a reduction of Ag^+ ions present in solution to AgNPs as sharp peaks associated with AgNPs were observed in the diffractogram of TOCNF-DAC-AgNPs and TOCNF-DAC-CMCS-AgNPs nanocomposite (Ito *et al.*, 2018). The sharp peaks at $2\theta = 28, 32, 38, 45, 55,$ and 59 are associated with AgNPs and they correspond to the silver crystal planes (111), (200), (220), and (311), respectively (Xu *et al.*, 2019; Ito *et al.*, 2018).

4.8.7 DSC Thermogram of Cellulose Chitosan Composite Films

DSC thermograms of TOCNF-DAC-CS, TOCNF-DAC-CS-AgNPs, TOCNF-DAC-CMCS and TOCNF-DAC-CMCS-AgNPs are shown in figure 4.93 – 4.97.

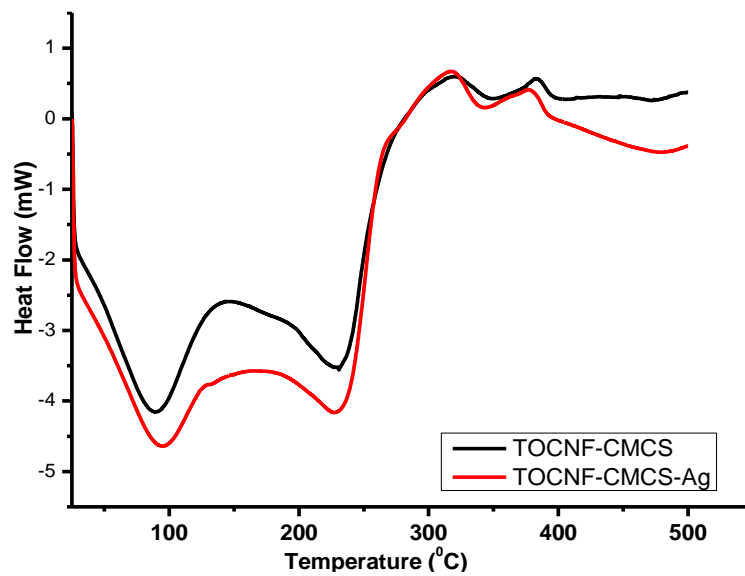


Figure 4.93: DSC thermogram of TOCNF-CMCS and TOCNF-CMCS Composites

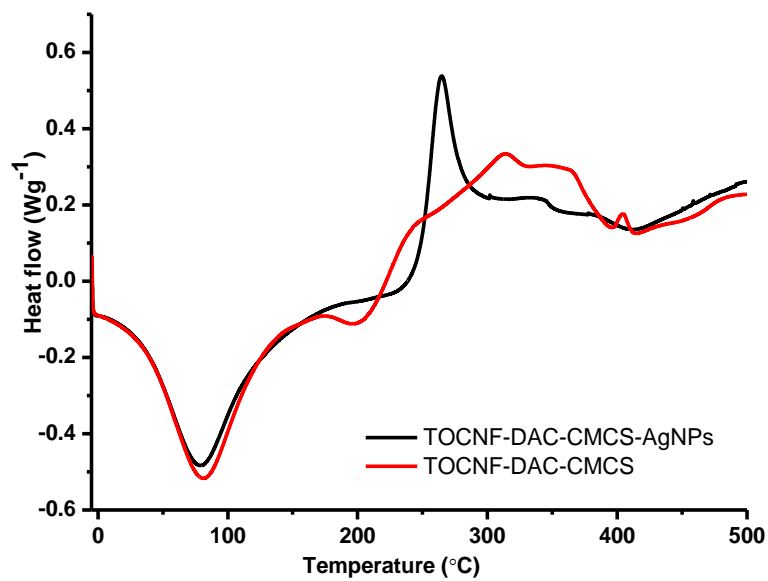


Figure 4.94: DSC thermogram of TOCNF-DAC-CMCS and TOCNF-DAC-CMCS-AgNPs Composite

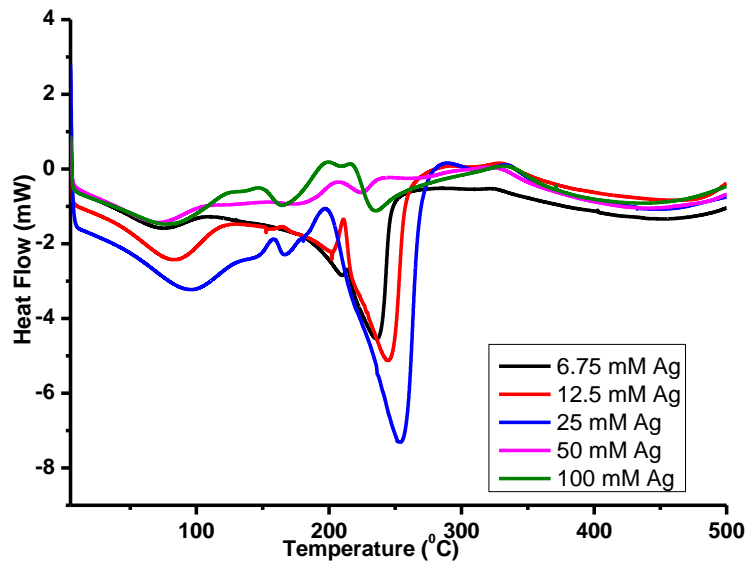


Figure 4.95: DSC thermogram of TOCNF-DAC-CS-AgNPs films with different AgNPs content

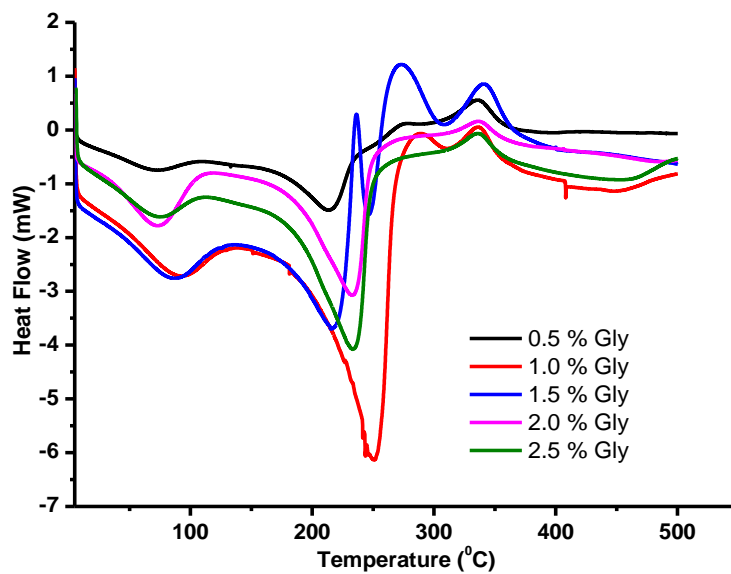


Figure 4.96: DSC thermogram of TOCNF-DAC-CS-AgNPs films with different glycerin (Gly) content

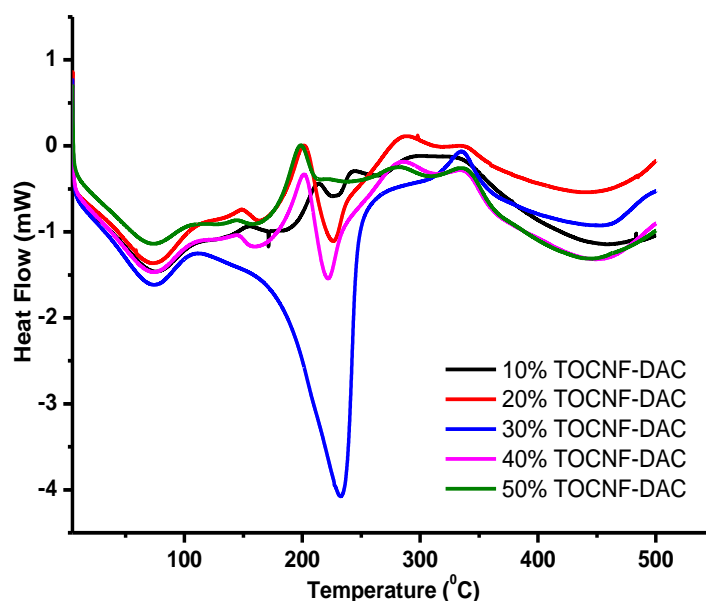


Figure 4.97: DSC thermogram of TOCNF-DAC-CS-AgNPs films with different TOCNF-DAC content

From figure 4.93 - 4.97, it can be observed that while TOCNF-CMCS and TOCNF-CMCS-AgNPs had two endothermic degradations centered at 95 °C and 228 °C, TOCNF-CMCS composite had one endothermic peak centred at 85 °C and an exothermic peak centred at 339 °C. The initial endothermic peak in both composite films can be attributed to water adsorbed on the surface of the films which has been reported to evaporate at this temperature. As for TOCNF-DAC-CMCS composite films, absence of cellulose degradation endothermic peak reported to occur between 230-350 °C can be attributed to changes in cellulose structure upon TOCNF-DAC oxidation which was observed earlier and has been reported. The reaction between TOCNF-DAC and CMCS can also be observed from the DSC thermograms of TOCNF-DAC-CMCS in which an exothermic peak associated with CS was observed at 265 °C while an endothermic peak associated with cellulose degradation was absent (Figure 4.97) (Szymańska-Chargot *et al.*, 2019).

4.8.8 TGA Thermograms of Cellulose Chitosan Composite Films

The influence of glycerin content on thermal stability were evaluated using TGA and results are depicted in figure 4.98. It was observed from the TGA/DTGA thermograms

that variation of glycerin content had little effect on the residual ash after thermal analysis but influence the thermal degradation temperature. From table 4.20, it can be observed that the onset degradation temperature was dependent on the glycerin content as a glycerin content of 1% the onset degradation temperature was found to be 181 °C. Increasing the glycerin content reduced the thermal degradation temperature are at higher glycerin content the degradation temperature reduced (Figure 4.98 - 4.99, Table 4.20).

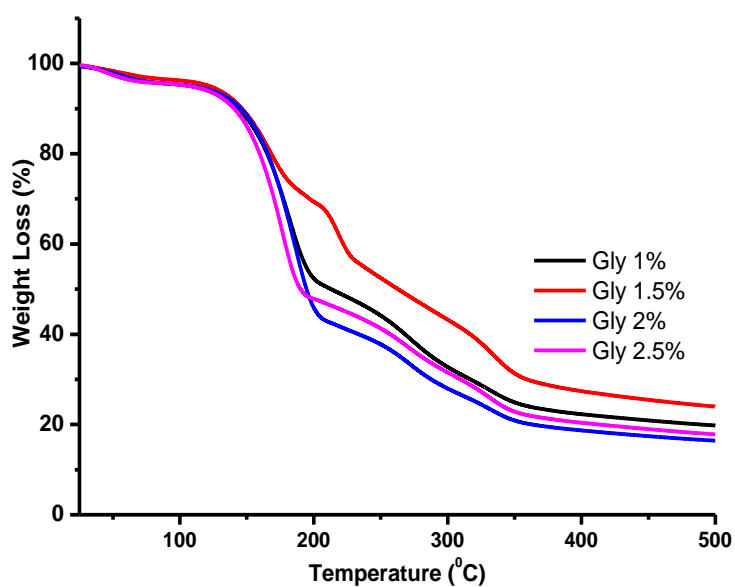


Figure 4.98: TGA thermograms of TOCNF-DAC-CS films with different Glycerin content

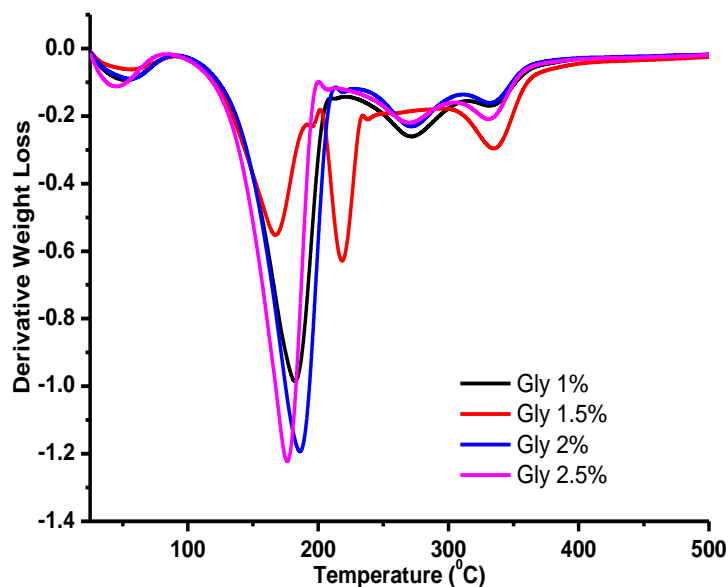


Figure 4.99: DTGA thermograms of DACNF-CS films with different Glycerin content

Table 4.20: Peak temperature and residual ash of composite films with different plasticizer content

Sample	T ₁ (°C)	T ₂ (°C)	T ₃ (°C)	T ₄ (°C)	Ash (%)
1.0 % Gly	55.0	181	273	333	20
1.5% Gly	55.0	168	218	336	24
2.0 % Gly	55.0	187	273	333	16
2.5 % Gly	42.5	177	273	333	18

Figure 4.98 - 4.99 depict the TGA/DTGA thermograms showing the influence of AgNPs content on the thermal degradation of the composite films as shown by their onset degradation temperatures. It was observed that an increase in the concentration of silver ions used during preparation of the composite films resulted in differences in the thermal profile of the resulting films. The first peak observed in all the composite films was attributed to evaporation of water from the composite films while the second peak present in all the samples and lied between 165-190 °C was associated with decomposition of cellulose nanofibers within the composite films. Pure glycerin has been reported to undergo pyrolysis around 255 °C hence the peak at 273 °C were linked to this process. The increase in the residual ash and the degradation temperature of

TOCNF-DAC-CS-AgNPs films were attributed to the presence of the metallic nanoparticles which acted as inorganic nanofillers (Ito *et al.*, 2018).

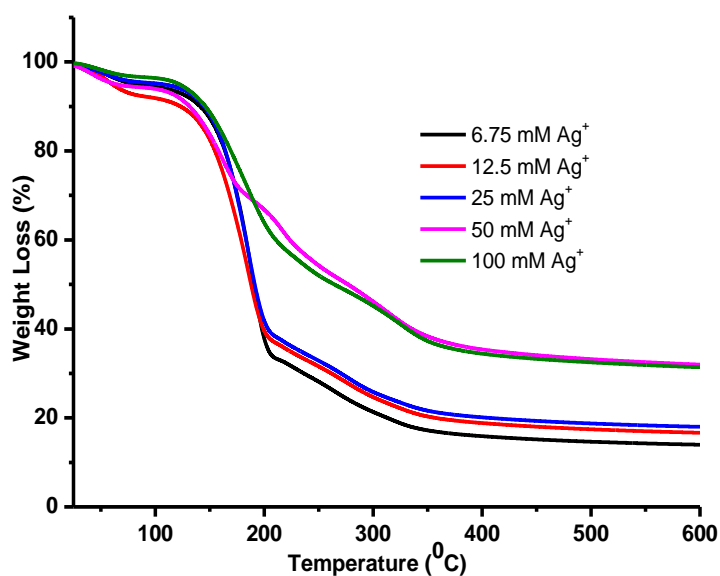


Figure 4.100: TGA thermograms of TOCNF-DAC-CS films with different AgNPs content

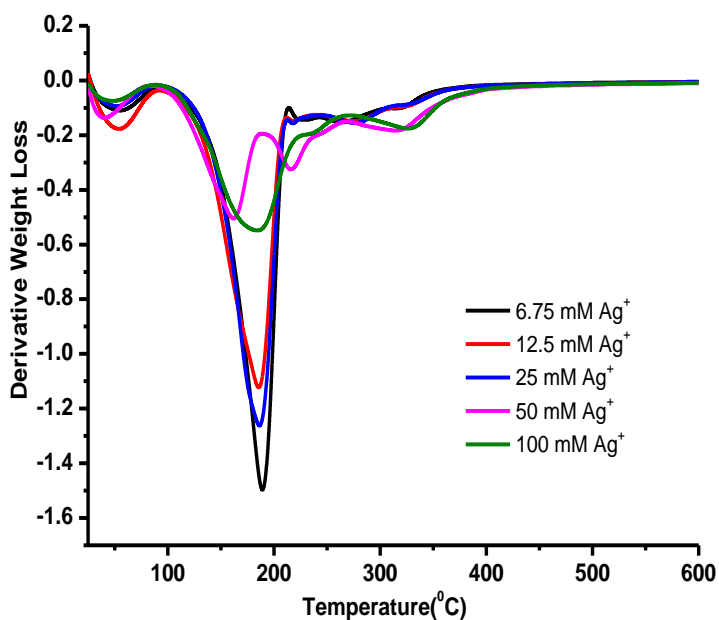


Figure 4.101: DTGA thermograms of TOCNF-DAC-CS films with different AgNPs content

Table 4.21: Peak temperature and residual ash of composite films with different AgNPs content

Sample	T ₁ (°C)	T ₂ (°C)	T ₃ (°C)	T ₄ (°C)	Ash (%)
6.75 Mm Ag ⁺	55	189	267	321	14.1
12.5 Mm Ag ⁺	52	186	274	321	16.4
25 Mm Ag ⁺	54	186	275	329	18.1
50 Mm Ag ⁺	39	162	217	316	32.1
100 Mm Ag ⁺	47	186	-	330	31.1

Moreover, the higher degradation temperature observed can be linked to AgNPs since inorganic nanofillers such as AgNPs have been reported to increase the mechanical, thermal, biological, physical and chemical properties of the resulting composite materials (Jamroz, *et al.*, 2019).

Figure 4.102 and 4.103 depicts the TGA/DTGA thermograms of composite films containing different TOCNF content with the films. From the thermograms obtained, all the composite films had four degradation cycles which are linked to evaporation methanol found in glycerin which occurs between 40 – 60 °C, degradation of cellulose and pyrolysis of glycerin that occurs at 250 °C.

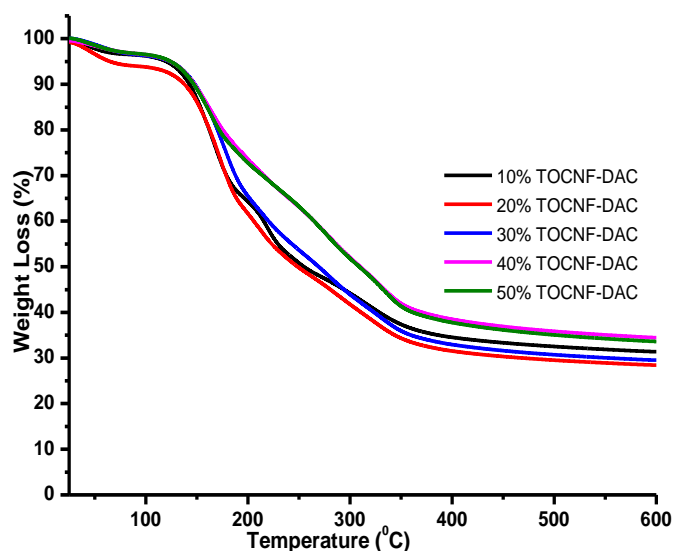


Figure 4.102: TGA thermograms of TOCNF-DAC-CS films with different TOCNF content

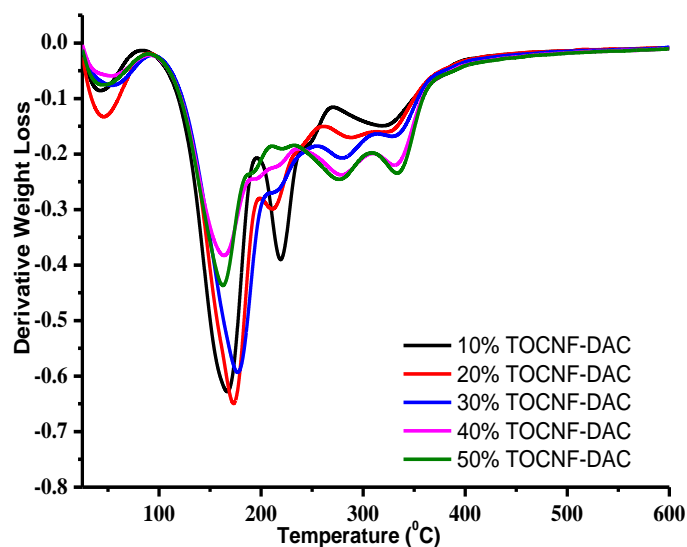


Figure 4.103: DTGA thermograms of TOCNF-DAC-CS films with different TOCNF content

Table 4.22: Peak temperature and residual ash of composite films with different TOCNF content

Sample	T ₁ (°C)	T ₂ (°C)	T ₃ (°C)	T ₄ (°C)	T ₅ (°C)	Ash (%)
10 % TOCNF	42	166	219	-	323	31
20 % TOCNF	46	172	212	289	329	28
30 % TOCNF	54	178	-	279	330	29
40 % TOCNF	50	162	-	280	333	35
50 % TOCNF	48	162	-	276	334	34

However, increase in TOCNF content in the composite films reduced the onset degradation temperature which starts at 120 °C with maximum degradation observed at 168 °C where maximum weight loss during thermal analysis was observed.

Figure 4.104 - 4.105 shows TGA/DTGA thermograms of TOCNF-DAC-CMCS, DACNF-CMCS-AgNPs composite films. From figure 4.107 - 4.108, the thermograms of TOCNF-DAC-CMCS, TOCNF-DAC-CMCS-AgNPs composite films revealed that TOCNF-CMCS had three degradation stages with an ash content of 34.7% while TOCNF-DAC-CMCS-AgNPs had two degradation stages with an ash content of 33.6%.

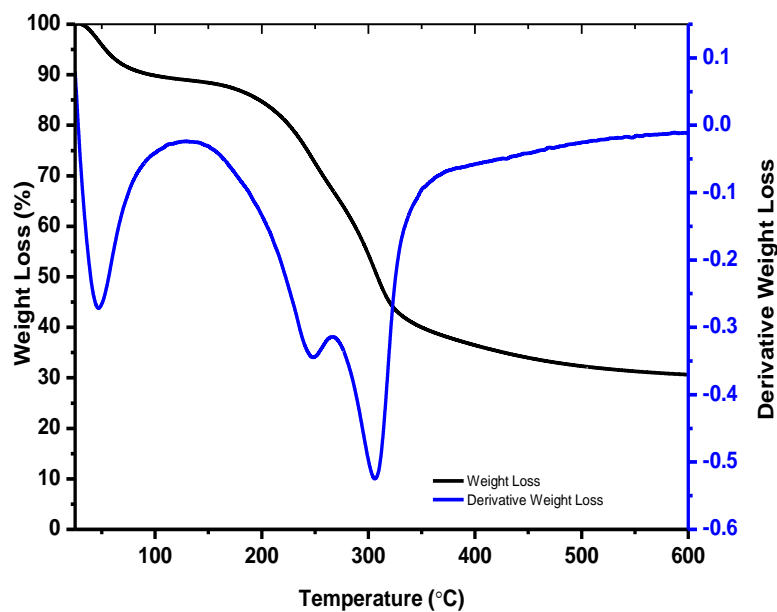


Figure 4.104: TGA and DTGA Thermogram of TOCNF-DAC-DAC-CMCS

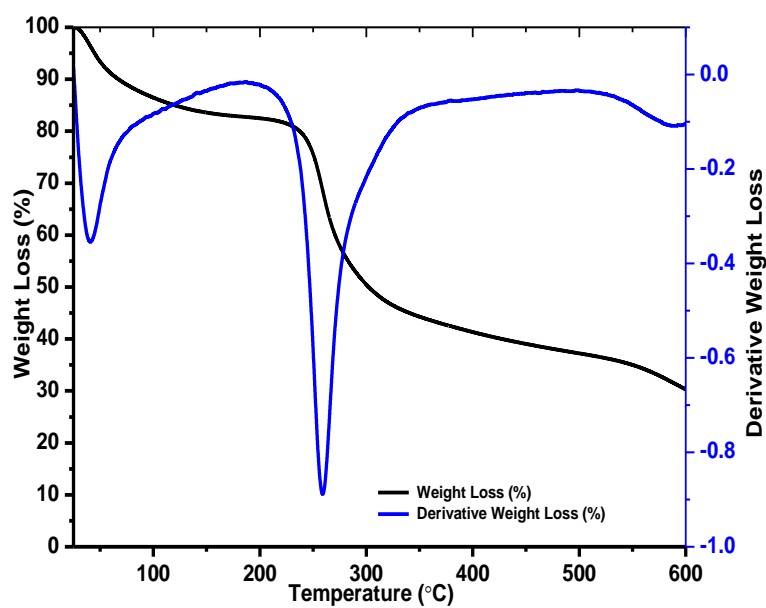


Figure 4.105: TGA and DTGA Thermogram of TOCNF-DAC-CMCS-AgNPs

Table 4.23: Peak temperature and residual ash of TOCNF-CMCS and TOCNF-CMCS-AgNPs

Sample	T ₁ (°C)	T ₂ (°C)	T ₃ (°C)	T ₄ (°C)	Ash (%)
TOCNF-CMCS	81.7	177.7	224.0	266.3	34.7
TOCNF-CMCS-AgNPs	81.7	249.2	-	-	33.6
TOCNF-DAC-CMCS	47.5	247.7	308.9	-	25.5
TOCNF-DAC-CMCS-AgNPs	40.2	259.5	-	-	30.3

On the other hand, TOCNF-DAC-CMCS composite films had two degradation stages with an ash content of 25.5% which was lower than for both TOCNF-CMCS and TOCNF-CMCS-AgNPs. Presence of AgNPs embedded within the TOCNF-CMCS composite films matrix was expected to increase the ash content of the films but in the current study this was not the case. However, the thermal stability and residual ash of TOCNF-CMCS-AgNPs increased as compared to neat films which had four degradation stages (Ghasemzadeh, *et al.*, 2016; Jamroz, *et al.*, 2019).

4.8.9 SEM Micrographs of Cellulose Chitosan Composite Films

The morphology of TOCNF-DAC-CMCS and TOCNF-DAC-CS-AgNPs were evaluated using SEM and the results are shown in plate 4.12-4.13. When compared to the micrographs of native cellulose, TOCNF, DAC, TOCNF-DAC, chitosan and carboxymethyl chitosan, micrographs of the composite before solvent casting appeared to be porous with fibers intertwined within themselves.

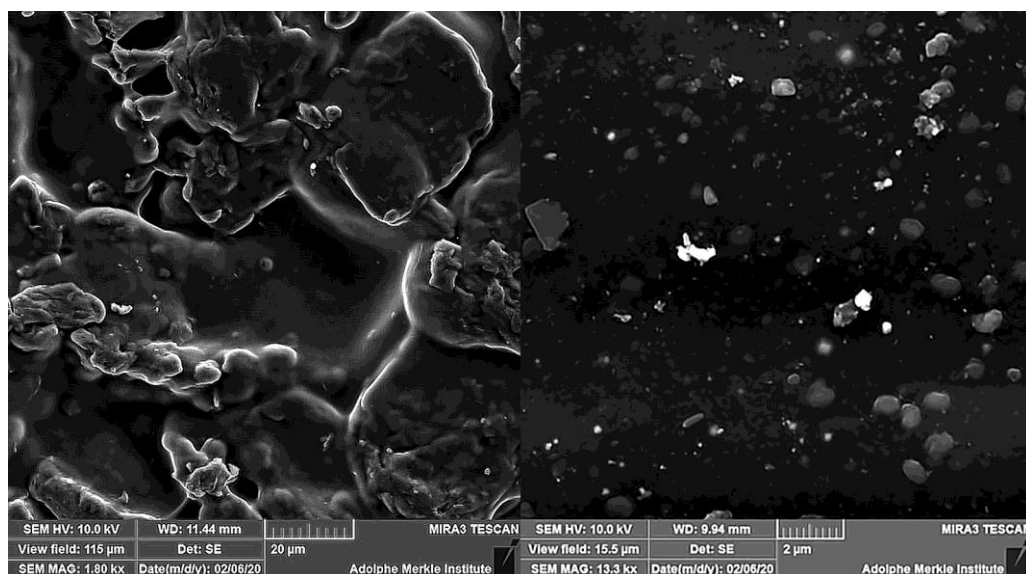


Plate 4.12: SEM Micrographs of TOCNF-DAC-CMCS and TOCNF-DAC-CMCS-AgNPs

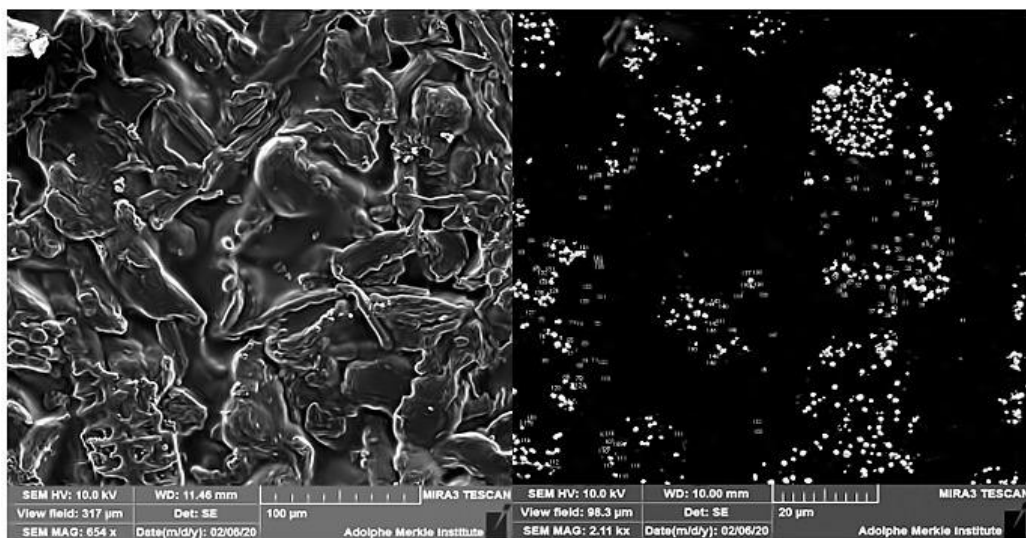


Plate 4.13: SEM micrographs of TOCNF-DAC-CS and TOCNF-DAC-CS-AgNPs

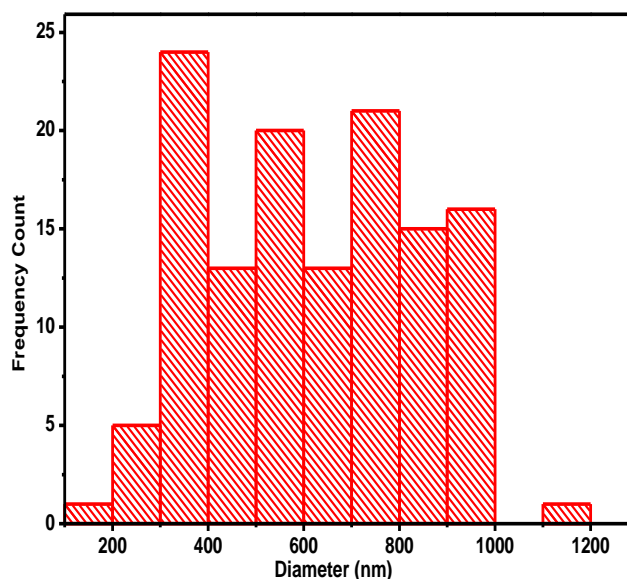


Figure 4.106: Size distribution of AgNPs distributed on TOCNF-DAC-CS-AgNPs composite films.

While TOCNF had a porous structure of fibers comprising of small and short fibers linked together, DAC had a small surface comprising of long fibers like native cellulose, and carboxymethyl cellulose having short smooth surfaces. On the other hand, the TOCNF-DAC-CMSC had a different morphology which consisted of a mesh-like surface, an indication of porous surface. As for TOCNF-DAC-CS-AgNPs composite, the films had a smooth surface with silver nanoparticle clearly visible and embedded within the matrix of the films. The AgNPs were estimated to be between 100 - 800 nm in size and spherical in nature (Figure 4.106) but larger in size than those that were synthesized using *L. trifolia* extract. TOCNF-DAC-CS films prepared in the absence of AgNPs had a rough surface consisting of kinks and valleys unlike films embedded with AgNPs. As it can be observed (Plate 4.12-4.13), incorporation of AgNPs within the composite matrix altered morphology of the composite possibly due to interaction between the nanoparticles and TOCNF-DAC-CS (Tanigawa, *et al.*, 2008).

4.8.10 Silver Release Kinetics

The amount of silver released was followed spectrophotometrically using a Uv-vis spectrophotometer and the results are depicted in figure 4.107. The slow release of AgNPs from the composite films as a function of time resulted in a gradual increase in the plasmon resonance peak of AgNPs being observed and attributed to their release from the films into the solution.

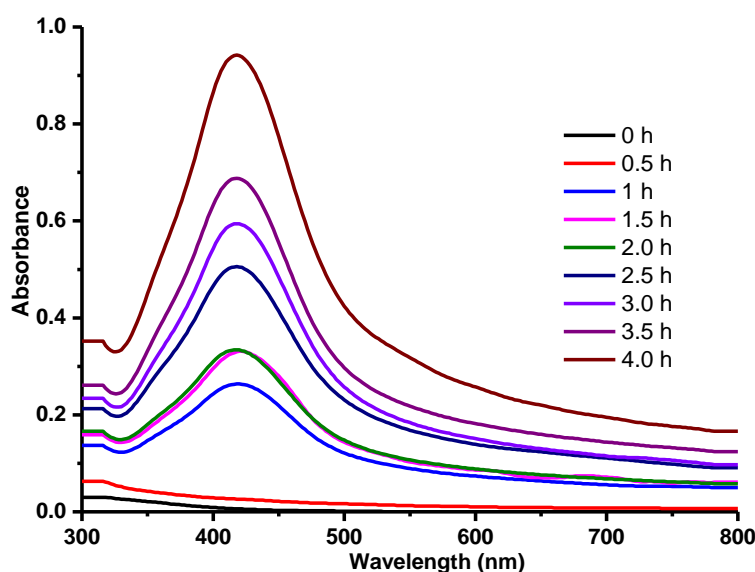


Figure 4.107: Slow release of AgNPs from TOCNF-DAC-CS-AgNPs composite films

Increase in time resulted in a subsequent increase in the λ_{\max} observed and this was attributed to an increase in the number of particles that diffused from the film into the solution (Li *et al.*, 2018). This gradual increase in the plasmon resonance peak is also an indication of the gradual increase in the concentration of the nanoparticles released, which is an indication that the composite can act as a slow-release device.

To determine the amount of silver ion being released, their concentration was measured using ICP-OES and the results are depicted in figure 4.108. It was observed that increasing the incubation time of the films in water resulted in a subsequent increase in the concentration of silver ion released from the composite films.

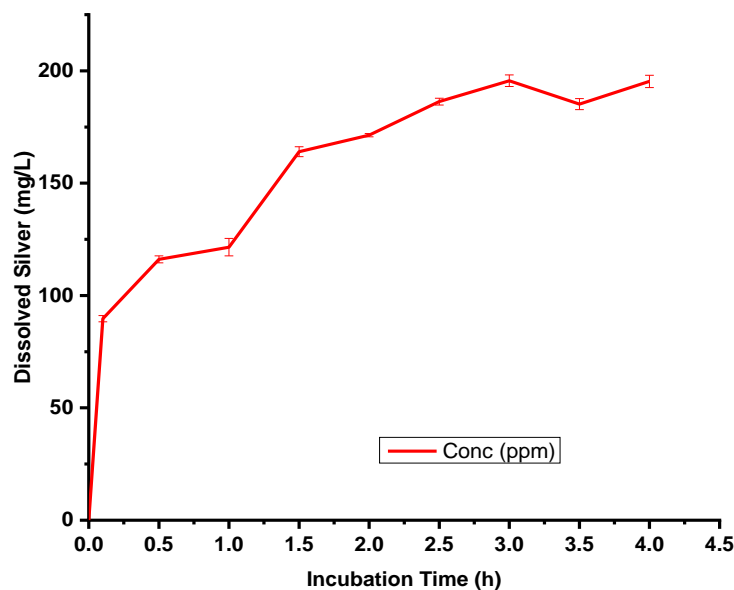


Figure 4.108: Total silver ion released from AgNPs-composite films as determined by ICP-MS

The amount of silver ions released from the composite films increased with increase in diffusion time with the highest concentration observed when the films had stayed in the solution for 4 h. Similar observations were made when AgNPs were embedded within chitosan-PEG hydrogels and titanium dioxide nano capsules in which the concentration of AgNPs released gradually increased over several days (Masood *et al.*, 2019; Tao *et al.*, 2017; Hérault *et al.*, 2020). It is worth mentioning that diffusion of a molecule or nanoparticles such as AgNPs loaded into a polymer matrix usually implies water penetration in the matrix, hydration, swelling, diffusion of the dissolved substance and or erosion of the gelatinous layer. The release mechanism is dependent on the loading efficiency, the solution pH, and the nature of the encapsulated substance and polymer used (Thai *et al.*, 2020).

To determine the rate in which the nanoparticles were released from the films, the experimental data was fitted in kinetic equations and the results are depicted in figure 4.109. By fitting the experimental data to first order and second order rate equations, it was found that the release of silver ions into the solution followed first order kinetics as compared to second order kinetics (Appendix GG) as the R for first order kinetics

was found to be closer to one with the rate of silver ion released being 26.5 ppm/h (Appendix HH). The Pearson's R for first order kinetics was found to be 0.9117 while that for second order kinetics was found to be 0.8843 (Appendix Q) (Ebbing and Gammon, 2016).

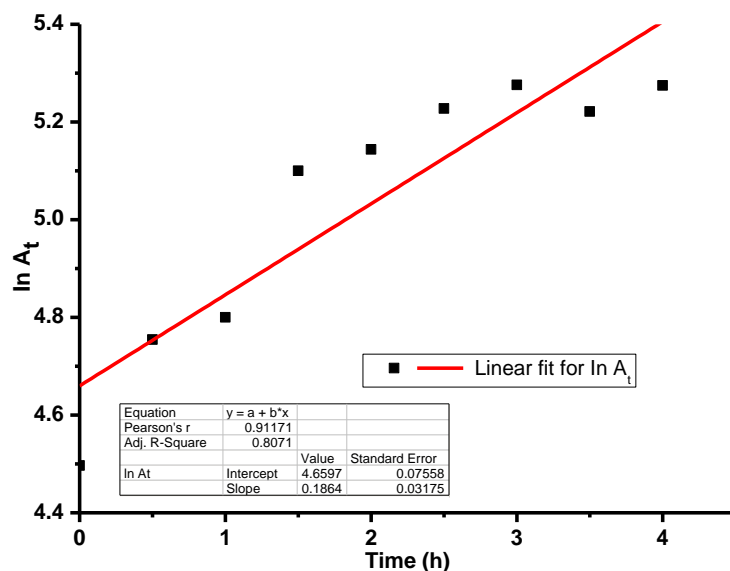


Figure 4.109: Pseudo first order plot for silver ion released from composite films.

4.8.11 *In-vitro* Antimicrobial Activity of Cellulose Chitosan Composite

The antimicrobial activity of neat TOCNF-DAC-CS and TOCNF-DAC-CS-AgNPs composite films were evaluated using disc diffusion assay and the results are shown in figure 4.113. From plate 4.14 - 4.15, the antimicrobial activity of TOCNF-DAC-CS-AgNPs and standard antimicrobials have been shown. Incorporation of AgNPs on the TOCNF-DAC-CS matrix results in the reduction in the antimicrobial activity of the composite films against *C. alibicans* and *P. mirabilis* but an increase antimicrobial activity against *B. subtilis*, *S. aureus*, and *P. aeruginosa* (Figure 4.110).

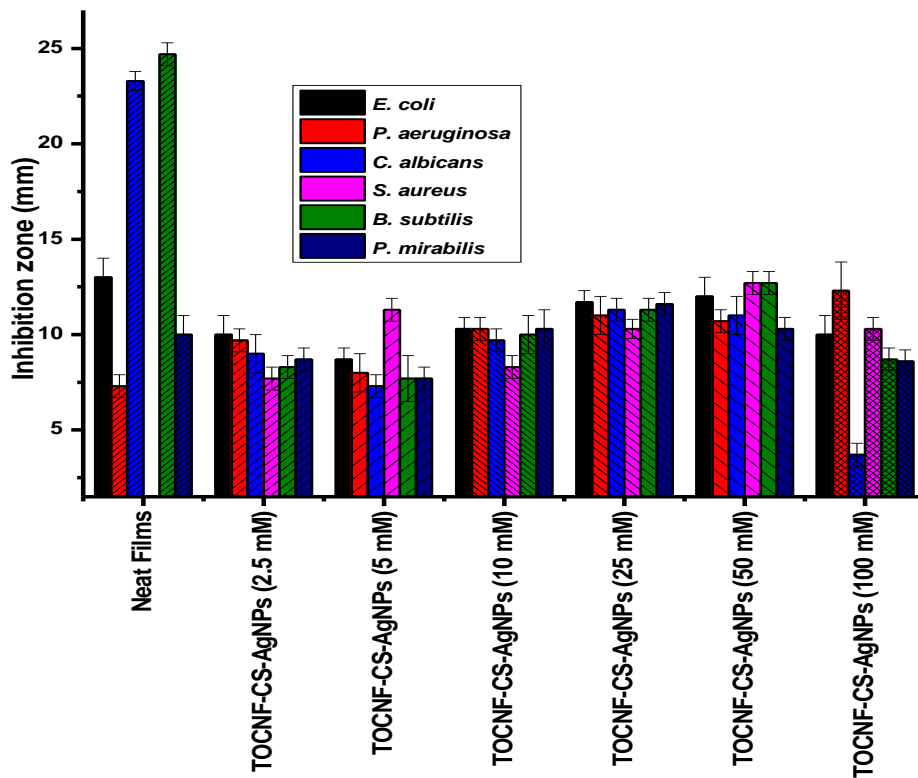


Figure 4.110: Inhibition zones of TOCNF-DAC-CS and TOCNF-DAC-CS-AgNPs

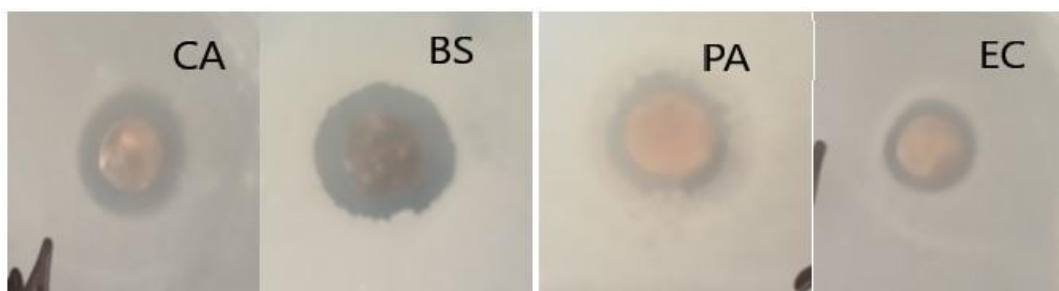


Plate 4.14: Zone of Inhibition of AgNPs composite films prepared using 25 mM AgNO₃.

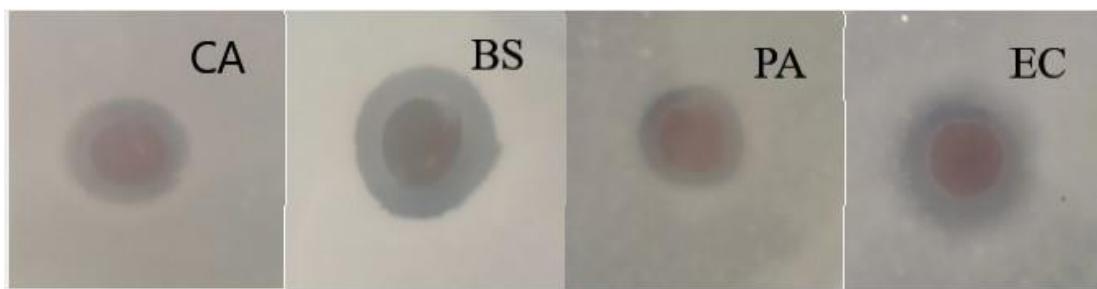


Plate 4.15: Zone of Inhibition of AgNPs composite films prepared using 50 mM AgNO₃.

When comparing the antimicrobial activity of neat TOCNF-DAC-CS with that of TOCNF-DAC-CS-AgNPs films, it was observed that neat films had a higher antimicrobial activity against *C. albicans* and *P. mirabilis* but not *S. aureus*. On the other hand, TOCNF-DAC-CS-AgNPs had moderate antimicrobial activity on the selected microorganism organism though the zone of inhibition was lower as compared to the neat TOCNF-DAC-CS films. This clearly demonstrates that the antimicrobial activity especially against *S. aureus* was because of the presence of AgNPs impregnated inside the composite films (Ghasemzadeh *et al.*, 2016). Moreover, increase in the antimicrobial activity of the composite film was observed to be dependent on the concentration of Ag ions used to synthesize AgNPs. This can be attributed to the fact that when the concentration of silver ions used during in-situ synthesis of AgNPs was increased from 2.5 mM to 100 mM, there was a subsequent increase in the number of AgNPs in the composite films. This increase resulted in the availability of more AgNPs being released from the composite films hence the slight increase in the zone of inhibition with a subsequent increase in the concentration of the oxidant. In general, the effects of NPs have been found to depend on the NP concentration, physiology, and metabolism of the given species, as well as the selective permeability of intracellular membranes and the kind of bacterial cell (Khan, *et al.*, 2020). When compared with standard antimicrobial drug, TOCNF-DAC-CS-AgNPs composite films had a higher antimicrobial activity against all microorganism under study apart from *E. coli* irrespective of the concentration of the oxidant used during AgNPs synthesis (table 3.35). In a similar study, Dong and Li, (2018) reported that CS-DACNC-AgNPs (10%) had moderate antimicrobial activity against the

growth of *Pseudomonas aeruginosa*(C) (7.45 mm), *Pseudomonas aeruginosa*(S) (6.68 mm), *Klebsiella pneumoniae*(C) (6.90 mm), *Streptococcus pneumoniae*(C) (8.32 mm), *Escherichia coli*(C) (6.96 mm), *Escherichia coli*(S) (6.71 mm), and *Enterobacter cloacae*(C) (10.48 mm). The films prepared using CS-DAC-AgNPs also inhibited the growth of three fungal species which include *Candida albicans*(C) (6.41 mm), *Candida glabrata*(C) (7.19 mm) and *Candida krusei*(C) (5.89 mm) (Dong and Li, 2018). El-Naggar *et al.*, (2016) also studied the effect of incorporating AgNPs in chitosan matrix and they reported that the developed dressing had a total average inhibition of 14.67 mm and 15.67 mm against *S. aureus* and for *P. aeruginosa* respectively. While cellulose does not to inhibit the growth of bacteria unless it is modified, chitosan on the other hand has been reported to have bacteriostatic/bactericidal activity hence it is able to control growth of microorganism. Its antimicrobial activity has been reported to be 11.88 and 14.11 mm for *S. aureus* and *P. aeruginosa* respectively (Rabea *et al.*, 2003; El-Naggar *et al.*, 2016). The antimicrobial activity of chitosan is enhanced below pH 6 because, at this pH value, the positive charge on C-2 of the glucosamine monomer is more soluble and has better antimicrobial activity than chitin. This antimicrobial activity is not well understood but it has been reported that due to the interaction between positively charged chitosan molecules and negatively charged microbial cell membranes, leakage of intracellular constituents occurs which led to cell death (Rabea *et al.*, 2003; Ghasemzadeh *et al.*, 2016). Chitosan can also act as a chelating agent that selectively binds trace metals, activate several defense processes in the host tissue, acts as a water binding agent, thereby inhibiting various enzymes leading to cell death (Rabea *et al.*, 2003). As such incorporation of AgNPs within the polymer matrix enhances the antimicrobial activity of the TOCNF-DAC-CS-AgNPs composite films due to presence of reactive oxygen species generated when metallic nanoparticles are incorporated (Khan *et al.*, 2020).

4.8.12 *In-vivo* Wound Healing Studies

The ability of the developed dressings to promote wound healing was evaluated using a nude rabbit and the results are depicted in plate 4.16. From the observations done on the wound surface (Plate 4.16), it was concluded that an infectious disease had not

occurred around the wounded part of the skin when this composite was used as a dressing (Tanigawa *et al.*, 2008; Masood *et al.*, 2019).

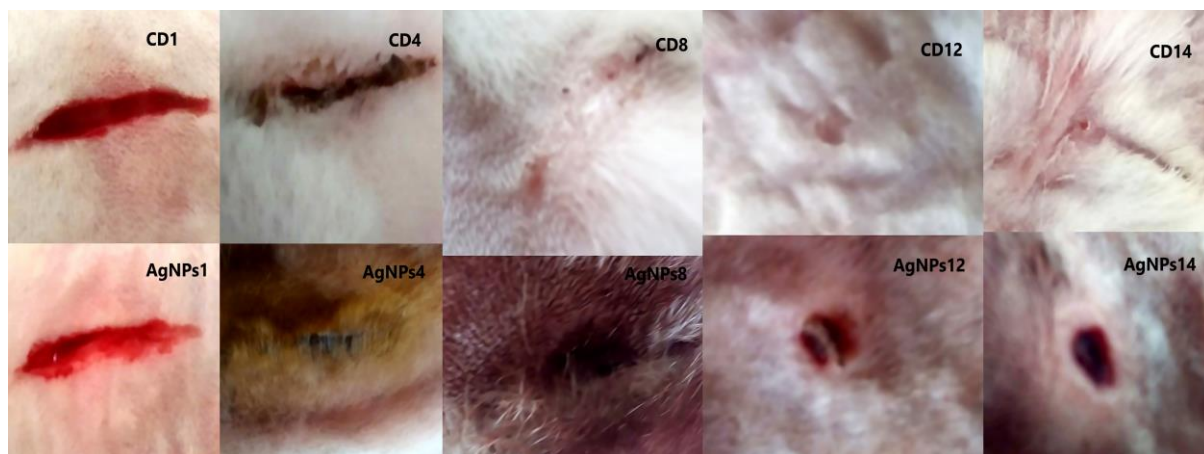


Plate 4.16: Wound healing process of composite films (CNF) and cotton gauze (C) after fourteen days

The discolouration surrounding the wounds treated with silver containing composite was attributed to the slow release of AgNPs from the dressing. This release aided in the wound healing as it was observed that the wounds covered with silver containing composite were on the proliferative stage which was an indication that the healing process had already begun after 24 h (Masood *et al.*, 2019). In the control group (Plate 4.16), the wounds were still fresh after 24 h an indication that the proliferation stage had not begun hence it was concluded silver containing composite increased the rate at which the healing process takes place. On the fourth day, the incisions made on the skin were completely closed and the hair that had been removed had begun to grow, an indication that the healing process was almost complete. Wound healing normally consists of four highly integrated processes; haemostasis, inflammation, proliferation, and tissue remodelling or resolution. In the proliferation stage filling of the wound contraction and epithelialization occur and these are usually an indication of wound healing. Masood *et al* 2018 reported that silver containing chitosan polyethylene glycol (CS-PEG) composite films aided wound healing in diabetes induced rabbits in which the rate of wound healing was observed to be higher in silver containing CS-PEG composite films. Chitosan has been reported to accelerate wound healing while

silver on the other hand inhibits the growth of microorganisms thereby combining these two materials positively impacts the way a wound progress (Masood *et al.*, 2019).

CHAPTER FIVE

CONCLUSIONS AND RECOMENDATIONS

5.1 Conclusions

The main goal of this study was to develop cellulose-chitosan metal nanocomposites films from *O. sativa*, *O. niloticus* and silver nanoparticles for wound dressing applications. Cellulose nanofibrils were isolated from *O. sativa* and subsequently modified by introduction of carboxylic and carbonyl groups in their structure. Chitosan isolated from *O. niloticus* was evaluated for its suitability to develop the nanocomposite films through its ability to form film after solvent casting. The inability of *O. niloticus* chitosan to form films resulted in use of commercial chitosan as the base for preparing the nanocomposite as commercial chitosan can form films. The nanocomposite films were prepared through solvent casting a solution consisting of oxidized cellulose nanofibrils, commercial chitosan and silver nitrate in plastic moulds. Presence of carbonyl and carboxylic functional groups within the cellulose network resulted in the reduction of silver ions in solution to silver nanoparticles which upon solvent casting of the solution, nanocomposite films with the ability to release silver nanoparticles were developed. These composite films had the ability to inhibit the growth of selected microorganisms under study and to prevent the development of infection on wounds inflicted on nude rabbits. As such, we conclude that:

- i. Oxidation of cellulose hydroxyl groups using 2,2,6,6-Tetramethylpiperidin-1-yl) oxyl and potassium periodate introduced carboxyl and carbonyl groups on cellulose, respectively.
- ii. Presence of these groups on cellulose led to a Schiff base reaction with chitosan and reduction of silver ions to AgNPs in the resultant composite films.
- iii. Depending on the composition of the composite films, there were changes in the crystallinity, thermal stability, morphology, water retention, transmittance, and tensile strength of the composite films.
- iv. Incorporation of cellulose nanofibrils and AgNPs on chitosan matrix resulted in an increase in the tensile strength of the resulting nanocomposite films.

- v. Presence of AgNPs enhanced the antimicrobial activity and wound healing properties of the nanocomposite films.

5.2 Recommendations

- i. Further studies should be undertaken to evaluate the pH responsiveness of the composite films.
- ii. Properties of composite films fabricated with sorbitol as a plasticizer instead of glycerin should be explored.
- iii. Incorporation of other antimicrobial nanoparticles such as copper oxide and zinc oxide in the composite materials should also be explored.
- iv. Encapsulation of antibiotics on carboxymethyl chitosan cellulose hydrogels as a smart delivery for biomedical applications should be explored.
- v. Fabrication of wound dressings using alginate to enhance water retention in wound dressing should be studied.

REFERENCES

- Abou-Zeid, R. E., Dacrory, S., Ali, K. A., and Kamel, S. (2018). Novel method of preparation of tricarboxylic cellulose nanofiber for efficient removal of heavy metal ions from aqueous solution. *International Journal of Biological Macromolecules*, 119, 207-214.
- Abreu, F. D., and Campana-Filho, S. P. (2005). Preparation and characterization of carboxymethylchitosan. *Polimeros*, 15(2), 79-83.
- Afonso, C. R., Hirano, R. S., Gaspar, A. L., Chagas, E. L., Carvalho, R. A., Silva, F. V., . . . Yoshida, C. P. (2019). Biodegradable antioxidant chitosan films useful as an anti-aging skin mask. *International Journal of Biological Macromolecules*, 132, 1262-1273.
- Ahmad, N., Ang, B. C., Amalina, M. A., and Bong, C. W. (2018). Influence of precursor concentration and temperature on the formation of nanosilver in chemical reduction method. *Sains Malasiana*, 47(1), 157-168.
- Ahmed, S., Ahmad, M., Swami, B. L., and Ikram, S. (2016). A review on plants extract mediated synthesis of silver nanoparticles for antimicrobial applications: a green expertise. *Journal of Advanced Research*, 7(1), 17-28.
- Akmaz, S., Dilaver Adiguzel, E., Yasar , M., and Erguven, O. (2013). The effect of Ag content of the chitosan-silver nanoparticle composite material on the structure and antibacterial activity. *Advances in Materials Science and Engineering*, 2013, 1-6.
- Al Sagheer , F. A., Al-Sughayer, M. A., Muslim, S., and Elsabee, M. Z. (2009). Extraction and characterization of chitin and chitosan from marine sources in Arabian Gulf. *Carbohydrate Polymers*, 77(2), 410-419.
- Alam, M. N., and Christopher , L. P. (2018). Natural cellulose-chitosan crosslinked superabsorbent hydrogels with superior swelling properties. *ACS Sustainable Chemistry and Engineering*, 6, 8736-8742.

- Amidi, S., Mojab, F., Moghaddam, A. B., Tabib, K., and Kobarfard, F. (2012). A simple electrochemical method for the rapid estimation of antioxidant potentials of some selected medicinal plants. *Iranian Journal of Pharmaceutical Research*, 11(1), 117.
- Andhoga, J., Macharia, A. G., Maikuma, I. R., Wanyonyi, Z. S., Ayumba, B. R., and Kakai, R. (2002). Aerobic pathogenic bacteria in post operative wounds at Moi Teaching and Referral Hospital. *East African Medical Journal*, 640-644.
- Anicuta, S. G., Dobre, L., Stroescu, M., and Jipa, I. (2010). Fourier Transform Infrared Spectroscopy characterization of antimicrobial films containing chitosan. *Analele Universităţii din Oradea Fascicula: Ecotoxicologie, Zootehnie și Tehnologii de Industrie Alimentară*, 1234 - 1240.
- Anshup Venkataraman, J.S., Subramaniam, C., Kumar, R. R., Priya, S., Kumar, T. S., Omkumar, R. V., . . . Anshup, T. (2005). Growth of gold nanoparticles in human cells. *Langmuir*, 21(25), 11562-11567.
- ASTM D882-10. (2010). *Standard Test Method for tensile properties of thin plastic sheeting*. West Conshohocken, Pennsylvania: ASTM International.
- Audic, J. L., and Chaufer, B. (2005). Influence of plasticizers and crosslinking on the properties of biodegradable films made from sodium caseinate. *European Polymer Journal*, 41(8), 1943-1942.
- Auxenfans, T., Cronier, D., Chabbert, B., and Paes, G. (2017). Understanding the structural and chemical changes of plant biomass following steam explosion pretreatment. *Biotechnology for Biofuels*, 10(1), 36.
- Azam, A., Ahmed, A. S., Oves, M., Khan, M. S., Habib, S. S., and Memic, A. (2012). Antimicrobial activity of metal oxide nanoparticles against Gram-positive and Gram-negative bacteria: a comparative study. *International Journal of Nanomedicine*, 6003-6009.

- Baptista, P. V., McCusker, M. P., Carvalho, A., Ferreira, D. A., Mohan, N. M., Martins, M., and Fernandes, A. R. (2018). Nano-Strategies to Fight Multidrug Resistant Bacteria—"A Battle of the Titans". *Frontiers in Microbiology*, 9, 1-26.
- Barbash, V. A., Yaschenko, O. V., and Shniruk, O. M. (2017). Preparation and properties of nanocellulose from organosolv straw pulp. *Nanoscale Research Letters*, 12(1), 1-9.
- Barbosa, L. C., Maltha, C. R., Demuner, A. J., Casal, C. M., Reis, E. L., and Colodette, J. L. (2013). A rapid method for quantification of carboxyl groups in cellulose pulp. *Bioresources*, 1(8), 1043-1054.
- Basavaraja, S. D., Balaji, D., Bedre, M. D., Raghunandan, D., Swamy, P. P., and Venkataraman, A. (2011). Solvothermal synthesis and characterization of acicular α -Fe₂O₃ nanoparticles. *Bulletin of Materials Science*, 34(7), 1313-1317.
- Begun, P. S., Joseph, R., Joseph, D., Kumar, P., and Ayswarya, E. P. (2013). Synthesis, characterization and application of Rice husks nanosilica in natural rubber. *International Journal of Science, Environment and Technology*, 2(5), 1027 - 1035.
- Besbes, I., Villar, M. R., and Boufi, S. (2011). Nanofibrillated cellulose from alfa, eucalyptus and pine fibres: preparation, characteristics and reinforcing potential. *Carbohydrate Polymers*, 86(3), 1198-1206.
- Bhimte, N. A., and Tayade, P. T. (2007). Evaluation of microcrystalline cellulose prepared from sisal fibers as a tablet excipient: A technical note. *AAPS PharmSciTech*, 8(1), E56 - E62.
- Bilo, F., Lodolo, M., Borgese, L., Benassi, L., Depero, L. E., and Bontempi, E. (2015). Evaluation of heavy metals contamination from environment to food matrix by TXRF: The case of rice and rice husk. *Journal of Chemistry*, 2015, 1 - 13.

- Blaine, R. L. (2013). *Determination of polymer crystallinity by DSC*. New Castle DE: TA Instruments.
- Born, M., Carrupt, P. A., Zini, R., Bree, F., Tillement, J. P., Hostettmann, K., and Testa, B. (1996). Electrochemical behaviour and antioxidant activity of some natural polyphenols. *Helvetica Chimica Acta*, 79(4), 1147-1158.
- Boufi, S., and Chaker, A. (2016). Easy production of cellulose nanofibrils from corn stalk by a conventional high speed blender. *Industrial Crops and Products*, 93, 39 - 47.
- Brett, D. (2008). A Review of collagen and collagen-based wound Dressings. *Wounds: a compendium of clinical research and practice*, 20(12), 347 - 356.
- Cady, N. C., Behnke, J. L., and Strickland, A. D. (2011). Copper- Based Nanostructured Coatings on Natural Cellulose: Nanocomposites Exhibiting Rapid and Efficient Inhibition of a Multi- Drug Resistant Wound Pathogen, *A. baumannii*, and Mammalian Cell Biocompatibility *In Vitro*. *Advanced Functional Materials*, 21(13), 2506-2514.
- Cai, H., An, X., Cui, J., Li, J., Wen, S., Li, K., . . . Shi, X. (Eds.). (2013). Facile hydrothermal synthesis and surface functionalization of polyethyleneimine-coated iron oxide nanoparticles for biomedical applications. *ACS Applied Materials and Interfaces*, 5(5), 1722 - 1731.
- Camacho, D. H., Gerongay, S. R., and Macalinao, J. P. (2013). Cladophora cellulose-polyaniline composite for remediation of toxic chromium (VI). *Cellulose Chemistry and Technology*, 47, 125 - 132.
- Cengiz, A., Kaya, M., and Bayramgil, N. P. (2017). Flexural stress enhancement of concrete by incorporation of algal cellulose nanofibers. *Construction and Building Materials*, 149, 289-295.

- Cerqueira, J. C., Penha, J. D., Oliveira, R. S., Guarieiro, L. N., Melo, P. D., Viana, J. D., and Machado, B. A. (2017). Production of biodegradable starch nanocomposites using cellulose nanocrystals extracted from coconut fibers. *Polimeros*, 27(4), 320-329.
- Cekli, L., Bayatsarmadi, B., Sekine, R., Sarkar, B., Shen, A., Scheckel, K. G., . . . Donner, E. (2016). Analytical characterisation of nanoscale zero-valent iron: a methodological review. *Analytica Chimica Acta*, 903(2016), 13-35.
- Chen, C., Sun, W., Yao, W., Wang, Y., Ying, H., and Wang, P. (2018). Functional polymeric dialdehyde dextrin network capped mesoporous silica nanoparticles for pH/GSH dual-controlled drug release. *RSC Advances*, 8(37), 20862-20871.
- Chen, Y., Wu, Q., Huang, B., Huang, M., and Ai, X. (2014). Isolation and characteristics of cellulose and nanocellulose from lotus leaf stalk agrowastes. *Bioresources*, 10(1), 684 - 696.
- Chung, I. M., Park, I., Seung-Hyun, K., Thiruvengadam, M., and Rajakumar, G. (2016). Plant-mediated synthesis of silver nanoparticles: their characteristic properties and therapeutic applications. *Nanoscale Research Letters*, 11(40), 1-14.
- Ciolacu, D., Ciolacu, F., and Popa, V. I. (2011). Amorphous cellulose—structure and characterization. *Cellulose Chemistry and Technology*, 45(1), 13-21.
- Corgie, S. C., Smith, H. M., and Walker, L. P. (2011). Enzymatic transformations of cellulose assessed by quantitative high-throughput fourier transform infrared spectroscopy (QHT- FTIR). *Biotechnology and Bioengineering*, 108(7), 1509 - 1520.
- Courvallin, P. (2008). Predictable and unpredictable evolution of antibiotic resistance. *Journal of Internal Medicine*, 264(1), 4 - 16.

- da Silva Perez, D., Montanari, S., and Vignon, M. R. (2003). TEMPO-mediated oxidation of cellulose III. *Biomacromolecules*, 4(5), 1417-1425.
- Daicho, K., Saito, T., Fujisawa, S., and Isogai, A. (2018). The crystallinity of nanocellulose: Dispersion-induced disordering of the grain boundary in biologically structured cellulose. *ACS Applied Nano Materials*, 1(10), 5774-5785.
- Dakal, T. C., Kumar, A., Majumdar, R. S., and Yadav, V. (2016). Mechanistic basis of antimicrobial actions of silver nanoparticles. *Frontiers in Microbiology*, 7, 1-17.
- Dang, L. N., and Seppala, J. (2015). Electrically conductive nanocellulose/graphene composites exhibiting improved mechanical properties in high-moisture condition. *Cellulose*, 22, 1799 - 1812.
- de Queiroz Antonio, R. S., Lia Fook, B. R., de Oliveira Lima, V. A., de Farias Rached, R. I., Lima, E. P., da Silva Lima, R. J., . . . Lia Fook, M. V. (2017). Preparation and characterization of chitosan obtained from shells of shrimp (*Litopenaeus vannamei* Boone). *Marine Drugs*, 15(5), 141.
- Deng, Y., Ren, J., Chen, G., Li, G., Wu, X., Wang, G., . . . Li, J. (2017). Injectable in situ cross-linking chitosan-hyaluronic acid based hydrogels for abdominal tissue regeneration. *Scientific Reports*, 7(1), 1-13.
- Desbrieres, J., and Guibal, E. (2010). Polysaccharide for metal ion recovery - A focus on chitosan. In G. Crini, and P. M. Badot, *Sorption processes and pollution: Conventional and non-conventional sorbents for pollutant removal from wastewaters* (pp. 272 - 293). Besancon, France: Presses Universitaires de Franche-Comte.
- Dinda, V., Gunturu, R., Kariuki, S., Hakeem, A., Raja, A., and Kimanga, A. (2013). Pattern of pathogens and their sensitivity isolated from surgical site infections

at the Aga Khan University Hospital, Nairobi, Kenya. *Ethiopian Journal of Health Sciences*, 23(3), 141 - 148.

Dong, F., and Li, S. (2018). Wound dressings based on chitosan-dialdehyde cellulose nanocrystals-silver nanoparticles: Mechanical strength, antibacterial activity and cytotoxicity. *Polymers*, 10, 1-13.

Dufresne, A. (2008). Polysaccharide nano crystal reinforced nanocomposites. *Canadian Journal of Chemistry*, 86(6), 484 - 494.

Duri, S., El-Zahab, B., and Tran, C. D. (2013). Polysaccharide Ecocomposite Material: Synthesis, Characterization and Application for Removal of Pollutants. *ECS Transactions*, 50(11), 573-594.

Ebbing, D., and Gammon, S. D. (2016). *General Chemistry* (Vol. 11). Boston, Massachusetts, United States of America: Cengage Learning.

Ebrahiminezhad, A., Zare-Hoseinabadi, A., Sarmah, A. K., Taghizadeh, S., Ghasemi, Y., and Berenjian, A. (2017). Plant-mediated synthesis and applications of iron nanoparticles. *Molecular Biotechnology*, 1-15.

El Achaby, M., El Miri, Hannache, H., Gmouth, S., Trabadelo, V., Aboulkas, A., and Youcef, H. B. (2018). Cellulose nanocrystals from Miscanthus fibers: insights into rheological, physico-chemical properties and polymer reinforcing ability. *Cellulose*, 25(11), 6603-6619.

Elgrishi, N., Rountree, K. J., McCarthy, B. D., Rountree, E. S., Eisenhart, T. T., and Dempsey, J. L. (2018). A Practical Beginner's Guide to Cyclic Voltammetry. *Journal of Chemical Education*, 95(2), 197-206.

El-hefian, E. A., Elgannoudi, E. S., Mainai, A., and Yahaya, A. H. (2010). Characterization of chitosan in acetic acid: Rheological and thermal studies. *Turkish Journal of Chemistry*, 34(2010), 47-56.

- El-Naggar, M. Y., Gohar, Y. M., Sorour, M. A., and Waheeb, M. G. (2016). Hydrogel dressing with a nano-formula against methicillin-resistant *Staphylococcus aureus* and *Pseudomonas aeruginosa* diabetic foot bacteria. *Journal of Microbiology and Biotechnology*, 26(2), 408-420.
- Errokh, A., Magnin, A., Putaux, J. L., and Boufi, S. (2018). Morphology of the nanocellulose produced by periodate oxidation and reductive treatment of cellulose fibers. *Cellulose*, 25(7), 3899-3911.
- Errokh, A., Magnin, A., Putaux, J. L., and Boufi, S. (2019). Hybrid nanocellulose decorated with silver nanoparticles as reinforcing filler with antibacterial properties. *Material Science and Engineering C*, 105, 1-9.
- Eslami, S., Ebrahimzadeh, M. A., and Biparva, P. (2018). Green synthesis of safe zero valent iron nanoparticles by *Myrtus communis* leaf extract as an effective agent for reducing excessive iron in iron-overloaded mice, a thalassemia model. *RSC Advances*, 8(46), 26144-26155.
- Estefan, G., Sommer, R., and Ryan, J. (2013). *Methods of soil, plant, and water analysis: A manual for the west, Asia and North Africa region* (3 ed.). Beirut, Lebanon: ICARDA.
- Fan, H., Wang, L., Zhao, K., Li, N., Shi, Z., Ge, Z., and Jin, Z. (2010). Fabrication, mechanical properties, and biocompatibility of graphene-reinforced chitosan composites. *Biomacromolecules*, 11(9), 2345 - 2351.
- Farahnaky, A., Saberi, B., and Majzoobi, M. (2013). Effect of glycerol on physical and mechanical properties of wheat starch edible films. *Journal of Texture Studies*, 44(3), 176-186.
- Fitz, B. D., Looney, D., Craven, T. L., Dey, C., and Garg, A. (2017). *United States of America Patent No. 15/450,706*.

- Fitzmaurice, S. D., Sivamani, R. K., and Isseroff, R. R. (2011). Antioxidant therapies for wound healing: a clinical guide to currently commercially available products. *Skin Pharmacology and Physiology*, 24(3), 113-126.
- Ghasemzadeh, H., Mahboubi, A., Karimi, K., and Hassani, S. (2016). Full polysaccharide chitosan-CMC membrane and silver nanocomposite: synthesis, characterization, and antibacterial behaviors. *Polymers for Advanced Technologies*, 27(9), 1204 - 1210.
- Gilbert, J. C., and Martin, S. F. (2016). *Experimental Organic Chemistry: A Miniscale Approach*. Boston: Cengage Learning.
- Govindaraju, K., Basha, S. K., Kumar, V. G., and Singaravelu, G. (2008). Silver, gold and bimetallic nanoparticles production using single-cell protein (*Spirulina platensis*) Geitler. *Journal of Materials Science*, 43(15), 5115-5122.
- Guinesi, L. S., and Cavalheiro, E. G. (2006). The use of DSC curves to determine the acetylation degree of chitin/chitosan samples. *Thermochimica Acta*, 444(2), 128-133.
- Guirguis, O. W., Gehan, T., Esawy, M. A., Elkader, N. R., Mahmoud, H. M., Mostafa, H. M., and Abdel-Zaher, N. A. (2016). Exposure of chitosan to UV/ozone: Structural information and antibacterial activity. *Journal of Applied Pharmaceutical Science*, 6(12), 124 - 130.
- Hérault, N., Wagner, J., Abram, S. L., Widmer, J., Horvath, L., Vanhecke, D., . . . Fromm, K. (2020). Silver-Containing Titanium Dioxide Nanocapsules for Combating Multidrug-Resistant Bacteria. *International Journal of Nanomedicine*, 15, 1267-1281.
- Herlekar, M., Barve, S., and Kumar, R. (2014). Plant-Mediated Green Synthesis of Iron Nanoparticles. *Journal of Nanoparticles*, 2014, 1-10. doi:10.1155/2014/140614

- Hoenich, N. A. (2006). Cellulose for medical applications: Past, Present, and Future. *Bioresources Journal*, 1(2), 270 - 280.
- Hoffman, A. S. (2012). Hydrogels for Biomedical applications. *Advanced Drug Delivery Reviews*, 18 - 23.
- Hoglund, E. (2015). *Production of dialdehyde cellulose and periodate regeneration: Towards feasible oxidation processes*. Retrieved from <http://kau.diva-portal.org>: <http://kau.diva-portal.org/smash/record.jsf?pid=diva2:860429&ddswid=1692>
- Hon, D. N., and Shiraishi, N. (2000). *Wood and cellulosic chemistry, revised, and expanded*. New York: Marcel Dekker.
- Hong, S. I., and Rhim, J. W. (2008). Antimicrobial activity of organically modified nano-clays. *Journal of Nanoscience and Nanotechnology*, 8(11), 5818 - 5824.
- Hooshmand, S., Aitomaki, Y., Berglund, L., Mathew, A. P., and Oksman, K. (2017). Enhanced alignment and mechanical properties through the use of hydroxyethyl cellulose in solvent-free native cellulose spun filaments. *Composites Science and Technology*, 150(2017), 79 - 86.
- Hou, Y., Wang, X., Yang, J., Zhu, R., Zhang, Z., and Li, Y. (2018). Development and biocompatibility evaluation of biodegradable bacterial cellulose as a novel peripheral nerve scaffold. *Journal of Biomedical Materials Research Part A*, 106(5), 1288-1298.
- Hoyos-Arbeláez, J., Vázquez, M., and Contreras-Calderon, J. (2017). Electrochemical methods as a tool for determining the antioxidant capacity of food and beverages: A review. *Food Chemistry*, 221, 1371-1381.
- Hoyos-Arbeláez, J., Vázquez, M., and Contreras-Calderón, J. (2017). Electrochemical methods as a tool for determining the antioxidant capacity of food and beverages: A review. *Food chemistry*, 221, 1371-1381.

- Hu, Z., Zhai, R., Li, J., Zhang, Y., and Lin, J. (2017). Preparation and characterization of nanofibrillated cellulose from bamboo fiber via ultrasonication assisted by repulsive effect. *International Journal of Polymer Science*, 2017, 1-10.
- Huang, G., Wang, M., Hu, Y., Lv, S., and Li, C. (2017). Synthesis, characterization, and debromination reactivity of cellulose-stabilized Pd/Fe nanoparticles for 2, 2', 4, 4'-tetrabromodiphenyl ether. *PloS one*, 12(3), 1-17.
- Isogai, A. (2018). Development of completely dispersed cellulose nanofibers. *Proceedings of the Japan Academy, Series B*, 94(4), 161-179.
- Isogai, A., Saito, T., and Fukuzumi, H. (2011). TEMPO-oxidized cellulose nanofibers. *Nanoscale*, 3(1), 71-85.
- Ito, H., Sakata, M., Hongo, C., Matsumoto, T., and Nishino, T. (2018). Cellulose nanofiber nanocomposites with aligned silver nanoparticles. *Nanocomposites*, 4(4), 167-177.
- Jain, J., Arora, S., Rajwade, J. M., Omray, P., Khandelwal, S., and Paknikar, K. M. (2009). Silver nanoparticles in therapeutics: Development of an antimicrobial gel formulation for topical Use. *Molecular Pharmaceutics*, 6(5), 1388 - 1401.
- Jamroz, E., Kulawik, P., and Kopel, P. (2019). The effect of nanofillers on the functional properties of biopolymer-based films: A Review. *Polymers*, 11(4), 1-43.
- Jara-Palacios, M., Escudero-Gilete, M. L., Hernández-Hierro, J. M., Heredia, F. J., and Hernanz, D. (2017). Cyclic voltammetry to evaluate the antioxidant potential in winemaking by-products. *Talanta*, 165, 211-215.
- Jiang, F., and Hsieh, Y. L. (2018). Self-assembling of TEMPO oxidized cellulose nanofibrils as affected by protonation of surface carboxyls and drying methods. *ACS Sustainable Chemistry and Engineering*, 4(3), 1041-1049.

- Jiang, X. C., Chen, W. M., Chen, C. Y., Xiong, S. X., and Yu, A. B. (2011). Role of temperature in the growth of silver nanoparticles through a synergetic reduction approach. *Nanoscale Research Letters*, 6(1), 1-9.
- Johar, N., Ahmad, I., and Dufresne, A. (2012). Extraction, preparation and characterization of cellulose fibres and nanocrystals from rice husk. *Industrial Crops and Products*, 37(1), 93 - 99.
- Jorfi, M., and Foster, J. (2015). Recent Advances in Nanocellulose for Biomedical Applications. *Journal of Applied Polymer Science*, 132(14), 1 -19.
- Joshi, G. B., Heman, K. S., Sigh, M. N., and Shivakumar, H. G. (2011). Development of pH Sensitive hydrogel for Intestinal Delivery of Methyl Prednilone using Novel Chitosan Derivative. *International Journal of Pharmacy and Pharmaceutical Science*, 3(1), 200 - 203.
- Kallel, F., Bouaziz, F., Chaari , F., Belghith, L., Ghorbel, R., and Chaabouni, S. E. (2016). Interactive effect of garlic straw on the sorption and desorption of Direct Red 80 from aqueous solution. *Process Safety and Environmental Protection*, 102, 30 - 43.
- Kampalananwat, P., Supaphol, P., and Morlock, G. E. (2013). Electrospun nanofiber layers with incorporated photoluminescence indicator for chromatography and detection of ultraviolet-active compounds. *Journal of Chromatography*, 1299, 110 - 117.
- Kang, X., Wang, J., Wu, H., Aksay, I. A., Liu, J., and Lin, Y. (2009). Glucose oxidase–graphene–chitosan modified electrode for direct electrochemistry and glucose sensing. *Biosensors and Bioelectronics*, 25(4), 901 - 905.
- Kar, K. K., Rana, S., and Pandey, J. (2015). *Handbook of polymer nanocomposites processing, performance and application*. Verlag Berlin Heidelberg: Springer.

- Karimi, E. Z., Vahdati, K. J., Zebarjad, S. M., Bataev, I. A., and Bannovm, A. G. (2014). A novel method for fabrication of Fe catalyst used for the synthesis of carbon nanotubes. *Bulletin of Materials Science*, 2014, 1031-1038.
- Karimi, K., and Taherzadeh, M. J. (2016). A critical review of analytical methods in pretreatment of lignocelluloses: Composition, imaging, and crystallinity. *Bioresource Technology*, 200, 1008 - 1018.
- Katepetch, C., Rujiravanit, R., and Tamura, H. (2013). Formation of nanocrystalline ZnO particles into bacterial cellulose pellicle by ultrasonic-assisted in situ synthesis. *Cellulose*, 20(3), 1275 - 1292.
- Keffous, F., Belboukhari, N., Sekkoum, K., Djeradi, H., Cheriti, A., and Aboul-Enein, H. Y. (2016). Determination of the antioxidant activity of *Limoniastrum feei* aqueous extract by chemical and electrochemical methods. *Cogent Chemistry*, 2(1), 1186141.
- Keshari, A. K., Srivastava, R., Singh, P., Yadav, V. B., and Nath, G. (2018). Antioxidant and antibacterial activity of silver nanoparticles synthesized by *Cestrum nocturnum*. *Journal of Ayurveda and Integrative medicine*, 1-8.
- Khan, M. R., Fromm, K. M., Rizvi, T. F., Giese, B., Ahamad, F., Turner, R. J., . . . Marsili, E. (2020). Metal Nanoparticle–Microbe Interactions: Synthesis and Antimicrobial Effects. *Particle and Particle Systems Characterization*, 1-22.
- Kilmartin, P. A. (2001). Electrochemical detection of natural antioxidants: Principles and protocols. *Antioxidants and Redox Signaling*, 3(6), 941-955.
- Kim, M. H., Kim, T. H., Ko, J. A., Ko, S., Oh, J. M., and Park, H. J. (2019). Kinetic and thermodynamic studies of silver migration from nanocomposites. *Journal of Food Engineering*, 243, 1-8.
- Kimani, P. K., Kareru, P. G., Madivoli, E. S., Kairigo, P. K., Maina, E. G., and Rechab, S. O. (2016). Comparative Study of Carboxymethyl Cellulose Synthesis from

- Selected Kenyan Biomass. *Chemical Science International Journal*, 17(4), 1-8.
- Kimura, S., Isobe, N., Wada, M., Kuga, S., Ko, J. H., and Kim, U. J. (2011). Enzymatic hydrolysis of chitosan-dialdehyde cellulose hydrogels. *Carbohydrate polymers*, 83(4), 1850-1853.
- Kittur, F. S., Prashanth, K. H., Sankar, K. U., and Tharanathan, R. N. (2002). Characterization of chitin, chitosan and their carboxymethyl derivatives by differential scanning calorimetry. *Carbohydrate polymers*, 49(2), 185-193.
- Konwar, A., Kalita, S., Kotoky, J., and Chowdhury, D. (2016). Chitosan–Iron Oxide Coated Graphene Oxide Nanocomposite Hydrogel: A Robust and Soft Antimicrobial Biofilm. *ACS Applied Materials and Interfaces*, 8(32), 20625 - 20634.
- Kowshik, M., Deshmukh, N., Vogel, W., Urban, J., Kulkarni, S. K., and Paknikar, K. M. (2002). Microbial synthesis of semiconductor CdS nanoparticles, their characterization, and their use in the fabrication of an ideal diode. *Biotechnology and Bioengineering*, 78(5), 583-588.
- Kulkarni, S., Jadhav, M., Raikar, P., Barretto, D. A., Vootla, S. K., and Raikar, U. S. (2017). Green synthesized multifunctional Ag@ Fe₂O₃ nanocomposites for effective antibacterial, antifungal and anticancer properties. *New Journal of Chemistry*, 41(17), 9513-9520.
- Kumar, B., Smita, K., Cumbal, L., and Debut, A. (2014). Biogenic synthesis of iron oxide nanoparticles for 2-arylbenzimidazole fabrication. *Journal of Saudi Chemical Society*, 18, 364-369.
- Kumari, S., and Rath, P. K. (2014). Extraction and characterization of chitin and chitosan from (*Labeo rohita*) fish scales. *Procedia Materials Science*, 6, 482 - 489.

- Kumari, S., Rath, P., Kumar, A. S., and Tiwari, T. N. (2015). Extraction and characterization of chitin and chitosan from fishery waste by chemical method. *Environmental Technology and Innovation*, 3, 77-85.
- Kumirska, J., Czerwicka, M., Kaczynski, Z., Bychowska, A., Brzozowski, K., Thoming, J., and Stepnowski, P. (2010). Application of Spectroscopic Methods for Structural Analysis of Chitin and Chitosan. *Marine Drugs*, 8(5), 1567 - 1636.
- Laxminarayan, R., Duse, A., Wattal, C., Zaidi, A. K., Wertheim, H. F., Sumpradit, N., and Greko, C. (2013). Antibiotic resistance-the need for global solutions. *The Lancet Infectious Diseases*, 13(12), 1057 - 1098.
- Leguy, J. (2018). *Periodate oxidation of cellulose for internal plasticization and materials design*. Doctoral dissertation. Université Grenoble Alpes,.
- Leguy, J., Diallo, A., Putaux, J. L., Nishiyama, Y., Heux, L., and Jean, B. (2018). Periodate Oxidation Followed by NaBH₄ Reduction Converts Microfibrillated Cellulose into Sterically Stabilized Neutral Cellulose Nanocrystal Suspensions. *Langmuir*, 34(37), 11066-11075.
- Leguy, J., Nishiyama, Y., Jean, B., and Heux, L. (2018). Ultrastructural characterization of the core-shell structure of a wide range of periodate oxidized cellulose from different native sources by solid state ¹³C CP-MAS NMR. *ACS Sustainable Chemistry and Engineering*, 1-33.
- Lengke, M. F., Fleet, M. E., and Southam, G. (2007). Biosynthesis of silver nanoparticles by filamentous cyanobacteria from a silver (I) nitrate complex. *Langmuir*, 23(5), 2694-2699.
- Levard, C., Mitra, S., Yang, T., Jew, A. D., Badireddy, A. R., Lowry, G. V., and Brown Jr, G. E. (2013). Effect of chloride on the dissolution rate of silver nanoparticles and toxicity to E. coli. *Environmental Science and Technology*, 47(11), 5738-5745.

- Li, H., Wu, B., Mu, C., and Lin, W. (2011). Concomitant degradation in periodate oxidation of carboxymethyl cellulose. *Carbohydrate Polymers*, 84(3), 881-886.
- Li, J., Kang, L., Wang, B., Chen, K., Tian, X., Ge, Z., . . . Gao, W. (2018). Controlled release and long-term antibacterial activity of dialdehyde nanofibrillated cellulose/silver nanoparticle composites. *ACS Sustainable Chemistry and Engineering*, 7(1), 1146-1158.
- Lichtenstein, K., and Lavoine, N. (2017). Toward a deeper understanding of the thermal degradation mechanism of nanocellulose. *Polymer degradation and stability*, 146, 53-60.
- Lindh, J., Ruan, C., Strømme, M., and Mihranyan, A. (2016). Preparation of porous cellulose beads via introduction of diamine spacers. *Langmuir*, 32(22), 5600-5607.
- Liu, K., Lin, X., Chen, L., Huang, L., Cao, S., and Wang, H. (2013). Preparation of microfibrillated cellulose/chitosan-benzalkonium chloride biocomposite for enhancing antibacterium and strength of sodium alginate films. *Journal of Agricultural Food Chemistry*, 61, 6562 - 6567.
- Liu, X. D., Nishi, N., Tokura, S., and Sakairi, N. (2001). Chitosan coated cotton fiber: preparation and physical properties. *Carbohydrate Polymers*, 44(3), 233-238.
- Loke, W. K., Lau, S. K., Yong, L. L., Khor, E., and Sum, C. K. (2000). Wound dressing with Sustained Anti-microbial Capability. *Journal of Biomedical Materials Research*, 53(1), 8 - 17.
- Ma, B., Huang, Y., Zhu, C., Chen, C., Chen, X., Fan, M., and Sun, D. (2016). Novel Cu@SiO₂/bacterial cellulose nanofibers: Preparation and excellent performance in antibacterial activity. *Material Science Engineering*, 62, 656 - 661.

- Madivoli, E. S., Kareru, P. G., Gachanja, A. N., Mugo, S. M., Murigi, M. K., Kairigo, P. K., . . . Njunge, F. K. (2016). Adsorption of selected heavy metals on modified nanocellulose. *International Research Journal of Pure and Applied Chemistry*, 12(3), 1-9.
- Makarov, V. V., Love, A. J., Sinitsyna, O., Makarova, S. S., Yamnsky, I. V., Taliansky, M. E., and Kalinina, N. O. (2014). Green nanotechnologies: synthesis of metal nanoparticles using plants. *Acta Nature*, 6(1), 35-44.
- Markova, Z., Novak, P., Kaslik, J., Plachtova, P., Brazdova, M., Jancula, D., . . . Varma, R. (2014). Iron (II, III)–polyphenol complex nanoparticles derived from green tea with remarkable ecotoxicological impact. *ACS Sustainable Chemistry and Engineering*, 2(7), 1674-1680.
- Marslin, G., Siram, K., Maqbool, Q., Selvakesavan, R. K., Kruszka, D., Kachlicki, P., and Franklin, G. (2018). Secondary Metabolites in the Green Synthesis of Metallic Nanoparticles. *Materials*, 11(6), 1-25.
- Martin, C., Low, W. L., Amin, M. C., Radecka, I., Raj, P., and Kenward, K. (2013). Current trends in the development of wound dressings, biomaterials and devices. *Pharmaceutical Patent Analyst*, 2(3), 341 - 359.
- Masood, N., Ahmed, R., Tariq, M., Ahmed, Z., Masoud, M. S., Ali, I., . . . Hasan, A. (2019). Silver nanoparticle impregnated chitosan-PEG hydrogel enhances wound healing in diabetes induced rabbits. *International Journal of Pharmaceutics*, 559, 23-36.
- Masum, M. M., Siddiqa, M. M., Ali, K. A., Zhang, Y., Abdallah, Y., Ibrahim, E., . . . Li, B. (2019). Biogenic Synthesis of Silver Nanoparticles Using Phyllanthus emblica Fruit Extract and Its Inhibitory Action Against the Pathogen *Acidovorax oryzae* Strain RS-2 of Rice Bacterial Brown Stripe. *Frontiers in Microbiology*, 10, 1-19.

- Mehdizadeh, T., Tajik, H., Rohani, S. M., and Oromiehie, A. R. (2012). Antibacterial, antioxidant and optical properties of edible starch-chitosan composite film containing *Thymus kotschyianus* essential oil. *Veterinary Research Forum*, 3(3), 167 - 173.
- Menon, M. P., Selvakumar, R., and Ramakrishna, S. (2017). Extraction and modification of cellulose nanofibres derived from biomass for environmental application. *RSC Advances*, 7(68), 42750 - 42773.
- Miller-Chou, B. A., and Koenig, J. L. (2003). A review of polymer dissolution. *Progress in Polymer Science*, 28(8), 1223-1270.
- Mirza, A. U., Kareem, A., Nami, S. A., Khan, M. S., Rehman, S., Bhat, S. A., . . . Nishat, N. (2018). Biogenic synthesis of iron oxide nanoparticles using *Agrewia optiva* and *Prunus persica* phyto species: Characterization, antibacterial and antioxidant activity. *Journal of Photochemistry and Photobiology B: Biology*, 185, 262-274.
- Mittal, A. K., Chisti, Y., and Banerjee, U. C. (2013). Synthesis of metallic nanoparticles using plant extracts. *Biotechnology advances*, 31(2), 346-356.
- Mohammad, Z., Khalid, M., and Mehdi, B. (2013). Chitin and chitosan based blends, composites and nanocomposites. In S. Thomas, M. P. Visakh, and A. P. Mathew, *Advances in natural polymers, composites and Nanocomposites* (pp. 55-119). Heidelberg: Springer.
- Moore, T. L., Rodriguez-Lorenzo, L., Hirsch, V., Balog, S., Urban, D., Jud, C., . . . Petri-Finks, A. (2015). Nanoparticle colloidal stability in cell culture media and impact on cellular interactions. *Chemical Society Reviews*, 44(17), 6287-6305.
- Mos, Y. M., Vermeulen, A. C., Buisman, C. J., and Weijma, J. (2018). X-Ray Diffraction of Iron Containing Samples: The Importance of a Suitable Configuration. *Geomicrobiology Journal*, 35(6), 511-517.

- Mou, K., Li, J., Wang, Y., Cha, R., and Jiang, X. (2017). 2, 3-Dialdehyde nanofibrillated cellulose as a potential material for the treatment of MRSA infection. *Journal of Materials Chemistry B*, 5(38), 7876-7884.
- Mullah, M. F., Joseph, L., Arfat, Y. A., and Ahmed, J. (2017). Thermal Properties of Gelatin and Chitosan. In J. Ahmed, *Glass Transition and Phase Transitions in Food and Biological Materials* (pp. 281-304). Chichester, West Sussex: John Wiley and Sons Ltd.
- Murigi, M. K., Madivoli, E. S., Mathenyu, M. M., Kareru, P. G., Gachanja, A. N., Njenga, P. K., . . . Githua, M. (2014). Comparison of physicochemical characteristics of microcrystalline cellulose from four abundant kenyan biomasses. *Journal of Polymer and Textile engineering*, 1(2), 53-63.
- Nascimento, P., Marim, R., Carvalho, G., and Mali, S. (2016). Nanocellulose Produced from Rice Hulls and its Effect on the Properties of Biodegradable Starch Films. *Materials Research*, 19(1), 167 - 174.
- Ndikau, M., Noah, N. M., Andala, D. M., and Masika, E. (2017). Green synthesis and characterization of silver nanoparticles using *Citrullus lanatus* fruit rind extract. *International Journal of Analytical Chemistry*, 2017, 1-10.
- Neidrauer, M., Ercan, U. K., Bhattacharyya, A., Samuels, J., Sedlak, J., Trikha, R., . . . Suresh, G. J. (2014). Antimicrobial efficacy and wound-healing property of a topical ointment containing nitric-oxide-loaded zeolites. *Journal of Medical Microbiology*, 63(2), 203 - 209.
- Nematdoust, S., Najjar, R., Bresser, D., and Passerini, S. (2020). Partially Oxidized Cellulose grafted with Polyethylene Glycol mono-Methyl Ether (m-PEG) as Electrolyte Material for Lithium Polymer Battery. *Carbohydrate Polymers*, 240(2020), 1-10.

- Nicharat, A., Sapkota, J., Weder, C., and Foster, E. J. (2015). Melt processing of polyamide 12 and cellulose nanocrystals nanocomposites. *Journal of Applied Polymer Science*, 132(45), 1-10.
- Nishihara, Y., Nakajima, Y., Akashi, A., Tsujino, N., Takahashi, E., Funakoshi, K. I., and Higo, Y. (2012). Isothermal compression of face-centered cubic iron. *American Mineralogist*, 97((8-9)), 1417-1420.
- Nypelo, T., Amer, H., Konnerth, J., Potthast, A., and Rosenau, T. (2018). Self-Standing Nanocellulose Janus-Type Films with Aldehyde and Carboxyl Functionalities. *Biomacromolecules*, 19(3), 973-979.
- Ooko, E. A., Muchiri, M. N., Kamondo, B., Ochieng, D., Tuwei, P., and Wanjiku, J. (2009). Evaluation of anti-microbial activity of *Osyris lanceolata* (East African Sandalwood). In *Recent advances in forestry research for environmental conservation, improved livelihood and economic development. Proceedings of the 4th KEFRI Scientific Conference* (pp. 166-171). Nairobi: Kenya Forestry Research Institute.
- Osterling, S. R. (2015). Distributions Of Fiber Characteristics As A Tool To Evaluate Mechanical Pulps. *Doctrol dissertation submitted to Mid Sweden University*.
- Ouellette, R. J., and Rawn, D. J. (2019). *Principles of Organic chemistry*. Amsterdam, Netherlands: Elsevier.
- Pawar, B. G., Pinjari, D. V., Kolekar, S. S., Pandit, A. B., and Han, S. H. (2012). Effect of Sintering Temperatures on the Synthesis of SnO₂ Nanospheres. *ISRN Chemical Engineering*, 2012, 1-8.
- Peng, Y., Han, Y., and Gardner, D. J. (2012). Spray-drying cellulose nanofibrils: effect of drying process parameters on particle morphology and size distribution. *Wood and Fibre Science*, 44(4), 448 - 461.

- Phan, C. M., and Nguyen, H. M. (2017). Role of Capping Agent in Wet Synthesis of Nanoparticles. *The Journal of Physical Chemistry A*, 121(17), 3213-3219.
- Pinto, R. J., Neves, M. C., Neto, C. P., and Trindade, T. (2012). Composites of Cellulose and Metal Nanoparticles. In F. Ebrahimi, *Nanocomposites—New Trends and Developments* (pp. 1-26). London: Intech Open.
- Plappert, S. F., Quraishi, S., Pircher, S., Mikkonen, K. S., Veigel, S., Klinger, K. M., . . . Leibner, F. W. (2018). Transparent, flexible and strong 2, 3-dialdehyde cellulose films with high oxygen barrier properties. *Biomacromolecules*, 19(7), 2969-2978.
- Poletto, M. (2016). Thermal degradation and morphological aspects of four wood species used in lumber industry. *Revista Árvore*, 40(5), 941-948.
- Poletto, M., Ornaghi, H. L., and Zattera, A. J. (2014). Native cellulose: structure, characterization and thermal properties. *Materials*, 7(9), 6105 - 6119.
- Poletto, M., Pistor, V., and Zattera, A. J. (2013). Structural characteristics and thermal properties of native cellulose. In T. Van de Ven, and L. Godbout (Eds.), *Cellulose - Fundamental aspects* (pp. 45 - 68). Croatia: Intech Open. doi:10.5772/2705
- Ponce, C., Chanona, J., Garibay, V., Palacios, E., Calderon, G., and Sabo, R. (2013). Functionalization of Agave Cellulose Nanoparticles and its Characterization by Microscopy and Spectroscopy Techniques. *Microscopy and Microanalysis*, 19(S2): 200 - 201.
- Priebe, M., and Fromm, K. M. (2015). Nanorattles or Yolk–Shell Nanoparticles—What Are They, How Are They Made, and What Are They Good For?. *Chemistry—A European Journal*, 21(10), 3854-3874.
- Priebe, M., Widmer, J., Lova, N. S., Abram, S. L., Mottas, I., Woischnig, A. K., . . . Fromm, K. (2017). Antimicrobial silver-filled silica nanorattles with low

- immunotoxicity in dendritic cells. *Nanomedicine: Nanotechnology, Biology and Medicine*, 13(1), 11-22.
- Rabea, E. I., Badawy, M. T., Stevens, C. V., Smagghe, G., and Steurbaut, W. (2003). Chitosan as antimicrobial agent: applications and mode of action. *Biomacromolecules*, 4(6), 1457-1465.
- Rautaray, D., Ahmad, A., and Sastry, M. (2003). Biosynthesis of CaCO₃ crystals of complex morphology using a fungus and an actinomycete. *Journal of the American Chemical Society*, 125(48), 14656-14657.
- Raveendran, P., Fu, J., and Wallen, S. L. (2003). Completely “green” synthesis and stabilization of metal nanoparticles. *Journal of American Chemical Society*, 125(6), 13940 - 13941.
- Rezaei-Zarchi, S., Javeed Ghani, M., Soufian, S., Barzegari Firouzabadi, F., Bayanduri Moghaddam, A., and Mirjalili, S. H. (2010). Comparative study of antimicrobial activities of TiO₂ and CdO nanoparticles against the pathogenic strain of *Escherichia coli*. *Iranian Journal of Pathology*, 5(2), 83-89.
- Rhim, J. W., and Wang, L. F. (2014). Preparation and characterization of carrageenan-based nanocomposite films reinforced with clay mineral and silver nanoparticles. *Applied Clay Science*, 97, 174-181.
- Rhim, J. W., Park, H. M., and Hac, C. S. (2013). Bio-nanocomposites for food packaging applications. *Progress in Polymer Science*, 38(10), 1629– 1652.
- Ring, G. J., and Bacon, A. J. (1997). Multiple component analysis of fiber length distributions. *Tappi journal*, 80(1), 224 - 231.
- Riva, R., Ragelle, H., des Rieux, A., Jerome, C., Duhem, N., and Preat, V. (2011). Chitosan and Chitosan Derivatives in Drug Delivery and Tissue Engineering.

- In R. Jayakumar, M. Prabakaran, and R. Muzzarelli, *Chitosan for Biomaterials II* (pp. 19 - 37). Berlin: Springer.
- Roemhild , K., Wiegand, C., Hipler, U. C., and Heinze, T. (2013). Novel bioactive amino-functionalized cellulose nanofibers. *Macromolecules. Rapid communication*, *34*, 1767 - 1771.
- Rojas, J., Bedoya, M., and Ciro, Y. (2015). Current trends in the production of cellulose nanoparticles and nanocomposites for biomedical applications. In *Cellulose-Fundamental Aspects and Current Trends* (pp. 193-228). Vigo, Spain: Intech.
- Roy, D., Knapp, J. S., Guthrie, J. T., and Perrier, S. (2008). Antibacterial cellulose fiber via RAFT surface graft polymerization. *Biomacromolecules*, *9*, 91 - 99.
- Ruan, C. Q., Stromme, M., and Lindh, J. (2018). Preparation of porous 2,3-dialdehyde cellulose beads crosslinked with chitosan and their application in adsorption of Congo red dye. *Carbohydrate Polymers*, *181*, 200-207.
- Rwegasila , E., Mubofu, E. B., Nyandoro, S. S., Erasto, P., and Munissi, J. J. (2016). Preparation, Characterization and in Vivo Antimycobacterial Studies of Panchovillin-Chitosan. *International Journal of Molecular Sciences*, *17*(10), 1559.
- Saif, S., Tahir, A., and Chen, Y. (2016). Green synthesis of iron nanoparticles and their environmental applications and implications. *Nanomaterials*, *6*(11), 2-26.
- Saini, S., Belgacem, M. N., Salon, M. B., and Bras, J. (2016). Non leaching biomimetic antimicrobial surfaces via surface functionalisation of cellulose nanofibers with aminosilane. *Cellulose*, *23*, 1 - 16.

- Scarano, G., and Morelli, E. (2002). Characterization of cadmium- and lead-phytochelatin complexes formed in a marine microalga in response to metal exposure. *Biometals*, 15(2), 145-151.
- Sebastian, A., Nangia, A., and Prasad, M. N. (2018). A green synthetic route to phenolics fabricated magnetite nanoparticles from coconut husk extract: Implications to treat metal contaminated water and heavy metal stress in *Oryza sativa* L. *Journal of Cleaner Production*, 174, 355-366.
- Segal, L. G., Creely, J. J., Martin Jr, A. E., and Conrad, C. M. (1959). An empirical method for estimating the degree of crystallinity of native cellulose using the X-ray diffractometer. *Textile Research Journal*, 29(10), 786-794.
- Shah, M., Fawcett, D., Sharma, S., Tripathy, S. K., and Poinern, G. E. (2015). Green synthesis of metallic nanoparticles via biological entities. *Materials*, 8(11), 7278-7308.
- Shen, Y. (2015). Carbothermal synthesis of metal-functionalized nanostructures for energy and environmental applications. *Journal of Materials Chemistry A*, 3(25), 13114-13188.
- Shen, X., Shamshina, J. L., Berton, P., Gurau, G., and Rogers, R. D. (2016). Hydrogels based on cellulose and chitin: fabrication, properties, and applications. *Green Chemistry*, 18(1), 53 - 75.
- Silhavy, T. J., Kahne, D., and Walker, S. (2010). The Bacterial cell envelope. *Cold Spring Harbor Perspectives in Biology*, 1-16.
- Simić, A., Manojlović, D., Šegan, D., and Todorović, M. (2007). Electrochemical behavior and antioxidant and prooxidant activity of natural phenolicS. *Molecules*, 12(10), 2327-2340.

- Sinha, V. R., Singla, A. K., Wadhawan, S., Kaushik, R., Kumria, R., Bansal, K., and Dhawan, S. (2004). Chitosan microspheres as potential carrier for drugs. *International Journal of Pharmaceutics*, 274(1), 1 - 33.
- Siracusa, V. (2019). Microbial degradation of synthetic biopolymers waste. *Polymers*, 11, 1-18.
- Slavin, Y. N., Asnis, J., Hafeli, U. O., and Bach, H. (2017). Metal nanoparticles: understanding the mechanisms behind antibacterial activity. *Journal of Nanobiotechnology*, 15(1), 65.
- Socrates, G. (2004). *Infrared and Raman characteristic group frequencies: tables and charts*. West Sussex: John Wiley and Sons.
- Somchaidee, P., and Tedsree, K. (2018). Green synthesis of high dispersion and narrow size distribution of zero-valent iron nanoparticles using guava leaf (*Psidium guajava* L) extract. *Advances in Natural Sciences: Nanoscience and Nanotechnology*, 9(3), 1-9.
- Son, W. K., Youk, J. H., and Park, W. H. (2006). Antimicrobial cellulose acetate nanofibers containing silver nanoparticles. *Carbohydrate Polymers*, 65, 430 - 434.
- Stanckic, S., Suman, S., Haque, F., and Vidic, J. (2016). Pure and multi metal oxide nanoparticles: synthesis, antibacterial and cytotoxic properties. *Journal of Nanobiotechnology*, 14(1), 1-20.
- Stevens, E. S., and Poliks, M. D. (2003). Tensile Strength Measurements on Biopolymer Films. *Journal of Chemical Education*, 80(7), 810-812.
- Sudhakar, Y. N., Selvakumar, M., and Krishna Bhat, D. (2018). Biopolymer Electrolytes Fundamental applications in energy storage. In Y. N. Sudhakar, M. Selvakumar, and D. Krishna Bhat, *Biopolymer Electrolytes* (pp. 35-52). Amsterdam: Elsevier.

- Szczęsna-Antczak, M., Kazimierczak, J., and Antczak, T. (2012). Nanotechnology-Methods of Manufacturing Cellulose Nanofibres. *Fibres and Textiles in Eastern Europe*, 2(91), 8 - 12.
- Szymańska-Chargot, M., Chylińska, M., Pertile, G., Pieczywek, P. M., Cieślak, K. J., Zdunek, A., and Frac, M. (2019). Influence of chitosan addition on the mechanical and antibacterial properties of carrot cellulose nanofibre film. *Cellulose*, 26(18), 9613-9629.
- Tanigawa, J., Miyoshi, N., and Sakurai, K. (2008). Characterization of chitosan/citrate and chitosan/acetate films and applications for wound healing. *Journal of Applied Polymer Science*, 110(1), 608 - 615.
- Tao, G., Cai, R., Wang, Y., Song, K., Guo, P., Zhao, P., . . . He, H. (2017). Biosynthesis and Characterization of AgNPs–Silk/PVA Film for Potential Packaging Application. *Materials*, 10(6).
- Tarley, C. T., and Arruda, M. Z. (2004). Biosorption of heavy metals using rice milling by-products. Characterization and application for removal of metals from aqueous. *Chemosphere*, 54(7), 987 - 995.
- Terinte, N., Ibbert, R., and Schuster, K. C. (2011). Overview on native cellulose and microcrystalline cellulose I structure studied by X-ray diffraction (WAXD): Comparison between measurement techniques. *Lenzinger Berichte*, 89, 118-131.
- Thai, H., Nguyen, C. T., Thach, L. T., Tran, M. T., Mai, H. D., Nguyen, T. T., . . . Le, Q. V. (2020). Characterization of chitosan/alginate/lovastatin nanoparticles and investigation of their toxic effects in vitro and in vivo. *Scientific Reports*, 10(1), 1-15.
- Tian, T., Shi, X., Cheng, L., Luo, Y., Dong, Z., Gong, H., and Liu, Z. (2014). Graphene-based nanocomposite as an effective, multifunctional, and

recyclable antibacterial agent. *ACS Applied Materials and Interfaces*, 6(11), 8542 - 8548.

Torres, F. G., Troncoso, O. P., Torres, C., and Grande, C. J. (2013). Cellulose Based Blends, Composites and Nanocomposites. In T. Sabu, P. M. Visakh, and A. Mathew, *Advances in Natural Polymers, Composites and Nanocomposites* (pp. 21 - 54). Berlin: Springer.

Truskewycz, A., Shukla, R., and Ball, A. S. (2018). Phytofabrication of Iron Nanoparticles for Hexavalent Chromium Remediation. *ACS Omega*, 3(9), 10781-10790.

Vanaja, M., Paulkumar, K., Baburaja, M., Rajeshkumar, S., Gnanajobitha, G., Malarkodi, C., . . . Annadurai, G. (2014). Degradation of methylene blue using biologically synthesized silver nanoparticles. *Bioinorganic Chemistry and Applications*, 2014, 1-9.

Varshney, V. K., and Sanjay, N. (2011). Chemical Functionalization of Cellulose Derived from Nonconventional Sources. *Cellulose fibres: Bio and Nano-polymer composites*, 43 - 60.

Vasylevskiy, S., Kracht, S., Corcosa, P., Fromm, K. M., Giese, B., and Fueg, M. (2017). Formation of Silver Nanoparticles by Electron Transfer in Peptides and c- Cytochromes. *Angewandte Chemie International Edition*, 56(21), 5926-5930.

Vicente, A. A., Cerqueira, M. A., Hilliou, L., and Rocha, C. R. (2011). Protein-based resins for food packaging. In J. M. Lagaron, *Multifunctional and nanoreinforced polymers for food packaging* (pp. 610-648). Cambridge: Woodhead Publishing.

Vizireanu, S., Panaitescu, D. M., Nicolae, C. A., Frone, A. N., Chiulan, I., Ionita, M. D., . . . Dinescu, G. (2018). Cellulose defibrillation and functionalization by plasma in liquid treatment. *Scientific Reports*, 8(1), 1-14.

- Wang, L., Gardner, D. J., and Bousfield, D. W. (2017). Cellulose nanofibril-reinforced polypropylene composites for material extrusion: Rheological properties. *Polymer Engineering and Science*, 1-8. doi:10.1002/pen.24615
- Wang, L., Hu, C., and Shao, L. (2017). The antimicrobial activity of nanoparticles: present situation and prospects for the future. *International Journal of Nanomedicine*, 12, 1227-1249.
- Wang, S., and Copeland, L. (2012). New insights into loss of swelling power and pasting profiles of acid hydrolyzed starch granules. *Starch-Starke*, 64(7), 538-544.
- Wang, Z., Fang, C., and Megharaj, M. (2014). Characterization of iron–polyphenol nanoparticles synthesized by three plant extracts and their fenton oxidation of azo dye. *ACS Sustainable Chemistry and Engineering*, 2(4), 1022-1025.
- Wasiak, J., Cleland, H., Campbel, F., and Spinks, A. (2013). Dressing for superficial and partial thickness burns. *Cochrane Database of of Systematic reviews*(3), 1 - 88. doi:10.1002/14651858.CD002106.pub4.
- Wei, J., Du, C., Liu, H., Chen, Y., Yu, H., and Zhou, Z. (2016). Preparation and characterization of aldehyde-functionalized cellulosic fibers through periodate oxidization of bamboo pulp. *BioResources*, 11(4), 8386-8395.
- Weng, X., Huang, L., Chen, Z., Megharaj, M., and Naidu, R. (2013). Synthesis of iron-based nanoparticles by green tea extract and their degradation of malachite. *Industrial Crops and Products*, 51, 342-347.
- WHO. (2014). Antimicrobial resistance global report on surveillance. *World Health Organization*.
- Woo, H., Park, J., Lee, S., and Lee, S. (2014). Effects of washing solution and drying condition on reactivity of nano-scale zero valent irons (nZVIs) synthesized by borohydride reduction. *Chemosphere*, 97, 146 - 152.

- Xu, Q., Jin, L., Wang, Y., Chen, H., and Qin, M. (2019). Synthesis of silver nanoparticles using dialdehyde cellulose nanocrystal as a multi-functional agent and application to antibacterial paper. *Cellulose*, 26(2), 1309-1321.
- Xue, Y., Xiao, H., and Zhang, Y. (2015). Antimicrobial polymeric materials with quaternary ammonium and phosphonium salts. *International Journal of Molecular Sciences*, 16(2), 3626 - 3655.
- Yang, H., Chen, D., and Van de ven, T. G. (2015). Preparation and characterization of sterically stabilized nanocrystalline cellulose obtained by periodate oxidation of cellulose fibers. *Cellulose*, 22(3), 1743-1752.
- Yang, H., Sheikhi, A., and Van de Ven, T. G. (2016). Reusable green aerogels from cross-linked hairy nanocrystalline cellulose and modified chitosan for dye removal. *Langmuir*, 32, 11771-11779.
- Yang, J., Kwon, G. J., Hwang, K., and Kim, D. Y. (2018). Cellulose–Chitosan Antibacterial Composite Films Prepared from LiBr Solution. *Polymers*, 10(10), 1-7.
- Yang, X., Tu, Y., Li, L., Shang, S., and Tao, X. M. (2010). Well-dispersed chitosan/graphene oxide nanocomposites. *ACS Applied Materials and Interfaces*, 2(6), 1707 - 1713.
- Yasmeen, S., Kabiraz, M. K., Saha, B., Qadir, R., Gafur, A., and Masum, S. (2016). Chromium (VI) ions Removal from Tannery Effluent using Chitosan Microcrystalline Cellulose Composite as Adsorbent. *International Research Journal of Pure and Applied Chemistry*, 10(4), 1 - 14.
- Yildirim, N., and Shaler, S. (2017). A study on thermal and nanomechanical performance of cellulose nanomaterials (CNs). *Materials*, 10(7), 1-12.
- Yuan, Y., Chestnutt, B. M., Haggard, W. O., and Bumgardner, J. D. (2011). Deacetylation of chitosan: Material characterization and in vitro evaluation

via albumin adsorption and pre-osteoblastic cell cultures. *Materials*, 4(8), 1399-1416.

Yun'an Qing, L. C., Li, R., Liu, G., Zhang, Y., Tang, X., Wang, J., . . . Qin, Y. (2018). Potential antibacterial mechanism of silver nanoparticles and the optimization of orthopedic implants by advanced modification technologies. *International Journal of Nanomedicine*, 13, 3311-3327.

Zaidan, M. R., Noor Rain, A., Badrul, A. R., Adlin, A., Norazah, A., and Zakiah, I. (2005). In vitro screening of five local medicinal plants for antibacterial activity using disc diffusion method. *Tropical Biomedicine*, 22(2), 165 - 170.

Zhang, J., and Guyot, F. (1999). Thermal equation of state of iron and Fe 0.91 Si 0.09. *Physics and Chemistry of Minerals*, 26(3), 206-211.

Zhang, K., Huang, T. S., Yan, H., Hu, X., and Ren, T. (2020). Novel pH-sensitive films based on starch/polyvinyl alcohol and food anthocyanins as a visual indicator of shrimp deterioration. *International Journal of Biological Macromolecules*, 145, 768-776.

Zhang, L., Ge, H., Xu, M., Cao, J., and Dai, Y. (2017). Physicochemical properties, antioxidant and antibacterial activities of dialdehyde microcrystalline cellulose. *Cellulose*, 24(5), 2287-2298.

Zhang, X. Z., and Zhang, Y. H. (2013). Cellulases: characteristics, sources, production, and applications. In S. T. Yang, H. El-Ensashy, and T. Nutta, *Bioprocessing Technologies in Biorefinery for Sustainable Production of Fuels, Chemicals, and Polymers* (pp. 131-146). New Jersey : John Wiley and Sons.

Zhang, Y., Zheng, R., Ma, F., Zhang, Y., and Meng, Q. (2014). Characterization of Treated Rice Husk Adsorbent and Adsorption of Copper (II) from Aqueous Solution. *Biomed Research International*, 2014, 1 - 8.

- Zhou, Y., Saito, T., Bergstrom, L., and Isogai, A. (2018). Acid-Free Preparation of Cellulose Nanocrystals by TEMPO Oxidation and Subsequent Cavitation. *Biomacromolecules*, 19(2), 633-639.
- Zimet, P., Momburu, A. W., Momburu, D., Castro, A., Villanueva, J. P., Pardo, H., and Rufo, C. (2019). Physico-chemical and antilisterial properties of nisin-incorporated chitosan/carboxymethyl chitosan films. *Carbohydrates Polymers*, 219, 334-343.

APPENDICES

Appendix I: Peak temperatures, enthalpy of cellulose obtained from DSC curves

	T₁ (°C)	T_m (°C)	ΔH(J/g) (°C)	T₃ (°C)	T₄ (°C)
ATRH	104	242	-21.4	352	481
RHCE	108	340	-17.2	360	488
MTCE	121	246	-46.0	360	-
USCE	120	318	-20.8	346	483

APPENDIX II: Degradation temperatures and residual ash of rice husk after different treatment

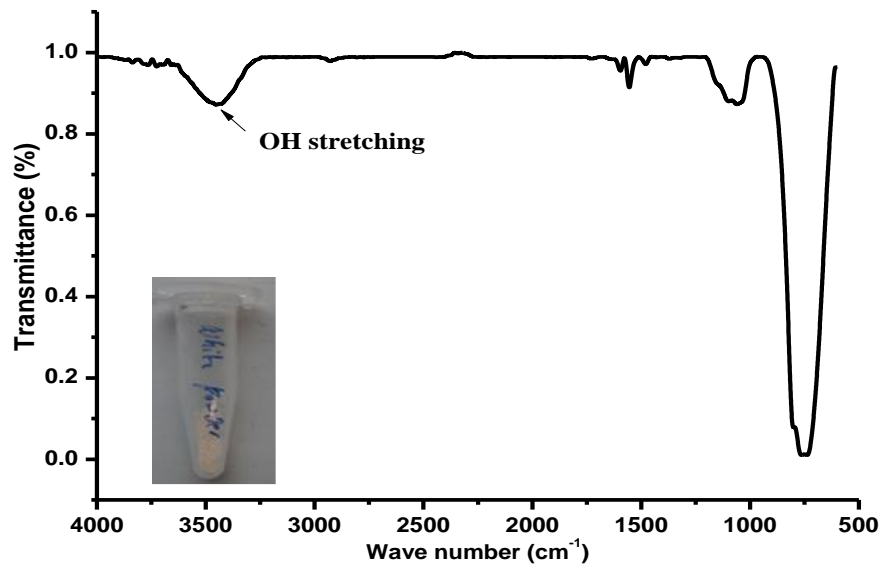
Sample	T₁(°C)	T₂(°C)	T₃(°C)	Residual Ash (%)
ATRH	60	310	-	40.7
RHCE	60	352	-	15.1
MTCE	60	298	-	24.2
USCE	60	335	-	11.0
TOCNF	60	247	302	27.5

**Appendix III: ANOVA of the effect KIO₃ concentration variation on the DO of
DAC**

Source of Variation	SS	df	MS	F	P-value	F crit
Between Groups	52.26	8	6.53	750.75	8.63E-12	3.23
Within Groups	0.078	9	0.009			
Total	52.33	17				

Appendix IV: ANOVA of the effect of reaction time variation on the DO of DAC

Source of Variation	SS	df	MS	F	P-value	F crit
Between Groups	55.95	7	7.9	5.46	1.45E-2	3.50
Within Groups	11.72	8	1.46			
Total	67.65	15				



Appendix V: FT-IR Spectra of KIO_3 generated after the oxidation of Cellulose with KIO_4 .

Appendix VI: Peak temperatures, enthalpy of DAC obtained from DSC curves.

Sample	T_{Peak 1} (°C)	T_{Peak 2} (°C)	T_{Peak 3} (°C)
D1	103	200	352
D2	102	201	362
D3	100	202	355
D4	102	196	349
D5	102	207	357
D6	102	186	334
D7	106	205	351
D8	109	200	323

Appendix VII: Peak temperature and residual ash of DAC with different DO

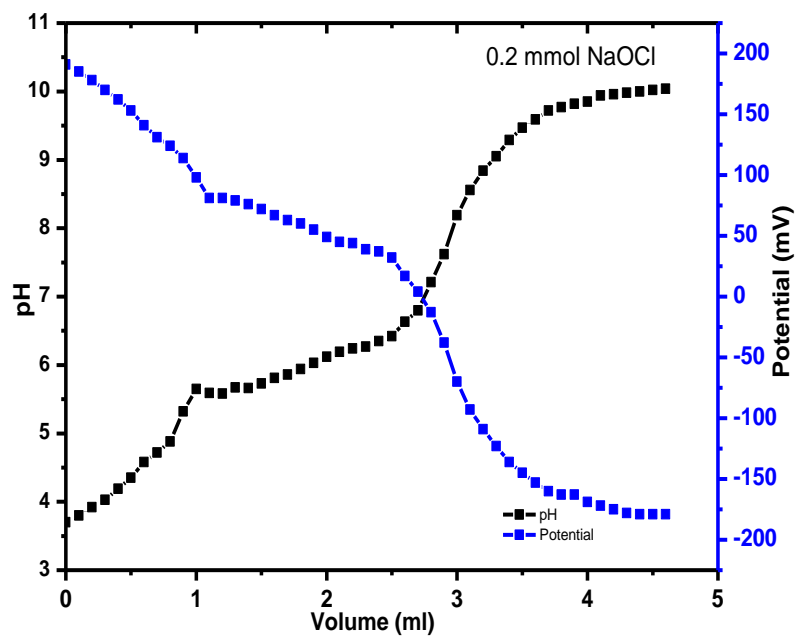
Sample	T₁(°C)	T₂(°C)	T₃(°C)	T₄(°C)	Residual Ash (%)
D1	43	201	343	-	14.8
D2	55	274	349	-	15.2
D3	51	253	330	-	17.2
D4	63	269	339	-	22.3
D5	49	210	345	-	15.6
D6	61	211	294	450	35.4
D7	61	208	337	-	19.2
D8	71	206	323	-	30.2

Appendix VIII: Peak temperature and residual ash of DAC with different DO

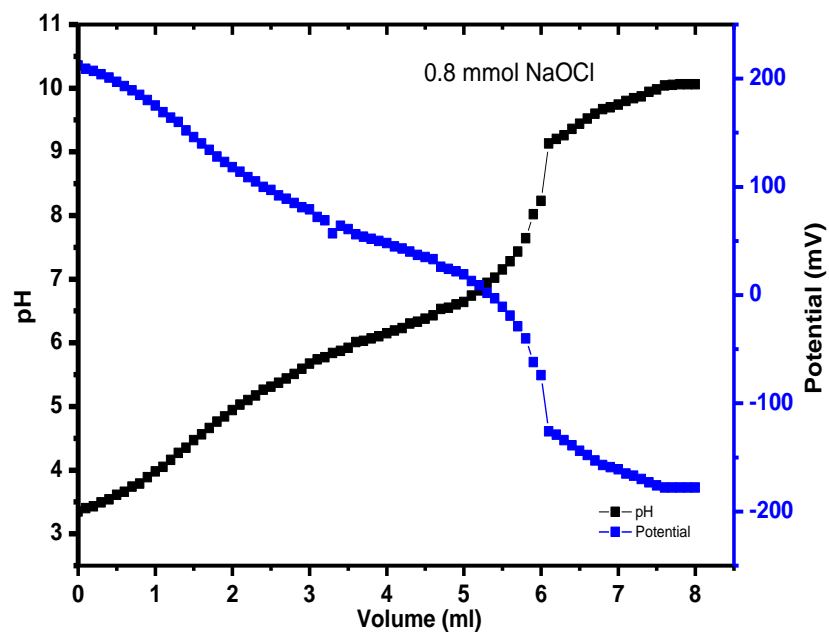
Oxidation Time	T₁(°C)	T₂(°C)	T₃(°C)	T₄(°C)	Residual Ash (%)
0.5 h	62	190	328	-	26.6
1 h	62	190	333	-	28.2
2 h	62	206	340	-	20.3
4 h	62	206	313	-	28.7
8 h	62	196	339	-	19.0
16 h	62	199	329	452	29.4
24 h	62	268	321	-	27.2

Appendix IX: Peak temperature and residual ash of DAC after different oxidation temperatures

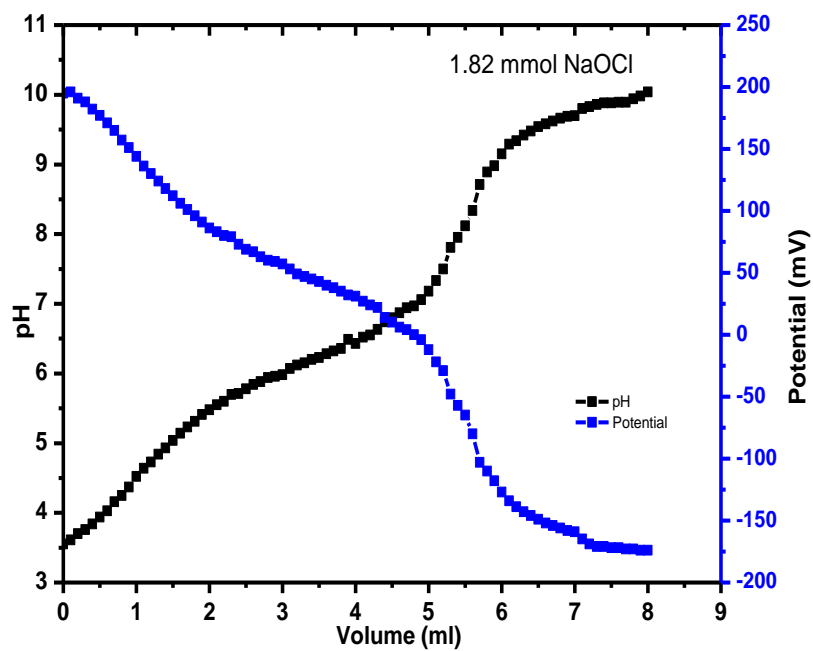
Sample	T₁(°C)	T₂(°C)	T₃(°C)	Residual Ash (%)
25°C	65	-	293	33.6
45°C	65	207	329	22.8
65°C	67	207	333	28.2



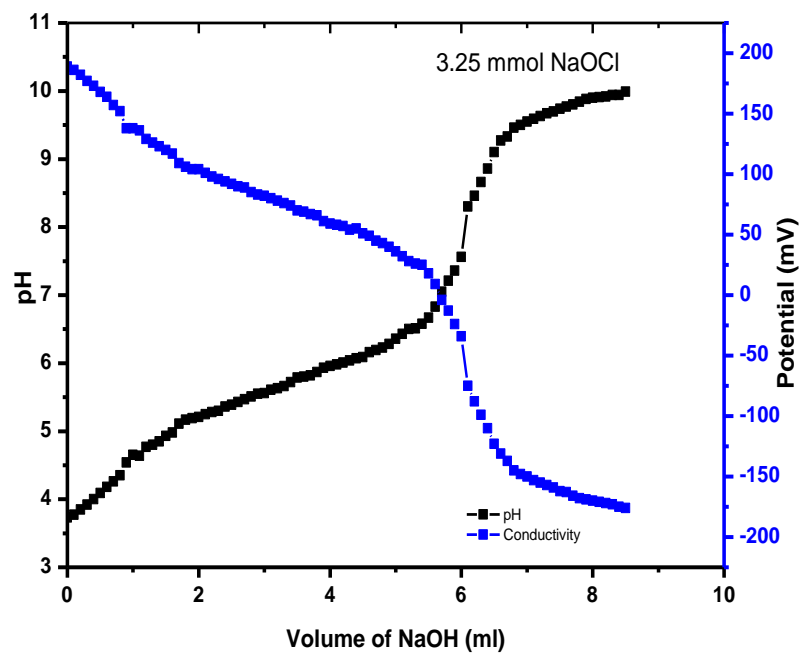
Appendix X: Potentiometric Titration of cellulose oxidized with 0.2 mmol NaOCl.



Appendix XI: Potentiometric Titration of cellulose oxidized with 0.8 mmol NaOCl.



Appendix XII: Potentiometric Titration of cellulose oxidized with 1.82 mmol NaOCl.



Appendix XIII: Potentiometric Titration of cellulose oxidized with 3.25 mmol NaOCl

**Appendix XIV: ANOVA of the effect NaOCl concentration variation on the DO
of TOCNF**

Source of Variation	SS	df	MS	F	P-value	F crit
Between Groups	33.84	4	8.46	179.03	1.39E-05	5.19
Within Groups	0.24	5	0.047			
Total	34.1	9				

**Appendix XV: ANOVA of the effect of cellulose source variation on the DO of
TOCNF**

Source of Variation	SS	df	MS	F	P-value	F crit
Between Groups	53.65	4	13.41	15.88	2.48E-4	3.49
Within Groups	8.45	10	0.847			
Total	62.1	14				

**Appendix XVI: Peak temperatures of TOCNF with different carboxyl content
obtained from DSC curves.**

[NaOCl] mM/g CE	T_{Peak 1} (°C)	T_{Peak 2} (°C)	ΔH(J/g) (°C)	T_{Peak 3} (°C)
T1 (0.05)	97	268	-63.5	354
T2 (0.2)	97	263	-317.8	347
T3 (0.8)	99	261	-277.8	337
T4 (1.82)	102	216		317
T5 (3.25)	102	237	-38.2	328

Appendix XVII: Peak temperature and residual ash of TOCNF with different oxidation time obtained from TGA-DTGA curves

Sample	T₁(°C)	T₂(°C)	Residual Ash (%)	DO
T1 (0.05)	63	321	13.3	2.21±0.11
T2 (0.2)	63	314	45.7	2.76±0.21
T3 (0.8)	57	323	22.6	3.90±0.34
T4 (1.82)	55	316	24.6	6.63±0.15
T5 (3.25)	63	323	38.6	6.37±0.16

Appendix XVIII: ANOVA of the effect of monochloroacetic acid concentration variation on the DS of chitosan

Source of Variation	SS	df	MS	F	P-value	F crit
Between Groups	1.24	6	0.21	1.75	0.181053	2.85
Within Groups	1.65	14	0.12			
Total	2.88	20				

Appendix XIX: ANOVA of the effect of monochloroacetic acid concentration variation on the swelling capacity of chitosan

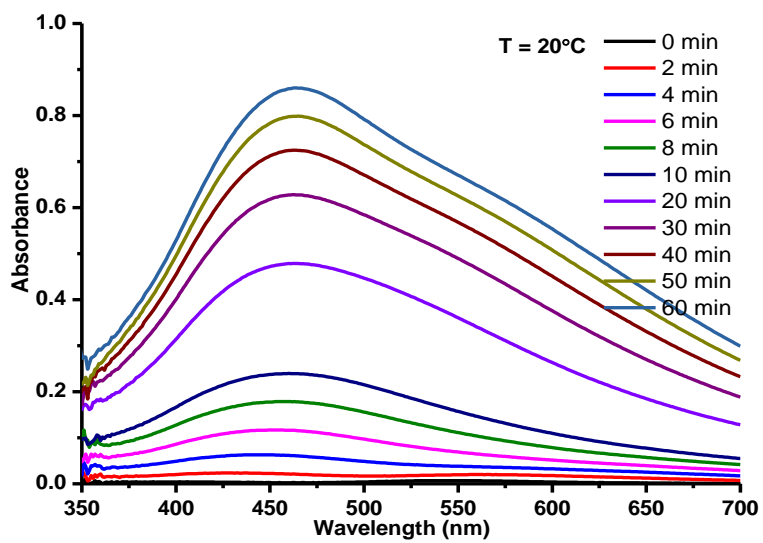
Source of Variation	SS	df	MS	F	P-value	F crit
Between Groups	541828.6	6	90304.76	116.34	3.95E-11	2.85
Within Groups	10866.67	14	776.19			
Total	552695.2	20				

Appendix XX: Peak temperatures, enthalpy of chitosan and carboxymethyl chitosan obtained from DSC curves.

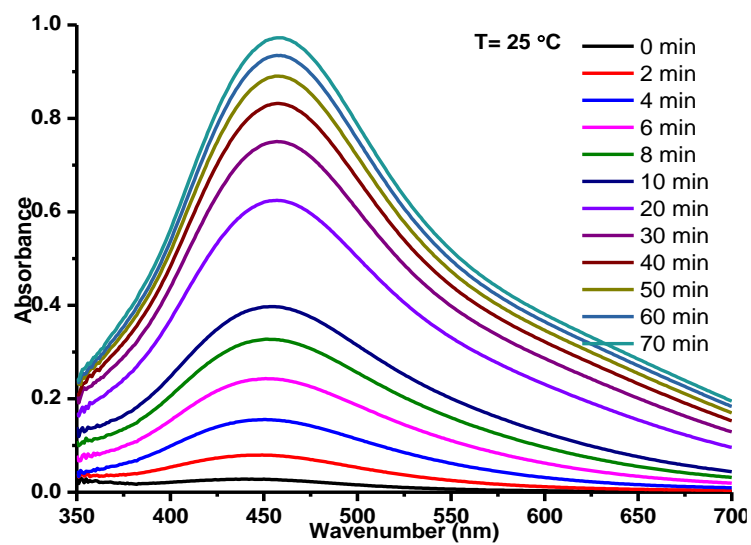
	T_{Peak 1} (°C)	T_{Peak 2} (°C)	T_{Peak 3} (°C)	T_{Peak 4} (°C)
COCS	102	121	268	304
ONCS	60	122	327	418
CMCS		92		

Appendix XXI: Peak temperature and residual ash of Chitosan (CS) and carboxymethyl chitosan (CMCS)

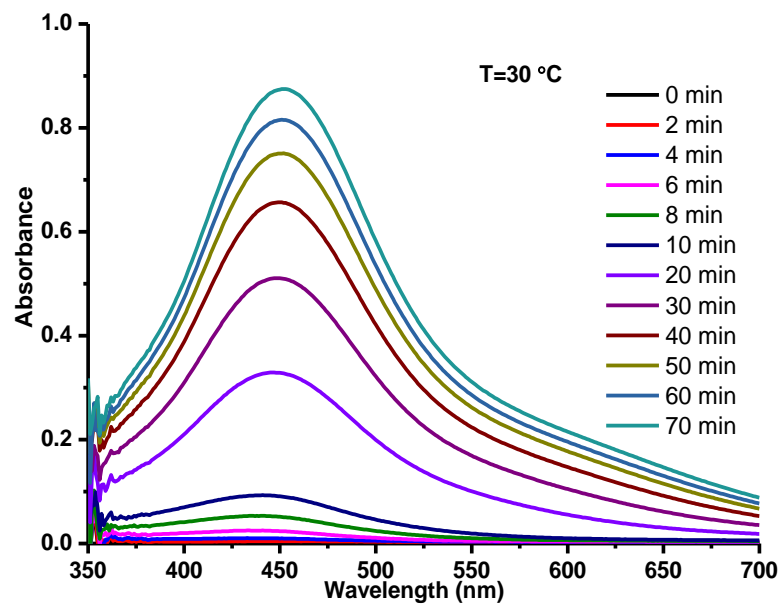
Sample	T₁(°C)	T₂(°C)	Residual Ash (%)
ONCS	68	460	89.6
COCS	64	300	38.7
CMCS	92	254	46.5



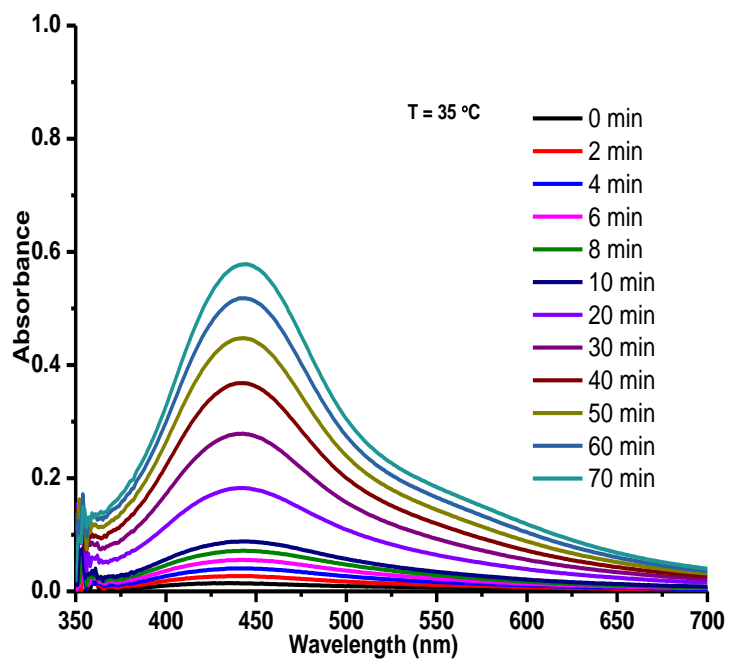
Appendix XXII: Biosynthesis of AgNPs using *L. trifolia* at 20 °C



Appendix XXIII: Biosynthesis of AgNPs using *L. trifolia* at 25 °C



Appendix XXIV: Biosynthesis of AgNPs using *L. trifolia* at 30 °C



Appendix XXV: Biosynthesis of AgNPs using *L. trifolia* at 35 °C

Appendix XXVI: Inhibition zones for standard antibiotics

Minimum inhibition zones (Mean \pm Standard deviation) in mm					
Antibiotic standards	EC	PA	CA	SA	BS
SX	17.0 \pm 1.4	14.0 \pm 0.0	9.0 \pm 0.0	8.0 \pm 0.0	12.0 \pm 0.0
GEN	13.0 \pm 0.0	9.0 \pm 0.0	NI	8.0 \pm 0.0	8.0 \pm 0.0
AMC	14.0 \pm 0.0	NI	NI	9.0 \pm 0.0	8.0 \pm 0.0
NX	28.0 \pm 0.0	14.0 \pm 0.0	NI	9 \pm 3	12.0 \pm 0.0
CTR	24.5 \pm 2.1	9.0 \pm 0.0	NI	32 \pm 1	NI
NIT	12.0 \pm 0.0	NI	NI	NI	8.0 \pm 0.0
OF	27.0 \pm 2.8	11.0 \pm 0.0	12.00 \pm 0.00	NI	9. \pm 1
NA	15.0 \pm 2.8	NI	NI	NI	9.0 \pm 0.0

KEY: SX: Sulphamethoxazole (25 μ g); GEN: Gentamicin (10 μ g); AMC: Amoxyclav (20/10 μ g); NX: Norfloxacin (10 μ g); CTR: Ceftriaxone (30 μ g); NIT: Nitrofurantoin (200 μ g); OF: Ofloxacin (10 μ g); NA: Nalidixic acid (30 μ g); NI: No inhibition; PA: *Pseudomonas aeruginosa*; BS: *Bacillus subtilis*; EC: *Escherichia coli*; CA: *Candida albicans*; SA: *Staphylococcus aureus*.

Appendix XXVII: ANOVA of the effect of glycerin content on the solubility of TOCNF-DAC-CS films

Source of Variation	SS	df	MS	F	P-value	F crit
Between Groups	575.06	4	143.77	12.73	7.83E-3	5.19
Within Groups	56.47	5	11.29			
Total	631.53	9				

Appendix XXVIII: ANOVA of the effect of glycerin content on the swelling of TOCNF-DAC-CS films

Source of Variation	SS	df	MS	F	P-value	F crit
Between Groups	14.46	4	3.61	0.51	0.73498	5.19
Within Groups	35.65	5	7.13			
Total	50.11	9				

Appendix XXIX: ANOVA of the effect of AgNPs content on the solubility of TOCNF-DAC-CS-AgNPs films

Source of Variation	SS	df	MS	F	P-value	F crit
Between Groups	256.62	4	64.15	30.49	1.05E-3	5.19
Within Groups	10.52	5	2.10			
Total	267.14	9				

Appendix XXX: ANOVA of the effect AgNPs content on the swelling of TOCNF-DAC-CS-AgNPs films

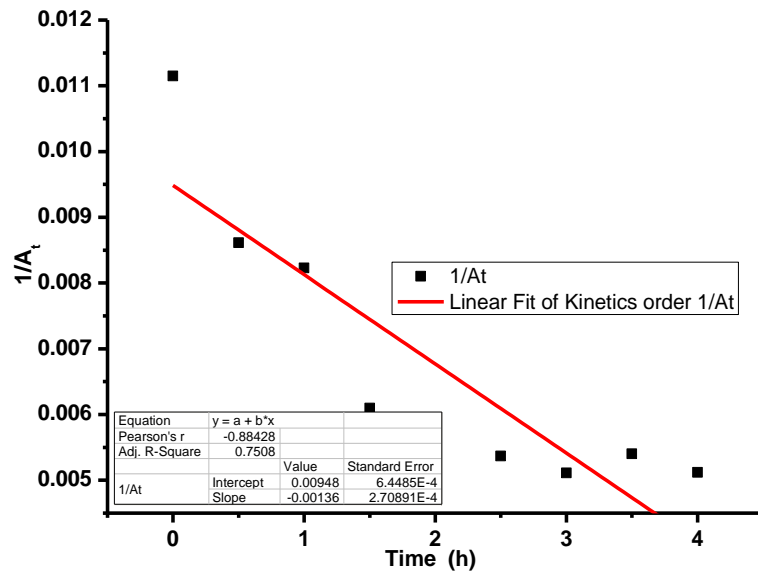
Source of Variation	SS	df	MS	F	P-value	F crit
Between Groups	20899.4	4	5224.84	396.17	1.94E-06	5.19
Within Groups	65.94	5	13.19			
Total	20965.3	9				

Appendix XXXI: ANOVA of the effect of TOCNF content on the solubility of TOCNF-DAC-CS-AgNPs films

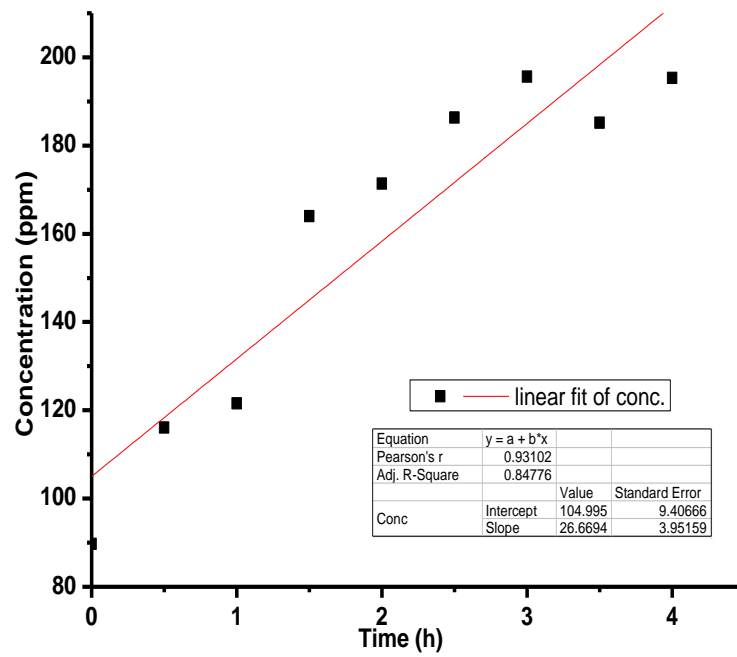
Source of Variation	SS	df	MS	F	P-value	F crit
Between Groups	596.35	4	149.10	22.03	2.25E-3	5.19
Within Groups	33.84	5	6.77			
Total	630.20	9				

**Appendix XXXII: ANOVA of the effect TOCNF content on the swelling of
TOCNF-DAC-CS-AgNPs films**

Source of Variation	SS	df	MS	F	P-value	F crit
Between Groups	348.86	4	87.22	16.28	2.23E-4	3.48
Within Groups	53.57	10	5.36			
Total	402.43	14				



Appendix XXXIII: Second order plot of silver ion release from composite films



Appendix XXXIV: Rate of silver ion released from composite films.

APPENDIX XXXV: PUBLICATION I



Research Article

Synthesis and characterization of dialdehyde cellulose nanofibers from *O. sativa* husks



Edwin Shigwenya Madivoli¹ · Patrick Gachoki Kareru¹ · Anthony Ngure Gachanja¹ · Samuel Mutuura Mugo² · David Sujee Makhanu³

© Springer Nature Switzerland AG 2019

Abstract

Periodate oxidation of cellulose breaks the C₂–C₃ bond of the glucose repeating units forming two vicinal aldehyde groups that are amenable to further reactions. In this article, effects of reaction conditions during the oxidation such as reaction time, oxidant concentration, and temperature on the aldehyde content were investigated and an optimized reaction condition identified. The synthesis of 2,3-dialdehyde cellulose (DAC) was confirmed by scanning electron microscopy, transmission electron microscopy (TEM), Fourier-transform infra-red spectroscopy (FT-IR), differential scanning calorimetry, thermal gravimetric analysis and wide-angle X-ray diffractometer (WXR). Formation of dialdehyde cellulose (DAC) was confirmed by the appearance of carbonyl peak in FT-IR spectra while a decrease in crystallinity of the fibers as a result of oxidation was confirmed by WXR. Morphological changes during oxidation were observed using SEM while the size of the fibers was confirmed by TEM, which showed the average length of the fibers decreased after oxidation as compared to native cellulose. Thermal degradation studies revealed that oxidation of cellulose decreased the thermal stability of the polymer as compared to native cellulose and was dependent on the aldehyde content. In conclusion, oxidation of native cellulose to dialdehyde cellulose had a profound effect on the thermal stability, degree of crystallinity, size and morphology of the polymer.

Keywords CNF · Dialdehyde cellulose · SEM · TEM · XRD · FTIR

1 Introduction

Cellulose, a linear polysaccharide comprising of glucose units cross linked with β-1,4-glycosidic bonds, is one of the most abundant and renewable natural resource [1]. It is held together by a network of inter and intramolecular hydrogen bonds as well as van der Waals forces which enhances its mechanical properties thereby finding applications as fabric, paper, boards, and in biomedical field such as dressing [2–4]. As such, there is need to take advantage of cellulose intrinsic properties which include

reactivity, lightness, biodegradability, and biocompatibility, to synthesize cellulose derivatives. The hydroxyl groups present on the surface of cellulose are often subjected to different chemical treatments such as carboxymethylation, methylation, hydroxyethylation, 2,2,6,6-Tetramethylpiperidine 1-oxyl (TEMPO) oxidation and peroxidation [5]. When reacted with periodate ions (IO₄⁻) at given reaction conditions, the ions cleave the C₂–C₃ bonds of the anhydroglucose units (AGU) thereby converting hydroxyl groups present at these two positions into aldehyde groups [4, 6]. As a result, the amorphous regions of cellulose chains

Electronic supplementary material The online version of this article (<https://doi.org/10.1007/s42452-019-0769-9>) contains supplementary material, which is available to authorized users.

✉ Edwin Shigwenya Madivoli, edwinshigwenya@gmail.com | ¹Chemistry Department, Jomo Kenyatta University of Agriculture and Technology, P. O Box 62,000-00200, Nairobi, Kenya. ²Chemistry Department, McEwan University, 10700-104 Avenue, Edmonton, AB T5J 4S2, Canada. ³Department of Physical and Biological Sciences, Karatina University, P. O Box 1957-10101, Karatina, Kenya.



SN Applied Sciences (2019) 1:723

| <https://doi.org/10.1007/s42452-019-0769-9>

Received: 13 May 2019 / Accepted: 12 June 2019

SN Applied Sciences
A SPRINGER NATURE journal

Published online: 14 June 2019

APPENDIX XXXVI: PUBLICATION II

Journal of Inorganic and Organometallic Polymers and Materials
<https://doi.org/10.1007/s10904-019-01432-5>



Facile Synthesis of Silver Nanoparticles Using *Lantana trifolia* Aqueous Extracts and Their Antibacterial Activity

Edwin Shigwenya Madivoli¹ · Patrick Gachoki Kareru¹ · Anthony Ngure Gachanja¹ · Samuel Mutuura Mugo² · David Sujee Makhanu³ · Sammy Indire Wanakai¹ · Yahaya Gavamukulya⁴

Received: 28 November 2019 / Accepted: 26 December 2019
© Springer Science+Business Media, LLC, part of Springer Nature 2020

Abstract

Synthesis of metallic nanoparticles using secondary metabolites present in plant extracts has attracted attention. In this study, *Lantana trifolia* aqueous extracts were used to synthesize silver nanoparticles (AgNPs) which were then screened for their antimicrobial activity. The morphology, size and functional groups present in AgNPs was evaluated using electron microscopy and Fourier transform infrared spectroscopy (FT-IR). The role of temperature, reaction time and concentration of precursor ion were evaluated by measuring the surface plasmon resonance of AgNPs using UV-Vis spectroscopy. The crystal structure, hydrodynamic diameters and redox potential were evaluated using powder X-ray diffractometer (PWXRD), dynamic light scattering (DLS) and cyclic voltammetry respectively. The data obtained in this study revealed that increase in the reaction time led to an increase in surface plasmon resonance of AgNPs while the increase in temperature from 20 to 35 °C increased the rate of AgNPs synthesis. The XRD diffractogram revealed that the particles were composed of silver with $2\theta = 38.36, 44.428, 54.89, \text{ and } 57.87$, corresponding to the silver crystal planes of (111), (200), (220), and (311). The diameters of the nanoparticles were between 35 and 70 nm, and they had moderate antimicrobial activity against *E. coli*, *P. aeruginosa*, *C. albicans*, *S. aureus* and *B. subtilis*.

Keywords Silver nanoparticles · Morphology · Antimicrobial activity

1 Introduction

Bacterial resistance is a major public health concern because of its negative impact on the health care system as existing antibiotics lose efficacy [1]. Metallic nanoparticles effect

antimicrobial activity through membrane protein damage, super peroxide radicals or generation of ions that can interfere with cell granules. These particles have the potential to inhibit formation of advanced glycation end products and they can be used as anticancer therapies [2, 3]. Moreover, metallic nanoparticles such as silver nanoparticles (AgNPs) have been reported to alter the metabolic activity of bacteria and preventing biofilm formation [4]. The antibacterial characteristics of AgNPs are influenced by their size, shape, concentration and colloidal state. With respect to size, smaller nanoparticles have a large surface area in contact with the bacterial cells and they can reach the cytoplasm of the cell as compared to larger nanoparticles. Hence, for enhanced antibacterial activity, the size of the nanoparticles should be less than 50 nm but for the case of silver it has been reported that they have increased stability, biocompatibility and enhanced antimicrobial activity if their size is between 10 and 15 nm [5]. The AgNPs can be synthesized through electrochemical or photochemical reduction and by controlled chemical reduction of Ag ions in solution. These wet-chemical methods involve reduction of Ag ions in solution

Electronic supplementary material The online version of this article (<https://doi.org/10.1007/s10904-019-01432-5>) contains supplementary material, which is available to authorized users.

✉ Edwin Shigwenya Madivoli
edwinshigwenya@gmail.com

¹ Department of Chemistry, Jomo Kenyatta University of Agriculture and Technology, P.O Box 62, Nairobi 000-00200, Kenya

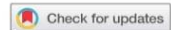
² Chemistry Department, McEwan University, 10700-104 Avenue, Edmonton, AB T5J 4S2, Canada

³ Department of Physical & Biological Sciences, Karatina University, P.O Box 1957-10101, Karatina, Kenya

⁴ Department of Biochemistry and Molecular Biology, Faculty of Health Sciences, Busitema University, P.O Box 1460, Mbale, Uganda

Published online: 01 January 2020

Springer



Isolation of Cellulose Nanofibers from *Oryza sativa* Residues via TEMPO Mediated Oxidation

Edwin S. Madivoli ^{a,b}, Patrick G. Kareru ^a, Anthony N. Gachanja ^a, Samuel M. Mugo ^c, David M. Sujee^d, and Katharina M. Fromm ^b

^aChemistry Department, Jomo Kenyatta University of Agriculture and Technology, Nairobi, Kenya; ^bDepartment of Chemistry, University of Fribourg, Fribourg, Switzerland; ^cChemistry Department, McEwan University, Edmonton, Alberta, Canada; ^dDepartment of Physical Sciences, Karatina University, Karuri, Kenya

ABSTRACT

Cellulose nanocrystals (CNCs) or cellulose nanofibers (CNFs) with different morphologies, chemical, mechanical and physical properties can be obtained when microcrystalline cellulose is subjected to enzymatic, chemical or mechanical treatment. With the aim of utilizing cellulose nanofibrils (CNFs) from *Oryza sativa*, we isolated microcrystalline cellulose using the Kraft process, followed by successive fiber fibrillation using mechanical grinding, then (2,2,6,6-Tetramethylpiperidin-1-yl)oxyl (TEMPO) mediated oxidation. Analysis of pulp fibers obtained after each treatment step revealed that fiber properties such as length, crystallinity and crystal size changed when the pulp was subjected to mechanical grinding, ultrasonication and TEMPO mediated oxidation. The degree of crystallinity of the fibers increased while crystal size and fiber length decreased after each treatment. TEMPO mediated oxidation led to a decrease in fiber length and an increase in degree of crystallinity of the fibers as compared to mechanical treatment and ultrasonication. It further introduced carboxyl functional groups (COOH) on the surface of the fibrils, which implies that the nanofibers obtained in this study could be further functionalized. Hence, TEMPO mediated oxidation offers the possibility of further chemical functionalization of cellulose nanofibers isolated from agricultural residues.

摘要

微晶纤维素经酶、化学或机械处理后，可以获得具有不同形貌、化学性质、机械性质和物理性质的纤维素纳米晶体(CNCs)或纤维素纳米纤维(CNFs)。为了利用来自水稻的纤维素纳米纤维(CNFs)，我们用牛皮纸法分离微晶纤维素，然后用机械研磨法连续纤维纤维颤，然后(2,2,6,6-四甲基哌啶-1-基)氧化(TEMPO)介导氧化。对每个处理步骤后得到的纸浆纤维进行分析，发现当纸浆经过机械研磨、超声波处理和TEMPO介导氧化处理后，纤维的长度、结晶度和晶体大小等特性发生了变化。各处理后纤维结晶度均有所提高，晶粒尺寸和纤维长度均有所减小。与机械处理和超声处理相比，TEMPO介导的氧化导致纤维长度缩短，纤维结晶度增加。进一步在纤维表面引入羧基官能团(COOH)，说明本研究得到的纳米纤维可以进一步功能化。因此，TEMPO介导氧化为进一步实现从农业残留物中分离的纤维素纳米纤维的化学功能化提供了可能。

KEYWORDS

Cellulose; morphology; particle size distribution


关键词

纤维素; 形态、particle size distribution 粒度分布

Introduction

There is great interest in the development of green, bio-based and biodegradable materials from natural resources to meet the demand for materials for engineering purposes (Collazo-Bigliardi,

CONTACT Edwin S. Madivoli  edwin.madivoli@jkuat.ac.ke  Chemistry Department, Jomo Kenyatta University of Agriculture and Technology, P.O Box 62,000-00200, Nairobi, Kenya

 Supplemental data for this article can be accessed on the publisher's website.

© 2020 Taylor & Francis


APPENDIX XXXVIII: PUBLICATION IV



Research Article

Phytofabrication of iron nanoparticles and their catalytic activity



Edwin Shigwenya Madivoli¹  · Patrick Gachoki Kareru¹ · Anthony Ngure Gachanja¹ · Samuel Mutuura Mugo² · David Sujee Makhanu³

© Springer Nature Switzerland AG 2019

Abstract

Metallic nanoparticles that have photocatalytic activity can be synthesized using aqueous plant extracts. The aim of this study was to synthesize iron nanoparticles using *Lantana trifolia* extracts and to evaluate their ability to degrade Congo red dye. The nanoparticles were characterized using UV–Vis spectrophotometer (UV–Vis), Fourier transform infrared spectrophotometer, wide angle X-ray diffractometer, dynamic light scattering, transmission electron microscopy (TEM), and thermal gravimetric analyzer to determine the functional groups, thermal properties, crystalline phases and diameter distribution of the particles. Cyclic voltammetry was used to evaluate the redox potential of the extracts while photocatalytic activity of the nanoparticles was evaluated using a UV–Vis spectrophotometer. Functional groups analysis revealed presence of secondary metabolites having OH and C=C groups while a redox potential of + 0.3 V was an indication that the extracts can reduce iron. The presence of sharp peaks at 2θ values of 19.87°, 20.22°, 22.88°, 28.81°, 32.73°, 35.32°, 38.45°, 40.23° and 41.08° correspond to cubic crystal system of iron nanoparticles while particle aggregation was observed on TEM micrographs which also indicated that they were less than 200 nm. In the presence of H₂O₂, the nanoparticles catalyzed degradation of Congo red dye in a first order reaction that was temperature dependent. In conclusion, secondary metabolites in *L. trifolia* can reduce metallic ion to iron nanoparticles which can degrade Congo red dye.

Keywords *L. trifolia* · Secondary metabolites · Iron nanoparticles · Photocatalyst

1 Introduction

Metallic nanoparticles have received great attention due to their unique physical, chemical and biological properties that makes them find applications in various fields such as medicine and in environmental remediation as photocatalysts [1]. During the past decade, many biological systems such as plants [2], algae [3], diatoms [4], bacteria [5], yeast [6], fungi [7], and human cells [8] have been used to transform inorganic metal ions into metal nanoparticles via the reductive capacities of the

metabolites found in these organisms. For iron nanoparticles, several physical and chemical production methods including mechanical milling [9], sodium borohydride [10, 11], ethylene glycol [12], solvothermal method [13], and carbothermal synthesis [14] have been employed for their preparation [15]. Iron nanoparticles synthesized by these methods rapidly agglomerate to form clusters due to interparticle Van der Waals and magnetic forces and may further undergo rapid oxidation [16, 17]. However, secondary metabolites found in plant extracts such as terpenoids, alkaloids, phenolic acids, polyphenols, sugars and

Electronic supplementary material The online version of this article (<https://doi.org/10.1007/s42452-019-0951-0>) contains supplementary material, which is available to authorized users.

✉ Edwin Shigwenya Madivoli, edwinshigwenya@gmail.com | ¹Chemistry Department, Jomo Kenyatta University of Agriculture and Technology, P.O. Box 62000-00200, Nairobi, Kenya. ²Chemistry Department, McEwan University, 10700-104 Avenue, Edmonton, AB T5J 4S2, Canada. ³Department of Physical and Biological Sciences, Karatina University, P.O. Box 1957-10101, Karatina, Kenya.



SN Applied Sciences (2019) 1:879

| <https://doi.org/10.1007/s42452-019-0951-0>

Received: 4 June 2019 / Accepted: 18 July 2019

Published online: 20 July 2019

SN Applied Sciences
A SPRINGER NATURE journal